CHARACTERISTICS OF CORN STARCH/CHITOSAN BLEND GREEN POLYMER ELECTROLYTES COMPLEXED WITH AMMONIUM IODIDE AND ITS APPLICATION IN ENERGY DEVICES

YUHANEES BINTI MOHAMED YUSOF

INSTITUTE OF GRADUATE STUDIES
UNIVERSITY OF MALAYA
KUALA LUMPUR

2017

CHARACTERISTICS OF CORN STARCH/CHITOSAN BLEND GREEN POLYMER ELECTROLYTES COMPLEXED WITH AMMONIUM IODIDE AND ITS APPLICATION IN ENERGY DEVICES

YUHANEES BINTI MOHAMED YUSOF

THESIS SUBMITTED IN FULFILMENT OF THE REQUIREMENTS FOR THE DEGREE OF DOCTOR OF PHILOSOPHY

INSTITUTE OF GRADUATE STUDIES
UNIVERSITY OF MALAYA
KUALA LUMPUR

2017

UNIVERSITY OF MALAYA
ORIGINAL LITERARY WORK DECLARATION

Name of Candidate: **YUHANEES BINTI MOHAMED YUSOF**

Matric No: **HHC120001**

Name of Degree: **Doctor of Philosophy (Ph.D)**

Title of Project Paper/Research Report/Dissertation/Thesis ("this Work"):

Characteristics of Corn Starch/Chitosan Blend Green Polymer

Electrolytes Complexed with Ammonium Iodide and Its Application in

Energy Devices

Field of Study: **Applied Science**

I do solemnly and sincerely declare that:

(1) I am the sole author/writer of this Work;
(2) This Work is original;
(3) Any use of any work in which copyright exists was done by way of fair dealing and for permitted purposes and any excerpt or extract from, or reference to or reproduction of any copyright work has been disclosed expressly and sufficiently and the title of the Work and its authorship have been acknowledged in this Work;
(4) I do not have any actual knowledge nor do I ought reasonably to know that the making of this work constitutes an infringement of any copyright work;
(5) I hereby assign all and every rights in the copyright to this Work to the University of Malaya ("UM"), who henceforth shall be owner of the copyright in this Work and that any reproduction or use in any form or by any means whatsoever is prohibited without the written consent of UM having been first had and obtained;
(6) I am fully aware that if in the course of making this Work I have infringed any copyright whether intentionally or otherwise, I may be subject to legal action or any other action as may be determined by UM.

Candidate's Signature   Date:

Subscribed and solemnly declared before,

Witness's Signature   Date:

Name:

Designation:

ABSTRACT

In the present work, a polymer electrolyte (PE) system comprises of corn starch/chitosan blend biopolymer electrolyte as host and ammonium iodide (NH_4I) as proton provider is prepared by solution casting technique. Fourier transform infrared spectroscopy (FTIR) analysis has proved the interactions between the components. The highest room temperature conductivity of $(3.04 \pm 0.32) \times 10^{-4}$ S cm^{-1} is obtained when the polymer host is doped with 40 wt.% NH_4I. The conductivity is further enhanced to $(1.28 \pm 0.07) \times 10^{-3}$ S cm^{-1} with the addition of 30 wt.% glycerol. Transport study has proved that the conductivity is influenced by the number density (n) and mobility of ions (μ). The conductivity-temperature analysis of all electrolytes is found to follow the Arrhenius rule. Dielectric studies confirm that the electrolytes obey non-Debye behavior. The ionic transference number measurement confirms that ion is the dominant conducting species. The cation transference number (t_+) for the highest conducting electrolyte (B3) is found to be 0.40. Thermogravimetric analysis (TGA) reveals that the plasticized electrolyte is stable up to 150°C. The characterization techniques including X-Ray diffraction (XRD), field emission scanning electron microscopy (FESEM) and differential scanning calorimetry (DSC) have verified the conductivity trend. Linear sweep voltammetry (LSV) is carried out prior to fabrication in electrochemical devices. B3 electrolyte is electrochemically stable up to 1.90 V and suitable to be applied in batteries and EDLCs. Cyclic voltammetry (CV) and galvanostatic charge-discharge measurements are carried out for EDLC characterization. The primary proton batteries are discharged at different constant currents while the secondary proton battery has been charged and discharged at 0.40 mA for 60 cycles.

ABSTRAK

Dalam penyelidikan kali ini, satu sistem elektrolit polimer (PE) yang terdiri daripada campuran kanji jagung/kitosan elektrolit biopolimer sebagai perumah dan amonium iodida (NH$_4$I) sebagai penyumbang proton telah dibangunkan melalui teknik penuangan larutan. Analisis spektroskopi inframerah transformasi Fourier (FTIR) telah membuktikan interaksi antara komponen-komponen. Kekoduksian tertinggi pada suhu bilik adalah $(3.04 \pm 0.32) \times 10^{-4}$ S cm^{-1} apabila perumah polimer itu dicampurkan dengan 40% berat amonium iodida. Kekonduksian ini kemudiannya ditingkatkan kepada $(1.28 \pm 0.07) \times 10^{-3}$ S cm^{-1} dengan penambahan 30% berat gliserol. Parameter pengangkutan telah membuktikan bahawa kekoduksian tersebut dipengaruhi oleh kepadatan dan mobility ion. Analisis kekonduksian (suhu) kesemua elektrolit ditemui mengikut hukum Arrhenius. Kajian dielektrik membuktikan bahawa semua elektrolit mematuhi teori tidak Debye. Pengukuran nombor pemindahan ion membuktikan bahawa ion adalah spesis koduksi yang dominan. Nombor pemindahan kation untuk elektrolit berkonduksi tertinggi (B3) adalah 0.40. Analisis gravimetri terma (TGA) mendedahkan bahawa elektrolit berplastik adalah stabil sehingga 150°C. Teknik-teknik pencirian termasuk teknik pembelauan sinar-X (XRD), pengimbas mikroskopi elektron (FESEM) dan pengimbas kalometri pembezaan (DSC) telah menyokong susunan kekonduksian. Pengimbasan voltametri linear (LSV) telah dijalankan sebelum fabrikasi dalam peralatan elektrokimia. Elektrolit B3 adalah stabil sehingga 1.90 V secara elektrokimia dan sesuai untuk aplikasi bateri dan EDLC. Kitaran voltametri (CV) dan pengukuran cas-nyahcas galvanostat telah dijalankan untuk pencirian EDLC. Bateri-bateri proton primer telah dicas pada arus malar yang berbeza manakala bateri proton sekunder telah dicas dan dinyahcas pada 0.40 mA untuk 60 kitaran.

ACKNOWLEDGMENTS

TABLE OF CONTENTS

LIST OF FIGURES

frequency region.

LIST OF TABLES

LIST OF SYMBOLS

A	: Pre-exponential factor		I_{SS}	: Steady state current
A_a	: Area of amorphous		J	: Current density
A_e	: Electrode-electrolyte contact area		k	: Boltzmann constant
A_T	: Area of total humps		l	: Distance between two coordinating sites
C	: Capacitance of CPE		m	: Mass of active material
C_0	: Vacuum capacitance		m_c	: Mass of charge carrier
C_1	: Capacitance at high frequency		M_i	: Imaginary parts of the electrical modulus
C_2	: Capacitance at low Frequency		M_r	: Real parts of the electrical modulus
C_s	: Specific capacitance		M^*	: Complex modulus Constant
d	: Interplanar spacing		n	: Number density of ions
e	: Electron charge		p	: Deviation of the plot from the axis
E_a	: Activation energy		p_1	: Deviation of the radius of the circle from the imaginary axis
E_{VTF}	: Pseudo-activation energy for conduction		p_2	: Deviation of the inclined adjacent line to the semicircle from the real axis
f	: Frequency		q	: Charge of ions
i	: Constant current		Q_S	: Specific discharge capacity
I_i	: Initial current			

r	: Internal resistance	V_0	: Potential at open circuit
R_b	: Bulk resistance	Z	: Valency of conducting species
R_c	: Charge transfer resistance	Z_{CPE}	: The impedance of CPE
R^2	: Regression value	Z_i	: Imaginary parts of Impedance
s	: Power law exponent	Z_r	: Real parts of impedance
t	: Thickness	Z^*	: Complex impedance data
t_e	: Transference number of electron	σ	: Conductivity
t_{ion}	: Transference number of ion	ε^*	: Complex dielectric Constant
t_{Mi}	: Relaxation time of M_i	ε_r	: Dielectric constant
$t_{plateau}$	: Discharge time at plateau region	ε_0	: Vacuum permittivity
t_+	: Transference number of cation	χ_c	: Degree of crystallinity
T	: Absolute temperature	ω	: Angular frequency
T_g	: Glass temperature	ω_{peak}	: Angular frequency of the M_i relaxation peak
T_0	: Ideal glass transition temperature	σ_{dc}	: Frequency independent dc conductivity
τ	: Travelling time of ions	μ	: Ionic mobility
υ_{as}	: Asymmetry vibration	λ	: Wavelength
υ_s	: Symmetry vibration	θ	: Bragg's angle
v	: Velocity of mobile ions		

LIST OF ABBREVIATIONS

ac	: Alternating current	EIS	: Electrochemical impedance spectroscopy
Al_2O_3	: Aluminium oxide	EMITf	: 1-ethyl-3-methylimidazolium trifluoromethane-sulfonate
BATS	: Butyltrimethyl ammonium bis(trifluromethyl sulfonyl) imide	ESR	: Equivalence series Resistance
$C_2H_4O_2$	: Acetic acid	FESEM	: Field emission scanning electron microscopy
CBH	: Correlated barrier Hopping	FTIR	: Fourier transform infrared
CMC	: Carboxymethyl Cellulose	H	: Hydrogen
CO_2	: Carbon dioxide	H_3O_+	: Hydronium ion
CPE	: Constant phase element	H_2O	: Water
Cu	: Copper	H_2SO_4	: Sulphuric acid
CV	: Cyclic voltammetry	H_3PO_4	: Phosphoric acid
dc	: Direct current	HCl	: Hydrochloric acid
DSC	: Differential scanning calorimetry	Li	: Lithium
EC	: Ethylene carbonate	$Li_2B_4O_7$	: Lithium tetraborate
EDLC	: Electrochemical double layer capacitor	LiBOB	: Lithium bis-(oxalato) borate

LiCF$_3$SO$_3$	: Lithium triflate	NH$_4$I	: Ammonium iodide
LiI	: Lithium iodide	NH$_4$NO$_3$	: Ammonium nitrate
LiPF$_6$	: Lithium hexa-fluorophosphate	NH$_4$SCN	: Ammonium thiocyanate
LiTf	: Lithium triflate	Ni	: Nickel
LSV	: Linear sweep voltammetry	NMP	: N-methyl pyrrolidone
MC	: Methylcellulose	OH$^+$	: Hydroxide ion
Mg	: Magnesium	OCP	: Open circuit potential
Mg(Tf)$_2$	: Magnesium triflate	PAN	: Polyacrylonitrile
MH	: Metal hydride	PC	: Propylene carbonate
MnO$_2$	: Manganese (IV) dioxide	PCL	: Poly ε–caprolactone
MWCNT	: Multiwalled carbon nanotube	PE	: Polymer electrolyte
Na	: Sodium	PEG	: Polyethylene glycol
NH$_4$Br	: Ammonium bromide	PEGDE	: Polyethylene glycol dimethylether
NH$_4^+$	: Ammonium ion	PEO	: Polyethylene oxide
N	: Nitrogen	PMA	: Polymethacrylate
NH$_4$CF$_3$CO$_3$	: Ammonium trifluromethane sulfonate	PMMA	: Polymethyl methacrylate
NH$_4$Cl	: Ammonium chloride	PTFE	: Poly-tetrafluoroethylene
NH$_4$ClO$_4$	: Ammonium perchlorate	PVA	: Polyvinyl alcohol
NH$_4$CH$_3$COO	: Ammonium acetate	PVAc	: Polyvinyl acetate
NH$_4$F	: Ammonium flouride		

PVdF	: Polyvinylidene fluoride
PVP	: Poly N-vinyl pyrrolidone
SPH	: Small polaron hopping
TGA	: Thermogravimetric analysis
TiO_2	: Titanium dioxide
TNM	: Transference number measurement
VTF	: Vogel-Tamman-Fulcher
V_2O_5	: Vanadium (V) Oxide
wt	: weight
XRD	: X-Ray diffraction
Zn	: Zinc
ZnO	: Zinc Oxide
$ZnSO_4 \cdot 7H_2O$	: Zinc sulphate heptahydrate

CHAPTER 1: INTRODUCTION

1.1   Research Background

Polymer electrolytes are ionic conductors which formed by salts dissolution in suitable polymers (Vincent, 1987). The phenomenon of ionic conductivity in solid state was identified by Michael Faraday in 1800s. In chemistry, solid state ionic was viewed as very successful solid state physics (Armand, 1994). A polymer chemist from Sheffield; Peter V. Wright first showed in 1975 that poly-ethylene oxide (PEO) can act as a host for the conduction of sodium and potassium ions, thus producing a solid electrical conductor polymer/salt complex (Wright, 1975). Michel Armand who had introduced the graphite intercalation compounds for electrodes was then realized that lithium/PEO complexes could be employed as solid electrolytes matching with perfect intercalation electrodes. This was a breakthrough and the beginning of a new world of polymer electrolytes, which encouraged researchers all over the world to work in this emerging branch of solid state ionics.

Since then, a large number of new ion conducting polymer electrolytes with mobile ions such as hydrogen, H^+ (Shukur, Ithnin, & Kadir, 2014); lithium, Li^+ (Teoh, Ramesh, & Arof, 2012); magnesium, Mg^{2+} (Jaipal Reddy & Chu, 2002) and sodium, Na^+ (Bhide & Hariharan, 2007) have been reported and their potential utility in various solid state electrochemical devices such as batteries (Ng & Mohamad, 2006; Kadir, Majid, & Arof, 2010; Jamaludin & Mohamad, 2010), fuel cells (Urban, Funke, Müller, Himmen, & Docter, 2001) , electrochemical double layer capacitor (EDLC) (Shukur, Ithnin, Illias, & Kadir, 2013; Arof et al., 2012; Pandey, Kumar, & Hashmi, 2011), dye-sensitized solar cells (Jayaweera et al., 2015; Yang et al., 2006) and sensors (Vonau et

al., 2012) have been demonstrated. In all electrochemical devices, polymer electrolytes act as electrode separator and provide fast transportation and electronic insulation of the ions between the electrodes (Ravindran, Vickraman, Sankarasubramanian, & Sornakumar, 2015).

Recently, a series of explosion of Samsung devices; a world well-known brand, has been reported due to batteries, which create stains on the company's reputation (Cheng, Jeong, & Dou, 2016). Polymer industry has issues regarding disposal of wastes which contribute towards environmental pollutions (Sakurai et al., 2000). In fact, in recent years, people around the world have started to develop materials that will not harm the environment, including in polymer industry. Natural polymers from renewable agriculture resources have attracted more attentions due to the environmental concern including the efforts towards producing the degradable garbage, protection of climate through the reduction of CO_2 released as well as the possible applications of agricultural resources for bioplastics production (Lörcks, 1998). Electrochemical energy production has been considered as an alternate energy sources since it is sustainable and environmental friendly. Moreover, the miniaturization and portable electronic devices such as laptop computers, calculators, cellular phones and digital watches have increased the demand for light weight rechargeable batteries (Ravindran et al., 2015).

In this work, polymer electrolyte (PE) based on natural polymers; starch/chitosan blend has been studied. Little attention has been paid towards proton-conducting polymer electrolytes using halides salts. To prepare the salted system, ammonium iodide (NH_4I) was doped in the most amorphous polymer blend to provide the charge carriers, H^+. Based on our knowledge, NH_4I has never been reported as proton provider in the fabrication of proton batteries and EDLC by other researchers.

The highest conducting electrolyte was then plasticized with glycerol to further enhance the conductivity. The highest conducting electrolyte in the plasticized system was fabricated in EDLC and proton batteries. Characterizations have been carried out thoroughly to understand and correlate the conductivity with other characteristics.

1.2   Objectives of the Thesis

The objectives of this work are as follows:

1. To prepare proton conducting starch/chitosan based polymer electrolytes from natural sources using solution cast technique.

2. To develop a polymer electrolyte system with improved conductivity by the addition of glycerol as plasticizer.

3. To evaluate the characteristics of the electrolytes using various techniques including thermogravimetric analysis (TGA) , differential scanning calorimetry (DSC), X-ray diffraction (XRD), field emission scanning electron microscopy (FESEM), fourier transform infrared (FTIR) and electrochemical impedance spectroscopy (EIS).

4. To fabricate and to evaluate the performance of proton batteries and EDLC.

1.3   Scope of the Thesis

This thesis is divided into 11 chapters. Chapter 1 describes briefly on the main objectives and the scope of this research. Chapter 2 focuses on the literature review, the overview of the previous and recent studies in polymer electrolytes and the introduction to the materials used in this work. Chapter 3 describes the details of the sample preparations and the techniques of characterizations involved in this work including

TGA, DSC, XRD, FTIR, FESEM and EIS. The methods of fabrication and characterizations of EDLC and proton batteries are also discussed in this chapter. Chapter 4 discusses the characterization of polymer blend prior to the selection of the most amorphous and miscible electrolyte to be doped with salt by using FTIR, XRD, TGA, DSC and FESEM. Chapter 5 discusses the FTIR results based on the interactions involved between starch, chitosan, NH_4I and glycerol. The electrical characteristics of the polymer electrolytes are discussed in Chapter 6. All important parameters such as impedance studies, high temperature conductivity, transference number and transport parameters are discussed in this chapter. Further electrical studies including dielectric constant, dielectric loss, electrical modulus and conduction mechanism are also discussed in this chapter. TGA and DSC results are presented in this chapter to support the conductivity trends in term of thermal stability of the electrolytes. XRD and FESEM results are presented and discussed in Chapter 7. The highest conducting polymer electrolyte is fabricated in electrochemical devices and the results are presented in Chapter 8. In Chapter 9, all results presented in the thesis are summarized and discussed shortly for better understanding. Chapter 10 concludes the thesis and some suggestions for future work.

CHAPTER 2: LITERATURE REVIEW

2.1   Introduction

An electrolyte is a substance that contains positively charged species (cation) and negatively charged species (anion) and acts as a medium for transferring the charges between a pair of electrodes (Subramaniam, Morris, Yee, & Chiam-Wen, 2012). These electrolytes are basically polymers containing salts, acids, plasticizer composite fillers and/ or ionic liquids which can provide ions in a system or device. A good electrolyte should satisfy few requirements including high ionic conductivity, compatibility with electrode material and wide electrochemical stability (Bhargav, Mohan, Sharma, & Rao, 2009). Ionic conductors or electrolytes are one of the crucial key components in electrochemical devices since ionic conduction has strong influence on a device performance (Hofmann, Schulz, & Hanemann, 2013; Rao, Geng, Liao, Hu, & Li, 2012).

Liquid electrolyte has been studied as a substance that conducts the electricity in an aqueous solution by migrating both cations and anions to the opposite electrodes (Subramaniam et al., 2012). Liquid electrolytes are preferable due to their high ionic conductivity (Deepa et al., 2002; Perera & Dissanayake, 2006). However, electrochemical devices that employs liquid electrolyte are exposed to weaknesses such as leakage, corrosion, solvent evaporation and hazardous to the environment (Chen, Lee, Vittal, & Ho, 2010; Freitas, Gonçalves, De Paoli, Durrant, & Nogueira, 2008). Many researchers have been searching for alternatives to replace liquid electrolytes such as inorganic or organic hole conductors (Kroeze et al., 2006), ionic liquids (Yamanaka et al., 2007) and polymer electrolyte or PE (Winie, Ramesh, & Arof, 2009). PEs have received wide attention for their thermal stability, the absence of corrosive solvent and

harmful gas, ease of fabrication, low volatility and easy to be handled (Gao & Lian, 2010; Winie et al., 2009).

2.2   Polymer Electrolytes (PE)

Polymer electrolyte (PE) is generally known as a membrane that possesses transport properties which can undergo two stages; dry solid-state polymer and gel/ plasticized polymer electrolyte (Stephan, 2006). PE is expected to replace the conventional liquid in the future due to its shape versatility, dimensional stability, easy to produce, film flexibility, electrochemical stability, safe in handling and life-long (Wu & Chang, 2007). Interactions of metal ions with polar polymers are mainly due to electrostatic forces and the formation of coordinating bonds (Rivas, Pereira, & Moreno-Villoslada, 2003). Polymer electrolytes have shown tremendous potential in the development of various kinds of electrochemical devices in the last 25-30 years. They possess high ionic conductivity which exceeds 10^{-5} S cm^{-1} with solid free-standing films, which is comparable to the conductivity of liquid electrolytes (Przyłuski & Wieczorek, 1991). These qualities establish PE as a potential candidate to be used in larger scale of electrochemical applications (Sudhakar & Selvakumar, 2012).

Proton conducting polymer electrolytes obtained by polar polymer-salt complexation have received considerable attention and have been extensively investigated for advanced electrochemical applications such as high energy density batteries, sensors and fuel cells (Colomban, 1992; MacCallum & Vincent, 1989). Other than Li$^+$ ion, combining ammonium salts with polymers is believed can produce good proton (H$^+$) ion conducting polymer electrolytes (Hashmi, Kumar, Maurya, & Chandra, 1990; Singh, Chandra, & Chandra, 2002). In order to enhance the ionic conductivity,

various approaches have been pursued including: (a) varying the polymers used for polymer blend (Kadir et al., 2010), (b) doped with different salts (Hema, Selvasekarapandian, Arunkumar, Sakunthala, & Nithya, 2009) (c) modify the degree of crystallinity by varying the ratios of polymers, salts or plasticizers (Shukur, Ithnin, & Kadir, 2014b), (d) plasticized the polymer electrolytes with high dielectric constant material (Shukur et al., 2013) and (e) form composite polymer electrolytes by the dispersion of nano or micron sized inert fillers (Ravindran et al., 2015).

The fundamental of ionic conduction in the polymer electrolytes is related to the covalent bonding between the polymer backbones and ions (Velazquez-Morales, Le Nest, & Gandini, 1998). The electron donor group in the polymer will form solvation onto the cation component in the doping salt and followed by the ion separation; leading to the ions hopping mechanism which then generates the ionic conductivity (Ganesan et al., 2008). However, if the ions are immobile and unable to move around, they may become poor conductors. Therefore, the polymer host should become a flexible form to provide enough space for the ions migration. PE serves three principal roles in a rechargeable battery. Firstly, it acts as the electrode separator that insulates the anode from the cathode in the battery which removes the requirement of inclusion of inert porous membrane between the electrolytes and electrodes interface (Walker Jr & Salomon, 1995). Secondly, it plays the role as a channel to generate ionic conductivity where ions are transported between the anode and cathode during charging and discharging (Xu, 2004). This induces the enhancement of energy density in the batteries with formation of thin film. In addition, it works as a binder to ensure good electrical contact with electrodes (Walker Jr & Salomon, 1995; Xu, 2004).

2.3   Natural Polymers

Natural polymers obtained from renewable sources have attracted attention from researchers in various material applications (Chang & Zhang, 2011; Hejazi & Amiji, 2003). The significance of eco-friendly materials has evolved over the last decade mainly due to environmental concerns and the realization of the petroleum resource shortage (Yu, Dean, & Li, 2006). The biodegradability of natural polymers is very crucial in the subject of controlling the environment which can prevent the premature degradation of the polymers used (Sudhakar, Selvakumar, & Bhat, 2013). Natural polymers such as protein and starch are the potential alternatives to petroleum-based polymers for certain applications (Yu et al., 2006). The continuous use of non-biodegradable polymer has caused serious issues regarding the earth-environment (Lu, Xiao, & Xu, 2009). The development of synthetic polymers by using monomers from natural resources also provides wide options of biodegradable polymers such as polyvinyl alcohol (PVA), polyethylene oxide (PEO), polyvinyl chloride (PVC) and polyvinylidene fluoride (PVdF) (Yu et al., 2006). However, the expensive price of these synthetic polymers demands us to continue with natural polymers as the main materials (Lu et al., 2009). PEs which produced from natural polymers for instance starch, chitosan, pectin and cellulose have aroused a lot of attentions due of their low prices, stability and good mechanical and electrical properties (Pawlicka, Sabadini, Raphael, & Dragunski, 2008; Tambelli et al., 2001; Velazquez-Morales et al., 1998).

Modern technologies create the opportunities to develop these biodegradable materials for applications in industrial and biomedical sectors (Tian, Tang, Zhuang, Chen, & Jing, 2012; Vroman & Tighzert, 2009). Some of them including starch, cellulose, chitosan and rubber, have been used widely today but many others remain

underutilized. Table 2.1 lists some other natural polymers and their applications in various fields.

Table 2.1: Examples of natural polymers and their applications.

Applications	Natural Polymers	References
Tissue Engineering	Collagen, glycosaminoglycans, Chitosan	Malheiro, Caridade, Alves, & Mano, 2010; Sarasam & Madihally, 2005; Sell et al., 2010; Suh & Matthew, 2000
Biomaterials	Chitosan	Martino, Pollet, & Avérous, 2011; Matet, Heuzey, Pollet, Ajji, & Avérous, 2013
Packaging	Starch, chitosan	Leceta, Guerrero, & De La Caba, 2013; Salleh, Muhamad, & Khairuddin, 2009; Tuhin et al., 2012
Agriculture	Starch, chitosan	Amaka et al., 2013; Dehnad, Mirzaei, Emam-Djomeh, Jafari, & Dadashi, 2014
Medication	Chitosan	Berger et al., 2004; Hejazi & Amiji, 2003
Fabrication in devices	Starch, cellulose, chitosan	Liew & Ramesh, 2015; Samsudin, Khairul, & Isa, 2012; Shukur et al., 2013

2.4 Starch

Starch is a green polysaccharide polymer which stored as granules in plants and served as the principle energy and carbohydrate in human and animal diets (Khiar & Arof, 2010). It is one of the most abundant biopolymers on earth which also inherent biodegradability and renewability. It is mainly composed of amylose; a linear (α-(1,4)-

linked D-glucopyranosyl) and branched amylopectin; with the same backbone structure of amylose but joint through α-(1,6)-linked polysaccharide chains (Pawlicka et al., 2008). The structures of amylose and amylopectin are shown in Figure 2.1.
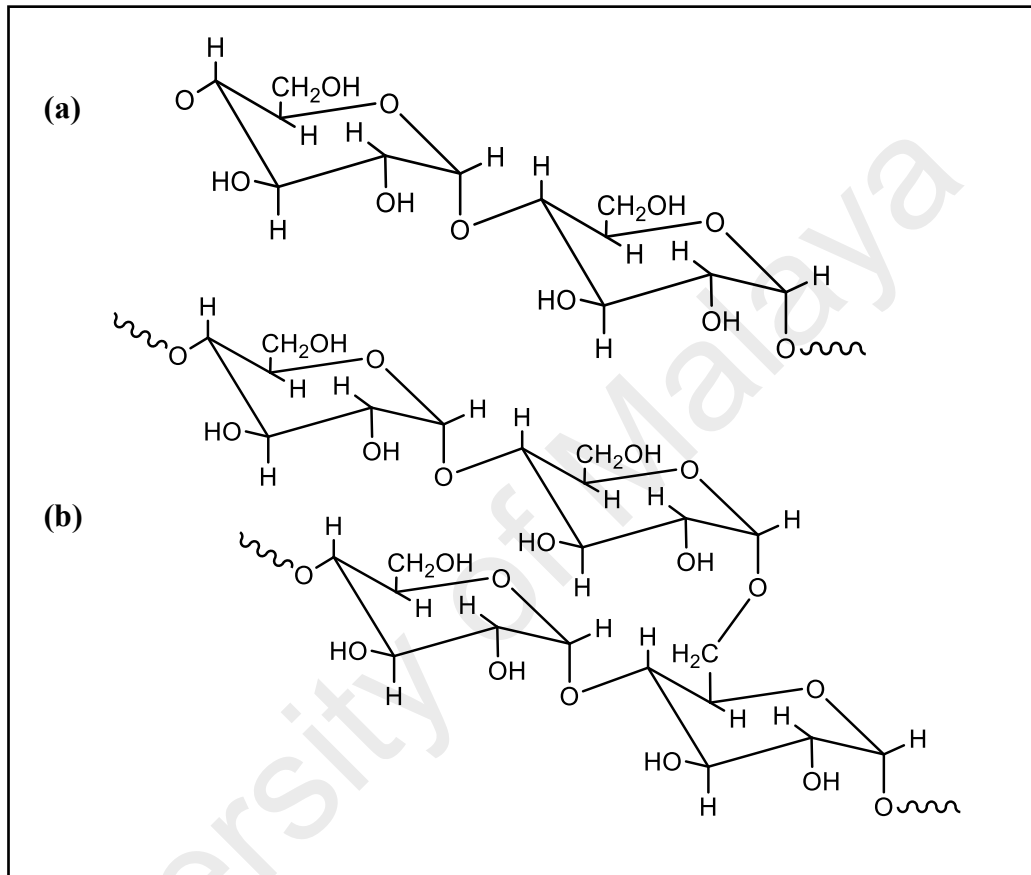
Figure 2.1: Molecular structure of (a) amylose and (b) amylopectin.

The relative amount of these substances however is depending upon the plant sources (Avella et al., 2005). Different types of starch sources such as potato, wheat, arrowroot and corn starches have been widely used (Tiwari, Srivastava, & Srivastava, 2011). Among these sources, corn starch has received the biggest attention because of availability, renewability, easily degradable and low in cost (Ghanbarzadeh, Almasi, & Entezami, 2010; Khiar & Arof, 2010).

2.4.1 Starch-Based Polymer Electrolyte

Since 1970s, starch has been incorporated with synthesized polymer matrix to convert starch into thermoplastic materials (Sen & Bhattacharya, 2000). Hydroxyl groups which are dominant in starch are available for reactions with alcohol and may participate in the formation of hydrogen bonds (Lu et al., 2009). Researchers discovered that starches derived from different botanical sources are various in composition, structure and polysaccharide constituents hence different in functionalities (Elgadir et al., 2012). It is proven that starch with high amylose content is highly amorphous compared to the starch with high amylopectin (Park, Ibáñez, Zhong, & Shoemaker, 2007). Amylopectin contains packing arrangement of double helices with high molecular weight which lowered the mobility of the polymer chains hence increased the crystalline phase (Liu, Xie, Yu, Chen, & Li, 2009; Richardson & Gorton, 2003). Corn starch contains 27 % of linear amylose which is higher compared to other types of starches, for instance, potato starch with 20 % amylose and tapioca with 17% amylose (Association, 2006). In polymer electrolytes, amorphous region is desirable that in turn will favor the ionic mobility which promoted by the segmental motion of the polymer host (Armand, 1994; Vincent, 1987). The application of starch in polymer electrolyte field has been investigated, as listed in Table 2.2.

Table 2.2: Review of earlier work on starch-based polymer electrolytes.

Electrolyte Composition	Conductivity, σ (S cm^{-1})	Devices	References
Starch-NH$_4$NO$_3$	2.83×10^{-5}	-	Khiar & Arof, 2010
Corn starch-LiClO$_4$-SiO$_2$	1.23×10^{-4}	-	Teoh et al., 2012
Potato starch-NH$_4$I	2.40×10^{-4}	-	Kumar, Tiwari, & Srivastava, 2012
Corn starch-LiOAc-glycerol	1.04×10^{-3}	EDLC	Shukur et al., 2014b

2.5   Chitosan

In recent years, chitosan receives a lot of interests in various fields, including in biomedicine, pharmaceutical and biotechnology (Berger et al., 2004; Burke, Yilmaz, Hasirci, & Yilmaz, 2002). Chitosan is one of the most abundant biopolymers in nature which is non-toxic, edible and biodegradable (Yu et al., 2006). Chitosan consists a lot of hydroxyl and amino groups, where both groups are possible to be grafted with desirable bioactive groups (Sugimoto, Morimoto, Sashiwa, Saimoto, & Shigemasa, 1998). It is a high molecular weight polysaccharide mainly composed of β-(1,4)-linked 2-amino-deoxy-D-glucopyranose which prepared by deacetylation of chitin (Berger et al., 2004; Sugimoto et al., 1998). The structure of chitosan is rigid through inter and intra molecular hydrogen bonding (Hejazi & Amiji, 2003). The structures of chitin and chitosan are shown in Figure 2.2.
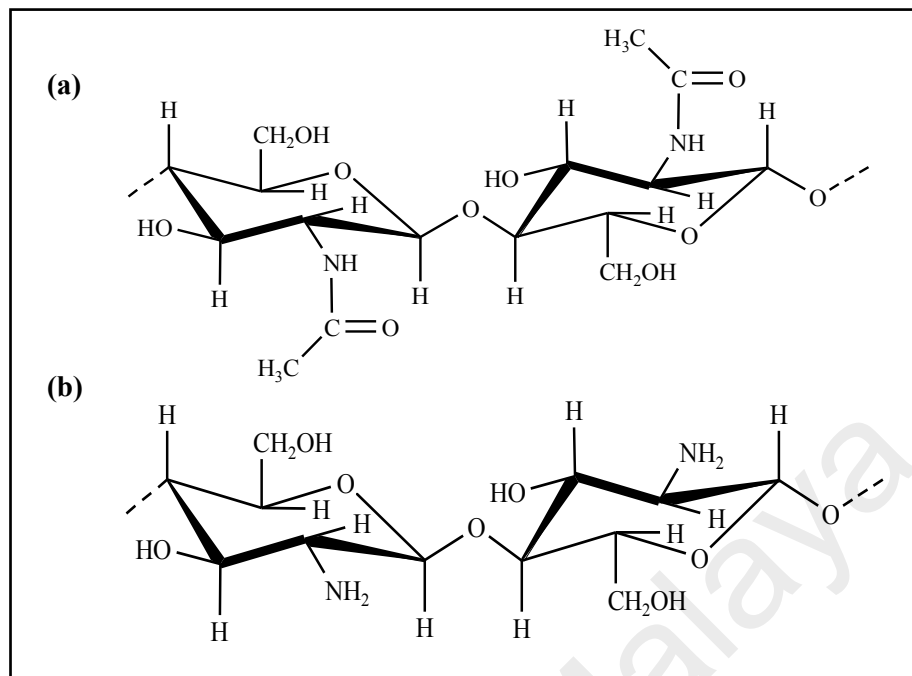
Figure 2.2: Structure of (a) chitin and (b) chitosan.

2.5.1 Chitosan-Based Polymer Electrolyte

Chitosan is naturally soluble in water. However the solubility depends on the degree of deacetylation of the solution. Chitosan with low degree of deacetylation contains low hydrogen bonding density because of the low number of amino groups in the polymer chains (Hejazi & Amiji, 2003). Chitosan can also be dissolved in some organic and inorganic acids and protonated at amino groups on the pyranose ring (Tuhin et al., 2012). The degree of deacetylation is believed could affect the rigidity of the polymer film (Chen, Lin, & Yang, 1994). The application of chitosan in polymer electrolyte field has received much attention, as listed in Table 2.3.

13

Table 2.3: Review of earlier works on chitosan-based polymer electrolytes.

Electrolyte Composition	Conductivity, σ(S cm^{-1})	Devices	References
Chitosan-iota-carrageenan-H$_3$PO$_4$-PEG	6.29×10^{-4}	EDLC	Arof, Shuhaimi, Alias, Kufian, & Majid, 2010
Chitosan acetate- H$_3$PO$_4$	4.90×10^{-4}	-	Majid & Arof, 2007
Chitosan acetate-AgNO$_3$	2.60×10^{-5}	Battery	Morni, Mohamed, & Arof, 1997
Chitosan-PEG-LiClO$_4$-EC-PC	1.10×10^{-4}	Supercapacitor	Sudhakar et al., 2013

2.6   Polymer Blending

Natural polymers mostly found as non-toxic and biocompatible due to their similarity with living tissues. However, some characteristics give major drawbacks to these biodegradable polymers including fast degradation rate, hydrophilic character and poor mechanical properties (Yu et al., 2006). Blend films are composed of two or more biopolymers and prepared by varying methods, such as multilayer procedures, conventional blends and injection moulding (Ban, Song, Argyropoulos, & Lucia, 2006; Famá, Gerschenson, & Goyanes, 2009; Vilaseca et al., 2007). New products prepared by a low cost and well used but promising techniques are required to improve and modify the physical and functional properties of the polymers. These new blends are extending the utilization of polymers from renewable resources into value-added products. The main objective of this method is to prepare a polymer blend with maximum performance without changing the properties of each component drastically.

2.6.1 Starch/chitosan Blend

Researchers have developed the blends of starch and polyolefins in 1970s and 1980s, but since the blends were not biodegradable, the objective of this method was considered failed (Yu et al., 2006). The research on polymer blend was continuously been carried out since then. According to previous researchers, when two or more biopolymers are blended together, the blends behaved differently compared to when they are presented individually (De Kruif & Tuinier, 2001; Elgadir et al., 2012; Piculell, Bergfeldt, & Nilsson, 1995). Starch granules are insoluble in cold water due to their semicrystalline structure. Heating of the aqueous suspension of starch will cause the swelling of the granules and disruption of the crystalline areas (Richardson & Gorton, 2003). However, excess of heating process results in irreversible swelling and will destroy the granules. The viscosity increases as the swelling of the granules increases. This process is called as gelatinization which is an important property of starch (Liu et al., 2009; Richardson & Gorton, 2003). Gelatinization is also known as the destruction of the crystalline structure in starch granules (Zobel, Young, & Rocca, 1988). Starch has been widely used to produce biodegradable films to replace plastic polymers due to its low cost and renewability (Xu, Kim, Hanna, & Nag, 2005). These films exhibit many similar characteristics with synthetic polymers such as odorless, tasteless, resistant to oxygen and transparent (Salleh et al., 2009). However, the application of starch is limited due to its sensitivity to moisture and brittleness (Xu & Hanna, 2005).

In order to overcome the weaknesses, many researchers have blended starch with other biopolymers (Jagannath, Nanjappa, Das Gupta, & Bawa, 2003; Liu et al., 2009; Lu et al., 2009; Mathew & Abraham, 2008). Chitosan which is commercially available from shellfish waste was discovered can form a good biopolymer film in term

of availability, mechanical strength, flexibility, nontoxic and biocompatibility (Mathew & Abraham, 2008; Salleh et al., 2009). Combining chitosan with other film-forming materials can improve the functional properties of chitosan films (Xu et al., 2005). This film can retain its integrity by maintaining the inter and intramolecular network (Stuchell & Krochta, 1994).

In a report by Xu et al. (2005), a study on water resistance, mechanical properties and compatibility of composite films based on starch and chitosan has been carried out. They found that the interactions between starch and chitosan can form a tough film which prevents the water molecules from diffusing through the films. The mechanical strength of starch film is believed can be improved when the starch is well-mixed with chitosan and consequently, the crystallinity region of the components is suppressed (Mathew & Abraham, 2008). Starch/chitosan blend films exhibit good properties due to the presence of a high density of amino groups and hydroxyl groups with inter and intra molecular hydrogen bondings (Lu et al., 2009). In polymer electrolyte, works by Khiar & Arof (2011) and Shukur, Majid, Ithnin, & Kadir (2013) obtained good conductivity values (10^{-5}) when they doped the starch/chitosan films with ammonium salts which proves that this is a promising blend for polymer electrolyte.

2.6.2   Acetic Acid as Solvent

Water solubility is one of the characteristics possessed by most natural polymers which contribute in raising their degradability and degradation speed. However, this characteristic contributes in limiting their application (Yu et al., 2006). Starch is one of the examples where its hydrophilicity behavior leads to poor mechanical properties in a humid environment (Tian et al., 2012). In order to improve the mechanical properties,

16

chemical modifications are required. One of the methods that have received attentions in recent years is acetylation. By acetylation, the hydrophilic hydroxyl groups in the anhydroglucose units of starch are converted to more hydrophobic acetyl groups, consequently improved the functional properties even though at low degree of substitution (Vroman & Tighzert, 2009). An acetylation process with a relatively low degree of substitution has been widely used in the food industries (Yang et al., 2006). Pretreatment with hot water with or without the presence of catalysts in order to activate the starch molecule is sometimes necessary to influence the reaction rate (Tabuchi, Saito, Kibi, & Ochi, 1993). Sugimoto et al. (1998) also reported that chitosan modified with PEG and acetylated using 2% acetic acid solvent has increased the solubility of chitosan.

Acetic acid is the simplest carboxylic acid with chemical formula $C_2H_4O_2$, as shown in Figure 2.3. Acetic acid can easily dissolve in water due to its low molecular weight and carboxylic structure. The carbonyl groups are expected to act as proton donors and exhibits low levels of hydration. Hence, many studies have been performed on proton-conducting electrolytes using acetic acid as solvent (Arof et al., 2010; Nik Aziz, Idris, & Isa, 2010). Polymer blending using 2% acetic acid as solvent has been reported to exhibit films with good mechanical strength (Bel'Nikevich, Bobrova, Bronnikov, Kalyuzhnaya, & Budtova, 2004). Shukur et al. (2013) have reported that blending starch/chitosan using acetic acid as solvent produced a polymer electrolyte film with good performance. Qiao, Yoshimoto, Ishikawa, & Morita (2002) also reported that the conductivity of the proton conducting polymeric gel membranes based on polyethylene oxide-modified polymethacrylate (PEO-PMA) containing polyethylene glycol dimethylether (PEGDE) and acetic acid as the doping solution is 6.20×10^{-4} S cm^{-1} at 20˚C.
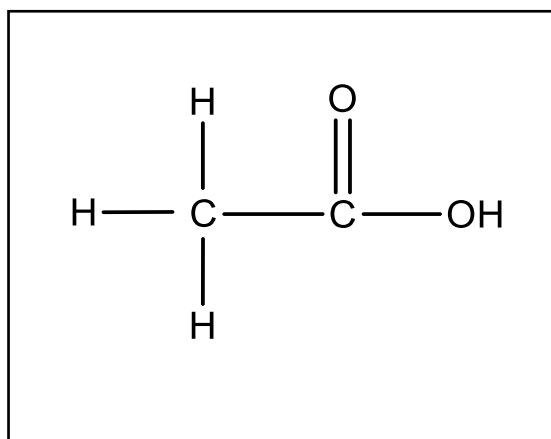
Figure 2.3: Structure of acetic acid.

2.7   Ammonium Iodide (NH₄I) As Proton Provider

Various complexes of polymeric matrices with strong, inorganic acids such as H_3PO_4, HCl and H_2SO_4 as proton provider have been investigated. However, conductivity which is less than 10^{-4} S cm^{-1} at room temperature is usually obtained (Kawahara, Morita, Rikukawa, Sanui, & Ogata, 2000). Over-oxidation of the anions from the strong acids has destroyed these polymer electrolyte films (Qiao et al., 2002; Raducha, Wieczorek, Florjanczyk, & Stevens, 1996; Trivedi, 1998). Since this type of polymer complexes suffer from chemical degradation and mechanical integrity, one can concludes that it is not a good choice for devices applications (Hema, Selvasekerapandian, Sakunthala, Arunkumar, & Nithya, 2008).

A polymer electrolyte which is prepared by dissolving a salt in a polymeric matrix is a method that has been widely performed. The dissociation of salt can be achieved either by using volatile solvents or by the same polymer whose atoms can be interacted with cations and separate them from the corresponding anions (Mendoza,

Paraguay-Delgado, & Hu, 2012). Most of the previous studies were focused on complexes of polymer with lithium salts such as $LiClO_4$ (Deepa et al., 2002; Sudhakar et al., 2013; Teoh et al., 2012), $LiCF_3SO_3$ (Perera & Dissanayake, 2006), $Li_2B_4O_7$ (Subramaniam et al., 2012) and LiI (Shukur, Ibrahim, Majid, Ithnin, & Kadir, 2013) where the electrical conductivity was determined as a function of salt concentration. However, producing these Li batteries faces a few drawbacks including requires high cost and having difficulty in handling and safety issues (Mishra, Hashmi, & Rai, 2014; Samsudin et al., 2014; Walker Jr & Salomon, 1995).

The proton (H^+) conducting polymer electrolytes have been widely studied for their potential applications in low current density devices (Ng & Mohamad, 2008). This is due to the low cost of electrode and electrolyte materials for developing a proton battery (Alias, Chee, & Mohamad, 2014; Samsudin et al., 2014). Proton batteries have been considered as a potential option due to the small ionic radii of the H^+ ions which in turn provide a better intercalation into the cathode surface (Mishra et al., 2014). Ammonium salts have already been reported as a good proton donor to the polymer-ammonium salts complexes (Kadir et al., 2010; Shukur et al., 2013). The protonic transport in these polymer electrolytes generally involves motion of groups like H^+, NH_4^+, H_3O^+ and OH^+ (Selvasekarapandian, Hirankumar, Kawamura, Kuwata, & Hattori, 2005). Many complexes of ammonium salt with different types of polymers have been investigated in various fields of research, as can be seen in Table 2.4. The protons (H^+) in polymer-ammonium complexes are covalently bound to the nitrogen, and consequently can form hydrogen bonds with other electronegative atom (Zhang & Wang, 2009).

According to Hema et al. (2009), lower lattice energy (605.3 kJ mol^{-1}) and larger anionic size of I ion (211 pm) lead to higher ionic conductivity compared to NH_4Br and NH_4Cl. A comparative study by the authors shows that a PVA-NH_4I electrolyte obtained a higher conductivity of 2.50×10^{-3} S cm^{-1}, compared to PVA-NH_4Br (5.70×10^{-4} S cm^{-1}) and PVA-NH_4Cl (1.00×10^{-5} S cm^{-1}). In the present work, the choice of NH_4I as the proton provider in starch/chitosan blend is expected to obtain a higher conductivity than starch/chitosan-NH_4Br; 9.72×10^{-5} S cm^{-1} (Shukur et al., 2013) and starch/chitosan-NH_4Cl; 6.47×10^{-7} S cm^{-1} (Shukur et al., 2014a) electrolytes.

Table 2.4: Review of earlier works using ammonium salts in polymer electrolytes.

Electrolyte Composition	Conductivity, σ (S cm^{-1})	Devices	References
Chitosan-PEO-NH4NO$_3$-EC	2.06×10^{-3}	EDLC	Shukur et al., 2013
Starch/chitosan-NH$_4$Br-EC	1.44×10^{-3}	-	Bel'Nikevich et al., 2004
PVA-chitosan-NH$_4$NO$_3$	1.60×10^{-3}	Proton batteries	Kadir et al., 2010
Starch/chitosan-NH$_4$NO$_3$	3.89×10^{-5}	-	Khiar & Arof, 2011
Chitosan-NH$_4$COOCH$_3$	3.83×10^{-3}	Proton batteries	Alias et al., 2014
MC-NH$_4$F	6.40×10^{-7}	-	Nik Aziz et al., 2010

2.7.1 Grotthus Mechanism

In polymer electrolytes, there are two possible mobile ionic species: cations and anions. The type of cation responsible for the ionic conductivity in the polymer blend-ammonium salt system has been identified to be H^+ (Chandra, Tolpadi, & Hashmi, 1988). Hashmi et al. (1990) reported that in PEO complexed with ammonium perchlorate (NH_4ClO_4), the conducting species is the H^+ ion. The H^+ ions of the salt will be coordinated with the nitrogen (N) atom of the amine group in chitosan (Hashmi et al., 1990). The NH_4^+ cations have four H ions attached with a tetrahedral formation. One of the four hydrogen atoms which is weakly bound, is easier to be dissociated with an influence of electric field. This conduction is known as Grotthus mechanism when the H ion is transferred from one site to another, hence leaving a vacancy which will be filled by another H ion from a neighboring site. Majid and Arof (2005) have also inferred that H^+ is the conducting species in a chitosan acetate-NH_4NO_3 sample.

2.8 Ionic Conduction

Ionic conductivity depends on salt concentration which proves that there is a specific interaction between the salt and the polymer matrix (Selvasekarapandian et al., 2005). Furthermore, polymer electrolyte conductivity is due to the transport of cations and anions in a polymer matrix (Johansson, Gogoll, & Tegenfeldt, 1996). Ionic conductivity, σ is closely related to the number and mobility of the charge carriers as given in this equation:

$$\sigma = nq\mu \tag{2.1}$$

where n, q and μ are number density, charge of ion and mobility of charge carriers, respectively.

2.8.1   Rice and Roth Model

Rice and Roth (Rice & Roth, 1972) proposed a hypothesis that there is an energy gap in an ionic conductor, where the mass of conducting ions, m can be thermally excited from localized ionic state to become free ions in which the ion extends throughout the medium with velocity, v. Even though the Rice and Roth equation was formulated for superionic conductors classified by (i) cationic disorders, (Zhai, Zhao, Yoshii, & Kume, 2004) β-alumina structure and (iii) defects, the equation can also be applied to correlate with ionic conductivity (Shuhaimi, Teo, Majid, & Arof, 2010). Number density of the charge carrier is a very crucial parameter in understanding the transport properties of polymer electrolytes (Shuhaimi et al., 2010). In this work, number density of mobile ions was computed using:

$$\sigma = \frac{2}{3}\left[\frac{(Ze)^2}{kTm_c}\right]nE_a\tau\exp\left(\frac{-E_a}{kT}\right) \tag{2.2}$$

where Z is the valency of conducting species, e is electron charge, T is absolute temperature, k is Boltzmann constant, m_c is mass of charge carrier, E_a is activation energy and τ is travelling time of ions. The equation given is depending on E_a which can

be obtained from the conductivity-temperature relationship. The value of τ was obtained using:

$$\tau = \frac{l}{v} \tag{2.3}$$

The value of τ can be used to determine the value of n using Equation (2.2). l is the distance between two coordinating sites while v is velocity of mobile ions, which is obtained using:

$$v = \sqrt{\frac{2E_a}{m_c}} \tag{2.4}$$

The ionic mobility, μ was calculated using the value of n:

$$\mu = \frac{\sigma}{ne} \tag{2.5}$$

(Shukur et al., 2013) reported that conductivity is controlled by mobility and number density of ions. The μ values lay within 10^{-4} cm^2 V^{-1} s^{-1} and n values are in the range of 10^{18} to 10^{19} cm^{-3}. They concluded that conductivity is controlled by these two parameters since the highest conducting electrolyte has the highest μ and n values, 6.86 $\times$ 10^{-4} cm^2 V^{-1} s^{-1} and 1.87 $\times$ 10^{19} cm^{-3}, respectively. Table 3.6 lists some transport parameters as reported by Shukur et al. (2013) for chitosan-PEO-NH$_4$NO$_3$-EC system.

Table 2.5: Transport parameters of chitosan-PEO-NH₄NO₃-EC system at room temperature (Shukur et al., 2013).

(wt.% EC)	σ (S cm^{-1})	E_a (eV)	τ (s)	n (cm^{-3})	μ (cm^2 V^{-1} s^{-1})
0	$(1.02 \pm 0.39) \times 10^{-4}$	0.23	1.51×10^{-13}	5.76×10^{18}	1.11×10^{-4}
10	$(1.72 \pm 0.14) \times 10^{-4}$	0.22	1.54×10^{-13}	6.72×10^{18}	1.60×10^{-4}
20	$(1.93 \pm 0.07) \times 10^{-4}$	0.22	1.54×10^{-13}	7.53×10^{18}	1.60×10^{-4}
30	$(2.49 \pm 0.37) \times 10^{-4}$	0.22	1.54×10^{-13}	9.74×10^{18}	1.60×10^{-4}
40	$(2.99 \pm 0.34) \times 10^{-4}$	0.22	1.54×10^{-13}	1.17×10^{19}	1.60×10^{-4}
50	$(5.10 \pm 0.17) \times 10^{-4}$	0.21	1.58×10^{-13}	1.38×10^{19}	2.30×10^{-4}
60	$(7.62 \pm 1.01) \times 10^{-4}$	0.20	1.61×10^{-13}	1.43×10^{19}	3.32×10^{-4}
70	$(2.06 \pm 0.39) \times 10^{-3}$	0.18	1.70×10^{-13}	1.87×10^{19}	6.86×10^{-4}
80	$(9.62 \pm 1.31) \times 10^{-4}$	0.20	1.61×10^{-13}	1.81×10^{19}	3.32×10^{-4}

2.9 Glycerol as Plasticizer

High ionic conductivities are obtained from polymer electrolytes with higher amorphous region (Noor, Ahmad, Talib, & Rahman, 2011). Various methods have been applied by researchers in order to improve their electrochemical and mechanical properties including copolymerization (Ban et al., 2006), cross linked polymer networks (Watanabe & Nishimoto, 1995), plasticization (Ramesh & Arof, 2001) and the addition of ceramic filler additive (Rajendran, Mahendran, & Krishnaveni, 2003). Utilization of plasticizers with high dielectric constant and low molecular weight can result in greater ion dissociation and increased the number of charge carriers for ionic transport (Noor et al., 2011). Table 2.6 shows the examples of plasticizers and the applications.

Table 2.6: Review of earlier works using plasticizers in polymer electrolytes.

Electrolyte Composition	Conductivity, σ (S cm^{-1})	Devices	References
PVC:LiCF$_3$SO$_3$:LiBF$_4$: **EC:PC**	2.80×10^{-3}	-	Ramesh & Arof, 2001
PAN-**EC**-LiCF$_3$SO$_3$ PAN-**PC**- LiCF$_3$SO$_3$	1.32×10^{-3} 8.64×10^{-4}	-	Noor et al., 2011
Chitosan–PEO–NH$_4$NO$_3$– **EC**	2.06×10^{-3}	EDLC	Shukur et al., 2013
PVA–chitosan- NH$_4$NO$_3$– **EC**	1.60×10^{-3}	Proton Battery	Kadir et al., 2010
MC-NH$_4$NO$_3$-**PEG200**	1.14×10^{-4}	Fuel cell	Arof et al., 2010
Starch/chitosan-NH$_4$Cl- **Glycerol**	5.11×10^{-4}	-	Shukur et al., 2014a

Glycerol is in alcohol group which is nontoxic to either human or environment (Tan, Aziz, & Aroua, 2013). The chemical structure of glycerol is shown in Figure 2.4. Glycerol has a high boiling point of 290˚C and low melting point of 18˚C (Speight & Speight, 2002). These characteristics will avoid glycerol from easily vaporized or solidified at room temperature, thus limit the ionic mobility (Speight & Speight, 2002).
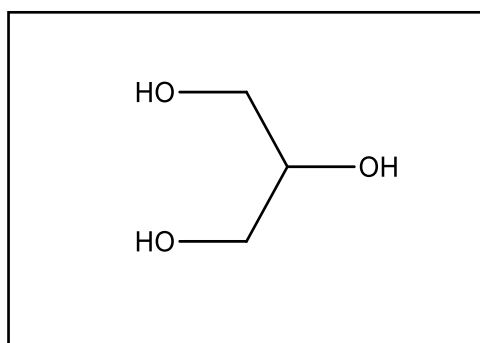
Figure 2.4: Chemical structure of glycerol.

The glycerol dielectric constant value (ε) of 42.5 is considered high which can weaken the attraction force between the cation and anion of salt as well as the polymer chains (Shukur & Kadir, 2015). New pathway provided for ions migration and more undissociated salt become free ions. The significant changes in local structures lead to increment in amorphous region and finally improve the ionic conductivity (Subramaniam et al., 2012).

2.10 Electrochemical Devices

Polymer electrolyte (PE) has been extensively studied in material science field, polymer science and electrochemistry, specifically in solid state energy devices such as solar cells, batteries and EDLCs (Naoi & Morita, 2008; Sudhakar & Selvakumar, 2012; Taib & Idris, 2014; Yang et al., 2006). PE is one of the major components in electrochemical devices and should exhibit sufficient ionic conductivity (Bhargav et al., 2009; Hatta et al., 2009). The proton (H^+) conducting polymer electrolytes have been widely studied in recent years for their potential applications in various electrochemical devices (Ng & Mohamad, 2008). The key factors for successful electrolytes include high ionic conductivity, sufficient mechanical strength, good chemical/environmental stability and acceptable production cost (Fujiwara et al., 2011; Qiao, Fu, Lin, Ma, & Liu, 2010).

These polymer electrolytes can overcome the drawbacks of liquid electrolytes such as reduce reactivity and leakage of electrolyte, improve safety and provide a better shape (Lim, Teoh, Liew, & Ramesh, 2014a). Recently, polymer electrolytes have been discovered as a potential electrolyte to be fabricated in EDLC and proton batteries (Park, Ahn, & Sung, 2002; Sivaraman, Hande, Mishra, Rao, & Samui, 2003). Li-ion batteries,

Zn-air batteries and Ni-MH (metal hydride) batteries are some of the battery systems that have been used widely in most electronic devices (Othman, Basirun, Yahaya, & Arof, 2001; Raj & Varma, 2010; Tarabay & Karami, 2015; Xu, Ivey, Xie, & Qu, 2015).

2.10.1 Proton Batteries

Solid state batteries play an important role in the development of science and technology as a portable electronic source and a backup power source in an aircraft (Samsudin et al., 2014). The development of solid state batteries has overcome the problems in conventional liquid electrolyte batteries including short life span, difficult to handle during manufacturing and the possibility of corrosiveness in the containers (Gauthier, Belanger, Kapfer, Vassort & Armand, 1987). At the early development of proton batteries, Li^+ ion batteries have become the most favorable among researchers to commercialize them due to its small ionic radii (Shukur et al., 2014b). However, people start to concern regarding a few drawbacks this type of batteries can cause to the environment and users, for example difficult to handle, high in cost and having safety issues (Samsudin et al., 2014).

For low current density battery applications, electrode and electrolyte materials with low cost are required in order to develop H^+ proton batteries as a potential alternative to Li^+ ion batteries (Alias et al., 2014). Besides, the development of natural biopolymer-based electrolytes has been commercialized in recent years to substitute the petrochemicals source usage, along with the friendliness to the environment (Ponez, Sentanin, Majid, Arof & Pawlicka, 2012). For example, batteries based on cellulose have been produced in 2011 and reported to date which portray good reviews by people

from various industries as a natural-resource based alternative battery (Kim et al., 2016). The diagram of proton battery can be seen in Figure 2.5.
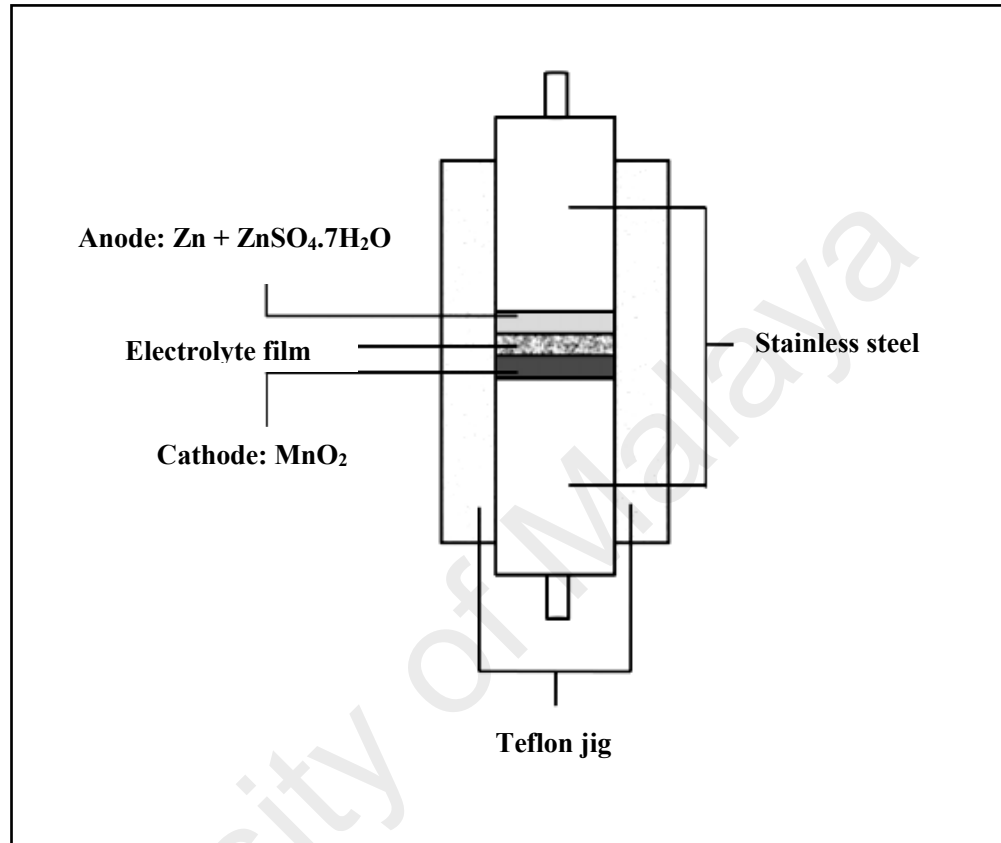
Figure 2.5: Diagram of proton battery (Samsudin, Lai, & Isa, 2014).

2.10.2 Electrical Double Layer Capacitor (EDLC)

Electrochemical supercapacitors have been developed as alternative power sources in many laboratories. Other than pseudocapacitor, another type of supercapacitors that have been widely used as memory backup device is EDLC (Tabuchi et al., 1993). EDLC is a type of supercapacitor where the energy is stored by charge separation across the blocking or polarizable electrode/electrolyte interfaces

(Arof et al., 2012). EDLCs are employing different electrolytes and various forms of electrodes which are still undergoing development as alternative power sources to rechargeable batteries (Simon & Gogotsi, 2008). Compared to batteries, EDLCs have identical electrodes, longer life times, high cyclabilities, high-power density and environmentally friendly features (Arof et al., 2010; Burke, 2000). The EDLC is basically stored the electric energy in the Helmholtz double-layers which formed in the electrolyte through ionic migration, without any chemical reaction occurred between the electrodes and electrolyte (Lim et al., 2014b). Positive and negative ionic charges within the electrolyte accumulate on the surface of the solid electrode and compensate the electronic charge at the electrode surface (Kotz & Carlen, 2000).

The EDLC device comprises of an electrolyte film and two porous electrodes sandwiching the film, as can be seen from Figure 2.6. The electrodes used in EDLC must possess good pore size and high surface area (Syahidah & Majid, 2013). Activated carbon has been reported as a promising candidate as an electrode due to its chemical stability, good conductivity and moderate cost (Lozano-Castello, Cazorla-Amoros, Linares-Solano, Shiraishi, Kurihara, & Oya 2003; Nian & teng, 2003; Okajima, Ohta & Sudoh, 2005).
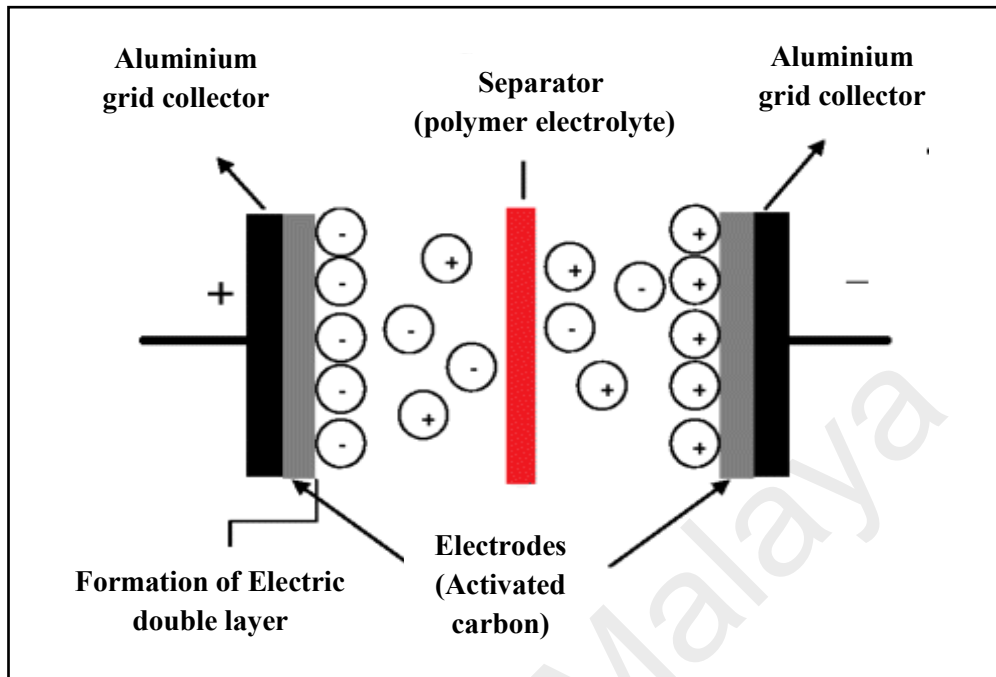
Figure 2.6: Diagram of an electric double-layer capacitor (Lim et al., 2014a).

2.11   Summary

In this chapter, literature review and background of the materials and some other important topics have been reviewed. The important information is gained and the knowledge is used for further discussion of the results. This chapter gives some previews that starch/chitosan based polymer electrolytes are suitable and can be used for further studies and investigation.

CHAPTER 3: EXPERIMENTAL METHODS

3.1 Introduction

In this work, three systems of starch/chitosan, starch/chitosan-salt (salted) and starch/chitosan-salt-plasticizer (plasticized) have been prepared. Ammonium iodide (NH$_4$I) as dopant will provide the charge carriers while the glycerol is employed as plasticizer. All polymer electrolytes were prepared via solution cast technique. The study on the starch/chitosan blend in this work is to determine the most suitable ratio to be chosen as the polymer host based on the degree of crystallinity. Starch/chitosan blend has been characterized using fourier transform infrared (FTIR), X-Ray diffraction (XRD), thermogravimetric analysis (TGA), differential scanning calorimetry (DSC) and field emission scanning electron microscopy (FESEM) techniques in order to determine its compatibility to be employed as the polymer host.

The blend is further doped with NH$_4$I to prepare the salted system. The electrolyte which attained the highest ionic conductivity was then be plasticized with glycerol. The polymer electrolytes were characterized using several techniques including FTIR, electrochemical impedance spectroscopy (EIS), XRD, FESEM, TGA, DSC and transference number measurement (TNM). The highest conducting electrolyte from the plasticized system was used in the fabrication of electrical double layer capacitor (EDLC) and proton batteries. A corn starch (Unilever) and a highly viscous chitosan with viscosity of 800-2000 cP, molecular weight of approximately 310000 to 375000 and degree of deacetylation of > 75% (Sigma-Aldrich) were used to prepare the polymer blend. Ammonium iodide (NH$_4$I) was procured from HmbG while acetic acid and glycerol were purchased from SYSTERM.

3.2   Electrolytes preparation

3.2.1   Starch/chitosan System

Corn starch with different weight percentages (x wt.%) were dissolved in 100 mL of 1% acetic acid while heated at 80°C for 20 min. After the solutions were cooled to room temperature, (100-x) wt.% of chitosan was then added to the solutions. The mixtures were stirred using magnetic bar stirrers until homogeneous solutions were obtained. All solutions were cast into different plastic Petri dishes and left to dry to form films at room temperature in a drying cabinet. All samples were peeled out and kept in a desiccator filled with silica gel desiccants for further drying. Table 3.1 summarizes the compositions of the polymer blend.

FTIR analysis has been carried out to study the molecular interactions between the polymers. This method is performed using Spotlight 400 Perkin-Elmer spectrometer in the wavenumber range of 400 - 4000 cm^{-1} at a resolution of 1 cm^{-1}. Siemens D5000 X-ray diffractometer with X-rays of 1.54 Å wavelengths generated by a Cu Kα source were employed for XRD measurements of the polymer blend films. The variation of the 2θ angle was from 5° to 80°. The decomposition temperature was studied from TGA analysis using Perkin-Elmer Pyris 1 TGA equipment. The determination of glass transition temperature, T_g for selected samples from DSC analysis was carried out using TA Instruments Q200. The cross-sections of the polymer blend films were examined using a Hitachi SU8220 FESEM.

Table 3.1: The ratio content of starch/chitosan electrolyte.

Designations	Starch: chitosan compositions (wt. %)	Polymer blend	
		Starch (g)	Chitosan (g)
PB0	100 : 0	1.00	0.00
PB1	90 : 10	0.90	0.10
PB2	80 : 20	0.80	0.20
PB3	70 : 30	0.70	0.30
PB4	60 : 40	0.60	0.40
PB5	50 : 50	0.50	0.50
PB6	40 : 60	0.40	0.60
PB7	30: 70	0.30	0.70
PB8	20 : 80	0.20	0.80
PB9	10 : 90	0.10	0.90
PB10	0 : 100	0.00	1.00

3.2.2 Starch/chitosan-NH$_4$I (Salted System)

The polymer blend electrolytes of salted system were prepared by dissolving 0.80 g of starch in 100 mL of 1% acetic acid while heated at 80°C for 20 min. After the solution was cooled to room temperature, 0.20 g of chitosan was added and stirred until it is fully dissolved. Different amounts of NH$_4$I were added into the solution and stirred until the solutions become homogenous. All solutions were cast onto plastic Petri dishes and left to dry in a drying cabinet for 3 days. Later, the dried films were kept in a dessicator filled with silica gel desiccants for further drying. Table 3.2 summarizes the compositions of the prepared polymer blend-salt system. A4 sample was chosen to be added with glycerol.

Table 3.2: The compositions and designations of electrolytes in salted system.

Designations	PB2 : NH₄I compositions (wt.%)	Salted system		
		Starch (g)	Chitosan (g)	NH₄I (g)
PB2	100 : 0	0.80	0.20	0
A1	90 : 10	0.80	0.20	0.1111
A2	80 : 20	0.80	0.20	0.2500
A3	70 : 30	0.80	0.20	0.4286
A4	60 : 40	0.80	0.20	0.6667
A5	50 : 50	0.80	0.20	1.0000
A6	40 : 60	0.80	0.20	1.5000

3.2.3 Starch/chitosan-NH₄I-Glycerol (Plasticized System)

0.80 g of corn starch was dissolved in 100 ml of 1% acetic acid at 80˚C for 20 min. After the solution cooled to room temperature, 0.20 g of chitosan was added. 0.667 g of NH₄I was added to the 4:1 starch/chitosan blend solution and stirred until homogeneous solution was obtained. Different amounts of glycerol were added to the starch/chitosan-NH₄I electrolyte solution and stirred until complete dissolution. All solutions were then cast into plastic Petri dishes and left for drying process at room temperature in a drying cabinet. The dried films were kept in a glass desiccator filled with silica gel desiccants for further drying. The compositions and designations of the electrolytes are presented in Table 3.3. B3 sample was chosen to be fabricated in electrochemical devices.

Table 3.3: The compositions and designations of electrolytes in plasticized system.

Designations	A4 : glycerol compositions (wt.%)	Plasticized System			
		Starch (g)	Chitosan (g)	NH4I (g)	Glycerol (g)
A4	100 : 0	0.80	0.20	0.667	0
B1	90 : 10	0.80	0.20	0.667	0.185
B2	80 : 20	0.80	0.20	0.667	0.417
B3	70 : 30	0.80	0.20	0.667	0.714
B4	60 : 40	0.80	0.20	0.667	1.111
B5	50 : 50	0.80	0.20	0.667	1.667

3.3   Electrolytes Characterization

3.3.1   X-Ray Diffraction (XRD)

The XRD technique was used to determine the atomic arrangements of crystal or amorphous structures of a material. XRD provides most definitive structural information. This technique was carried out by applying an X-ray beam onto the sample with wavelength, λ at different angles, θ. The interaction of the rays with the sample produces constructive interferences and a diffracted ray which satisfies the Bragg's condition:

$$2d \sin\theta = \lambda \tag{3.1}$$

where d is the interplanar spacing, θ is the Bragg's angle and λ is the wavelength (Liu, Chaudhary, Yusa, & Tadé, 2011). For structural characterization of the starch/chitosan blend films, the XRD measurements were carried out at room temperature using Siemens D5000 X-ray diffractometer where X-rays of 1.54 Å wavelengths were

generated by a Cu Kα source. The 2θ angle was varied from 5° to 80° by using a scanning rate of 0.1°/ 2 s.

The XRD patterns of chitosan-based electrolyte membranes with different concentrations of oxalic acid are shown in Figure 3.1. Fadzallah and co-workers (2014) reported that the presence of 40 wt.% oxalic acid in chitosan-based film gives the highest degree of amorphousness while chitosan powder gives the highest crystallinity .
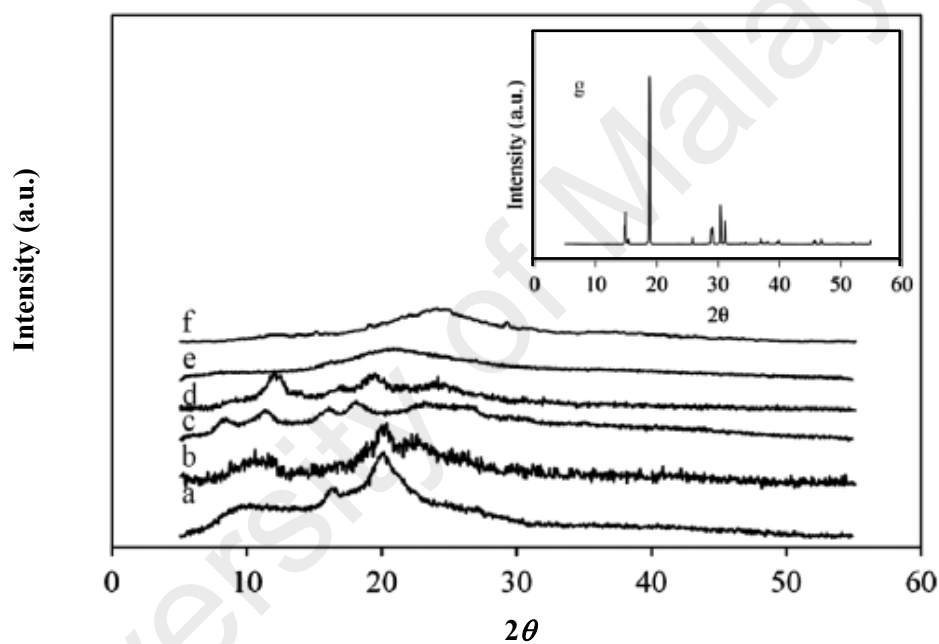
Figure 3.1: XRD patterns of (a) chitosan with the addition of (b) 10% oxalic acid, (c) 20% oxalic acid, (d) 30% oxalic acid, (e) 40% oxalic acid, (f) 50% oxalic acid and (g) pure oxalic acid (Fadzallah, Majid, Careem & Arof, 2014).

3.3.2 Field Emission Scanning Electron Microscopy (FESEM)

An electron microscope scans a focused electron beam over a surface to produce an image. The electrons of the beam interact with the atoms in the sample, producing various signals that can be detected and contain information about the surface

36

topography and morphology. In this work, FESEM has been used to study the cross-sections of the starch/chitosan blend and surface of salted and plasticized films for better and clearer images. A Hitachi SU8220 FESEM was used to study the cross-sections of blend films at 1K × magnification while Zeiss Auriga FESEM was used to examine the surface of the films in salted and plasticized systems at 1K × and 5K × magnifications. This study gives an insight of the surface morphology of the semi-crystalline polymer electrolyte.
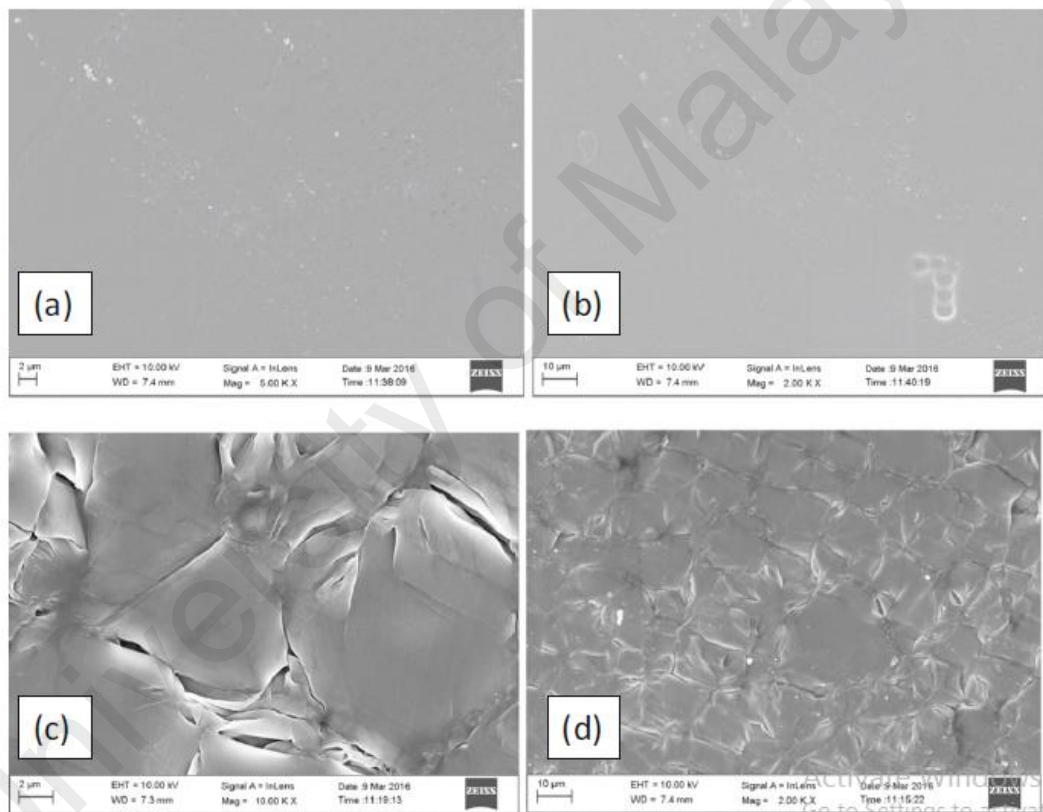
Figure 3.2: FESEM micrographs of 70PVAc-30PMMA in (a) and (b) and 70PVAc-30PMMA-30NH$_4$SCN in (c) and (d) (Chandra et al., 2016).

Figure 3.2 shows the surface morphology of polyvinyl acetate (PVAc) and polymethyl methacrylate (PMMA) blend electrolyte. It can be seen that the surface of 70PVAc-30PMMA film is smooth, proving the homogeneity of PVAc-PMMA blend. In contrast with 70PVAc-30PMMA-30NH$_4$SCN film, some voids and cavities can be detected within the membrane surface (Chandra et al., 2016). This leads to the conclusion that new kinetic path probably has been formed through the polymer-salt boundaries.

3.3.3 Fourier Transform Infrared (FTIR) Study

In FTIR, the IR radiation is passed through a sample. Some of the IR radiation is absorbed by the sample while the other is transmitted. The resulting spectrum represents the molecular absorption and transmission, creating a molecular fingerprint of the sample. FTIR can be used to identify the chemical compositions, chain structures and functional groups of the polymer electrolyte samples. This technique is carried out based on the fact that different bonds vibrate at different characteristic frequencies.

The FTIR studies were performed using Spotlight 400 Perkin-Elmer spectrometer in the wavenumber ranged from 400 to 4000 cm^{-1} at a resolution of 1 cm^{-1}. In this work, FTIR studies were performed to confirm the interactions between the polymers, polymer blend-salt and polymer blend-salt-plasticizer. Focus was given to the hydroxyl, amine and carboxamide groups.

Figure 3.3 depicts the FTIR spectra of poly(ε–caprolactone)(PCL)-ammonium thiocyanate (NH$_4$SCN) electrolytes displaying NH stretching and SCN bending in the regions. Woo, Majid, & Arof (2011a) discussed on the shifting of the NH band towards

lower wavenumber and overlapping with PCL spectrum with the incorporation of NH$_4$SCN. They also discussed on the formation of loosely-bound hydrogen bonds and interaction of carbonyl groups that reflected the interaction between the polymer host and the dopant salt.
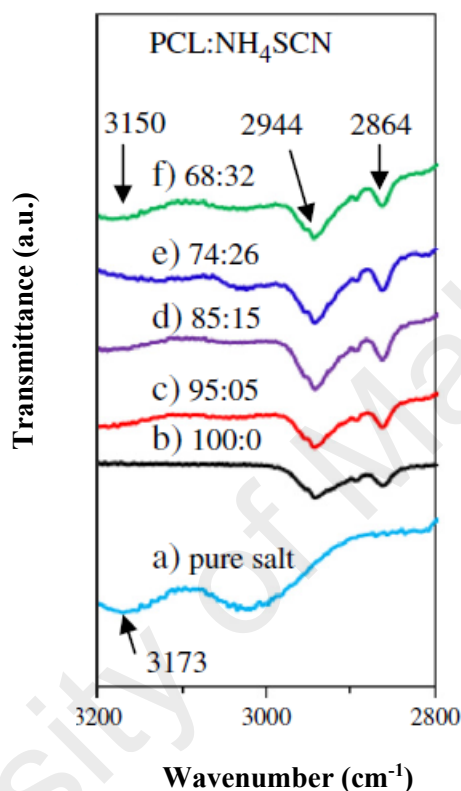
Figure 3.3: FTIR spectra of (a) pure NH$_4$SCN and complexes of PCL: NH$_4$SCN in the weight ratio of (b) 100:0, (c) 95:5, (d) 85:15, (e) 74:26, (f) 68:32 displaying NH stretching region (Woo et al., 2011a).

3.3.4 Thermogravimetric Analysis (TGA)

TGA is a method of thermal analysis where changes in weight of a material are measured as a function of temperature or time, with constant heating rate, under a controlled atmosphere. As the temperature increases, various components of the sample are decomposed and the weight percentage of the resulting mass change can be measured. TGA analysis was carried out using Perkin-Elmer Pyris 1 TGA equipment.

The samples were heated from room temperature to 800°C at a heating rate of 10°C min⁻¹ under argon gas flow. Mass of samples used for TGA measurements is around 3.0 - 5.0 mg.

Figure 3.4 shows an example of TGA thermogram of PVA-potassium hydroxide (KOH)-aluminium oxide (Al$_2$O$_3$)-propylene carbonate (PC) as reported by Mohamad and Arof (2006). The weight loss was found higher due to the decreased of thermal stability for the samples with higher plasticizer content.
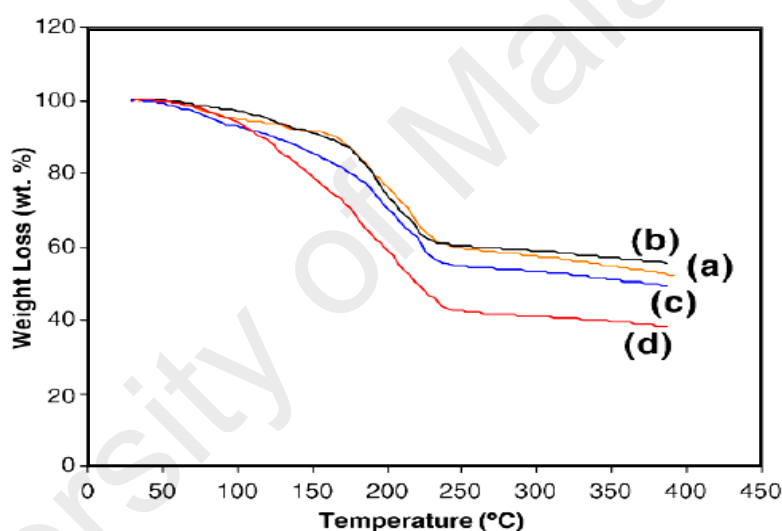
Figure 3.4: TGA thermograms of PVA-KOH-Al$_2$O$_3$-PC films where (a) PC0, (b) PC20, (c) PC40 and (d) PC60 (Mohamad and Arof, 2006).

3.3.5 Differential Scanning Calorimetry (DSC)

The determination of glass transition temperature, T_g is very useful to evaluate the miscibility of a polymer blend. Differential scanning calorimetry (DSC) was carried out using TA Instruments Q200. The samples were heated at a heating/cooling rate of 10°C min⁻¹ from -50 to 200°C.
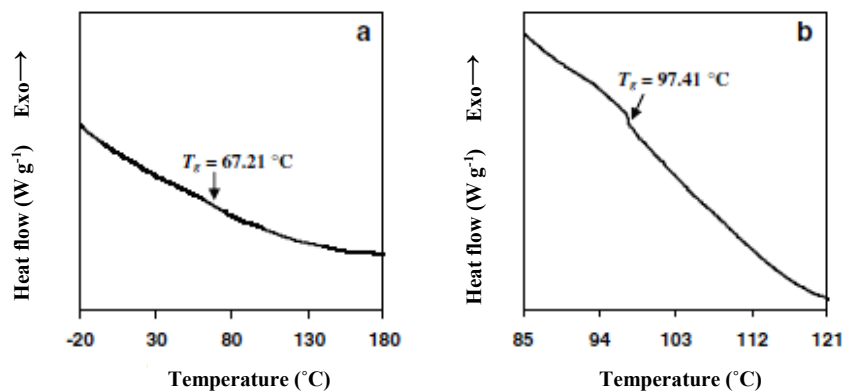
Figure 3.5: DSC thermograms of (a) pure starch film and (b) pure chitosan film (Shukur, et al., 2014a).

Shukur et al. (2014a) mentioned in their report that the ionic mobility depends on the segmental motion of the polymer chains in the amorphous phase which can be determined by the glass transition temperature, T_g.

3.3.6 Electrochemical Impedance Spectroscopy (EIS)

The polymer electrolyte films were cut into small discs of 1.60 cm diameter and sandwiched between two stainless steel electrodes of a conductivity holder. Figure 3.6 shows the picture of the conductivity holder used in this work.

The impedance of the films was measured using HIOKI 3532-50 LCR Hi-Tester that was interfaced to a computer in the frequency range between 50 Hz to 5 MHz from 298 to 343 K. The value of bulk resistance, R_b (Ω) obtained from the Cole-Cole plots as

Figure 3.6: Conductivity holder with blocking stainless steel electrodes.

shown in Figure 3.8, was used to calculate the conductivity, σ using the following equation:

$$\sigma = tR_b^{-1}A_e^{-1} \tag{3.2}$$

where t (in cm) is the thickness of the electrolytes and A_e (in cm^2) is the electrode-electrolyte contact area which is 3.142 cm^2. A digital micrometer (Mitutoyo Corp.) was employed to measure the thickness of the films.

The cole-cole plots depicted in Figure 3.7 are reported by Aziz, Majid, & Arof (2012) which consist of a semicircle at high frequency and an adjacent line at low frequency region for phthaloyl chitosan-based polymer electrolytes with 10 and 20 wt% NH$_4$SCN at room temperature. The R_b values were taken from the intercept of semicircle with the adjacent line.
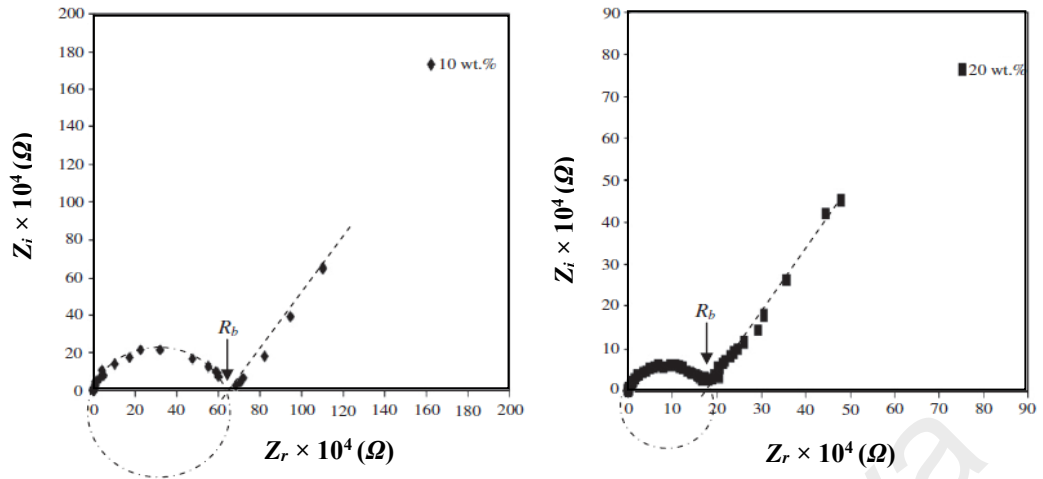
Figure 3.7: Impedance plots of phthaloyl chitosan-NH$_4$SCN at ambient temperature (Aziz et al., 2012).

3.3.7 Transference Number Measurements

In order to prove that the ionic conduction is contributed by ions, transference number measurements have been carried out. The ionic transference number has been evaluated using a V&A Instrument DP3003 digital dc power supply by employing Wagner's dc polarization technique. A constant dc potential of 0.80 V is applied to polarize the cell. The highest conducting electrolyte was sandwiched between stainless steel (SS) blocking electrodes with cell configuration SS/ B3 sample/SS at room temperature. In order to prove that the polymer electrolyte is an ionic conductor, the transference number of ions, t_{ion} must be larger than the transference number of electrons, t_e (Aziz et al., 2012). Figure 3.8 exhibits the plot of polarization current versus time at 303K for 75PVA:25 ammonium bromide (NH$_4$Br) (Hema et al., 2008). They found that the t_{ion} for all compositions of the PVA: NH$_4$Br electrolyte systems lie between 0.93 to 0.96, suggesting that the charge transport in these electrolyte films is predominantly ions.
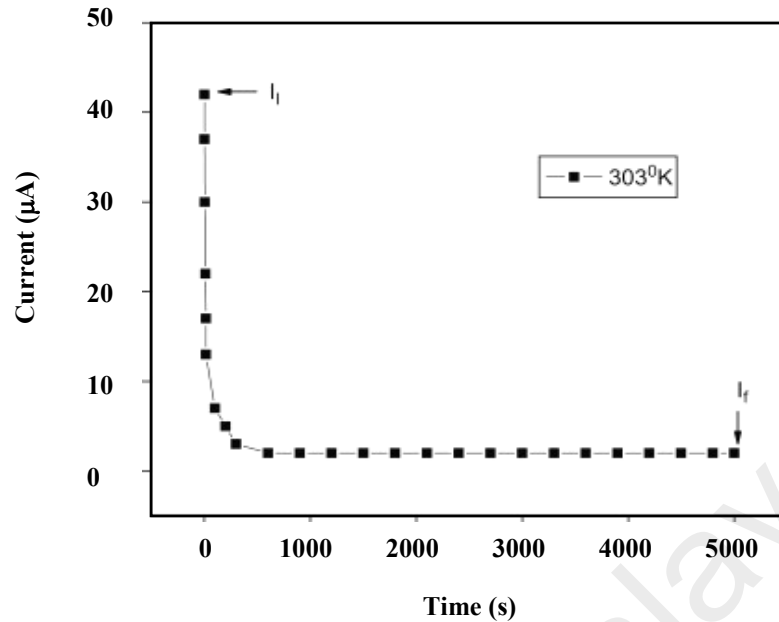
Figure 3.8: Polarization current as a function of time for 25 mol% NH₄Br-doped PVA polymer electrolyte (Hema et al., 2008).

Watanabe technique is employed to determine the cation (t_+) transference number. 0.40 g MnO₂ (Sigma-Aldrich), 0.08 g polytetrafluoroethylene (PTFE) and 0.04 g activated carbon (RP20, manufactured by Kuraray, Japan) were mixed for the electrodes preparation. The mixtures were grounded and hydraulic pressed for 20 minutes. The highest conducting electrolyte film was sandwiched between the electrodes and measured using V&A Instrument DP3003 digital dc power at 0.20 V. Figure 3.9 shows the current relaxation curve during dc polarization at applied voltage of 0.20 V as reported by Woo, Majid & Arof (2011b). They concluded that the value of t_+ which is 0.21; indicates the existence of mobile ions or higher aggregation of the ions.
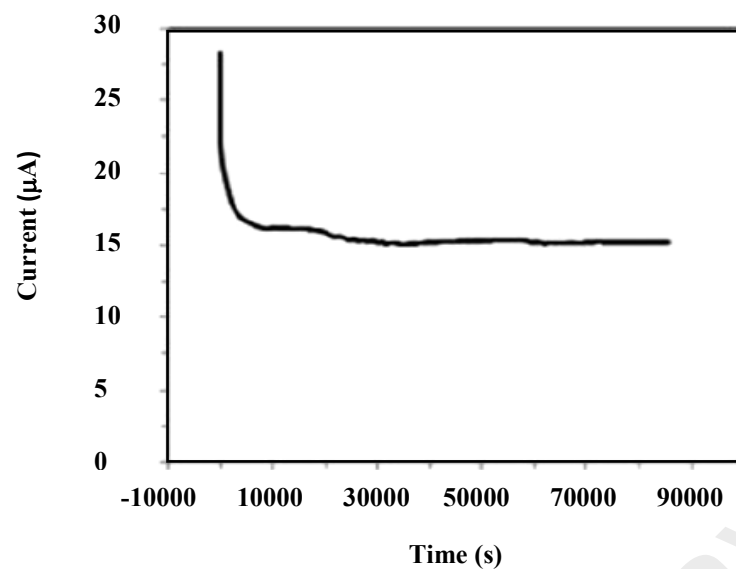
Figure 3.9: Transference number of PCL-26 wt.% NH₄SCN using MnO₂ electrodes (Woo et al., 2011b).

3.3.8   Linear Sweep Voltammetry

Linear sweep voltammetry (LSV) measurement was conducted employing a 3-electrode configuration where stainless steel electrodes were employed as working, counter and reference electrodes, as can be seen in Figure 3.10.
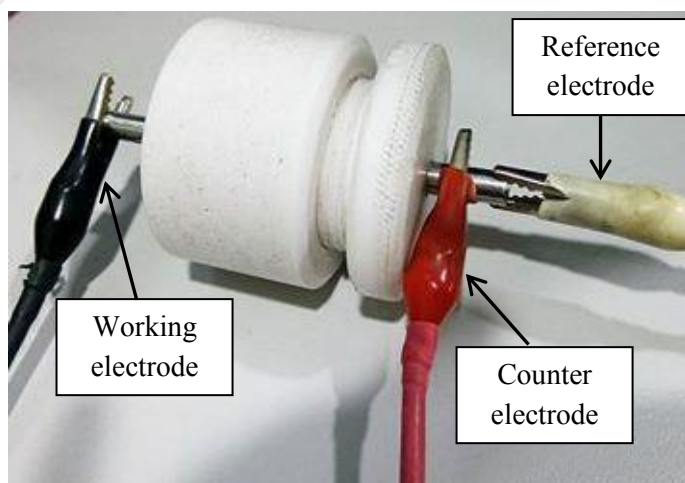
Figure 3.10: LSV with 3-electrode configuration.

A Digi-Ivy DY2300 potentiostat at a scan rate of 1 mV s^{-1} in a potential range of 0 V to 2.50 V was used to measure the electrochemical stability window. The current at the working electrode for LSV study was measured at room temperature while the potential between the working and reference electrodes was swept linearly in time. Figure 3.11 depicts the LSV curves of 49 wt.% starch-21 wt.% NH$_4$Br (ammonium bromide)-30 wt.% glycerol electrolyte at 10 mV s^{-1} using stainless steel electrodes. The decomposition voltage is detected around 1.66 V at room temperature (Shukur & Kadir, 2015a).
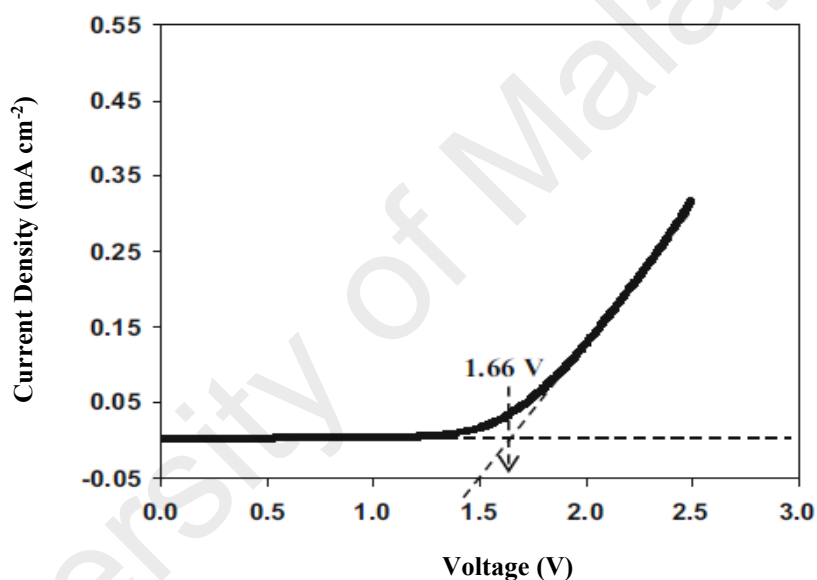
Figure 3.11: LSV for 49 wt.% starch-21 wt.% NH$_4$Br-30 wt.% glycerol electrolyte at 10 mV s^{-1} (Shukur & Kadir, 2015a).

3.4 Fabrication and Characterization of EDLC

3.4.1 Electrodes Preparation

To prepare the EDLC electrodes, 13 g of activated carbon (RP20, manufactured by Kuraray, Japan), 2 g polyvinylidene fluoride (PVdF) and 1 g of carbon black (Super

P) were mixed in 60 ml N-methylpyrrolidone (NMP) (EMPLURA). Homogeneous slurry was obtained after 24 hours of stirring. The slurry was then spread on an aluminium foil via doctor blade method with thickness of 0.25 mm. After heating at 60˚C, the electrodes were kept in a desiccator filled with silica gel desiccants prior to be used.

3.4.2   EDLC Fabrication

The fabrication has been carried out by sandwiching the electrolyte between two electrodes. In order to clamp and hold the EDLC tightly, perspex plates were employed as depicted in Figure 3.12. The performance of the fabricated EDLC was monitored using Neware battery cycler.
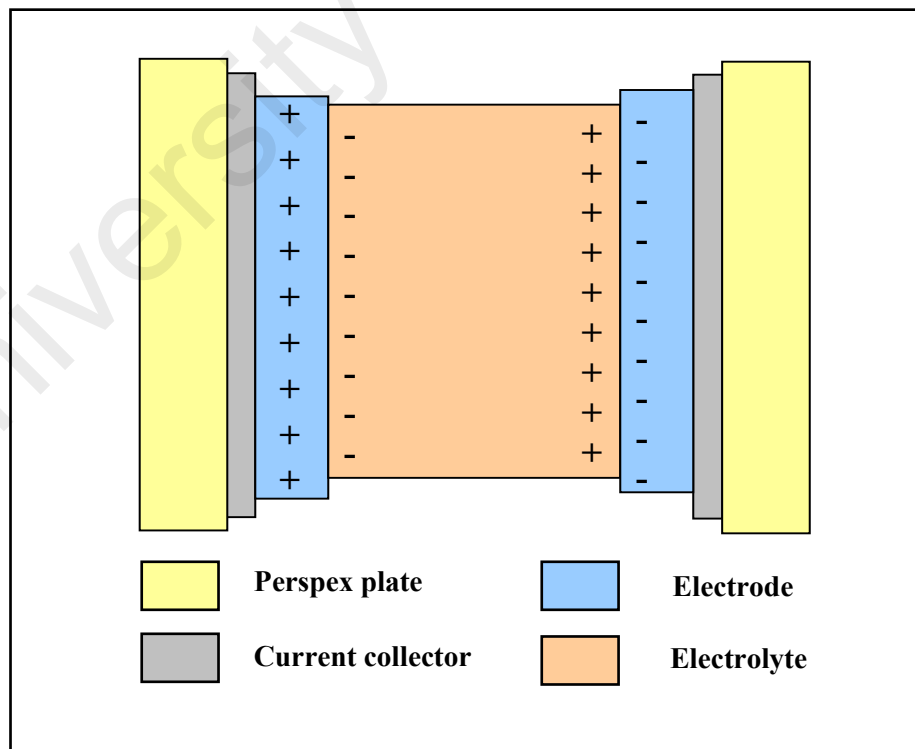
Figure 3.12: Picture of EDLC fabrication.

3.4.3 EDLC Characterization

The performance of EDLC was characterized using cyclic voltammetry (CV) and charge-discharge cycling at constant current. CV was carried out at room temperature using Digi-IVY DY2300 potentiostat between 0 to 0.85 V at different scan rates. An example of cyclic volatammogram of MC-NH$_4$NO$_3$-poly(ethylene glycol) (PEG) is shown in Figure 3.13. It can be seen from the figure that the shape of the voltammograms for the EDLCs with coated and uncoated electrodes is close to that of a rectangle (Shuhaimi, Teo, Woo, Majid, & Arof, 2012). This implies that the charge-discharge cycle occurs reversibly and the electrode/ electrolyte contact is responsible for the EDLC resistance.
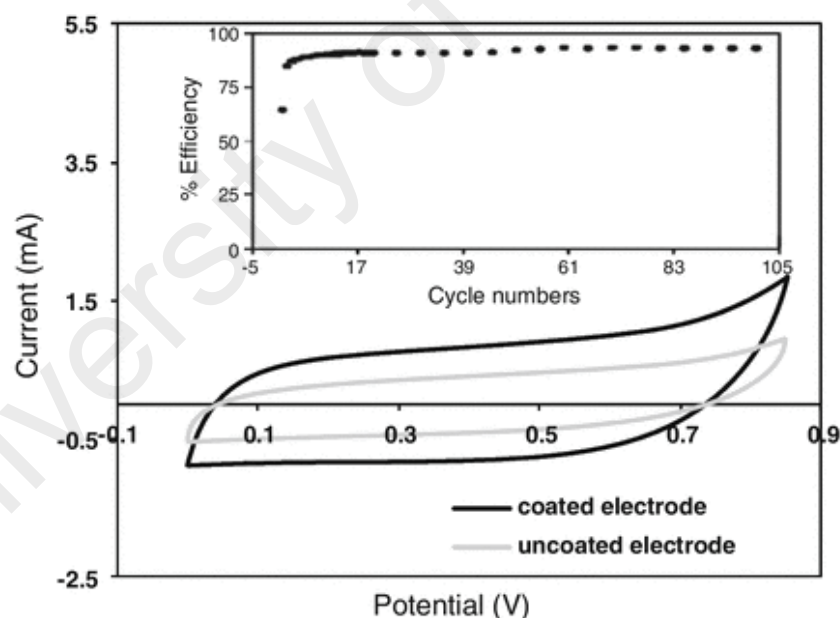
Figure 3.13: Cyclic voltammogram of the EDLC fabricated using uncoated and coated electrodes. Inset: efficiency of EDLC with PEG-coated electrodes for 100 cycles (Shuhaimi et al., 2012).

The galvanostatic charge-discharge characteristics of the EDLC were carried out in a voltage range between 0 to 0.85 V at a constant current density of 0.04 mA cm^{-2}.

The values of specific capacitance, C_s on selected cycles from the galvanostatic charge-discharge measurement were calculated, as well as the specific capacity (Q) values which refer to the amount of charge passing through the outer circuit per unit mass. Figure 3.14 represents typical charge-discharge curves of EDLC for PVA-lithium perchlorate (LiClO$_4$)-titanium dioxide (TiO$_2$) polymer electrolyte at 1 mA current reported by Lim, Teoh, Liew, & Ramesh (2014a). They reported that the initial drop in the potential during the discharging process is attributed to the internal resistance and equivalent circuit resistance (ESR) in the electrodes and electrolyte.
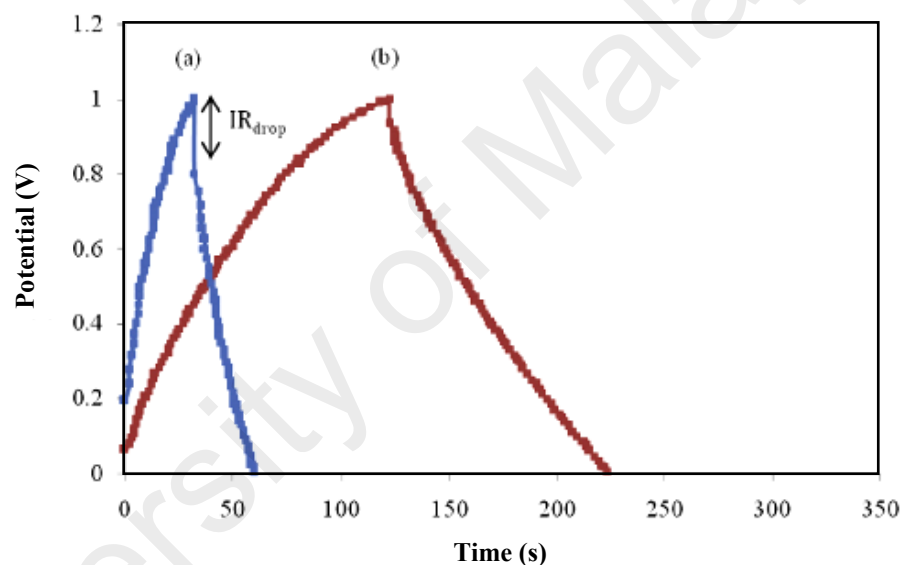
Figure 3.14: Charge-discharge pattern for (a) EDLC cell with 60PVA-40LiClO$_4$ and (b) EDLC cell with 55.2PVA-36.8LiClO$_4$-8TiO$_2$ at current of 1 mA (Lim et al., 2014a).

3.5   Proton Batteries

3.5.1   Primary Proton Batteries Fabrication

For the cathode preparation, 0.44 g MnO$_2$ (Aldrich), 0.04 g carbon black and 0.02 g PTFE were mixed and grounded in a pellet form. For the anode preparation, 0.31 g Zn (Merck), 0.15 g ZnSO$_4$·7H$_2$O (Univar), 0.02 g carbon black and 0.02 g PTFE were

mixed and grounded in a pellet form. The pellets were then pressed using hydraulic pressing for 15 min before fabrication by sandwiching the highest conducting electrolyte between the cathode and the anode pallets. The proton batteries were then packed in CR2032 coin cells as shown in Figure 3.15.

Figure 3.15: Picture of CR2032 coin cell.

The open circuit potential (OCP) of the batteries was measured at an open circuit condition for 24 hours. OCP values represent the full potential of a battery since the potential does not share its potential with any other load. An example of OCP of a proton battery can be seen in Figure 3.16, which shows the OCP of 85 wt.% of poly(vinyl) chloride (PVC) doped with ammonium trifluoromethane sulfonate ($NH_4CF_3CO_3$) + 15 wt.% butyltrimethyl ammonium bis (trifluoromethyl sulfonyl) imide (BATS) electrolyte at room temperature. They suggested that the voltage was higher in the first 2 hours due to a voltage delay before stabilized at ~1.30 V after 24 hours of storage (Deraman, Mohamed & Subban, 2013).

All batteries in the present work were discharged at different constant currents; 0.10, 0.20, 0.50, 1.00 and 2.00 mA; at room temperature using Neware battery cycler. Figure 3.17 shows discharge profiles of proton batteries of carboxymethyl cellulose (CMC)-NH_4Br at different constant currents as reported by Samsudin et al. (2014). The discharge curves shows that their batteries can perform longer at 0.10 and 0.25 mA
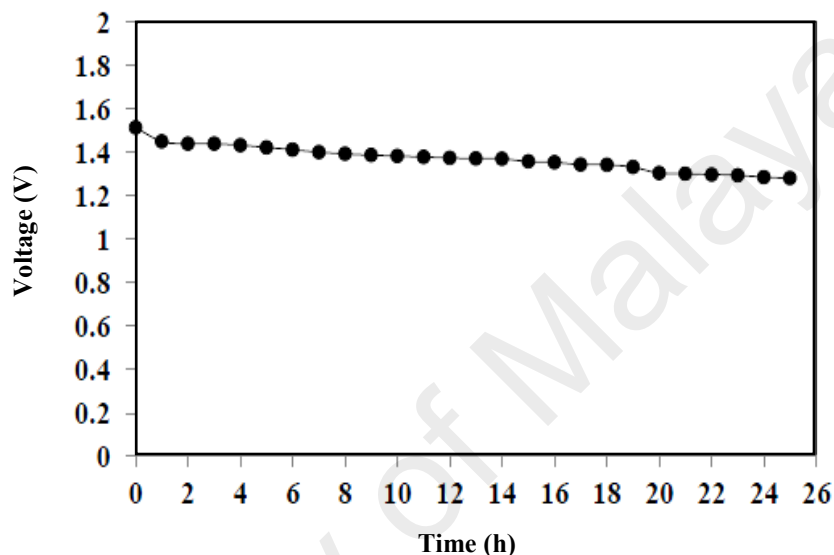
Figure 3.16: OCP of proton battery at room temperature for 85 wt.% (PVC-$NH_4CF_3CO_3$) + 15 wt.% BATS polymer electrolyte (Deraman et al., 2013).
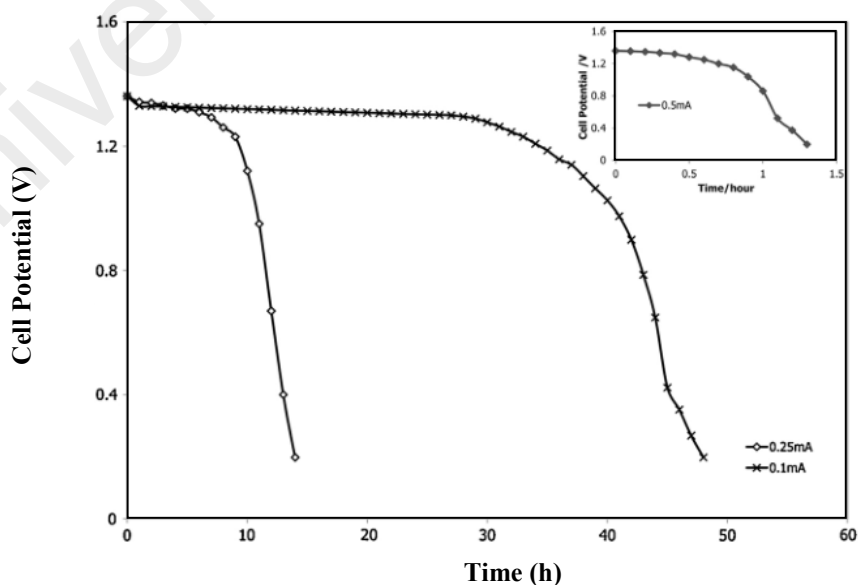
Figure 3.17: Discharge curves of CMC -NH_4Br proton battery at 0.1, 0.25 and 0.5 mA (Samsudin et al., 2014).

compared to 0.50 mA, before the voltage dropped immediately. This was attributed to the internal resistance of the battery which resulted in maximum power transfer, hence higher discharge capacity is obtained. They concluded that their proton battery is more suitable for lower current applications.

3.5.2 Secondary Proton Batteries

For the cathode preparation for secondary batteries, 0.41 g MnO_2 (Aldrich), 0.02 g carbon black, 0.02 g PTFE and 0.05 g of the highest conducting electrolyte solution were mixed and grounded in a pellet form. The anode pellet was prepared using similar method with the primary proton battery. The pellets were then pressed using hydraulic pressing for 15 min before the fabrication by sandwiching the highest conducting electrolyte between the cathode and the anode pallets. The proton batteries were then packed in CR2032 coin cells as shown in Figure 3.15. Figure 3.18 depicts the discharge-charge characteristic for CMC-NH_4Br at room temperature as reported by Samsudin et al. (2014). The battery was discharged with a constant current of 0.25 mA and performs up to 12 cycles. They concluded that the electrode-electrolyte surface contact has reduced during the 11th cycle thus decreased the cell potential.
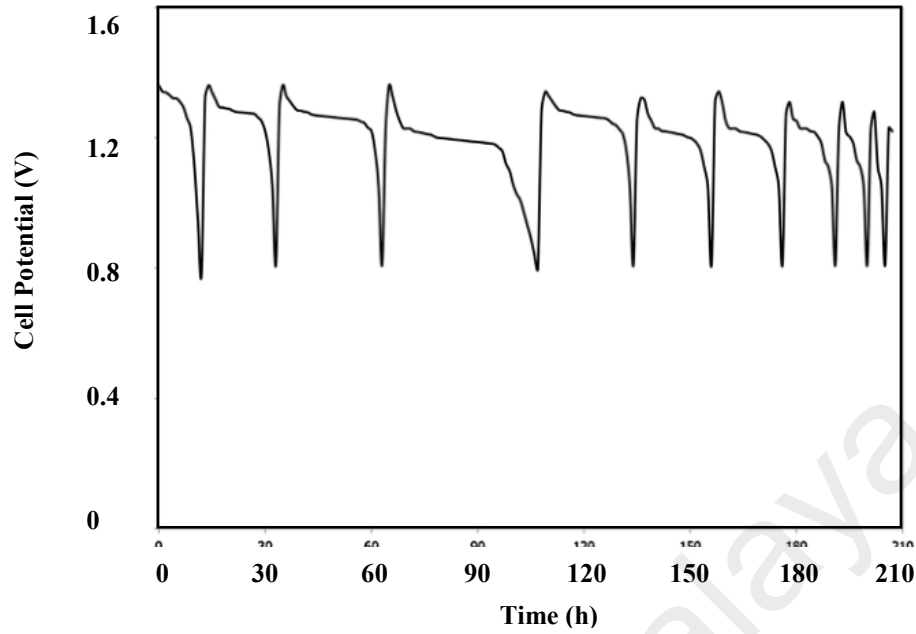
Figure 3.18: Discharge-charge curves of CMC-NH$_4$Br proton battery at room temperature (Samsudin et al., 2014).

3.6 Summary

From this chapter, the steps involved in the electrolytes preparation in starch/chitosan, salted and plasticized systems have been described. All samples were characterized using few techniques as discussed in the chapter. The highest conducting sample was used in the fabrication of EDLC and proton batteries.

CHAPTER 4 : CHARACTERIZATIONS OF POLYMER BLENDS

4.1 Introduction

For many years, blending of polymers is believed to be a useful and effective method to develop new polymeric materials with improved mechanical stability (Rajendran et al., 2003). Polymer blending is a low-cost method which contributes in the development of a new product with better performance (Yu et al., 2006). The miscibility of the blends is very important to assure that the combination of the polymers can form good inter macromolecular complexes (Rajendran et al., 2003).

Xu et al. (2005) have carried out a study on water resistance, mechanical properties and compatibility of composite films based on starch and chitosan. They found that the interactions between starch and chitosan can form a tough film which prevents the water molecules from diffusing through the films. Khiar & Arof (2011) and Shukur et al. (2013) obtained good conductivity values (10^{-5} S cm^{-1}) when they doped the starch/chitosan films with ammonium salts which proves that this is a promising blend for polymer electrolyte.

Several techniques have been used to study on the miscibility of the polymer blend host to check the influence of blend ratio on miscibility. The objective of this chapter is to understand the miscibility, amorphousness and compatibility of the starch/chitosan blend to serve as a polymer host based on FTIR, XRD, TGA, DSC and FESEM micrographs of the cross-sections polymer blend.

4.2   FTIR Analysis

FTIR spectroscopy was carried out to understand the interactions between the starch and chitosan in the blend film. As mentioned by Buraidah et al., blending two or more polymers will provide more interaction sites for the ions to hop and exchange, hence increase the conductivity (Buraidah & Arof, 2011). The infrared spectra of acetic acid, chitosan powder, PB10, starch powder, PB0 and PB2 films in the region of 2900 to 3800 cm^{-1} are presented in Figure 4.1. Acetic acid exhibits a broad band at 3295 cm^{-1} which is attributed to hydroxyl, OH stretch from carboxylic acid. This location is almost similar as reported by Alias et al. (2014). The hydroxyl bands of chitosan powder appear at 3330 cm^{-1}. Dissolving chitosan in acetic acid has shifted the bands to 3354 cm^{-1}, as shown in PB10 spectrum. The hydroxyl bands of starch powder appear at 3262 cm^{-1} which then shifted to 3280 cm^{-1} in the spectrum of pure starch film (PB0) due to interaction with acetic acid. The ordered crystalline structures of starch were destroyed during gelatinization process leads to the exposure of OH groups. In acetic acid solution, the amino groups (NH_2) of chitosan backbone were protonated to NH_3^+ and form hydrogen bonds with OH from the starch (Bourtoom & Chinnan, 2008). When two or more substances are mixed, there are modifications in the characteristic spectra which reflect the interactions involving physical and chemical blends (Yin, Yao, Cheng, & Ma, 1999). Therefore, it can be seen that the hydroxyl band of PB2 film appears at 3288 cm^{-1}.
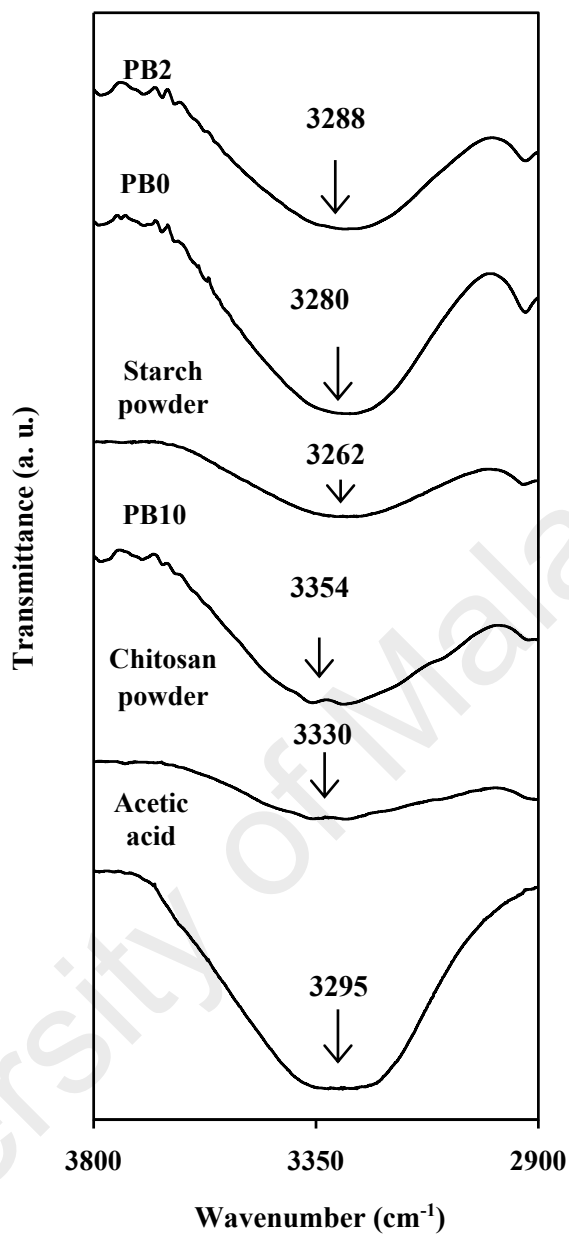
Figure 4.1: Infrared spectra of acetic acid, chitosan powder, PB10, starch powder PB0 and PB2 in the region of 2700-3900 cm⁻¹.

The schematic diagram of the interactions occurred between starch, chitosan and acetic acid in PB2 can be depicted in Figure 4.2. Starch and chitosan are interacted mainly through hydrogen bonding between the amylose group of starch and chitosan molecules (Mathew & Abraham, 2008). The branching structure of amylopectin has

greater steric hindrance thus prevents the chemical reactions to occur (Khanmirzaei and Ramesh, 2013).
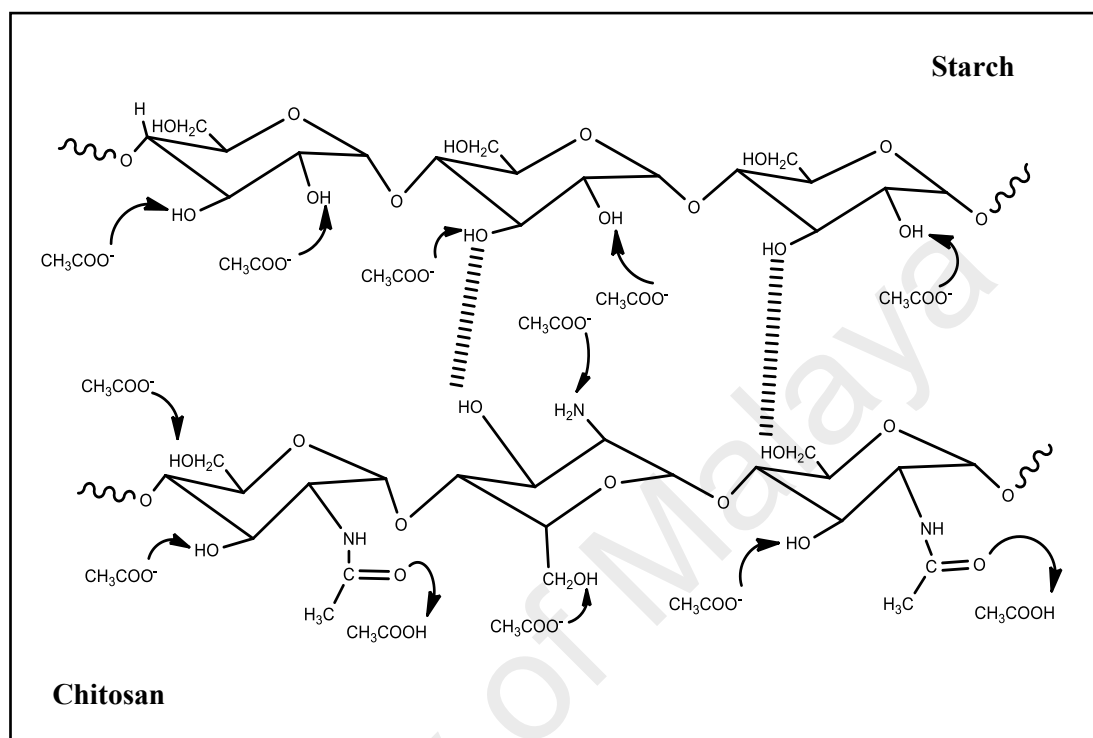
Figure 4.2: Schematic diagram of interaction between starch, chitosan and acetic acid in PB2 film (|||||||||||||||||| represents hydrogen bonds).

The carboxamide; O=C-NHR and amine; NH_2 bands exist at 1650 and 1573 cm^{-1}, respectively, in the spectrum of chitosan powder. Due to the interaction between chitosan and acetic acid (Osman & Arof, 2003), both bands appear at 1640 and 1549 cm^{-1}, respectively, in the spectra of PB10 as shown in Figure 4.3 (b). These positions are almost the same as reported by Buraidah & Arof (2011) and Kadir, Aspanut, Majid, & Arof (2011). The positions of the carboxamide and amine bands have shifted to 1639 and 1548 cm^{-1}, respectively in the spectra of PB2, which is comparable with the results reported by Xu et al. (2005). In a report by Liu, Adhikari, Guo, & Adhikari (2013), the position of the amide-I band at 1638.68 cm^{-1} in pure chitosan film has shifted to

1638.97 cm⁻¹ in starch/chitosan film due to the interactions between the hydroxyl groups of starch and the amino groups of chitosan, despite of the small shift in the spectrum.
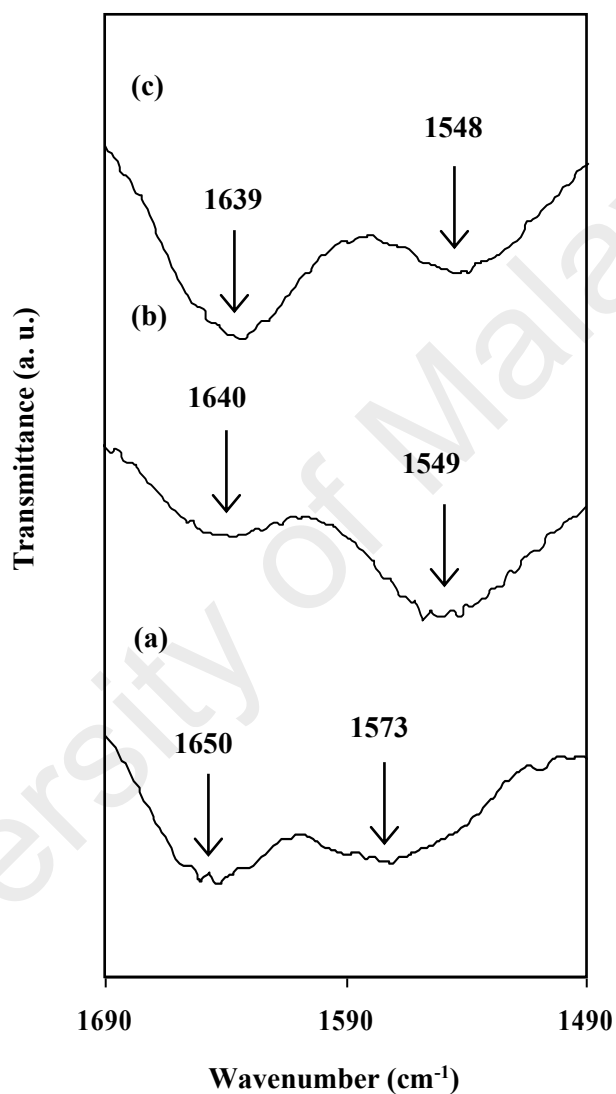
Figure 4.3: Infrared spectra of (a) chitosan powder, (b) PB10 and (c) PB2 in the region of 1490-1590 cm⁻¹.

It can be seen in Figure 4.4 that chitosan powder, PB10, starch powder, PB0 and PB2 films exhibit characteristic bands in the region of 955-1105 cm^{-1} attributed to saccharide stretching structure (Leceta, Guerrero et al., 2013; Liu et al., 2013; Tuhin et al., 2012). The C-O bond stretching in chitosan powder spectrum which is located at 1067 and 1029 cm^{-1} have shifted to 1063 and 1023 cm^{-1}, respectively, in chitosan film (PB10) spectrum. Alias et al. (2014) also reported the same phenomena when the band located at 1079 and 1036 cm^{-1} in chitosan powder have shifted to 1066 and 1016 cm^{-1}, respectively, when they dissolved chitosan powder in acetic acid to form the chitosan film.
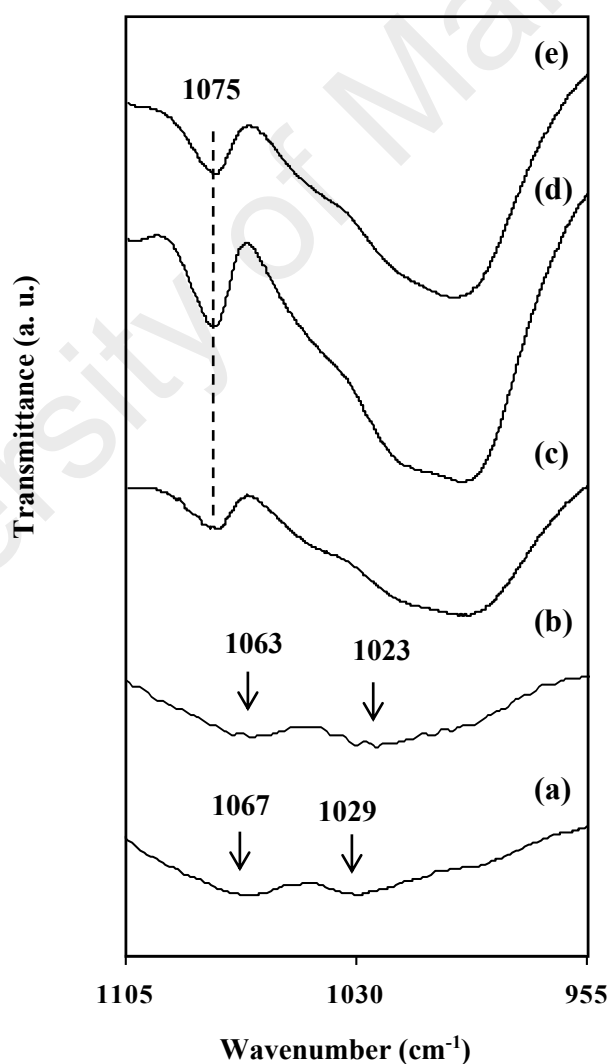
Figure 4.4: Infrared spectra of (a) chitosan powder, (b) PB10, (c) starch powder (d) PB0 and (e) PB2 in the region of 955-1105 cm^{-1}.

The C-O peaks located at 1075 cm^{-1} in starch powder, PB0 and PB2 spectra as shown in Figure 4.4 do not show any difference in wavenumber. However, the peak intensity in PB2 spectrum is found decreased, which is almost similar with the spectra reported by Mathew & Abraham (2008). They reported that the intensity of the peak at 1082 cm^{-1} in starch film is decreased in the spectrum of starch/chitosan film, which reflects the chemical interactions occur when two different substances are physically mixed. Due to the overlapping bands detected in the region of interest in starch powder, PB0 and PB2 spectra, deconvolution has been performed using OMNIC software with Lorentzian-Gaussian function to verify the individual peaks with the value of regression coefficient ~1. The deconvoluted spectra are presented in Figures 4.5 to 4.7. The other C-O characterization peaks are located at 990 and 1045 cm^{-1} in starch powder, PB0 and PB2 spectra without any changes in wavenumber. However, those peaks which are found intense and broad in starch powder get less intense in PB0 and PB2 spectra. These modifications reflect the interactions among the polymer molecules since any
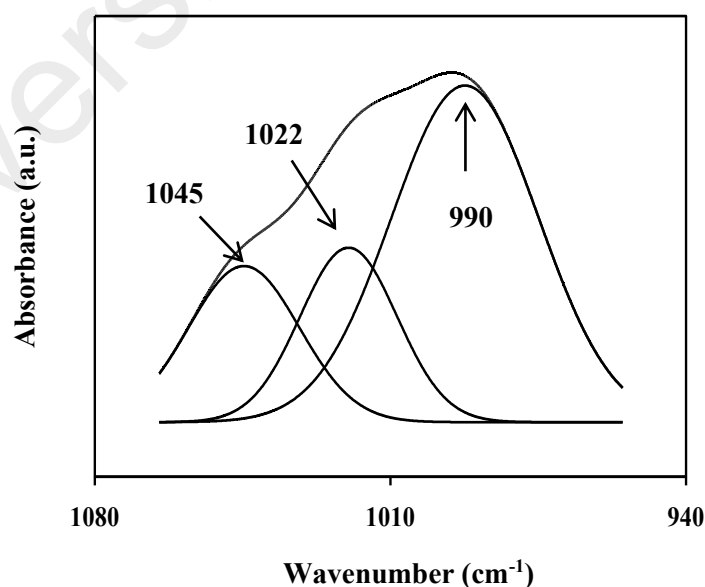
Figure 4.5: Deconvoluted of FTIR spectrum for starch powder in the region of 940-1080 cm^{-1}.

changes in either shape or intensity is correlated to chemical and physical interactions (Vicentini, Dupuy, Leitzelman, Cereda, & Sobral, 2005; Ramesh, Liew & Arof, 2011).

The peak located at 1022 cm^{-1} in starch powder spectrum is shifted to 1020 and 1007 cm^{-1} in PB0 and PB2, respectively. Besides shifting, the peak becomes broader with increasing intensity which proves a good interaction between the polymers. Mathew and Abraham (2008) reported a high intensity peak at 1029 cm^{-1} in the spectrum of starch/chitosan blend film. Vicentini et al. (2005) also reported that the C-O-H peak located at 1015 cm^{-1} in starch powder spectrum is shifted to 1012 cm^{-1} in the spectrum of starch film, which can be attributed to amorphous characteristic peak. Liu et al. (2013) reported the bands at 931, 1009 and 1077 cm^{-1} are resulted from the C-O in starch/chitosan film. Salleh et al. (2009) mentioned in their report that the absorbance peaks for chitosan films appeared at 1072 cm^{-1} is attributed to saccharide structures and C-O stretching vibrations, respectively. Teoh et al. (2012) also reported that the absorption at 995 and 1077 cm^{-1} are attributed to C-O-H and C-O stretching vibration in their starch sample.
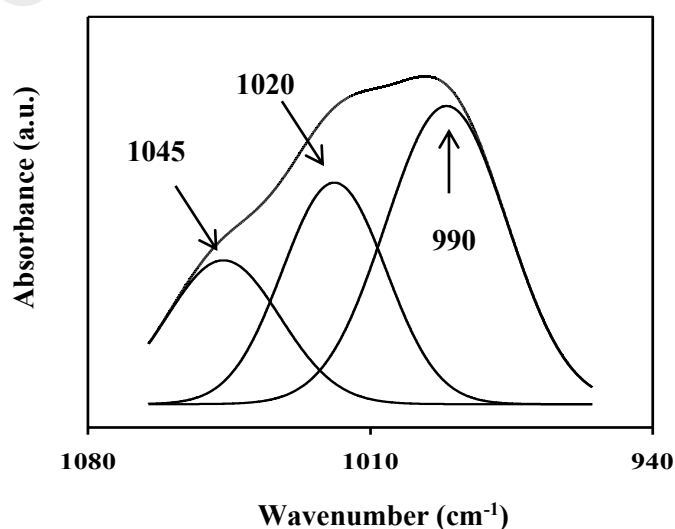
Figure 4.6: Deconvoluted of FTIR spectrum for PB0 in the region of 940-1080 cm^{-1}.
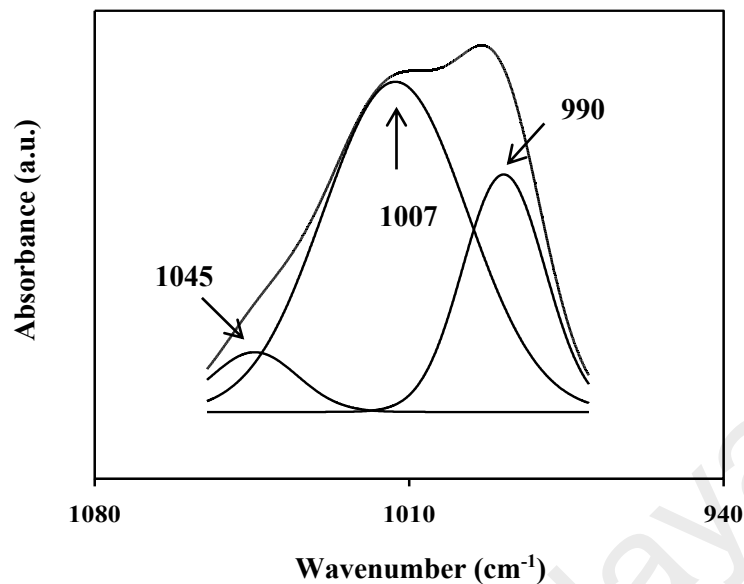
Figure 4.7: Deconvoluted of FTIR spectrum for PB2 in the region of 940-1080 cm^{-1}.

4.3   XRD Analysis

It is important to find the most suitable ratio of the polymer blend prior to serve as a polymer host. Chitosan is well-known of its properties such as good film-forming ability, flexible but mechanically strong and biodegradable (Liu et al., 2013). The amount of amylose and amylopectin in starch is closely related to the crystallinity of the blend film (Liu et al., 2013). Ratio of starch and chitosan plays important roles on the properties of the films such as miscibility, mechanical stability and water resistance (Bourtoom & Chinnan, 2008). To be exact, the choice is directed to the reduction in crystallinity of the polymer blend.

Deconvolution is found useful in polymer studies and has been carried out to obtain better views on the XRD patterns for further investigation on the crystallinity and structural changes due to overlapping patterns in the electrolytes (Galeski, Argon, &

Cohen, 1991). The amorphous peaks are broad but they underlie the sharp and narrow crystalline reflections. Figures 4.8 and 4.9 show the deconvoluted XRD diffractograms of starch/chitosan blend films. The baseline correction was done prior to fit multi-peaks using Gaussion distribution. The areas under the deconvoluted peaks were used to calculate the degree of crystallinity using equation:

$$\chi_c = \frac{A_T - A_a}{A_T} \times 100\%$$ (4.1)

with the aid of Origin 9.0 software using a non-linear least square fitting method, where A_T is the total humps and A_a is the amorphous area of the electrolyte (Fadzallah et al., 2014).

The deconvolution pattern of PB10, PB9, PB8, PB7, PB6 and PB5 blend films can be depicted in Figure 4.8. It can be observed that the PB10 diffractogram consists of two broad amorphous peaks at $2\theta = 19.3°$ and $38.9°$. Three crystalline peaks at $2\theta = 12.5°$, $16.1°$, and $22.4°$ have surfaced which similar with the peaks reported by Aziz et al. (2012) and Fadzallah et al. (2014).
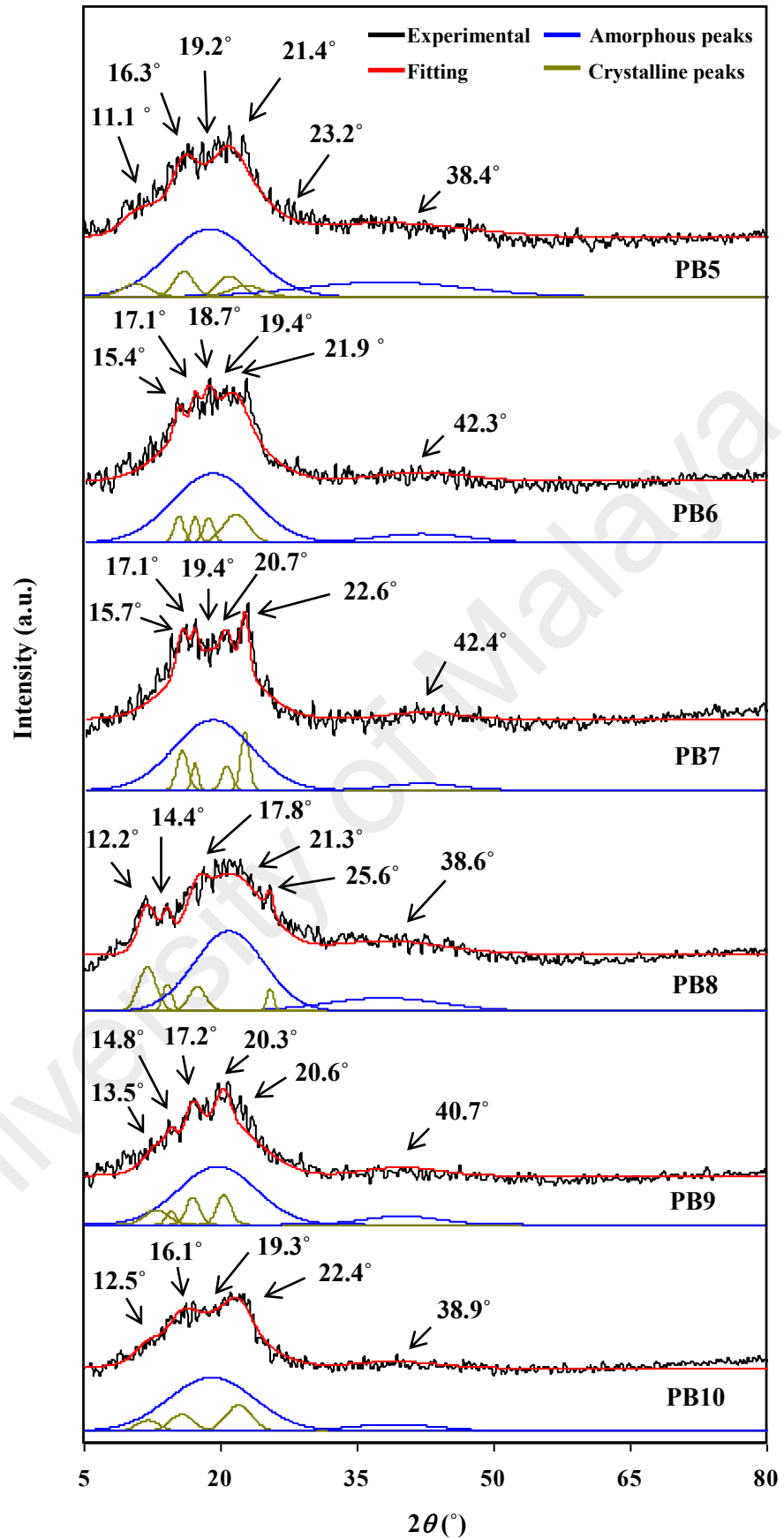
Figure 4.8: Deconvoluted XRD pattern of PB10 to PB5 blend films.

It is observed that new peaks start to appear as the chitosan is blended with starch. As can be seen in XRD pattern of PB9 in Figure 4.8, a new crystalline peak appears at $2\theta = 14.8°$, ensuring that the addition of 10 wt.% of starch has resulted on a slight modification to the film without changing the property individually which proven by the retaining of two amorphous peaks at $2\theta = 20.3°$ and $40.7°$. As the starch content increases, the locations of crystalline peaks change as well as the amorphous peaks location. All ratios; PB9, PB8, PB7, PB6 and PB5; exhibit four crystalline and two amorphous peaks in their XRD diffractograms.

Deconvolution of PB4, PB3, PB2, PB1 and PB0 films are shown in Figure 4.9. The XRD pattern of PB0 film reveals that there are five crystalline peaks appear at $2\theta = 13.7°$, $15.1°$, $16.7°$, $19.4°$ and $22.4°$ besides two amorphous peaks centered at $2\theta = 20.5°$ and $37.5°$. All patterns except PB4 reveal that there are four crystalline peaks with two broad amorphous peaks. However, crystalline peaks presented in PB4 at $2\theta = 14.5°$, $24.8°$ and $28.9°$ show higher intensity inferring that the crystallinity value has increased. The crystalline peaks for PB3 appear at $2\theta = 15.0°$, $17.3°$, $20.1°$ and $22.4°$ with two amorphous peaks appear at $2\theta = 19.2°$ and $35.4°$. These deconvolution patterns reveal that the polymers retained their individual behaviors in the polymer blend film due to the location of the crystalline and amorphous peaks. Further addition of starch has slightly shifted the crystalline peaks in PB2 to $2\theta = 14.2°$, $16.9°$, $23.9°$ and $27.9°$ while the amorphous peaks have shifted to $2\theta = 20.7°$ and $34.7°$. Deconvolution of PB1 pattern shows that the amorphous peaks are located at $2\theta = 20.4°$ and $35.1°$ which almost similar with PB2. The crystalline peaks with higher intensity appear at $2\theta = 16.1°$, $17.2°$, $19.5°$ and $22.5°$, showing that this ratio is also crystalline as the pure starch film (PB0).
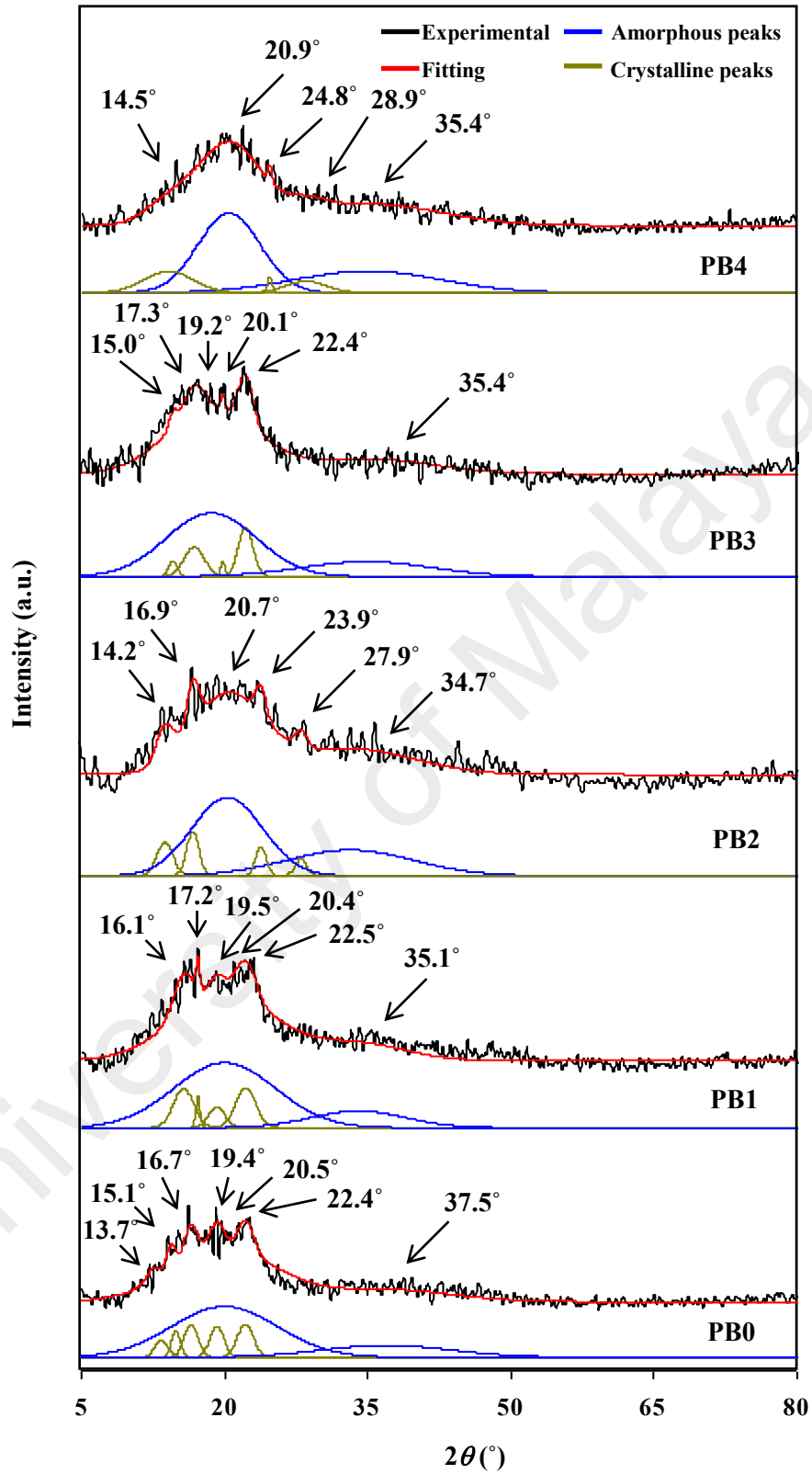
Figure 4.9: Deconvoluted XRD pattern of PB0 to PB4 blend films.

From the XRD patterns, it can be depicted that PB2 gives the broadest amorphous peaks with less intense crystalline peaks among other ratios. Based on the deconvoluted peaks, degree of crystallinity of the films have been calculated and listed in Table 4.1.

Table 4.1: Degree of crystallinity of starch/chitosan blend films.

Samples	Degree of crystallinity (X_c)
PB0	21.10
PB1	20.49
PB2	15.30
PB3	16.55
PB4	16.27
PB5	17.39
PB6	17.80
PB7	18.30
PB8	18.40
PB9	19.37
PB10	19.64

It is shown from the Table 4.1 that PB2 possesses the lowest crystallinity value. This proves that this ratio is the most amorphous polymer blend. The interactions between the hydroxyl groups of starch, chitosan and NH group from chitosan as discussed in FTIR analysis section, also play important roles in reducing the crystallization of the blend (Mathew & Abraham, 2008). Zhai et al. (2004) reported that an obvious improvement has been shown when chitosan was incorporated into starch and dried at room temperature. They claimed that the films tensile strength highly increased by incorporating 20% chitosan but difficult to form a homogenous starch/chitosan mixture with a higher content of chitosan. In their studies, XRD result

for a blend comprises of pure 20 wt% chitosan and 80 wt% corn starch shows the most amorphous pattern and therefore, the present result is in good agreement with Zhai et al. (2004). Literally, a blend of crystalline polymers with poor miscibility will result on the appearance of separate crystalline regions according to individual domain (Sakurai et al., 2000). In contrast, when the molecular chains of both polymers are mixed so well, they cannot crystallize but instead, need to be arranged in three-dimensional space in order to crystallize. It can be seen that the crystalline domains in PB2 are suppressed which proven by the lowest degree of crystallinity. This result also strengthens the fact that PB2 is the most amorphous blend ratio and suitable to serve as the polymer host.

Figure 4.10 exhibits the X-ray diffractograms of all ratios of the starch/chitosan blend films. Deconvolution technique has already presented where the diffractogram of the starch/chitosan blend films have additional crystalline peaks apart from the obvious peaks depicted in Figure 4.10. When all XRD patterns are combined, two obvious crystalline peaks can still be detected in PB0 film where the locations are almost similar with the peaks reported by Liu et al. (2013), Mathew & Abraham (2008) and Wu, Ji, Qi, Wang, & Zhang (2004). A broad crystalline peak was detected at $2\theta = 23°$ in the PB10 film which is comparable with XRD patterns by Mathew & Abraham (2008) and Hasegawa, Isogai, Onabe, Usuda, & Atalla (1992). However, as already been discussed and evaluated from XRD deconvolution pattern, PB2 pattern is abruptly changed where all crystalline peaks due to starch and chitosan are disappeared. Amorphous regions are formed by demolishing their individual crystalline regions and consequently proves that the polymers are miscible and well-mixed at the molecular level (Mathew & Abraham, 2008). Without deconvolution, it still can be concluded that PB2 is the most amorphous ratio among others as depicted in Figure 4.10.
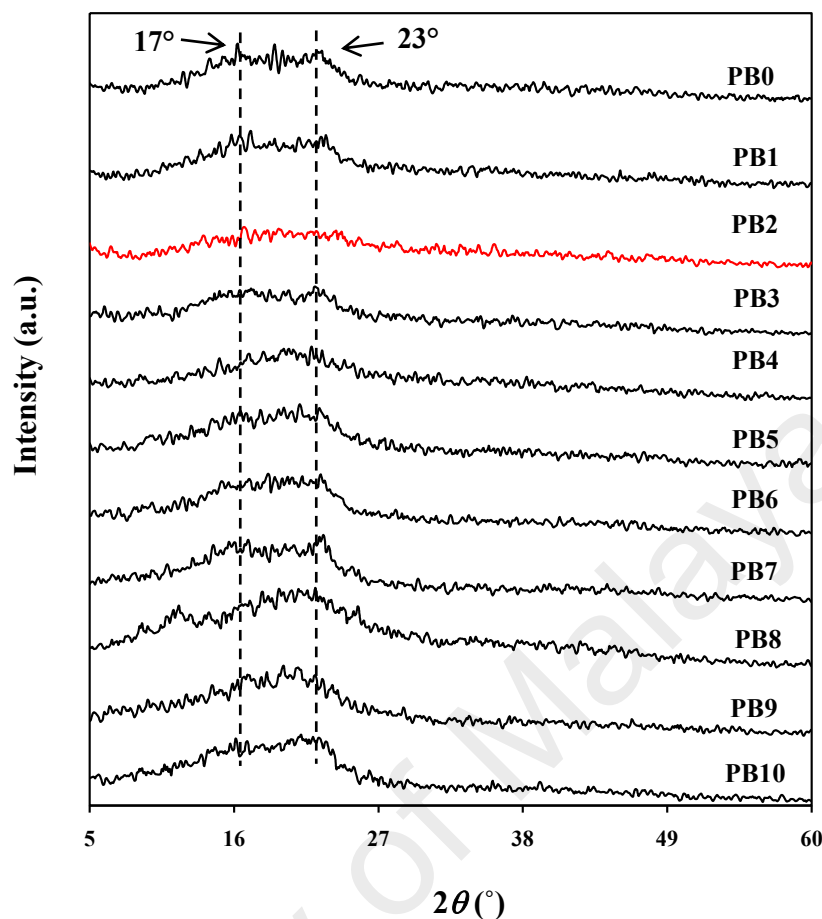
Figure 4.10: The XRD patterns of all ratios of starch/chitosan polymer blend.

4.4   TGA Analysis

TGA measurement is carried out to study the thermal stability and phase transition of the pure films and pure blend films. Figure 4.11 shows the TGA thermograms of PB0, PB10 and PB2 films. The thermal degradation initially starts as the temperature increased up to 150˚C due to dehydration of water, elimination of residue of acetic acid and impurities in the polymer electrolytes which involving around 10-12% weight loss (Lewandowska, 2009; Liew, Ramesh, & Arof, 2014a). The hydroscopic nature of the polymer also contributes to the insignificant weight loss at this stage (Lu et al., 2009), which is similar as reported by Noor et al. (2012) and

Lewandowska (2009). At 230-450˚C, major weight loss of ~50% in pure chitosan film (PB10) is attributed to the decomposition and deacetylation of chitosan (Wang et al., 2005). Compared to the decomposition of pure starch film (PB0) which starts at 280-410˚C with major weight loss ~85%, it can be seen that pure starch film can stand higher temperature compared to pure chitosan film.

According to Ramesh, Shanti, & Morris (2012), this one step huge weight loss process is attributed to the depolymerization of the polymer electrolyte. At this temperature, the monomers, which are amylose and amylopectin detached from their long polymer chain while forming aromatic and cross-linked structures as the degradation behaviors of starch and chitosan film individually are retained in the blend film. Starch/chitosan blend (PB2) film starts to decompose at around 270˚C and shows ~30% material left which proves that blending starch with chitosan has improved the film stability.
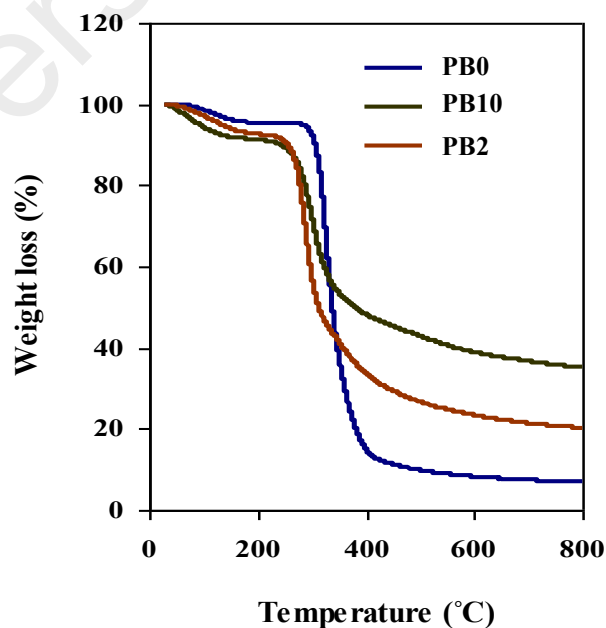
Figure 4.11: TGA thermograms of PB0, PB10 and PB2 films.

4.5   DSC Analysis

The thermal properties of the polymer blend electrolytes have been studied in order to verify the miscibility of the blend films. The values of T_g are taken as the midpoint of the heat capacity transition, from glassy state to rubbery condition (Lau & Mi, 2002). The T_g of natural polymers are still under discussion among most researchers (Liu, Yu, Liu, Chen, & Li, 2009; Neto et al., 2005). This affected by several properties of natural polymers such as degree of deacetylation, molecular weight and cystallinity which can present in wide variation depending on the source and extraction method, which lead to different values of T_g (Bonilla, Fortunati, Atarés, Chiralt, & Kenny, 2014; Neto et al., 2005; Rotta, Minatti, & Barreto, 2011). Processing conditions have an important role on the final blend materials, hence influenced the physical and thermal properties of the polymer blend. The T_g values of PB0 and PB10 can be depicted in Figure 4.12 and 4.13, respectively. The T_g of PB0 obtained is within the temperature range of 30 to 95˚C as reported by Zeleznak & Hoseney (1987) for starch containing 10-18 % moisture. The T_g of PB10 is close to the value reported by Liu et al. (2013) which is 82.1˚C with 18.18% moisture content.
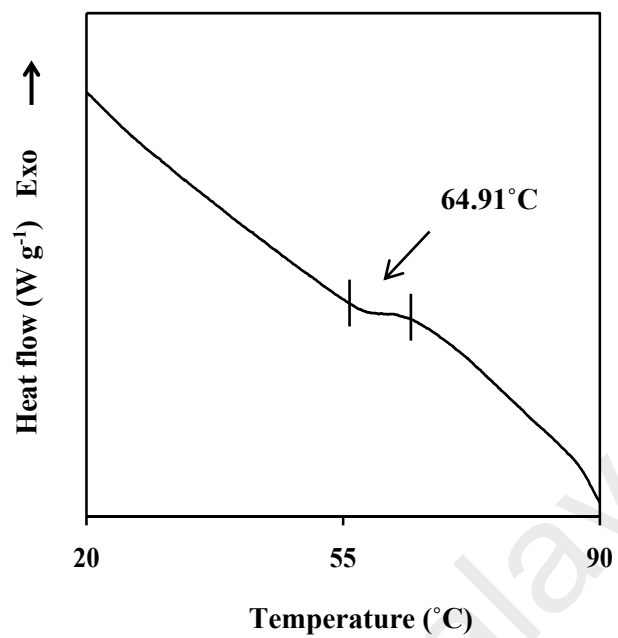
Figure 4.12: T_g of PB0 film.
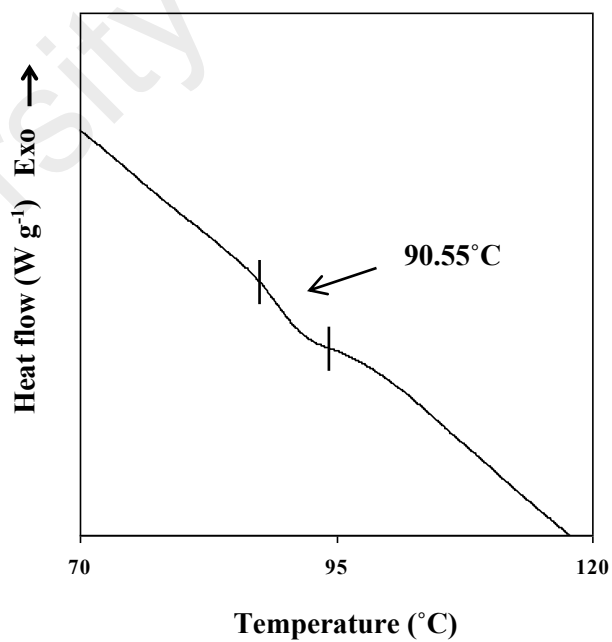
Figure 4.13: T_g of PB10 film.

Figures 4.14 to 4.20 depict the T_g value of selected blend films. The interactions effect of compatible and miscible polymers on T_g implies that the value will fall at intermediate range between the values of the individual pure polymers (Barbani et al., 2005; Bonilla et al., 2014; Lau & Mi, 2002). van den Broek, Knoop, Kappen, & Boeriu, (2015) reported that the influence of chitosan on the thermal properties of any polymer blends is different for each combination. PB1, PB2, PB3, PB4, PB5, PB6 and PB8 exhibit T_g values of 88.41, 86.51, 88.96, 88.81, 88.78, 87.29 and 88.74˚C, respectively. Each blend film possesses different T_g, implying the different ratio or content of starch and chitosan. However, the T_gs are in the intermediate range between the T_g of starch and the T_g of chitosan films. The shift in T_g value points to the good miscibility of both macromolecules (Bonilla et al., 2014; Cheung, Wan, & Yu, 2002).

The addition of starch with chitosan has interrupted the arrangement of molecule chains in starch, hence slightly shifts the T_g value of the starch film, confirming the interaction between these two polymers (Liu et al., 2013; Lopez et al., 2014). This phenomenon can be described in terms of intermolecular forces. In crystalline phase of starch, the interactions between polymeric chains are strong due to their chemical compatibility. When chitosan is added, there are modifications in the crystal lattice formulations and both polymers can interact mainly through hydrogen bonding (Cheung et al., 2002; Lau & Mi, 2002; van den Broek et al., 2015). However, the interactions between starch chains have become weaker, thus less energy is required to break them apart (Lopez et al., 2014). T_g of PB2 exhibits the lowest value, confirming the highly amorphousness of the blend compared to other ratios. These results are in good agreement with XRD observation and conclude that the components in the ratio are miscible with each other (Pareira, Paulino, Nakamura, Britta, Rubira, & Muniz, 2011).
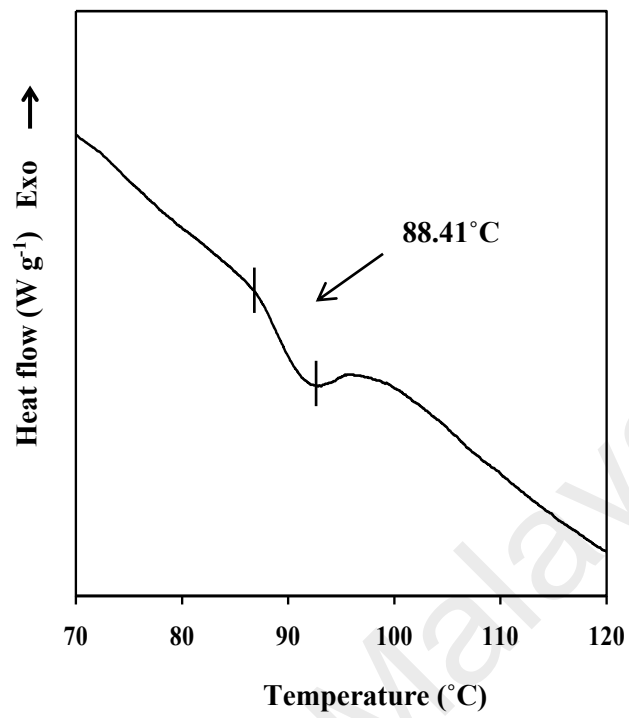
Figure 4.14: T_g of PB1 film.
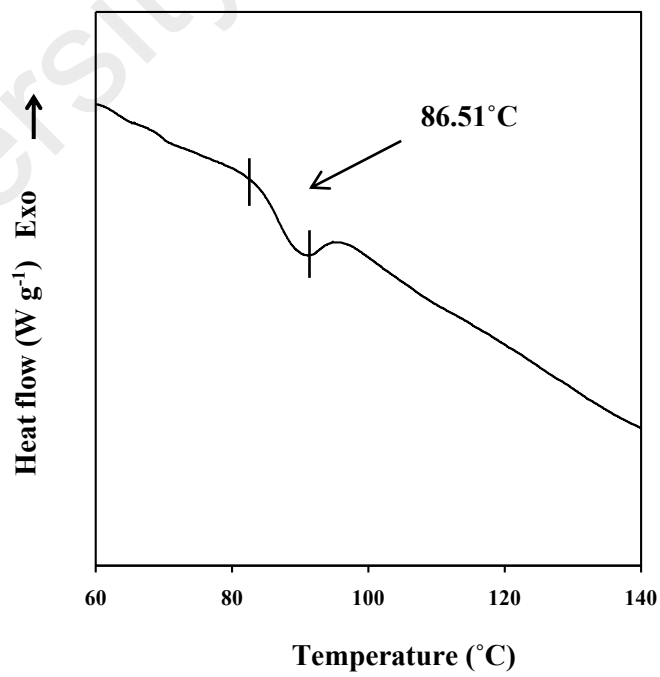
Figure 4.15: T_g of PB2 film.
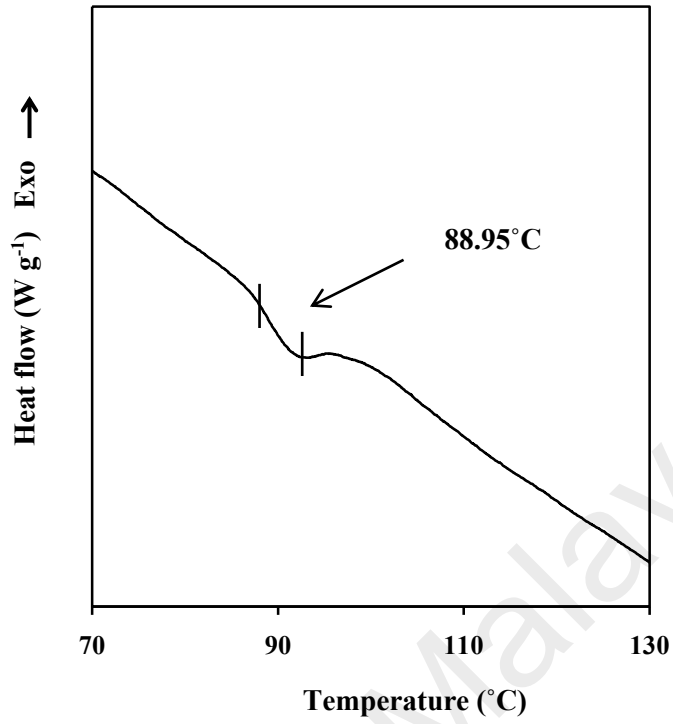
Figure 4.16: T_g of PB3 film.
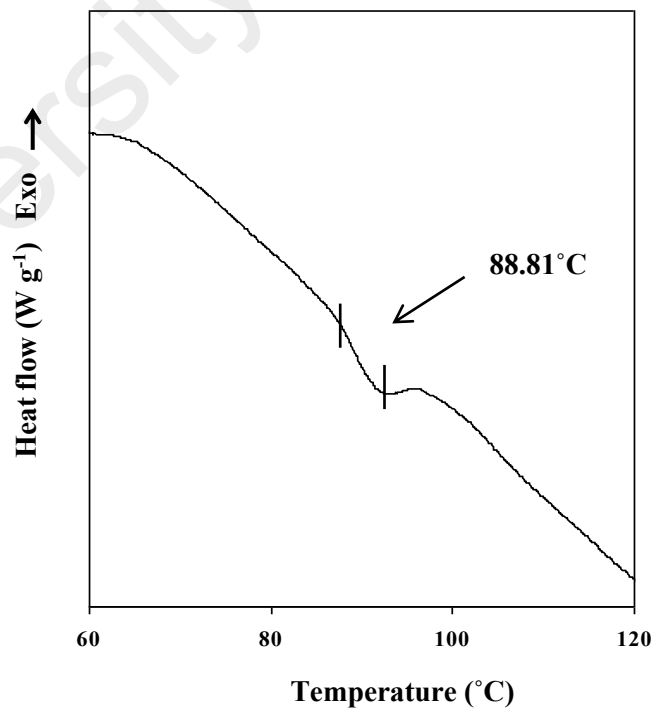
Figure 4.17: T_g of PB4 film.
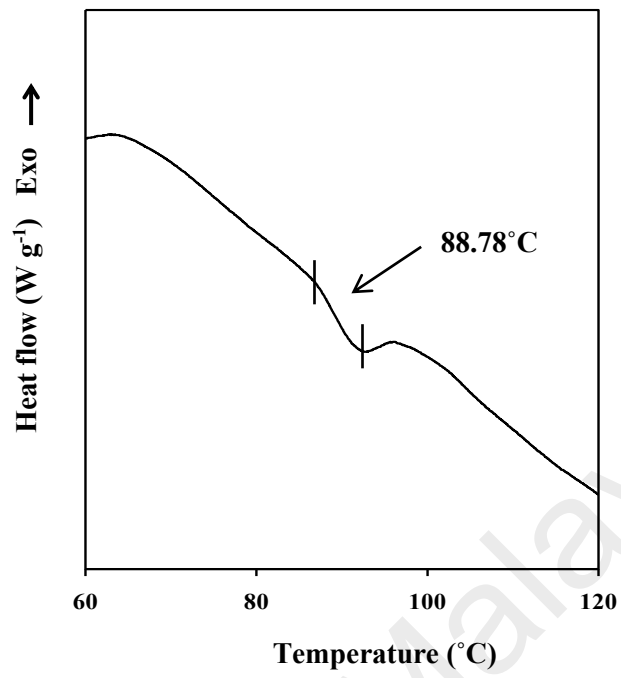
Figure 4.18: T_g of PB5 film.
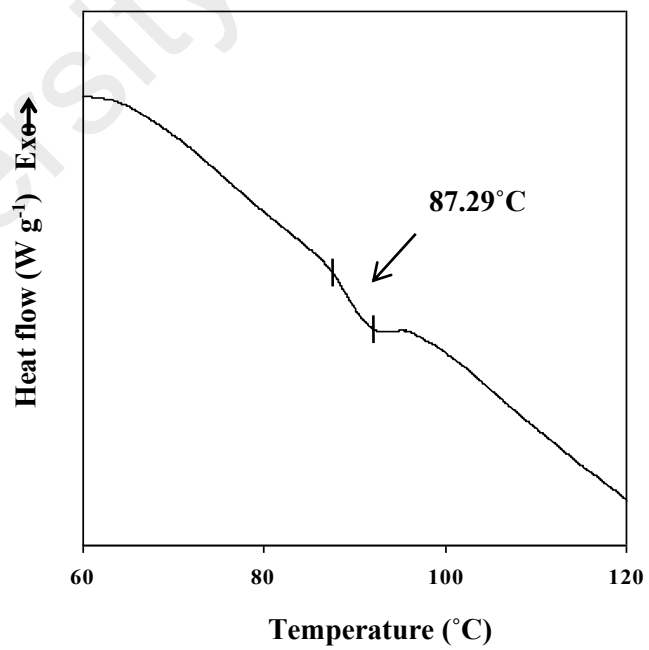
Figure 4.19: T_g of PB6 film.
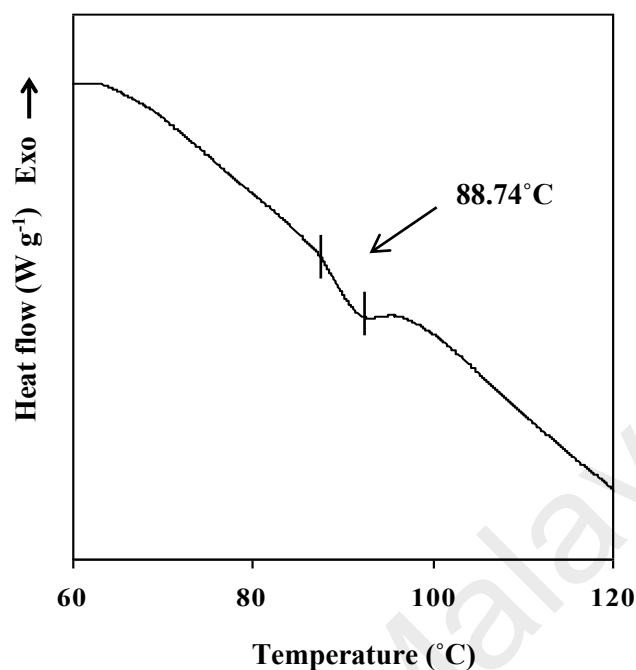
Figure 4.20: T_g of PB8 film.

4.6 FESEM Analysis

FESEM micrographs of cross-section of the blend film are crucial in confirming the miscibility between the starch and chitosan as the polymer host. Figures 4.21 (a) to (c) exhibit the micrographs of the cross-sections and the surface micrographs. As can be seen in Figure 4.21 (a) and (b), both starch (PB0) and chitosan (PB10) films exhibit rough cross-sections surface. Starch film possesses a shrinkage pattern film with some withered granules which consistent with the results reported by Salleh et al. (2009) and Liu et al. (2013). Muscat, Adhikari, Adhikari, & Chaudhary (2012) also reported that the starch films were brittle and highly cracked at room temperature. In contrast with starch film surface, chitosan film shows a smooth and homogenous surface. PB2 film

exhibits a similar surface pattern with PB10, as shown in Figure 4.21 (c). This result also has a similar pattern with the one reported by Liu et al. (2013), indicating the chitosan and starch are miscible into each other without the presence of undissolved starch granules. Literally, a blend of crystalline polymers with poor miscibility will result on the appearance of separate crystalline regions according to individual domain (Sakurai et al., 2000). The smooth cross-section of the blend has supported the fact that blending starch and chitosan will enhance the compatibility of the electrolyte to serve as polymer blend host. A report by Lopez et al. (2014) also exhibited a smooth, uniform and unlayered cross-section surface when corn starch is blended with chitosan, which is similar with the present work. Zhai et al. (2004) suggested that the interactions between starch and chitosan molecules resulted on the dispersion of chitosan microdomains within the starch matrix in the blend film especially between the chitosan and amylose of starch molecules, compared to the branched chain of amylopectin (Mathew & Abraham). The PB2 surface reveals slight traces of the starch granules from which the amylose molecules have leached out during gelatinization. From the smooth pattern obtained, it can be concluded that the mixture of starch and chitosan is compatible since the presence of chitosan has suppressed the crack and shrink which appear in starch film, hence make it a good candidate to serve as polymer host.
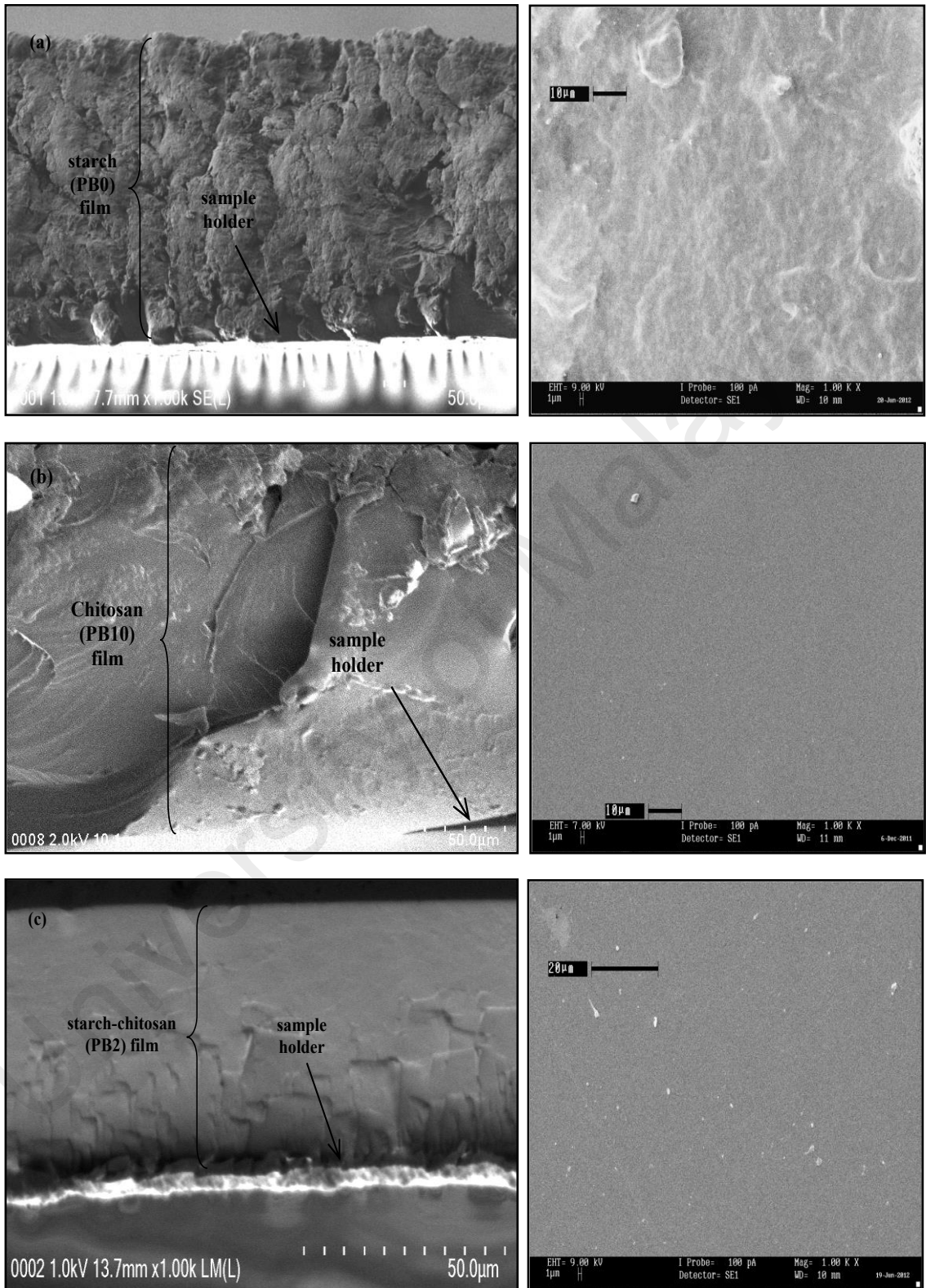
Figure 4.21: FESEM micrographs of PB0, PB10 and PB2 films.

4.7 Summary

FTIR analysis confirmed the interaction between acetic acid, starch and chitosan. To strengthen the XRD results, deconvolution has been carried out and crystallinity values have been calculated. When the molecular chains of both polymers are mixed so well, they cannot crystallize but instead, need to be arranged in three-dimensional space in order to crystallize. It can be seen that the crystalline domains in PB2 are suppressed which proven by the lowest degree of crystallinity. TGA analysis reveals that the degradation behaviors of starch and chitosan film individually are retained in the blend film. T_g values obtained from DSC are in good agreement with XRD observation and conclude that the components in PB2 are miscible with each other. Hence in the present study, PB2 blend is expected to host a reasonable fast ionic conduction compared to other blend compositions due to the interactions between the OH groups from starch and chitosan; and NH group from chitosan as discussed in FTIR analysis section, which resulted on the reduction of crystallinity region. FESEM micrographs also prove that the smooth pattern obtained for PB2 blend indicates that the starch and chitosan are miscible into each other. From all the results presented above, it can be proven that the blend of 80 wt.% starch and 20 wt.% chitosan is well formed and suitable to serve as polymer blend host.

CHAPTER 5: FOURIER TRANSFORM INFRARED (FTIR) STUDIES

5.1   Introduction

In this chapter, FTIR analysis is analyzed to determine the interactions of starch/chitosan-NH$_4$I and starch/chitosan-NH$_4$I-glycerol by observing the changes in the peak positions or wavenumbers of the functional groups that exist in the spectrum. These results can be used to identify the species and the chemical processes involved in the reactions occurred in the systems. Researchers have widely used FTIR as a direct method to monitor the band shifts or changes of the spectral peaks wavenumbers of certain functional groups in polymer electrolyte systems (Hema et al., 2009; Liu et al., 2013).

Polymer blending is an alternative to provide more complexation sites for ion migration and exchange which lead to the increase in ionic conductivity (Buraidah & Arof, 2011). Previous studies have shown that blending of polymers may enhance the conductivity value better than individual polymer host (Khiar & Arof, 2011; Shukur et al., 2013). As determined in Chapter 4, the blend of 80 wt.% starch and 20 wt.% chitosan has been proven to be the most amorphous blend to serve as the polymer blend host. The FTIR spectra of the blend also justified that the modifications from the blending technique resulted on the interactions among the electrolyte components (Shukur, 2015; Kadir et al., 2011). The starch and chitosan are interacted mainly through hydroxyl, amine and carboxamide groups. To ensure the polymer blend host can serve as an electrolyte, NH$_4$I salt is added into the system to provide the charge carriers. The addition of NH$_4$I has brought new functional groups hence new chemical interaction may occur, which can be studied from the FTIR results. The cation of the

doping salt will form a dative bond with nitrogen and/ or oxygen, thus a polymer-salt complex can be formed.

5.2 Interaction between Starch/chitosan-NH₄I (Salted System)

Figure 5.1 shows the FTIR spectra for polymer-salt complexes in the hydroxyl band region between 2900 to 3500 cm^{-1}. From the figure, it is observed that the addition of 10 and 20 wt.% NH$_4$I has down shifted the hydroxyl band of PB2 from 3288 cm^{-1} to 3286 and 3272 cm^{-1}, respectively. The hydroxyl band shifting trend is similar with the results reported by Shukur et al. (2013) when the blend of PEO-chitosan interacts with NH$_4$NO$_3$. Hydroxyl bands are found strong and broad in A1 and A2 electrolytes as depicted in Figure 5.1. The hydroxyl stretching bands remain under constant review, and differing viewpoints concerning the position and orientation of the hydroxyl groups exist (Frost & Johansson, 1998). Teoh et al. (2012) reported that the strong and wide absorption at 3309 of pure corn starch samples indicates the presence of OH groups in their system that is comparable with this work. When 30 wt.% of NH$_4$I is added, two peaks start to appear. The intensity of the peaks increases as the salt content increases. The appearance of those peaks is due to the overlapping of hydroxyl band, the asymmetry vibration; υ_{as} (NH$_4^+$) mode and symmetry vibration; υ_s (NH$_4^+$). The deconvolution technique using Lorentzian-Gaussian function is employed to extract the exact peak positions of the overlapping patterns and presented in Figure 5.2 and 5.3. Three deconvoluted peaks are obtained from A3 and A4 spectra. It can be seen that the addition of 30 and 40 wt.% NH$_4$I has shifted the hydroxyl band to 3324 and 3338 cm^{-1}, respectively. Another two peaks which located at 3179 and 3037 cm^{-1} in A3 and 3175 and 3047 cm^{-1} in A4 spectra are due to v_{as}(NH$_4^+$) and v_s(NH$_4^+$) peaks. On the addition of
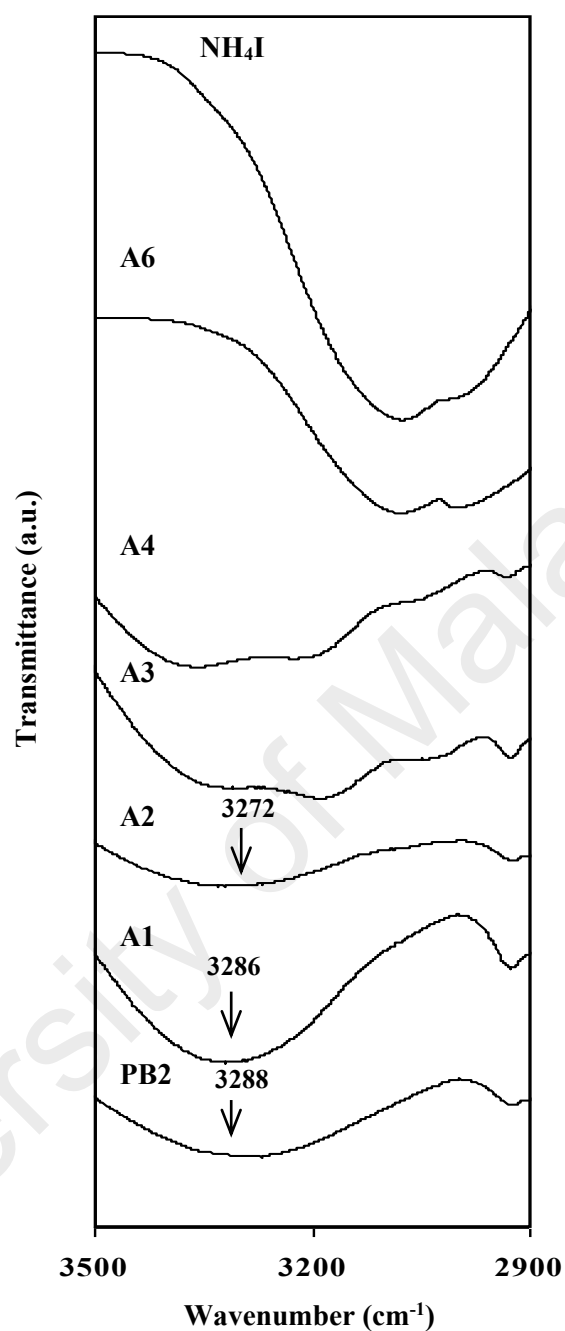
Figure 5.1: FTIR spectra for PB2 and selected electrolytes in salted system in the region of 2900-3500 cm^{-1}.

salt into the polymer host, the cation is expected to coordinate within the polymer host which may influence the original structure of the polymer backbone and affected certain infrared active mode of vibrations (Hema et al., 2009). This also another evidence of interaction between the cation and the hydroxyl group of the polymer blend (Kadir et al.,

2010). The anions, I⁻ and cations, NH_4^+ mostly interact with H and O atoms in starch and chitosan. Thus, both H and O atoms are occupied and difficult to form hydrogen bonds with water molecules (Ramesh et al., 2011).

(a)

(b)
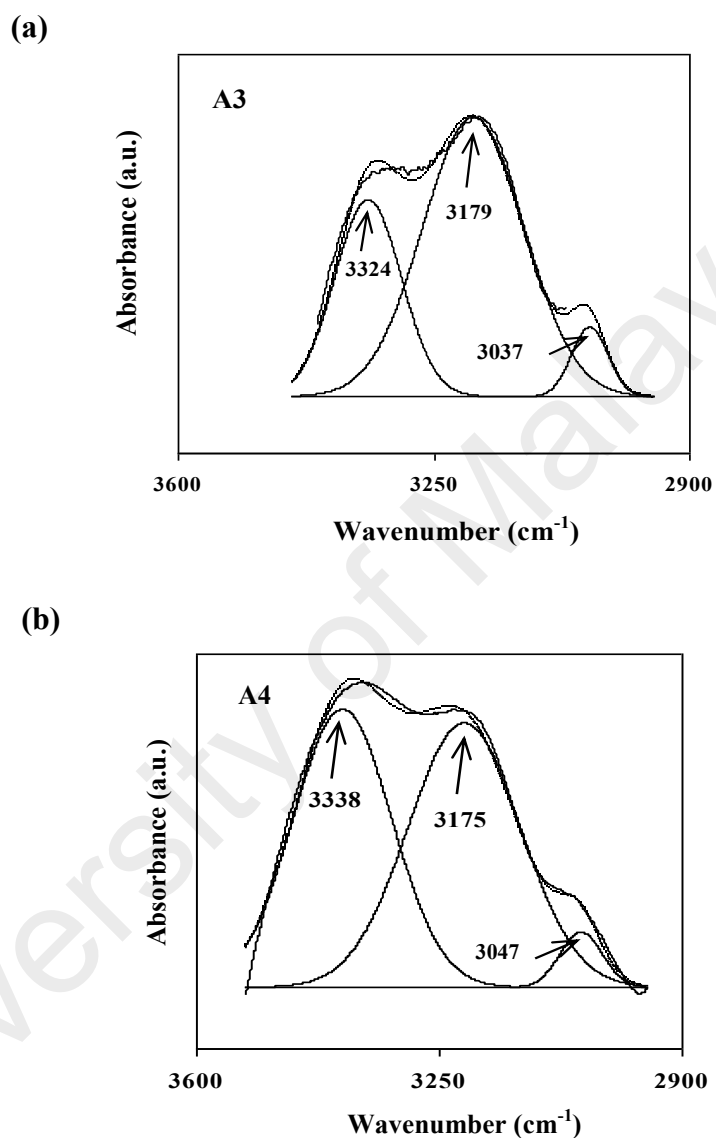
Figure 5.2: Deconvoluted FTIR spectra for A3 and A4 in the region of 2900-3600 cm⁻¹.

Further addition of 60 wt.% NH₄I, υ_{as} (NH_4^+) mode and υ_s (NH_4^+) mode seem to dominate and appear at 3057 and 2983 cm⁻¹, respectively, as depicted in Figure 5.3 (a). These two peaks are located at 3053 and 2981 cm⁻¹, respectively, in the spectrum of

pure NH₄I salt as shown in Figure 5.3 (b). Based on XRD results in Chapter 7, when more than 40 wt.% is added, the mobile ions tend to reassociate back to become neutral ion pairs. The significant appearance of υ_{as} (NH₄⁺) and υ_s (NH₄⁺) modes have shed some lights on the ions reassociation that will lead to conductivity decrement when more than 40 wt.% of NH₄I is added in the salted system.
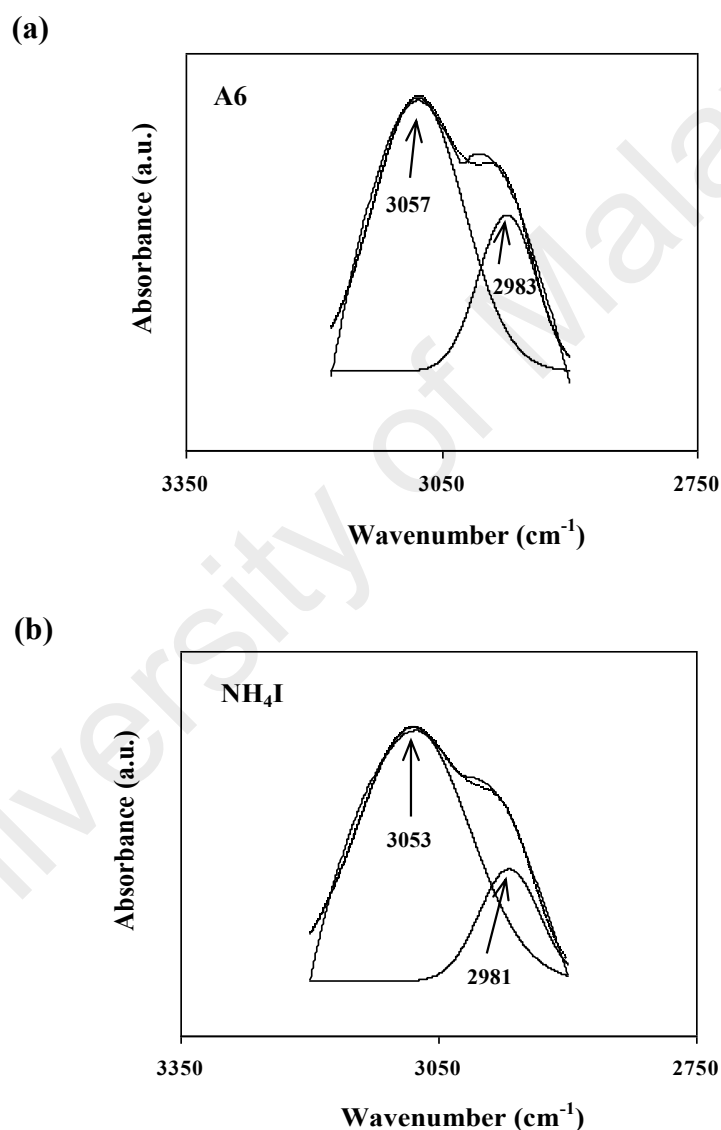
Figure 5.3: Deconvoluted FTIR spectra for A6 and pure NH₄I in the region of 2750-3350 cm⁻¹.

The carboxamide band is located at 1639 cm^{-1} in the spectum of PB2 electrolyte as depicted in Figure 5.4. The band is downshifted to 1635, 1627 and 1620 cm^{-1} in the addition of 10, 20 and 40 wt.%, respectively, inferring that complexation has occurred between the starch/chitosan blend and NH$_4$I salt. The shifting towards lower wavenumbers an indication of more hydrogen bonding interactions have occured between the components, where cations; H$^+$ and NH$_4^+$ will attach to C=O (Khoo, Frantzich, Rosinski, Sjöström, & Hoogstraate, 2003). When more than 40 wt.% salt is added, the band shifted to 1632 cm^{-1}. The shift towards higher wavenumber inferred
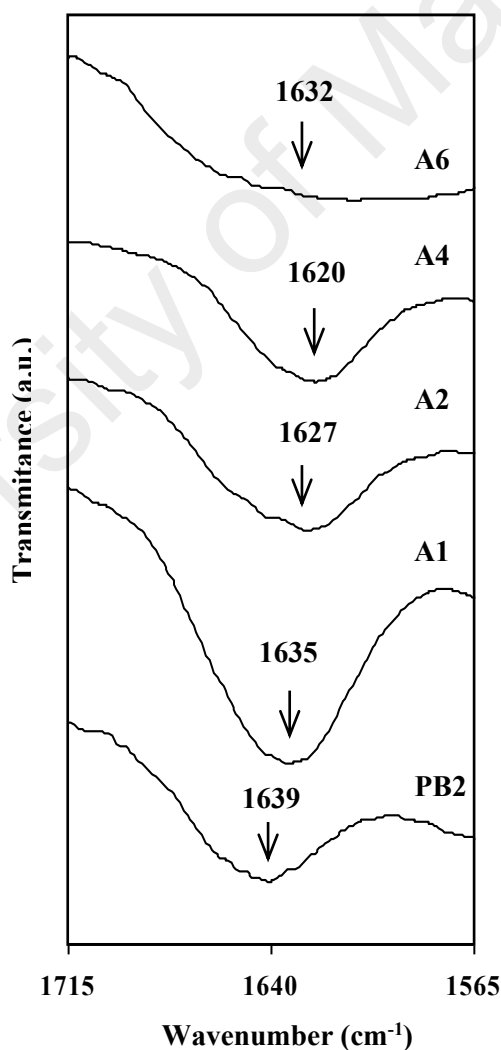
Figure 5.4: FTIR spectra for PB2 and selected electrolytes in the salted system in the region of 1565-1715 cm^{-1}.

that the saturation of salt leads to ions recombination hence reduced the interaction between the polymer host and the salt at oxygen atoms of carboxamide groups.

Figure 5.5 depicts the amine band region between 1490 to 1580 cm^{-1}. The amine band of PB2 is located at 1558 cm^{-1}. The addition of NH$_4$I up to 40 wt.% has shifted the band towards lower wavenumbers. This result proves the interaction within starch/chitosan-NH$_4$I electrolyte at nitrogen atom of amine group (Shukur et al., 2013). However, when more than 40 wt.% NH$_4$I is added, the amine band cannot be detected,
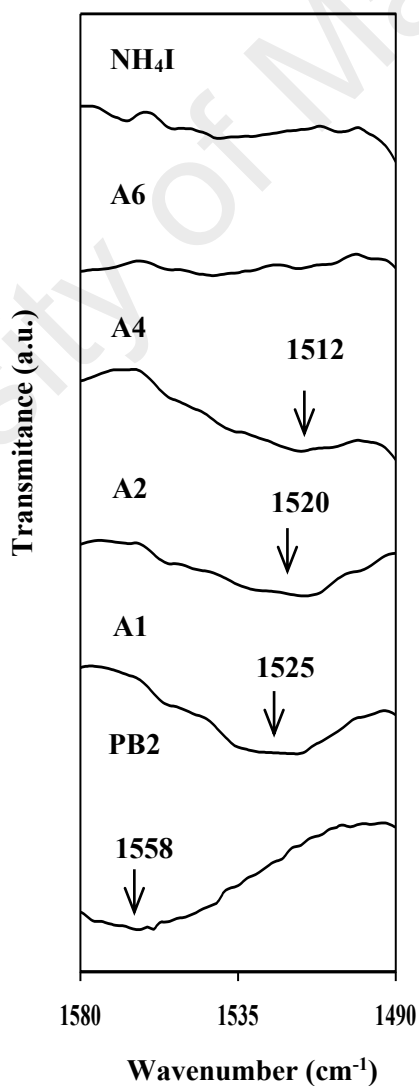
Figure 5.5: FTIR spectra for PB2 and selected electrolytes in the salted system in the region of 1490-1580 cm^{-1}.

suggesting that the electrolyte contains too much salt hence the ions reassociate back to form neutral ion pairs.

Figure 5.6 shows the saccharide bands region between 955 to 1055 cm^{-1}. These bands oftenly assigned as vibration modes of C-C and C-O stretching, and the bending mode of C-H bonds (Liu et al., 2013). The band observed at 1007 cm^{-1} in the spectrum of PB2 is attributed to C-O-H band vibration as reported by Bergo, Sobral, & Prison (2009) while the band at 990 cm^{-1} is attributed to the stretching vibration of C-O in C-O-
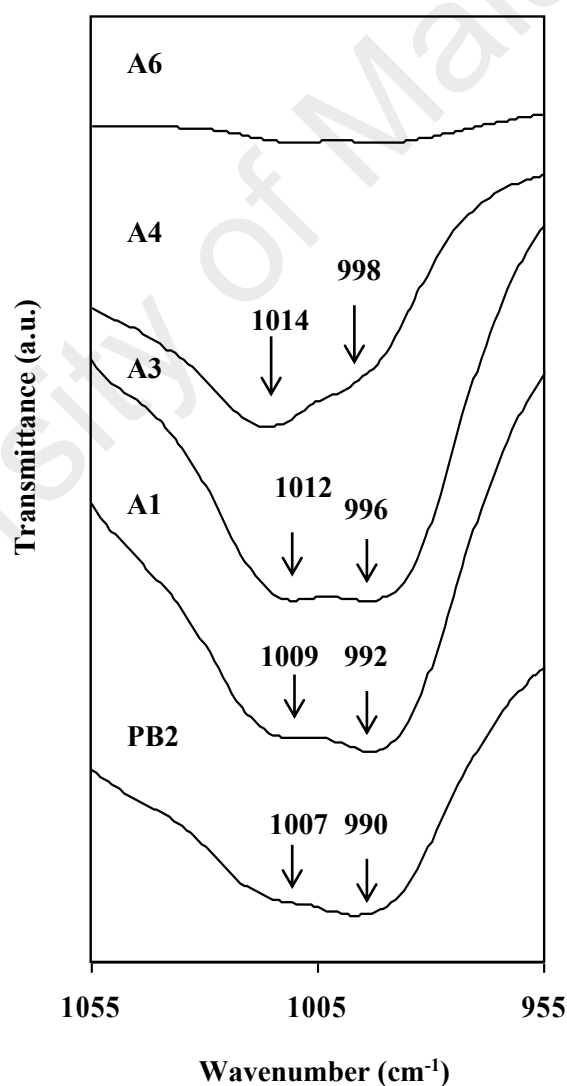
Figure 5.6: FTIR spectra for PB2 and selected electrolytes in the salted system in the region of 955-1055 cm^{-1}.

C group (Teoh et al., 2012). The bands exist in this region for PB2 have been further discussed in Chapter 4 and the deconvolution spectrum is presented in Figure 4.7. Both peaks are found shifted to higher wavenumbers up to 998 and 1014 cm^{-1} as the polymer blend is doped with NH_4I, proving the interactions between starch/chitosan with NH_4I (Ramesh et al., 2011). The new bands are located at new locations in A1, A3 and A4, respectively. However, when 60 wt.% of NH_4I is added, the intensity of the band becomes very low as depicted in Figure 5.6 due to overloaded of NH_4I within the polymer host. Deconvolution has been used to further analyze the FTIR spectra as can be seen in Figures 5.7 to 5.9.
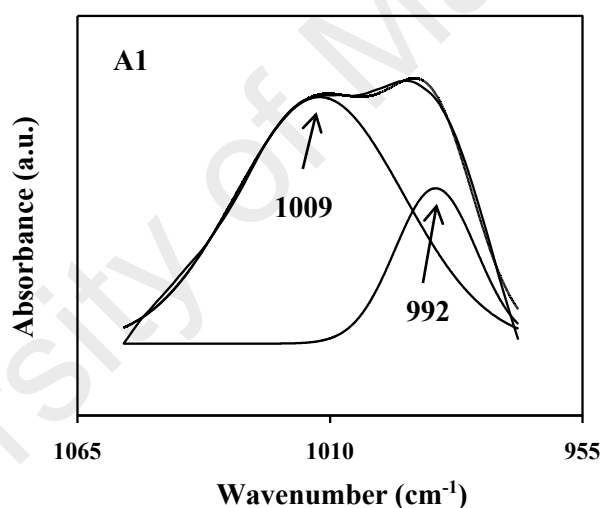
Figure 5.7: Deconvoluted FTIR spectra for A1 in the region of 955-1065 cm^{-1}.

The bands located at 1009 and 992 cm^{-1} in A1 have shifted to 1012 and 996 cm^{-1} respectively in A3 spectrum. The bands have further shifted to 1014 and 998 cm^{-1} in A4 spectra.
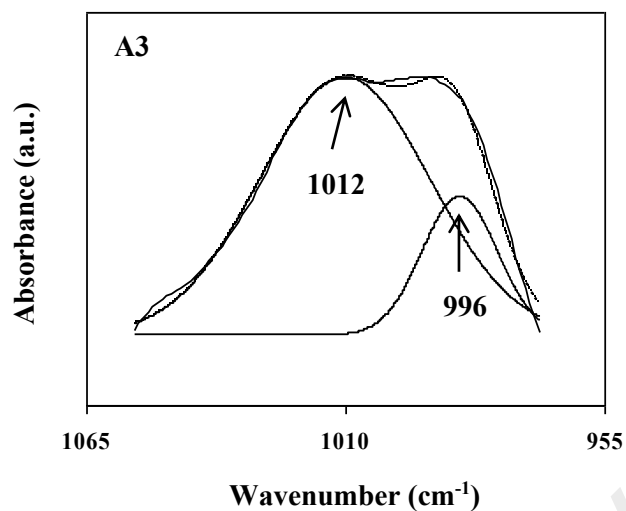
Figure 5.8: Deconvoluted FTIR spectra for A3 in the region of 955-1065 cm⁻¹.

The intensity of the band at 998 cm⁻¹ has reduced before almost disappear in the spectra of A6. Vicentini et al. (2005) reported that these bands are sensitive to crystallinity, hence any changes in shape and intensity within this region is correlated to the transition from amorphous to semicrystalline state or vice versa. This could strengthen the fact that the conductivity in this work have decreased due to the recrystallization of the salt.
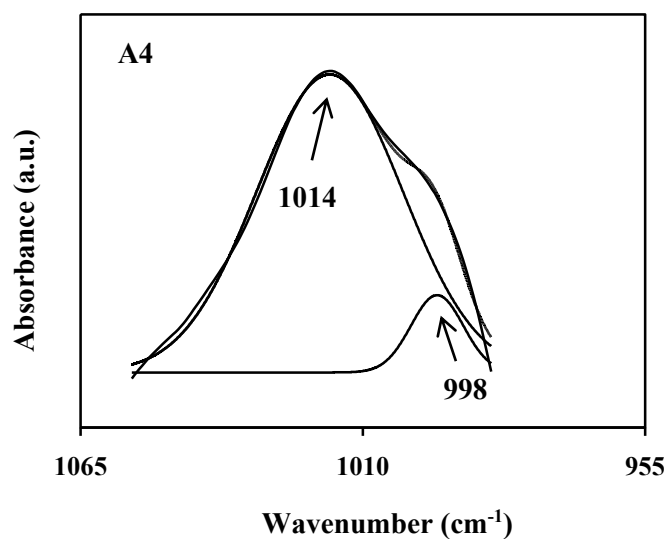
Figure 5.9: Deconvoluted FTIR spectra for A4 in the region of 955-1065 cm⁻¹.

5.3 Interaction between Starch/chitosan-NH4I-Glycerol (Plasticized System)

Figure 5.10 depicts the FTIR spectra of selected samples for plasticized system in the region of 3075-3595 cm^{-1}. The broad band is attributed to OH stretching vibration. This hydroxyl band has shifted to lower wavenumbers as the amount of glycerol increased, which implied that the addition of glycerol promotes the hydrogen bonding interactions between the electrolyte components (Nie, Stutzman, & Xie, 2005). Glycerol has multihydroxyl moiety structure and possesses the strong ability to interact with the
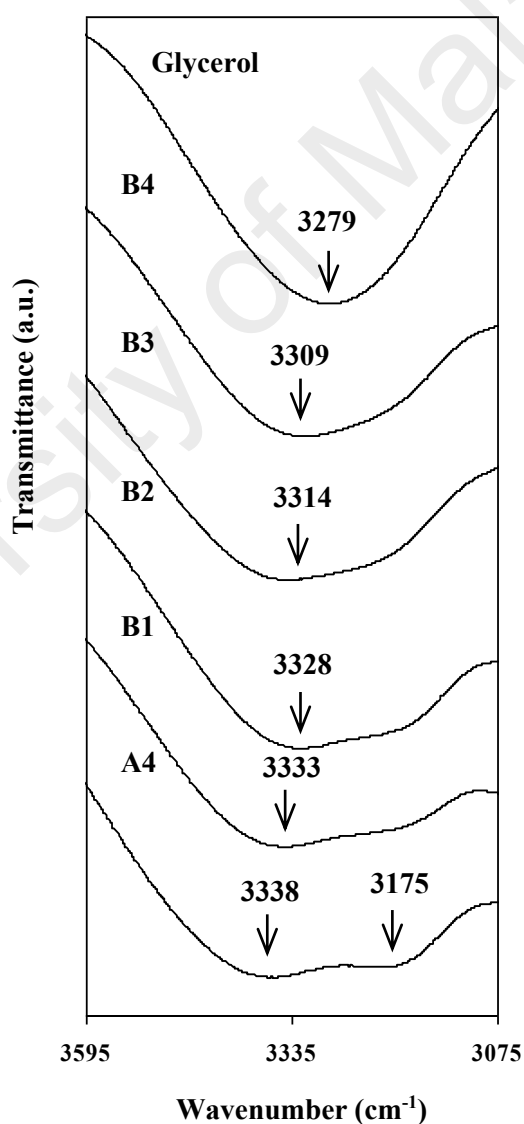
Figure 5.10: FTIR spectra for A4 and selected electrolytes in the plasticized system in the region of 3075-3595 cm^{-1}.

polysaccharide group through hydrogen bonding interactions (Shukur et al., 2014). According to Liu et al. (2013), when the glycerol concentration in the matrix is increased, more OH groups are available for starch-glycerol and/or chitosan-glycerol interactions. They reported that the hydroxyl band has shifted from 3339.57 cm^{-1} to 3336.82 cm^{-1} in starch/chitosan film containing 5 wt.% and 10 wt.% of glycerol, respectively. In B3 spectrum, a broad hydroxyl band starts to form due to the fact that further addition of glycerol allows the formation of linkages between the plasticizer which cause the salt to recrytallize, resulting in conductivity decrement.

To further identify the hydroxyl bands, deconvolution has been carried out for selected electrolytes in plasticized system as shown in Figures 5.11 to 5.14. From the deconvolution patterns, it can be observed that the hydroxyl band is more intense for the samples with higher glycerol concentrations. As depicted in Figure 5.11, there are three overlapping peaks in the spectrum of B1 electrolytes located at 3333, 3235 and 3172 cm^{-1}. The peaks at 3235 and 3172 cm^{-1} are correlated to υ_{as} (NH$_4^+$) and υ_s (NH$_4^+$) modes of the salt, which originated from A4 spectrum.
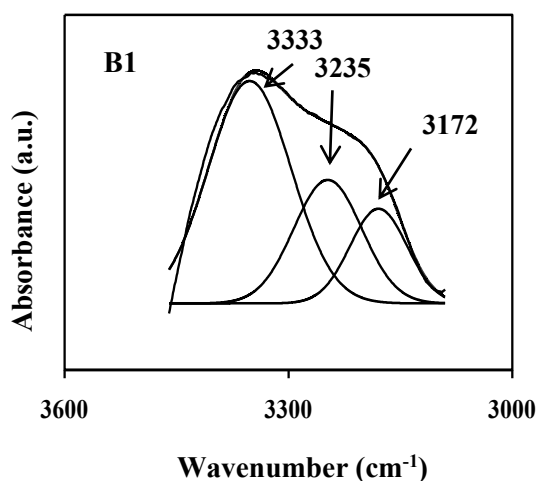
Figure 5.11: Deconvoluted FTIR spectrum for B1 in the region of 3000-3600 cm^{-1}.

The interaction between glycerol and the salted polymer blend is reflected by the changes of the characteristic spectra. Hydrogen bonding has formed between the OH group of starch/chitosan blend, NH_4^+ from salt, NH group from chitosan and oxygen atom from glycerol. In the deconvolution spectrum of B2, the bands shift to 3328, 3254 and 3163 cm^{-1} corresponded to the change in glycerol concentration as the peaks become closer to each other.
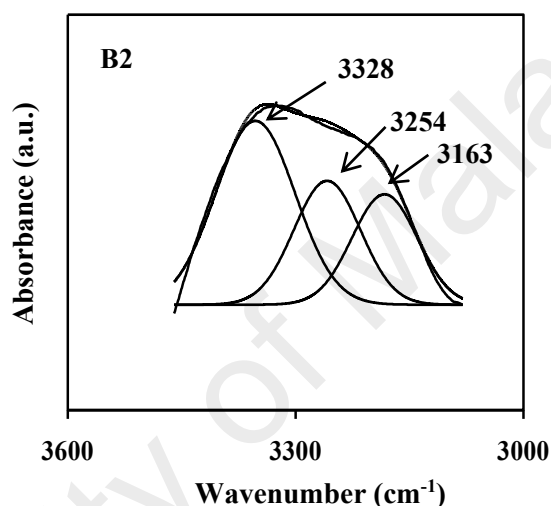
Figure 5.12: Deconvoluted FTIR spectrum for B2 in the region of 3000-3600 cm^{-1}.

The deconvoluted of FTIR spectrum for B3 is depicted in Figure 5.13. Two bands have merged hence only two bands appeared; one is a broad band located at 3314 cm^{-1} and that of the other is at 3195 cm^{-1}. The IR band shows the tendency to approach the glycerol position as the glycerol concentration is increased. This phenomenon is attributed to the hydrogen bonds formed between the hydroxyl groups of the glycerol and the salted polymer blend structures that do not contribute towards conductivity enhancement (Cerqueira, Souza, Teixeira, & Vicente, 2012; Liu et al., 2013).
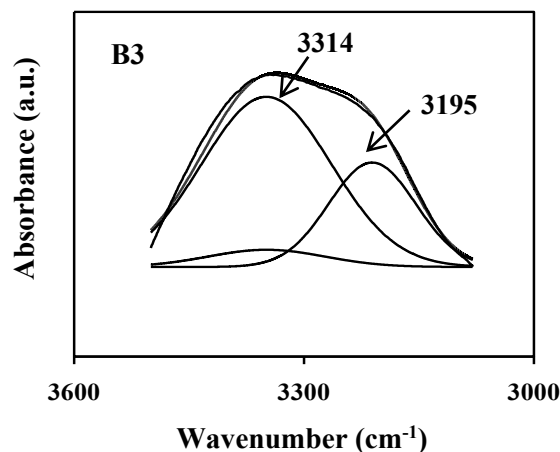
Figure 5.13: Deconvoluted FTIR spectrum for B3 in the region of 3000-3600 cm^{-1}.

The addition of plasticizer promotes ions dissociation hence more free ions will interact with polymer host at the hydroxyl band as evidenced by the band shifting. During ionic conduction, the O atom in hydroxyl groups of glycerol will complex with cations (H$^+$ and NH$_4^+$). This has been verified by FTIR analysis as reported by Kadir et al. (2011) and Shukur (2015). In B4 deconvoluted FTIR spectrum, the hydroxyl bands shifted to 3309 and 3180 cm^{-1}. As shown in Figure 5.14, the band appeared at 3180 cm^{-1} has become less intense indicating that too much of glycerol exist in the polymer blend. This phenomenon leads to the lack of interactions between the salted polymer blend and the glycerol when the glycerol content is more than 40 wt.%. As reported by Shalu, Singh & Singh (2015), the amount of uncomplexed ionic liquid (IL) is increased as they increased the IL content. It can be seen from the increasing intensity of the deconvoluted *y* peak located at 3106 cm^{-1} which attributed to the excess IL and failed to complex with the polymer host. The increased of glycerol-glycerol interaction is associated with the decrement in ionic conductivity. Cerqueira et al. (2012) also reported that the deconvolution origins two more peaks with higher intensity of OH bonds for the sample containing highest concentration of glycerol. Figure 5.15 shows

the deconvolution pattern of glycerol where only one broad band due to hydroxyl band can be detected at 3279 cm^{-1}.
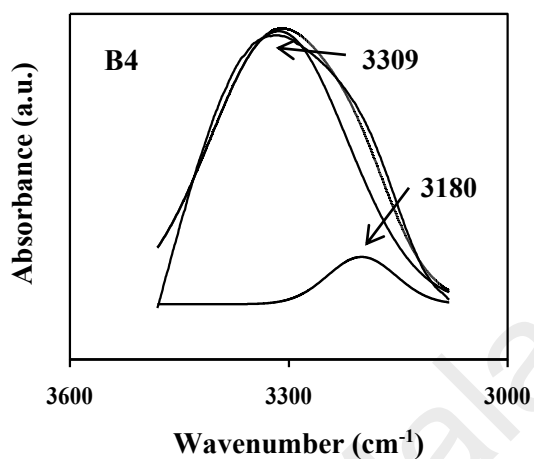
Figure 5.14: Deconvoluted FTIR spectrum for B4 in the region of 3000-3600 cm^{-1}.
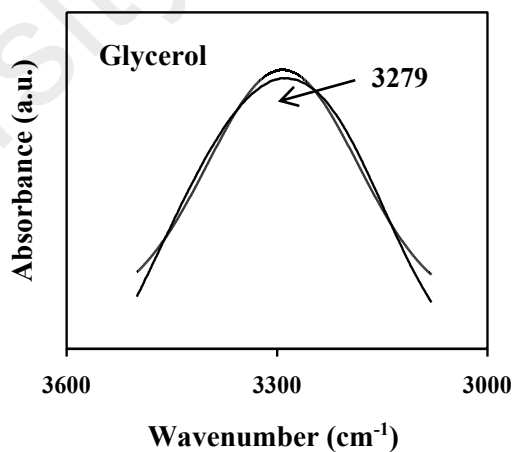
Figure 5.15: Deconvoluted FTIR spectrum for glycerol in the region of 3000-3600 cm^{-1}.

Figure 5.16 depicts the FTIR spectra of selected plasticized samples in the region of 1560-1700 cm^{-1}. The peak located at 1620 cm^{-1} in the spectrum of A4 that is attributed to carboxamide group, has shifted to higher wavenumbers up to 1634 cm^{-1} after the glycerol is added. This indicates that the addition of glycerol promotes the bonding interactions among starch, chitosan, NH$_4$I and glycerol (Liu et al., 2013).
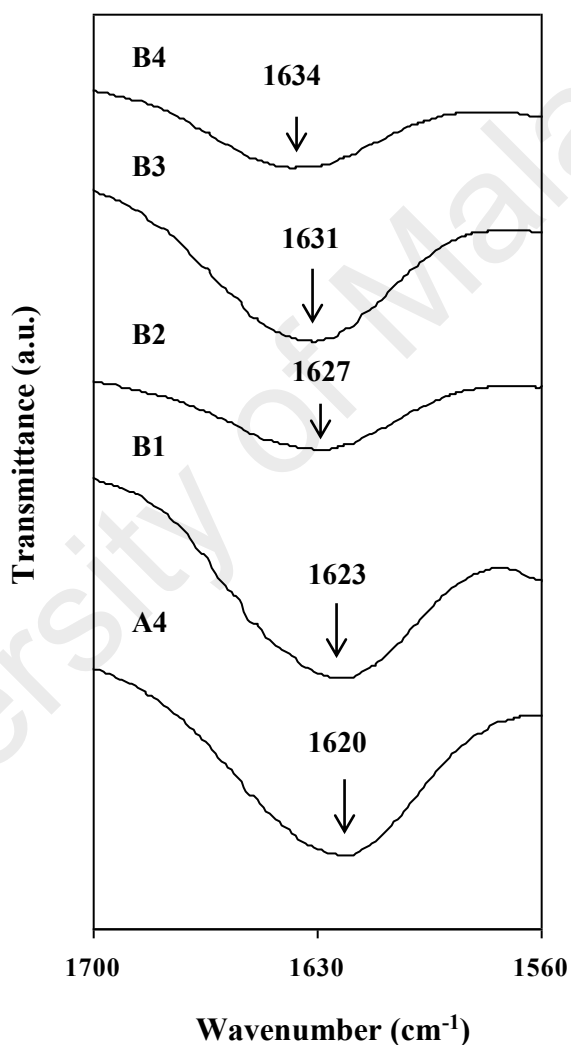
Figure 5.16: FTIR spectra for A4 and selected samples in plasticized system in the region of 1560-1700 cm^{-1}.

Figure 5.17 depicts the FTIR spectra of selected plasticized samples in the region of 1490-1570 cm^{-1}. The peaks located in this region are attributed to amine group, shifted towards higher wavenumbers as the glycerol concentration increases. The absorption at amine bands suggests the interactions between glycerol and salted starch/chitosan at nitrogen atom of amine group, even at low plasticizer content. However, the intensity of the band has decreased when more than 30 wt.% of glycerol is
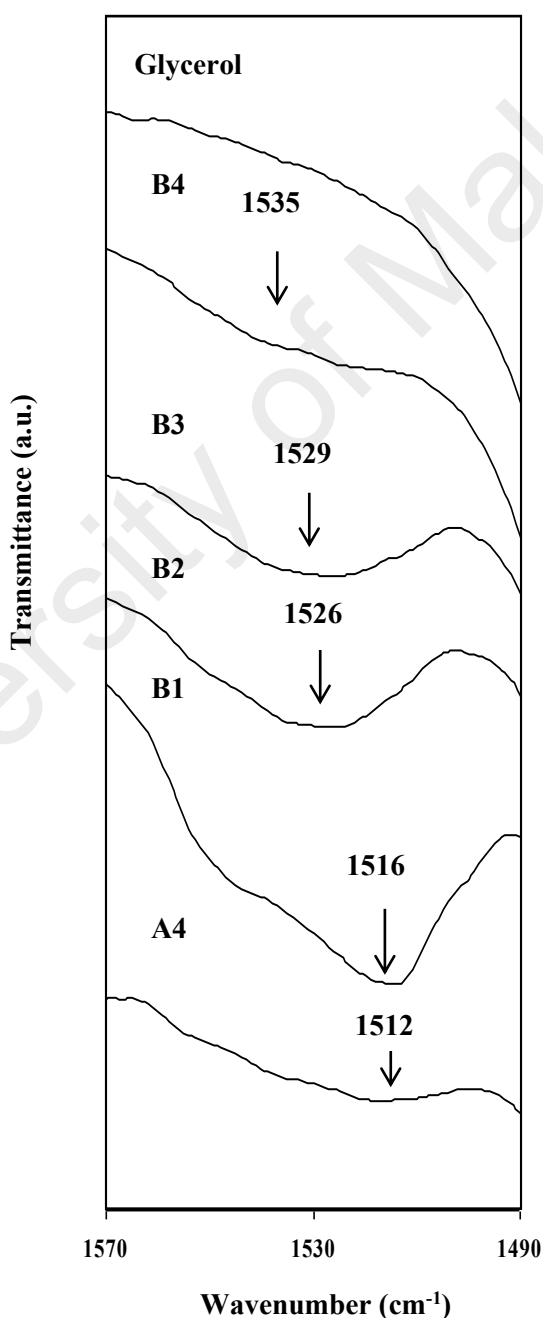
Figure 5.17: FTIR spectra for A4 and selected samples in plasticized system in the region of 1490-1570 cm^{-1}.

added. When too much glycerol is added, the glycerol molecules tend to form bridges among themselves hence decreased the interactions with other molecules (Liew and Ramesh, 2015).

Figure 5.18 depicts the FTIR spectra of selected samples for the system in the region of 955-1055 cm^{-1}. The peaks observed at 1014 cm^{-1} in the spectrum of A4 sample has shifted to 1016 cm^{-1} in the spectrum of B1 and further increased to higher
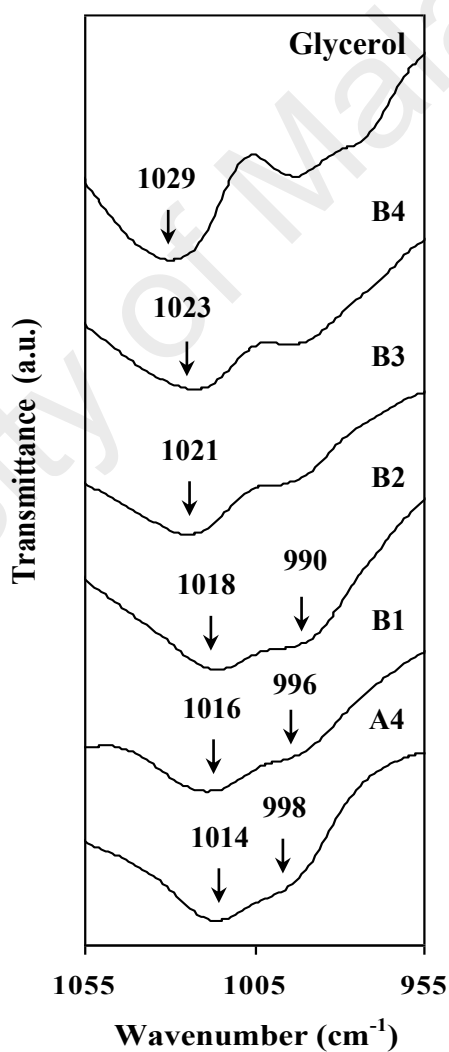
Figure 5.18: FTIR spectra for A4 and selected samples in plasticized system in the region of 955-1055 cm^{-1}.

wavenumbers with the increment of glycerol content. This can be associated with the C-O-H and C-O-C vibrations (Vicentini et al., 2005). As the glycerol concentration increases, Bergo et al. (2009) reported that the peak observed at 1011.8 cm^{-1} in the spectrum of starch film without glycerol shifted to higher wavenumbers once the glycerol is added, which is comparable with this work. Ramesh et al. (2011) also reported an upward shifting at 1011 cm^{-1} due to C-O stretching mode of corn starch in their plasticized corn starch-LiPF$_6$ system. These bands are also correlated to amorphous characteristic of the material (Vicentini et al., 2005, Ramesh et al., 2011).

The deconvolution patterns of B1 and B2 samples in the region of 960-1080 cm^{-1} are depicted in Figure 5.19 and 5.20, respectively. The C-O-H and C-O-C bands at 1014 and 998 cm^{-1}, respectively, in A4 spectrum have shifted to 1016 and 996 cm^{-1} in B1 spectrum due to the interaction of salted polymer blend with glycerol. The changes within this region are believed to be reliable indicators to justify the interactions occur between glycerol with other components (Liu et al., 2013).
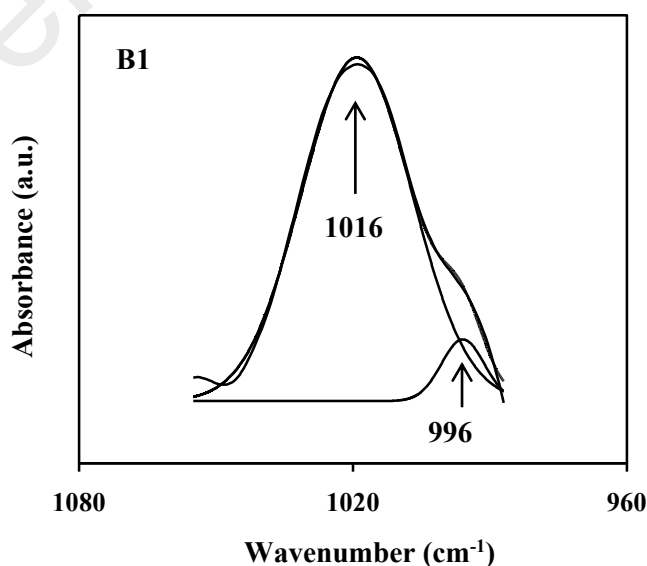
Figure 5.19: Deconvoluted FTIR spectrum for B1 in the region of 960-1080 cm^{-1}.

As the glycerol concentration increases, the band at 1016 cm^{-1} has shifted to 1018 cm^{-1} in B2. Meanwhile, the band located at 996 cm^{-1} has shifted to 990 cm^{-1} in B2, and the intensity of this band starts to increase. When more than 20 wt.% of glycerol is added, the band at 990 cm^{-1} in B2 has separated and grown apart from the band at 1018 cm^{-1}, following the glycerol spectrum as depicted in Figure 5.18.
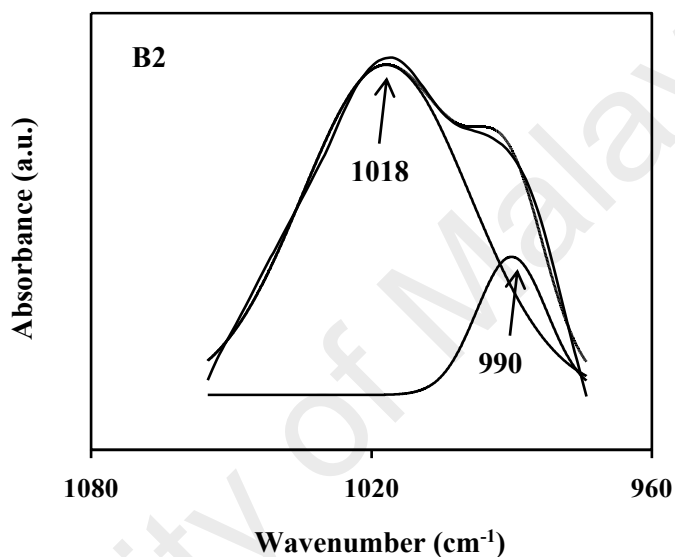
Figure 5.20: Deconvoluted FTIR spectrum for B2 in the region of 960-1080 cm^{-1}.

The possible interactions occur within plasticized system is illustrated in Figure 5.21. H$^+$ and NH$_4^+$ are the charge species which play important roles in conduction mechanism.
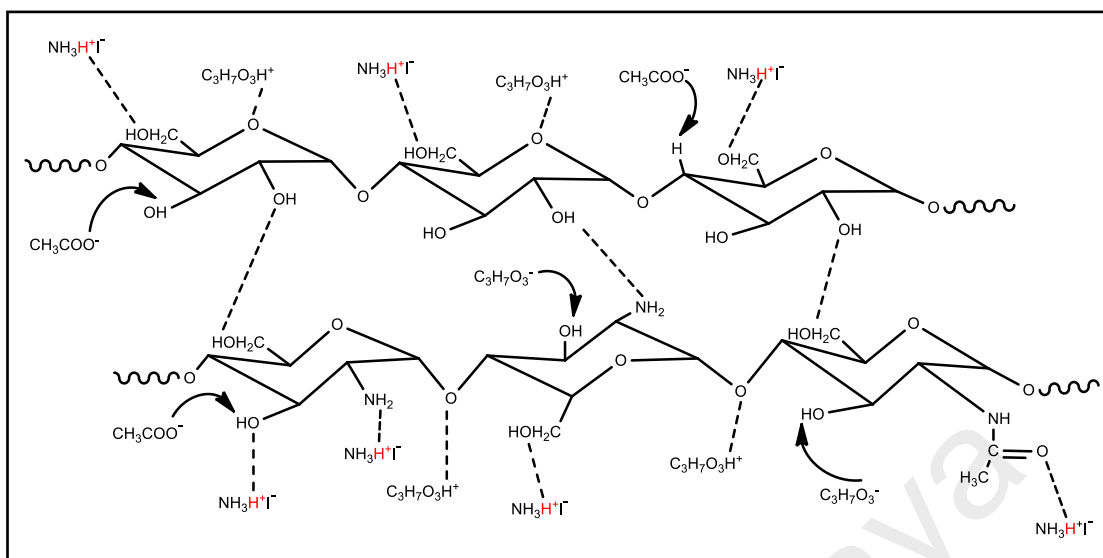
Figure 5.21: Schematic diagram of possible interactions in plasticized system. H^+ plays an important role in conduction mechanism.

5.4   Summary

The interactions between the polymer blend, NH_4I and glycerol are proven from the changes in wavenumbers at hydroxyl, amine, carboxamide and saccharides (C-O-H and C-O-C) regions. The hydrogen bonding has formed between the OH group of starch/chitosan blend, H^+ and NH_4^+ from salt, NH_2 group from chitosan and OH group of glycerol thus reflected through FTIR spectra. The nitrogen atoms of amine groups also provide the coordination sites for the cations to move around. Glycerol possesses hydroxyl groups where the oxygen atom will complex with cations (H^+ and NH_4^+) during ionic conduction. The addition of glycerol in electrolytes will provide new pathways for ion conduction which can dissociate more salt to become free ions hence promotes the interactions with the polymer host.

CHAPTER 6: ELECTROCHEMICAL IMPEDANCE SPECTROSCOPY STUDIES

6.1   Introduction

Electrical conductivity is the most significant study concerning polymer electrolytes. The main objective of this chapter is to study the conductivities at room and elevated temperatures, to understand the electrical conduction trend and transport mechanism in starch/chitosan-NH_4I and starch/chitosan-NH_4I-glycerol systems. From this chapter, the effect of incorporating salt and plasticizer can be investigated based on the ionic conductivities. The Rice and Roth model is employed to determine the mobility and number density of the ions which leads to a better understanding of the conductivity variation.

The conductivity trend can be further understood by dielectric studies and give a better understanding about the conductive behavior of polymer electrolyte (Ramesh, Yahaya, & Arof, 2002). The dielectric study helps to understand the trend of conductivity and also gives the important insights of the polarization effect at the electrode/ electrolyte interfaces (Howell, Bose, Macedo, & Moynihan, 1974). The dielectric constant determines the amount of charge that can be stored by a material and correlates the conductivity with the increase in free mobile ions (Khiar, Puteh, & Arof, 2006). In this chapter, dielectric properties such as dielectric constant, dielectric loss, ion relaxation and electrical modulus in salted and plasticized systems will be discussed.

6.2   Impedance Studies

Figures 6.1and 6.2 depict the Cole-Cole plots of selected samples in salted system at room temperature. It can be seen from Figure 6.1(a) that A1 shows an incomplete semicircle curve while the Cole-Cole plots of A3 Figure 6.1(b) consist of a semicircular at high frequency and an adjacent line at low frequency region.

The equivalent circuits corresponding to the Cole-cole plots are also provided with the figure. The semicircle represents the bulk conductivity due to the parallel combination of bulk resistance and bulk capacitance of the polymer electrolytes (Malathi et al., 2010) while the adjacent line is attributed to the effect of electrode polarization, which is a characteristic of diffusion process (Samsudin et al., 2012). The value of bulk resistance (R_b) for Figure 6.1(a) which only consists of a semicircle is determined from the intercept of the semicircle with the real axis. The R_b value for Figure 6.1 (b) is determined from the interception of semicircle with the adjacent line, as shown in the figure.

When the capacitance is ideal, only the tilted line will appear in the impedance plot of A4 while the semicircle part has disappeared as can be seen in Figure 6.2 (a). The equivalent circuit corresponding to the Cole-cole plot is provided with the figure.

(a)

(b)
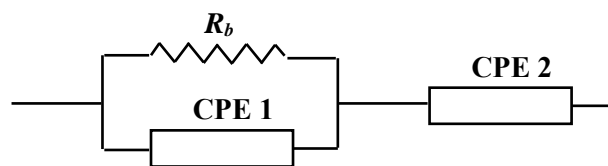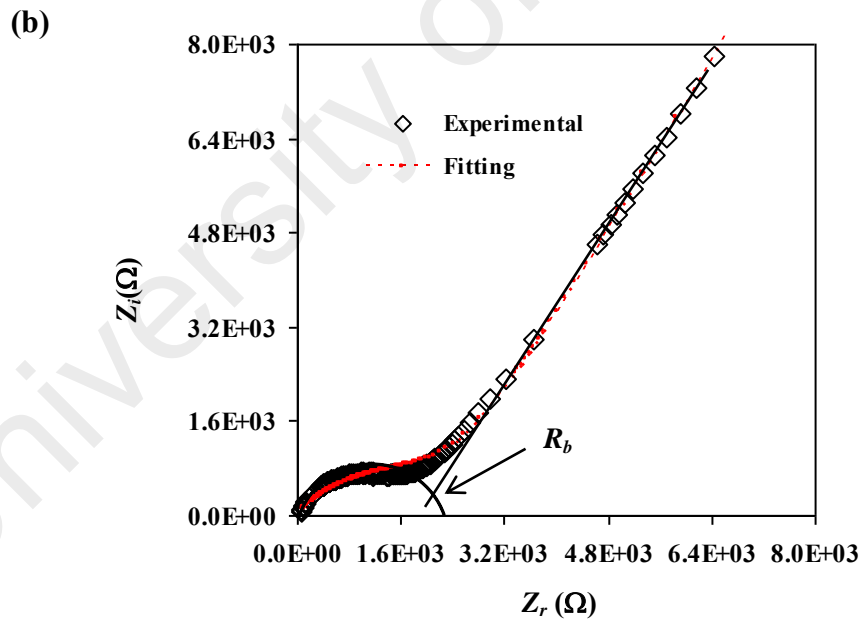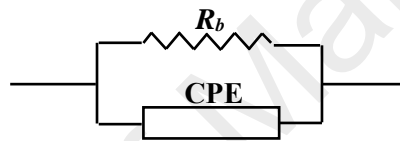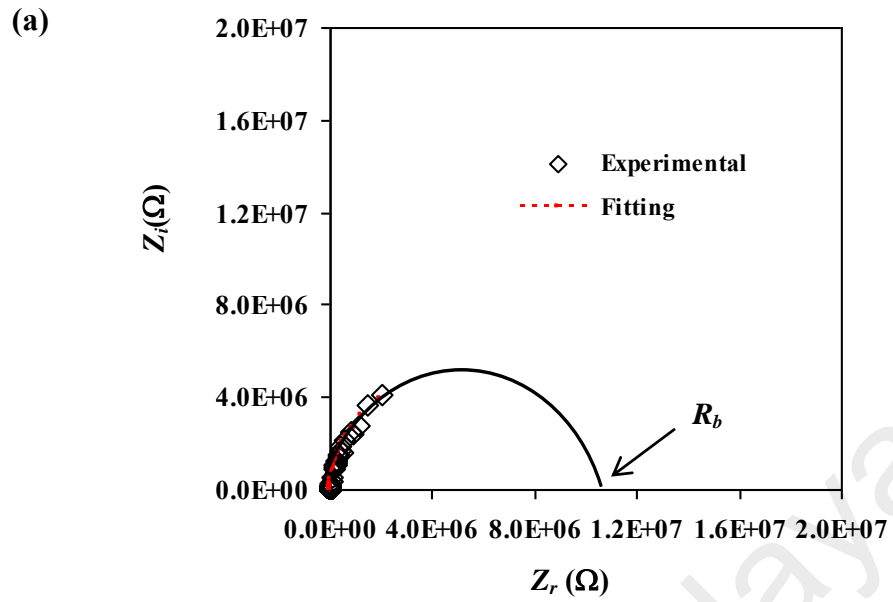
Figure 6.1: Cole-Cole plot of (a) A1 and (b) A3 at room temperature. Provided below each figures are the corresponding equivalent circuit.

(a)

(b)
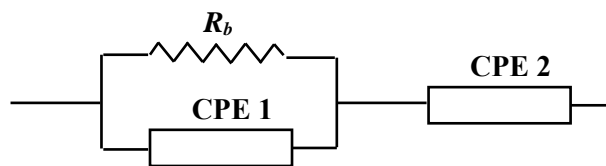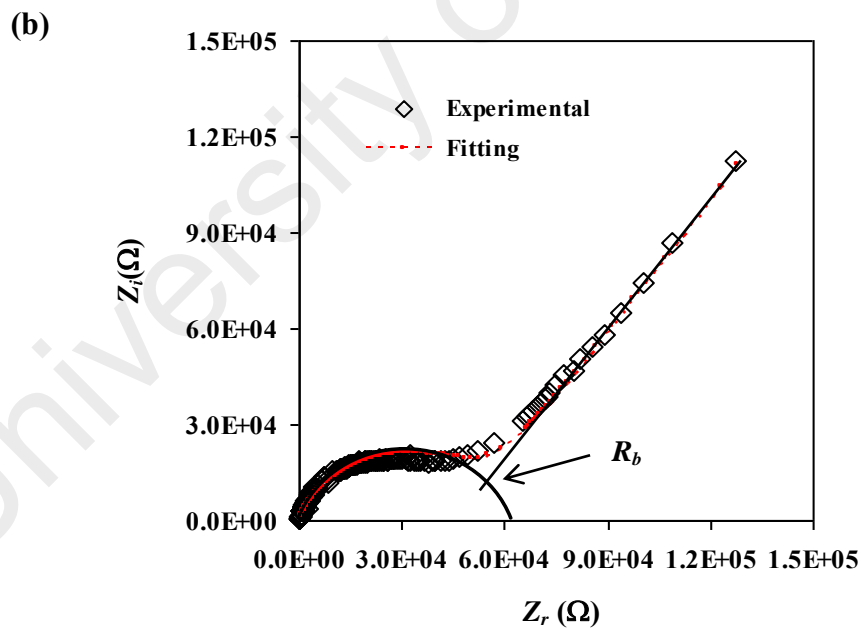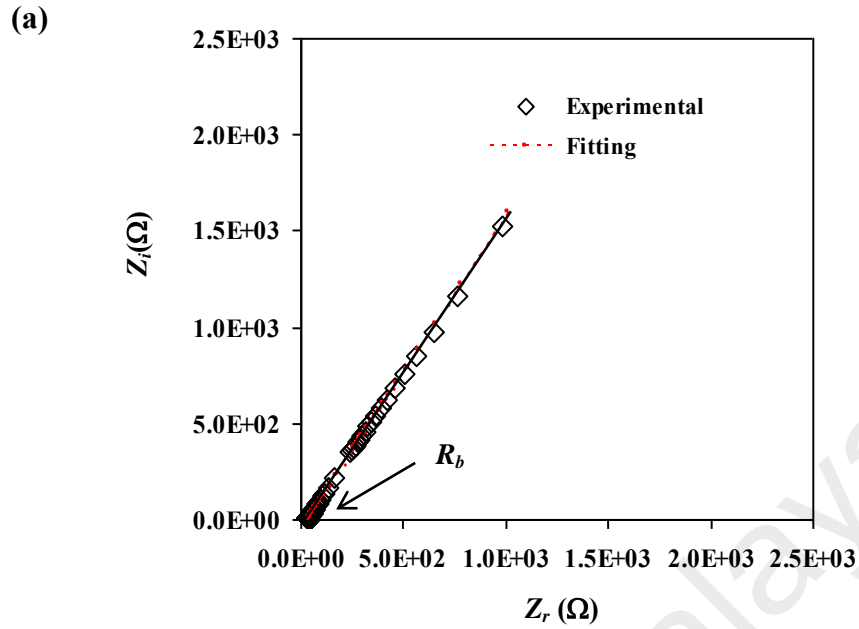
Figure 6.2: Cole-Cole plot of (a) A4 and (b) A6 at room temperature. Provided below each figures are the corresponding equivalent circuit.

The tilted line which inclined at an angle (θ) less than 90° suggests that only the resistive component of the polymer prevails (Hema et al., 2008). The R_b value is determined by the interception of the line with the real axis as shown in the figure. The R_b value is found increased in A6. It is also observed in Figure 6.2 (b) that the semicircle part for A6 is bigger compared to A3 due to different ionic conductivity when different amount of salt was added. Ion aggregation occurs as the salt content has been increased to 60 wt.% which leads to conductivity decrement. The blocking electrodes were used; hence the electrode/electrolyte surface is regarded as a capacitance (Samsudin et al., 2012).

Figure 6.3 (a)-(c) shows the Cole-Cole plots of selected samples in plasticized system at room temperature. The plasticized Cole-Cole plots show the same pattern as A4. Only the adjacent lines appear in the impedance plot while the semicircle parts have disappeared.

The electrical equivalent circuit representation can provide a complete picture of the systems, other than providing the outcomes in faster and simpler way (Han & Choi, 1998). In the present work, A1 consists only the semicircle arc, hence the equivalent circuit can be represented by a parallel combination of R_b and constant phase element (CPE). The corresponding equivalent circuit can be seen in Figure 6.1 (a). CPE is commonly used in a model instead of a capacitor to compensate the inhomogeneity in the electrolytes (Qian et al., 2001). The impedance of CPE (Z_{CPE}) can be expressed as:
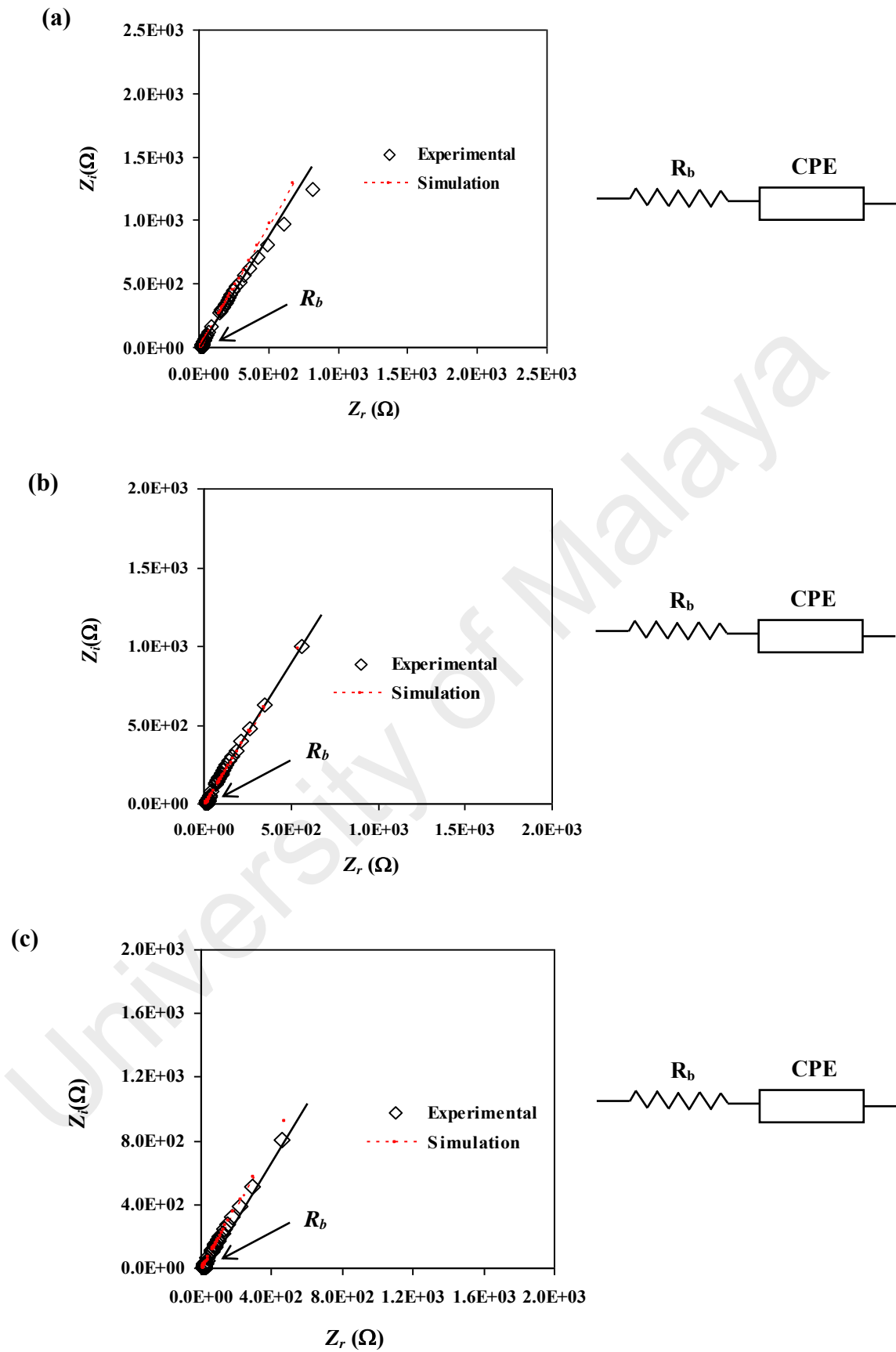
Figure 6.3: Cole-Cole plot of (a) B2 (b) B3 and (c) B4 at room temperature.

$$Z_{CPE} = \frac{1}{C\omega^p} \left[\cos\left(\frac{\pi p}{2}\right) - i\sin\left(\frac{\pi p}{2}\right) \right] \tag{6.1}$$

where C is the capacitance of CPE, ω is angular frequency and p is related to the deviation of the plot from the axis (Malathi et al., 2010).

The real and imaginary parts of impedance, Z_r and Z_i of the equivalent circuits, which consists of semicircular curves, can be expressed by:

$$Z_r = \frac{R_b + R_b^2 C\omega^p \cos\left(\frac{\pi p}{2}\right)}{1 + 2R_b C\omega^p \cos\left(\frac{\pi p}{2}\right) + R_b^2 C^2 \omega^{2p}} \tag{6.2}$$

$$Z_i = \frac{R_b^2 C\omega^p \sin\left(\frac{\pi p}{2}\right)}{1 + 2R_b C\omega^p \cos\left(\frac{\pi p}{2}\right) + R_b^2 C^2 \omega^{2p}} \tag{6.3}$$

As can be seen in Figure 6.1 (b) and 6.2 (b), A3 and A6 consist of a semicircle and an inclined adjacent line. These equivalent circuits are represented by a parallel combination of R_b and CPE with another CPE in series (Shukur et al., 2014a) as can be seen in Figure 6.1 (b). The values of Z_r and Z_i from the equivalent can be expressed by:

$$Z_r = \frac{R_b + R_b^2 C_1 \omega^{p_1} \cos\left(\frac{\pi p_1}{2}\right)}{1 + 2R_b C_1 \omega^{p_1} \cos\left(\frac{\pi p_1}{2}\right) + R_b^2 C_1^2 \omega^{2p_1}} + \frac{\cos\left(\frac{\pi p_2}{2}\right)}{C_2 \omega^{p_2}} \tag{6.4}$$

$$Z_i = \frac{R_b^2 C_1 \omega^{p_1} \sin\left(\frac{\pi p_1}{2}\right)}{1 + 2R_b C_1 \omega^{p_1} \cos\left(\frac{\pi p_1}{2}\right) + R_b^2 C_1^2 \omega^{2p_1}} + \frac{\sin\left(\frac{\pi p_2}{2}\right)}{C_2 \omega^{p_2}} \tag{6.5}$$

where C_1 is the capacitance at high frequency, C_2 is the capacitance at low frequency, p_1 is the deviation of the radius of the circle from the imaginary axis, and p_2 is the deviation of the inclined adjacent line to the semicircle from the real axis. The increased in number of mobile charge carriers leads to the decrease in R_b values (Arof et al., 2014).

It can be observed in Figure 6.2 (a) that the semicircle is absent in the Cole-Cole plot. The addition of glycerol also leads to the disappearance of the semicircle as can be seen in Figure 6.3. This satisfies the following equation:

$$C = \frac{\varepsilon_0 \varepsilon_r A}{d} \tag{6.6}$$

where ε_0 is vacuum permittivity and ε_r is dielectric constant. Due to its high dielectric constant, glycerol dissociates more salt to become free ions, hence increases the stored charge in plasticized electrolyte together with the value of ε_r (Shukur et al., 2013). The increasing ε_r will increase the value of capacitance. The equivalent circuit for this type of plot can be represented by a combination of R_b and CPE in series (Shuhaimi et al., 2012) as can be seen in Figure 6.3. The value of Z_r and Z_i associated to the equivalent circuit can be expressed as:

$$Z_r = R_b + \frac{\cos\left(\frac{\pi p}{2}\right)}{C\omega^p} \tag{6.7}$$

$$Z_i = \frac{\sin\left(\frac{\pi p}{2}\right)}{C\omega^p} \tag{6.8}$$

Tables 6.1 and 6.2 list the parameters of the circuit elements for selected samples in unplasticized and plasticized systems, respectively. The values of capacitance for plasticized electrolytes are higher compared to the unplasticized electrolytes. This suggests that the addition of plasticizer may create new pathways for ion conduction and promotes the ions dissociation hence increases the number density and mobility of ions.

Table 6.1: Parameters of the circuit elements for selected electrolytes in salted system at room temperature.

Samples	p (rad)	C (F)
A1	0.96	2.86×10^{-10}
*A3	p_1 0.58 p_2 0.69	C_1 3.73×10^{-7} C_2 9.62×10^{-7}
A4	0.65	8.16×10^{-6}
*A6	p_1 0.78 p_2 0.61	C_1 1.72×10^{-9} C_2 1.55×10^{-7}

(*Where; A3 and A6 consist of a semicircle and a spike)

Table 6.2: Parameters of the circuit elements for selected electrolytes in plasticized system at room temperature.

Samples	p (rad)	C (F)
B2	0.70	7.60×10^{-6}
B3	0.69	1.76×10^{-5}
B4	0.70	1.69×10^{-5}

Figures 6.4 and 6.5 show the Cole-Cole plots at selected temperatures for B3 electrolyte. The equivalent circuit for B3 at various temperatures is represented by a combination of R_b and CPE in series. The value of Z_r and Z_i associated to the equivalent circuit are calculated using Equations (6.7) and (6.8). Table 6.3 shows the parameters of the circuit elements at various temperatures for B3. It is observed that the values of capacitance are increased as the temperature increased. At high temperature, the R_b values are decreased due to the increased in segmental motion of the polymer chains.

Table 6.3: Parameters of the circuit elements for B3 at various temperatures.

Temperature (K)	p (rad)	C (F)
298	0.69	1.76×10^{-5}
303	0.69	1.92×10^{-5}
308	0.69	1.98×10^{-5}
313	0.69	2.35×10^{-5}
318	0.69	2.47×10^{-5}
323	0.68	2.86×10^{-5}
328	0.68	3.39×10^{-5}
333	0.67	4.17×10^{-5}
338	0.66	4.76×10^{-5}
343	0.65	8.33×10^{-5}
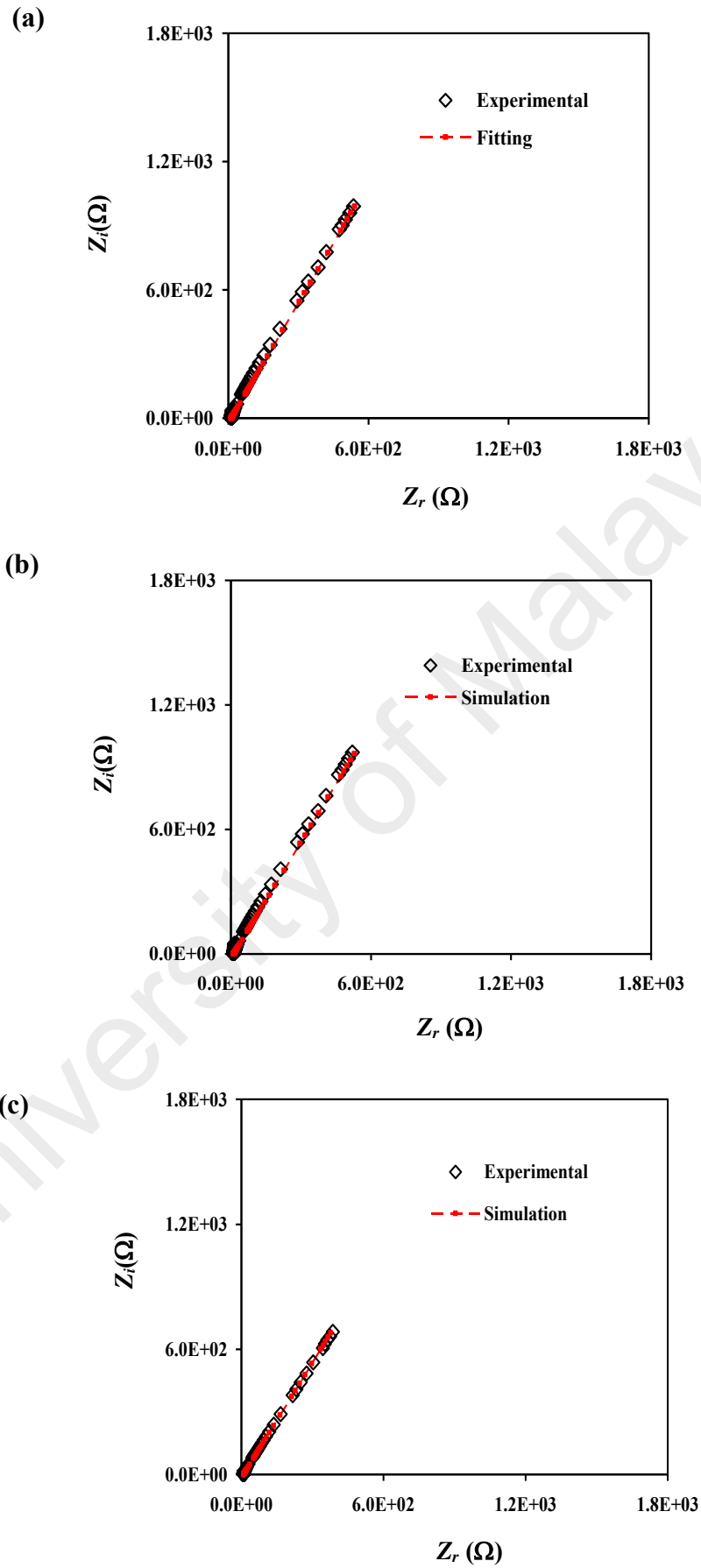
Figure 6.4: Cole-Cole plot of B3 at (a) 303, (b) 308 and (c) 323 K.
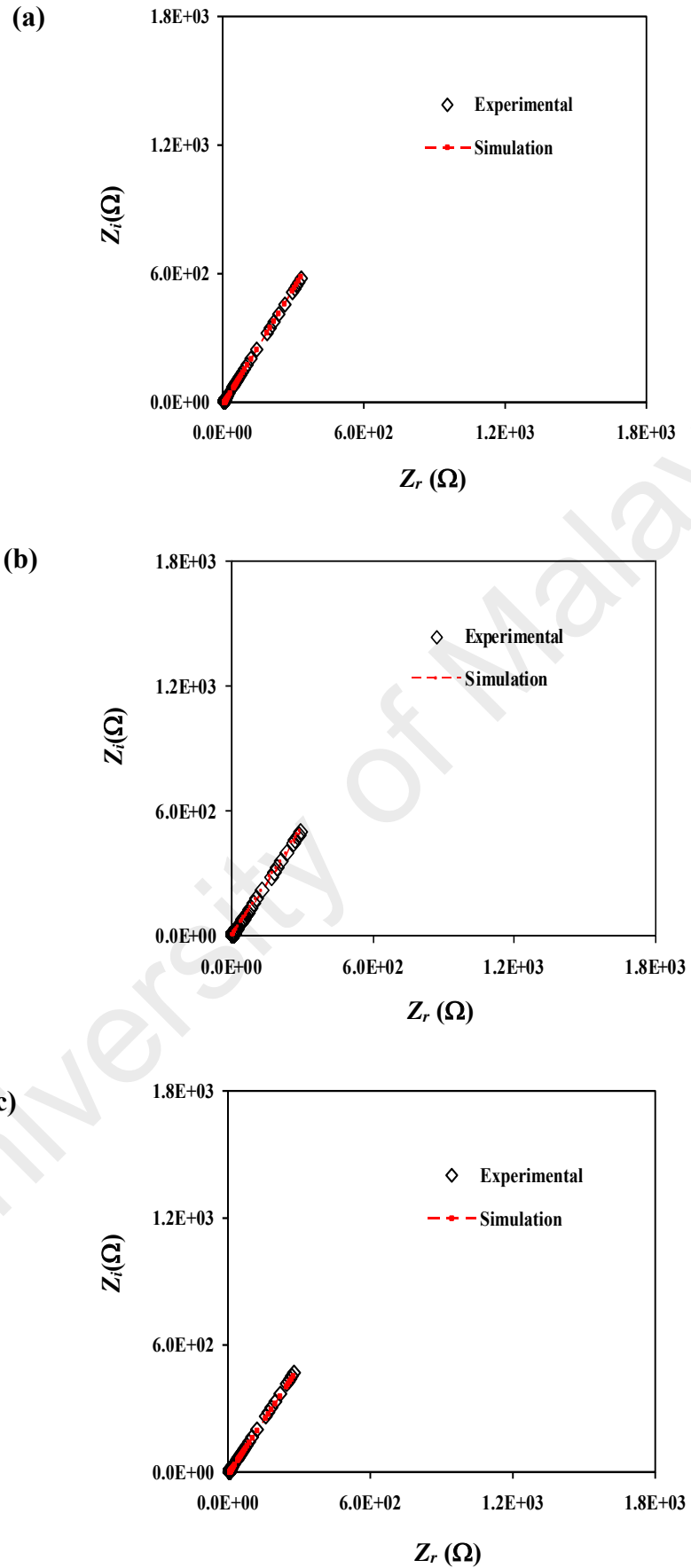
Figure 6.5: Cole-Cole plot of B3 at (a) 328, (b) 333 and (c) 338 K.

6.3 Conductivity Studies at Room Temperature

Variation of room temperature conductivity as a function of NH_4I concentration is presented in Figure 6.6. The conductivity of electrolytes depends upon charge carriers concentration. Hence, when charge carriers or ions concentration are changed by doping the polymer with different concentration of salt, the conductivity is also expected to change (Kumar et al., 2012). It can be seen that the conductivity increases from 3.05×10^{-10} S cm^{-1} to 1.71×10^{-9} S cm^{-1} with the incorporation of 10 wt.% NH_4I with the polymer blend. The ionic conductivity increases as the salt content increases up to $(3.04 \pm 0.32) \times 10^{-4}$ S cm^{-1} with the addition of 40 wt.% NH_4I. This increment may be attributed to the increase in the number of mobile charge carriers (Khiar & Arof, 2010) and also in amorphous nature of polymer electrolytes which will be verified by XRD analysis in Chapter 7. As a result, the energy barrier is reduced thereby facilitates a faster ionic transportation (Hema et al., 2009). Kumar et al. (2012) reported that the highest conductivity of starch-NH_4I electrolyte was $\sim 2.40 \times 10^{-4}$ S cm^{-1}.

A higher conductivity value obtained in this work proves that the host which has undergone the polymer blending method contributes in the conductivity enhancement of an electrolyte. Buraidah & Arof (2011) also reported that the conductivity of 55 wt.% chitosan-45 wt.% NH_4I is increased when they blend chitosan with PVA in their 55 wt.% (chitosan-PVA)-45 wt.% NH_4I system; from 3.73×10^{-7} S cm^{-1} to 1.77×10^{-6} S cm^{-1}. According to the authors, there will be more sites for ion migration in the polymer blend; hence, ions exchange can easily take place leading to an increase in conductivity (Buraidah & Arof, 2011). After the optimized concentration of 40 wt.% NH_4I, the conductivity starts to decrease because the distance between dissociated ions became too close, which enable them to recombine and form neutral ion pairs that do not

contribute in conductivity (Kadir et al., 2010). The films become brittle with the addition of more than 60 wt.% NH₄I.
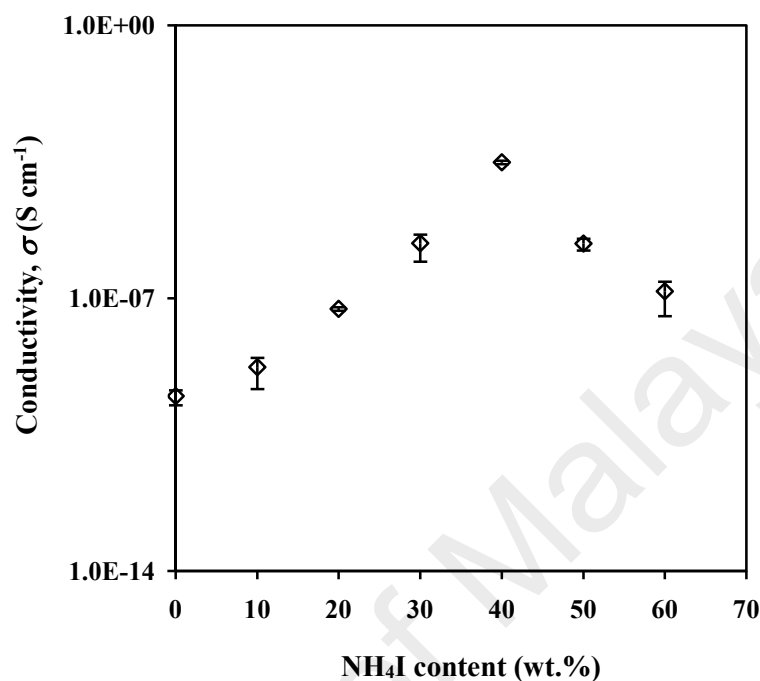
Figure 6.6: Effect of NH₄I content on conductivity at room temperature.

Figure 6.7 represents the variation of room temperature conductivity as a function of glycerol concentration. The conductivity value of glycerol free film increased from $(3.04 \pm 0.32) \times 10^{-4}$ S cm⁻¹ to a maximum value of $(1.28 \pm 0.07) \times 10^{-3}$ S cm⁻¹ with 30 wt.% of glycerol (B3). Glycerol possesses a high dielectric constant which can weaken the Coulombic force between cation and anion of the salt hence promotes the dissociation of salt, NH₄I to become free mobile ions, NH₄⁺ and I⁻ (Gondaliya, Kanchan, & Sharma, 2013). The plasticizer molecules size which is relatively small compared to polymer molecules will penetrate the polymer matrix hence create attractive forces while reducing the cohesive forces between the polymer chains resulting the segmental mobility increment (Sekhar, Kumar, & Sharma, 2012).

Moreover, the addition of plasticizer can create alternative pathways for ion conduction which may increase the ionic mobility (Buraidah, Teo, Majid, & Arof, 2009; Ramesh & Arof, 2001). Marcondes et al. (2010) reported that the ions mobility is high as the glycerol concentration is increased up to 30 wt.%. Good ionic conduction and film forming properties are obtained at 30 wt.% of glycerol and further addition is not suggested due to difficulty in handling.
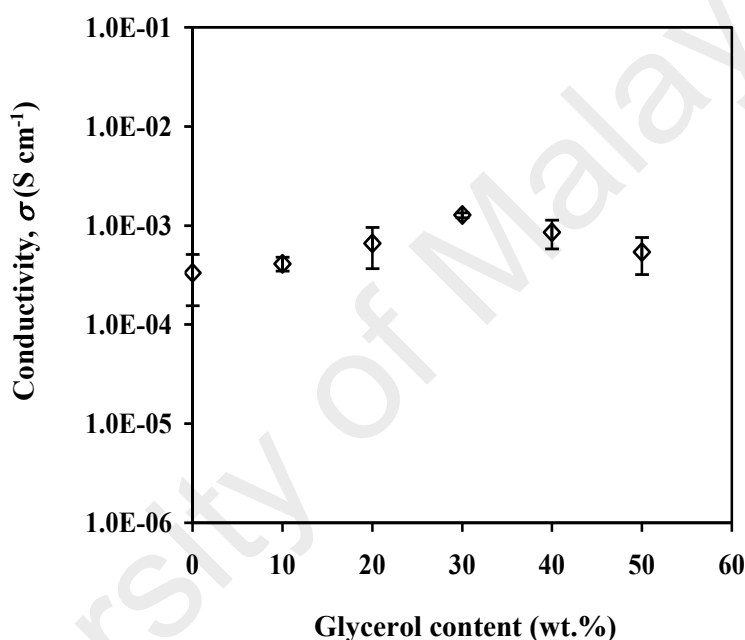
Figure 6.7: Effect of glycerol content on conductivity at room temperature.

A work by Shukur, Yusof, Zawawi, Illias, & Kadir (2013) reported that when glycerol was added to the chitosan-NH$_4$SCN based electrolytes, the conductivity increases from $(1.81 \pm 0.50) \times 10^{-4}$ to $(1.51 \pm 0.12) \times 10^{-3}$ S cm^{-1}. From Figure 6.7, it can be observed that further addition of glycerol decreases the conductivity due to the fact that the increase in glycerol content allows the formation of microcrystalline linkages which promote recrystallization of salt (Bergo, Sobral, & Prison, 2009). This may also cause the displacement of host polymer by plasticizer molecules within the

salt complexes which reduced the ionic mobility resulting in a drop in conductivity (Suriani & Mohd, 2012). Film formation has been disabled when more than 50 wt.% of glycerol is added into polymer blend.

6.4   Conductivity at Elevated Temperatures

Temperature has a strong influence on ionic conductivity (Noor et al., 2011). The conductivity-temperature relationship is verified whether it obeys Arrhenius or VTF rules by converting the data into a plot of log σ versus $1000T^{-1}$. The VTF rule is dominant for ion transport which depending on the polymeric chain movement (Ayala, Agudelo, & Vargas, 2012). This model can be described by the following equation:

$$\sigma = \frac{A}{T^{1/2}} \exp\left[\frac{-E_{VTF}}{k(T-T_0)}\right] \tag{6.9}$$

where, σ is the conductivity, A is the pre-exponential factor, E_{VTF} is the pseudo-activation energy for conduction, k is the Boltzmann constant, T is the absolute temperature and T_0 is the thermodynamic glass transition or ideal glass transition temperature. T_0 is obtained by trial and error, but usually the value is 50° lower than the glass transition temperature. If a plot exhibits a linear relationship with the correlation factor is more than 0.90, this proves that the electrolytes are temperature dependence (Harun, Ali, Ali, & Yahya, 2011; Jones, 2014).

The polymer chain acquires faster internal modes where bonding rotations produce motions to favor inter- and intra-chain ion hopping (Harun et al., 2011). This phenomenon is represented as Arrhenius, hence the conductivity can be expressed as:

$$\sigma = \sigma_0 \exp\left[\frac{-E_a}{kT}\right]$$

(6.10)

where σ_0 is a pre-exponential factor, E_a is the activation energy of conduction and k is Boltzmann constant. The activation energy, E_a of these polymer electrolytes is obtained from the slope of the plot based on this equation.

Figures 6.8(a) and (b) represent the temperature dependence of ionic conductivity for all compositions of starch/chitosan-NH_4I and plasticized starch/chitosan-NH_4I electrolytes. The regression values, R^2 are almost 1 and therefore implies that the plots of log σ versus $1000T^{-1}$ are Arrhenian (Winie et al., 2009). It can be seen that temperature plays an important role in the conductivity increment since the electrolyte became less viscous at high temperature hence increased the chain flexibility (Yang, Fu, & Gong, 2008). This phenomenon assists the conductivity increment due to the increased in ions free volume and their segmental mobility (Rajendran, Sivakumar, & Subadevi, 2004). The vibrational energy of the ions is sufficient to move against the hydrostatic pressure produced by the neighboring atoms (Shukur, Ithnin, & Kadir, 2014b). As the segmental motions occur, the free volume around the polymer chain caused an augmentation among the mobile ions thus leads to the increase in conductivity (Kadir et al., 2010; Noor et al., 2011; Samsudin et al., 2012).

(a)
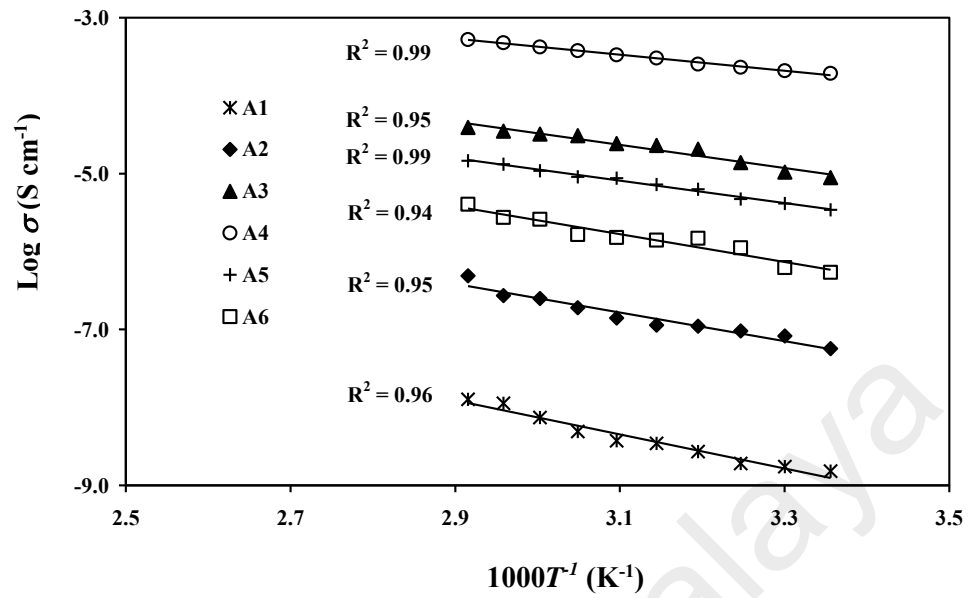
(b)
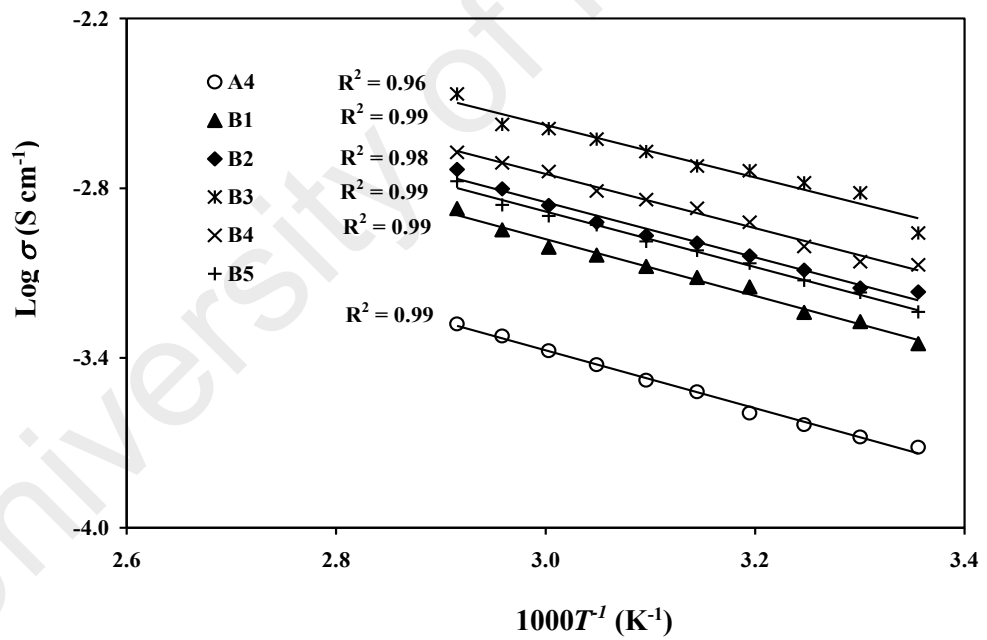
Figure 6.8: Conductivity of (a) starch/chitosan-NH_4I and (b) starch/chitosan-NH_4I-glycerol system at elevated temperatures.

All electrolytes do not show any abrupt change in conductivity values with temperature provided that the electrolytes are amorphous in nature (Michael, Jacob, Prabaharan, & Radhakrishna, 1997). Pawlicka et al. (2008) reported that the highest conducting sample in the starch-based PEs with conductivities varied from 10^{-6} S cm^{-1} to 10^{-4} S cm^{-1} follows Arrhenius rule. Many other researchers reported that their electrolytes obey Arrhenius rule since linear relationships are observed in their plots (Bhavani, Ravi, & Rao, 2008; Samsudin et al., 2012; Yang et al., 2008).

The activation energy decreases with increasing conductivity as shown in Figure 6.9 (a) and (b). The highest conducting sample in salted system possesses an E_a value of 0.200 eV while the lowest E_a in plasticized system is 0.182 eV. A work by Buraidah & Arof (2011) reported that the highest conducting sample in chitosan-PVA-NH$_4$I system with conductivity of 1.77×10^{-6} S cm^{-1} has the lowest activation energy of 0.380 eV. This result implies that the ions in highly conducting samples require lower energy for migration. The rapid ionic conduction also aided by the plasticizer, which promotes mobility of the ions by providing easier pathways (Bhide & Hariharan, 2007). The correlations between conductivity and E_a of polymer electrolytes reported by many researchers have shown similar behavior (Buraidah et al., 2009; Khiar et al., 2006; Majid & Arof, 2005).
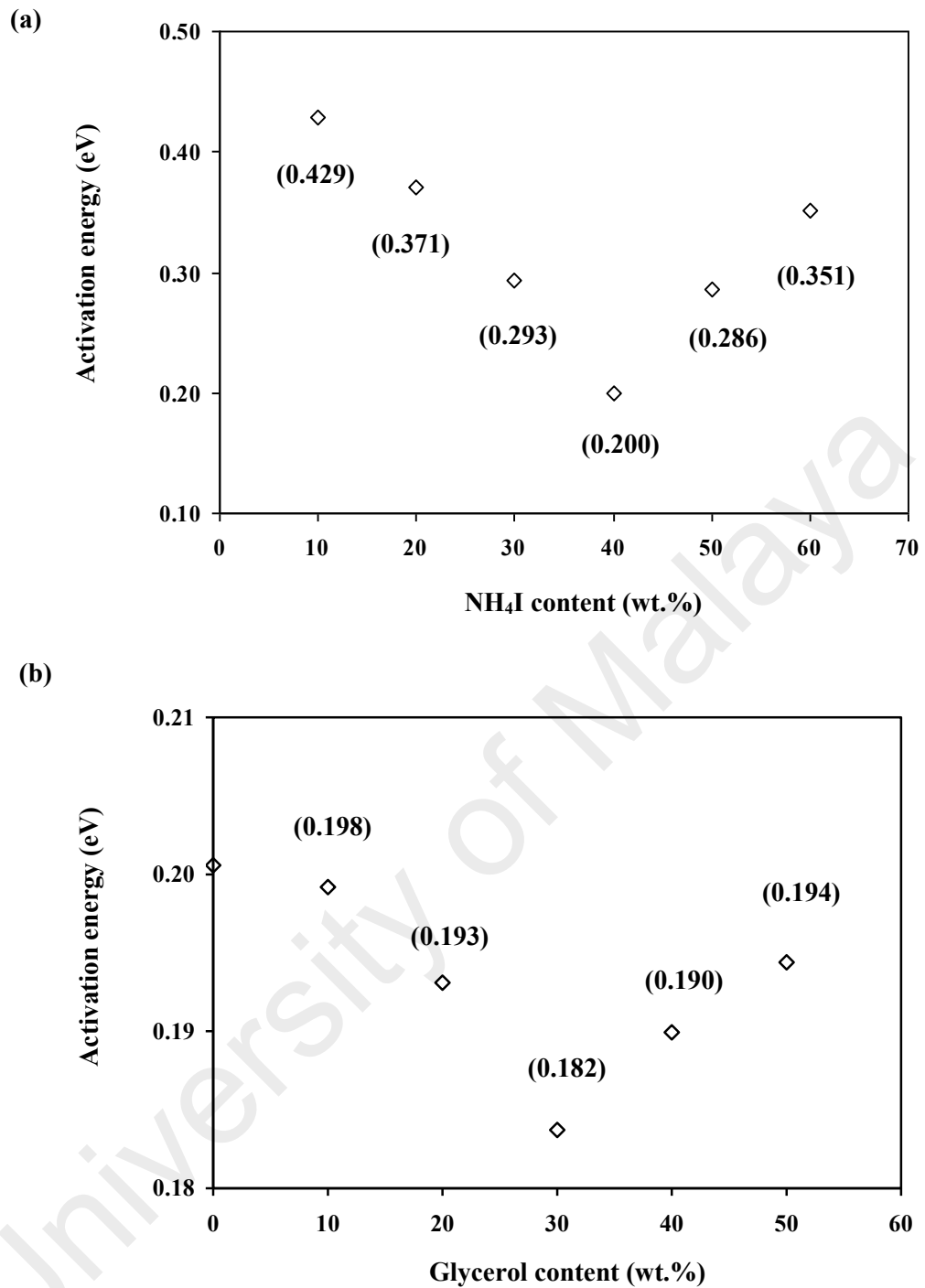
Figure 6.9: E_a values of (a) starch/chitosan-NH$_4$I and (b) starch/chitosan-NH$_4$I-glycerol electrolytes.

6.5   Ionic Transport Analysis

In general, conductivity is depending on mobility, μ and number of mobile ions, n (Majid & Arof, 2005). By employing the Rice and Roth model using Equation (2.2) and (2.3), the travelling time (τ), μ and n can be calculated. These properties are known as transport parameters, which are important in order to assess the performance of the electrolytes (Arof, Amirudin, Yusof, & Noor, 2014). It is necessary to know the type of conduction ion since its mass is one of the important parameters. In this work, H^+ ion from NH_4I is the conducting species which can be explained by Grotthus mechanism; where NH_4I is considered as the proton source (Hashmi et al., 1990).

l is the distance between two complexation sites. The value of l is used in order to calculate the value of τ. Since this work is using a polymer blend, various values of l are used. In a report by Khiar & Arof (2010), the l between two adjacent amylose fibers in starch is taken as 10.4 Å. This distance is used because the cations are easily attached to the amylose compound compared to amylopectin. The α-1,6-D-glucosidic linkages of amylopectin is a branched polysaccharide, hence it possess a less stable structure and more steric effect compared to the α-1,4-D-glucosidic linkages of amylose (Khiar & Arof, 2010). By taking $l = 10.4$ Å, the transport parameters of all electrolytes in salted and plasticized systems are calculated and exhibited in Tables 6.4 and 6.5, respectively.

Table 6.4: Transport parameters of starch/chitosan-NH_4I system at room temperature using $l = 10.4$ Å.

Sample	σ (S cm^{-1})	τ (s)	n (cm^{-3})	μ (cm^2 V^{-1} s^{-1})
A1	$(1.71 \pm 1.24) \times 10^{-9}$	1.15×10^{-13}	1.64×10^{17}	6.50×10^{-8}
A2	$(5.31 \pm 0.58) \times 10^{-8}$	1.23×10^{-13}	5.31×10^{17}	6.24×10^{-7}
A3	$(2.57 \pm 1.70) \times 10^{-6}$	1.39×10^{-13}	1.29×10^{18}	1.25×10^{-5}
A4	$(3.04 \pm 0.32) \times 10^{-4}$	1.68×10^{-13}	5.50×10^{18}	3.45×10^{-4}
A5	$(2.51 \pm 0.83) \times 10^{-6}$	1.39×10^{-13}	1.26×10^{18}	1.25×10^{-5}
A6	$(1.49 \pm 1.14) \times 10^{-7}$	1.27×10^{-13}	7.03×10^{17}	1.32×10^{-6}

Table 6.5: Transport parameters of starch/chitosan-NH_4I-glycerol system at room temperature using $l = 10.4$ Å.

Sample	σ / S cm^{-1}	τ / s	n / cm^{-3}	μ / cm^2 V^{-1} s^{-1}
B1	$(4.12 \pm 0.65) \times 10^{-4}$	1.69×10^{-13}	6.93×10^{18}	3.71×10^{-4}
B2	$(6.63 \pm 2.97) \times 10^{-4}$	1.71×10^{-13}	9.30×10^{18}	4.45×10^{-4}
B3	$(1.28 \pm 0.07) \times 10^{-3}$	1.76×10^{-13}	1.20×10^{19}	6.63×10^{-4}
B4	$(8.56 \pm 2.75) \times 10^{-4}$	1.72×10^{-13}	1.08×10^{19}	4.96×10^{-4}
B5	$(5.39 \pm 2.18) \times 10^{-4}$	1.70×10^{-13}	7.84×10^{18}	4.29×10^{-4}

In chitosan, l between two units of amine is 10 Å as reported by Kadir et al. (2010). Tables 6.6 and 6.7 list the transport parameters of the electrolytes in salted and plasticized systems, respectively, using $l = 10$ Å.

Table 6.6: Transport parameters of starch/chitosan-NH$_4$I system at room temperature using $l = 10.0$ Å.

Sample	σ (S cm^{-1})	τ (s)	n (cm^{-3})	μ (cm^2 V^{-1} s^{-1})
A1	$(1.71 \pm 1.24) \times 10^{-9}$	1.10×10^{-13}	1.71×10^{17}	6.25×10^{-8}
A2	$(5.31 \pm 0.58) \times 10^{-8}$	1.19×10^{-13}	5.52×10^{17}	6.00×10^{-7}
A3	$(2.57 \pm 1.70) \times 10^{-6}$	1.34×10^{-13}	1.34×10^{18}	1.20×10^{-5}
A4	$(3.04 \pm 0.32) \times 10^{-4}$	1.61×10^{-13}	5.72×10^{18}	3.32×10^{-4}
A5	$(2.51 \pm 0.83) \times 10^{-6}$	1.34×10^{-13}	1.31×10^{18}	1.20×10^{-5}
A6	$(1.49 \pm 1.14) \times 10^{-7}$	1.22×10^{-13}	7.31×10^{17}	1.27×10^{-6}

Table 6.7: Transport parameters of starch/chitosan-NH$_4$I-glycerol system at room temperature using $l = 10.0$ Å.

Sample	σ / S cm^{-1}	τ / s	n / cm^{-3}	μ / cm^2 V^{-1} s^{-1}
B1	$(4.12 \pm 0.65) \times 10^{-4}$	1.62×10^{-13}	7.21×10^{18}	3.57×10^{-4}
B2	$(6.63 \pm 2.97) \times 10^{-4}$	1.64×10^{-13}	9.67×10^{18}	4.28×10^{-4}
B3	$(1.28 \pm 0.07) \times 10^{-3}$	1.69×10^{-13}	1.25×10^{19}	6.38×10^{-4}
B4	$(8.56 \pm 2.75) \times 10^{-4}$	1.66×10^{-13}	1.12×10^{19}	4.77×10^{-4}
B5	$(5.39 \pm 2.18) \times 10^{-4}$	1.64×10^{-13}	8.15×10^{18}	4.13×10^{-4}

A work by Leal Filho, Seidl, Correia, & Cerqueira (2000) reported that the hydroxyl-hydroxyl distances in starch are in the range of 5.4 to 11.0 Å. Hence, the average point as $l = 8.2$ Å has been taken to calculate the transport parameters of the electrolytes in salted and plasticized systems, as listed in Tables 6.8 and 6.9, respectively.

Table 6.8: Transport parameters of starch/chitosan-NH₄I system at room temperature using $l = 8.2$ Å.

Sample	σ (S cm⁻¹)	τ (s)	n (cm⁻³)	μ (cm² V⁻¹ s⁻¹)
A1	$(1.71 \pm 1.24) \times 10^{-9}$	9.03×10^{-14}	2.08×10^{17}	5.12×10^{-8}
A2	$(5.31 \pm 0.58) \times 10^{-8}$	9.73×10^{-14}	6.74×10^{17}	4.92×10^{-7}
A3	$(2.57 \pm 1.70) \times 10^{-6}$	1.10×10^{-13}	1.63×10^{18}	9.83×10^{-6}
A4	$(3.04 \pm 0.32) \times 10^{-4}$	1.32×10^{-13}	6.98×10^{18}	2.72×10^{-4}
A5	$(2.51 \pm 0.83) \times 10^{-6}$	1.10×10^{-13}	1.59×10^{18}	9.83×10^{-6}
A6	$(1.49 \pm 1.14) \times 10^{-7}$	1.00×10^{-13}	8.92×10^{17}	1.04×10^{-6}

Table 6.9: Transport parameters of starch/chitosan-NH₄I-glycerol system at room temperature using $l = 8.2$ Å.

Sample	σ / S cm⁻¹	τ / s	n / cm⁻³	μ / cm² V⁻¹ s⁻¹
B1	$(4.12 \pm 0.65) \times 10^{-4}$	1.33×10^{-13}	8.79×10^{18}	2.93×10^{-4}
B2	$(6.63 \pm 2.97) \times 10^{-4}$	1.35×10^{-13}	1.18×10^{19}	3.51×10^{-4}
B3	$(1.28 \pm 0.07) \times 10^{-3}$	1.39×10^{-13}	1.53×10^{19}	5.23×10^{-4}
B4	$(8.56 \pm 2.75) \times 10^{-4}$	1.36×10^{-13}	1.37×10^{19}	3.91×10^{-4}
B5	$(5.39 \pm 2.18) \times 10^{-4}$	1.34×10^{-13}	9.94×10^{18}	3.38×10^{-4}

Tables 6.10 and 6.11 list the average values of the transport parameters for salted and plasticized systems at room temperature. All transport parameters in Tables 6.4 to 6.9 using different l values show that the increasing conductivity value is influenced by the increasing mobility and number density of ions in the salted and plasticized systems.

Table 6.10: Average values of transport parameters of starch/chitosan-NH$_4$I system at room temperature, where $l = 9.5$ Å.

Sample	$\sigma\,(\text{S cm}^{-1})$	$\tau\,(\text{s})$	$n\,(\text{cm}^{-3})$	$\mu\,(\text{cm}^2\,\text{V}^{-1}\,\text{s}^{-1})$
A1	$(1.71 \pm 1.24) \times 10^{-9}$	1.05×10^{-13}	1.81×10^{17}	5.96×10^{-8}
A2	$(5.31 \pm 0.58) \times 10^{-8}$	1.13×10^{-13}	5.86×10^{17}	5.72×10^{-7}
A3	$(2.57 \pm 1.70) \times 10^{-6}$	1.28×10^{-13}	1.42×10^{18}	1.14×10^{-5}
A4	$(3.04 \pm 0.32) \times 10^{-4}$	1.54×10^{-13}	6.07×10^{18}	3.16×10^{-4}
A5	$(2.51 \pm 0.83) \times 10^{-6}$	1.28×10^{-13}	1.39×10^{18}	1.14×10^{-5}
A6	$(1.49 \pm 1.14) \times 10^{-7}$	1.16×10^{-13}	7.75×10^{17}	1.21×10^{-6}

Table 6.11: Average values of transport parameters of starch/chitosan-NH$_4$I-glycerol system at room temperature, where $l = 9.5$ Å.

Sample	$\sigma\,/\,\text{S cm}^{-1}$	$\tau\,/\,\text{s}$	$n\,/\,\text{cm}^{-3}$	$\mu\,/\,\text{cm}^2\,\text{V}^{-1}\,\text{s}^{-1}$
B1	$(4.12 \pm 0.65) \times 10^{-4}$	1.55×10^{-13}	7.64×10^{18}	3.40×10^{-4}
B2	$(6.63 \pm 2.97) \times 10^{-4}$	1.57×10^{-13}	1.03×10^{19}	4.08×10^{-4}
B3	$(1.28 \pm 0.07) \times 10^{-3}$	1.61×10^{-13}	1.33×10^{19}	6.08×10^{-4}
B4	$(8.56 \pm 2.75) \times 10^{-4}$	1.58×10^{-13}	1.19×10^{19}	4.55×10^{-4}
B5	$(5.39 \pm 2.18) \times 10^{-4}$	1.56×10^{-13}	8.64×10^{18}	3.93×10^{-4}

The highest conducting sample in salted system with incorporation of 40 wt.% NH$_4$I has the highest average n and μ values of 6.07×10^{18} cm^{-3} and 3.16×10^{-4} cm^2 V^{-1} s^{-1}, respectively. A work by Shuhaimi et al. (2010) reported the n value of methyl cellulose doped with 25 wt.% NH$_4$NO$_3$ electrolyte was 4.86×10^{18} cm^{-3} which is comparable with the present result. The addition of 50 and 60 wt.% of NH$_4$I decreases the number density and mobility of ions due to excess of salt which form more ion pairs, leading to conductivity decrement.

For the plasticized system, the average value of n lies between 10^{18} and 10^{19} cm^{-3} and all μ values are in the range of 10^{-4} cm^2 V^{-1} s^{-1}. From Table 6.11, it can be concluded that the increasing conductivity value is influenced by the increasing mobility and number density of ions. The highest conducting sample for this system has the highest average n and μ values of 1.33×10^{19} cm^{-3} and 6.08×10^{-4} cm^2 V^{-1} s^{-1}, respectively. Shukur et al. (2013) reported that the n value of chitosan-PEO-NH$_4$NO$_3$ plasticized with 70 wt.% ethylene carbonate (EC) electrolyte was 1.87×10^{19} cm^{-3} which is comparable with the present result.

The change in conductivity with glycerol composition is mainly due to the change in free ion concentration. When the total amount of salt is the same, the change in n observed should be ascribed to the permittivity effect of the plasticizer. Due to the high dielectric constant of glycerol, increasing the glycerol content will increase the degree of ion dissociation, thus the conductivity is increased by the increase in the number of free ions (Winie et al., 2009). The presence of glycerol in the electrolyte system produced more mobile ions and reduced the viscosity of the electrolyte which leads to an increase in ionic mobility (Arof et al., 2010).

6.6   Transference Number Analysis

The conducting species involved within an electrolyte can be measured by transference number analysis. The highest conducting electrolyte was sandwiched between two conducting species transparent electrodes which in this work is the stainless steel (SS) foils. The contribution of total ionic conductivity of the polymer electrolyte is determined by polarizing the blocking electrode cell configuration of SS/B3/SS and monitoring the potentiostatic current as a function of time. The ions will

be blocked while electrons are transparent to the electrodes. The transference numbers coresponding to ionic (t_{ion}) and electronic (t_e) have been evaluated using the equations:

$$t_{ion} = \frac{(I_i - I_{SS})}{I_i} \qquad\qquad (6.11)$$

$$t_e = 1 - t_{ion} \qquad\qquad (6.12)$$

where I_i is the initial current and I_{SS} is the steady state current. The current flow within an electrode will show a rapid drop with time if it is an ionic conductor, which in the case of non ionic conductor, it will not happen (Yap, 2012). A similar pattern is shown in Figure 6.10 where the current drop rapidly at the initial stage before being saturated at 0.30 μA. The steady state current is achieved when the movement is balanced by diffusion process. t_{ion} and t_e for the B3 sample are found 0.991 and 0.009, respectively.
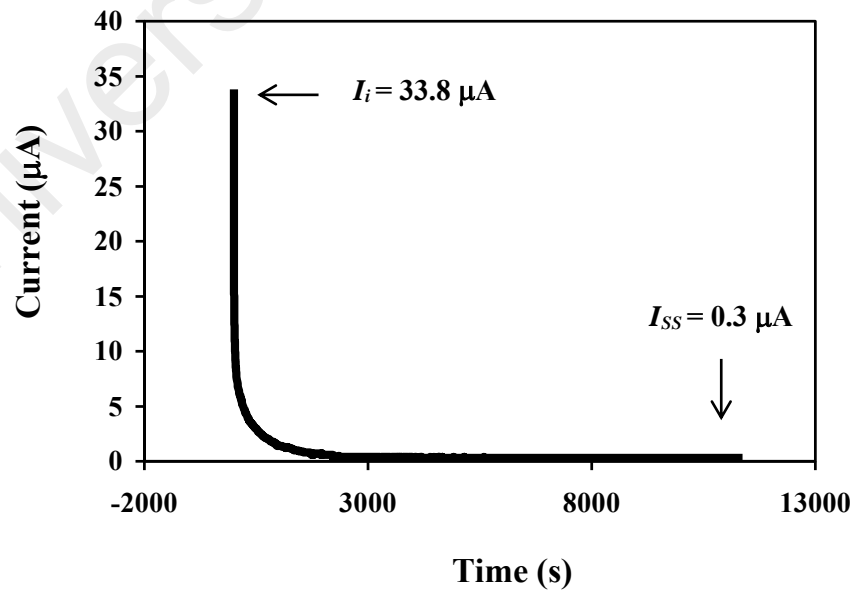
Figure 6.10: Current relaxation curve during dc polarization for blocking electrodes (SS/ B3/SS).

From the results, it can be seen that the transference number for ions is much larger compared to the transference number for electrons. This suggests that in these polymer electrolytes, the charge transport is predominantly due to ions (Woo et al., 2011b). Shukur & Kadir (2015a) reported that the t_{ion} and t_e for the highest conducting electrolyte in starch-NH$_4$Br-glycerol system were 0.98 and 0.02, respectively, which is comparable with the results presented in this work.

In polymer electrolyte system, it is well-known that different ions have different mobilities thus carry different portion of the total current (Ghosh, Wang, & Kofinas, 2010). Both cation and anion have chances to move; hence it is important to clarify the cation transference number. In battery, only cations are responsible for intercalation and deintercalation processes at cathode during charge-discharge cycle (Arof, Shuhaimi, Amirudin, Kufian, Woo, & Careem, 2014; Shukur & Kadir, 2015b). Cation transference number analysis is applicable for electrolytes with two mobile ions sandwiched between two electrodes, which are blocking electrodes for one ion but non-blocking electrodes for the other (Watanabe, Nagano, Sanui, & Ogata, 1988). MnO$_2$ was chosen to be the reversible electrodes because it is transparent to the cations and electrons, hence suitable for anions blocking.

The proton transference number was determined by Watanabe's technique and calculated using:

$$t_+ = \frac{R_b}{\dfrac{\Delta V}{I_{ss}} - R_c} \tag{6.13}$$

where ΔV is the bias voltage from dc polarization, R_b is the bulk resistance and R_c is charge transfer resistance (Woo et al., 2011b). The values of R_b and R_c were measured from a complex impedance plot using reversible MnO_2 electrodes. R_c is attributed to the charged-discharged at the electrode/electrolyte interface. Figure 6.11 depicts the plot of polarization current against time for MnO_2/ B3/ MnO_2 cell. I_{ss} is found to be 47.5 μA after 3841 s. The R_b and R_c values are obtained from the impedance plot depicted in Figure 6.12. The inset in Figure 6.12 demonstrates the ohmic portion of I_{ss} up to 1.80V before it deviates from linearity. The value of t_+ is found to be 0.40. Other reports show that the cation transference numbers ranged from 0.21 to 0.46 (Arof et al., 2012; Shukur & Kadir, 2015a; Woo et al., 2011b). Although the transference number may affected by the ions association, it still offers an insight into the ion transport process (Watanabe et al., 1988). The long molecular chain within starch and chitosan can also be linked with each other and build a network through hydrogen bonding thus possible to limit the mobility of the large size of iodide, I^- ion. This results on the higher cation transference number since H^+ is smaller in size (Arof et al., 2012).
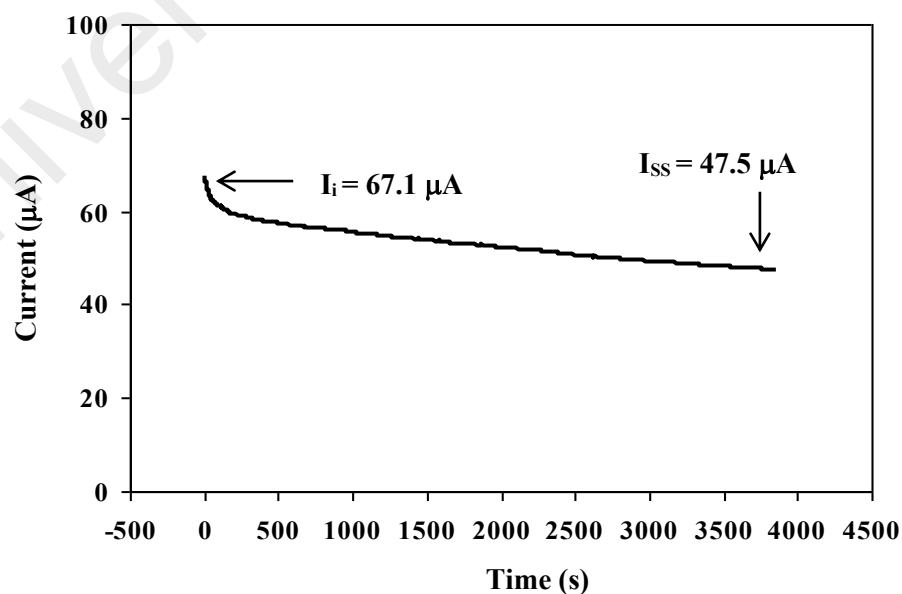
Figure 6.11: Transference number of B3 at room temperature using MnO_2 electrodes.
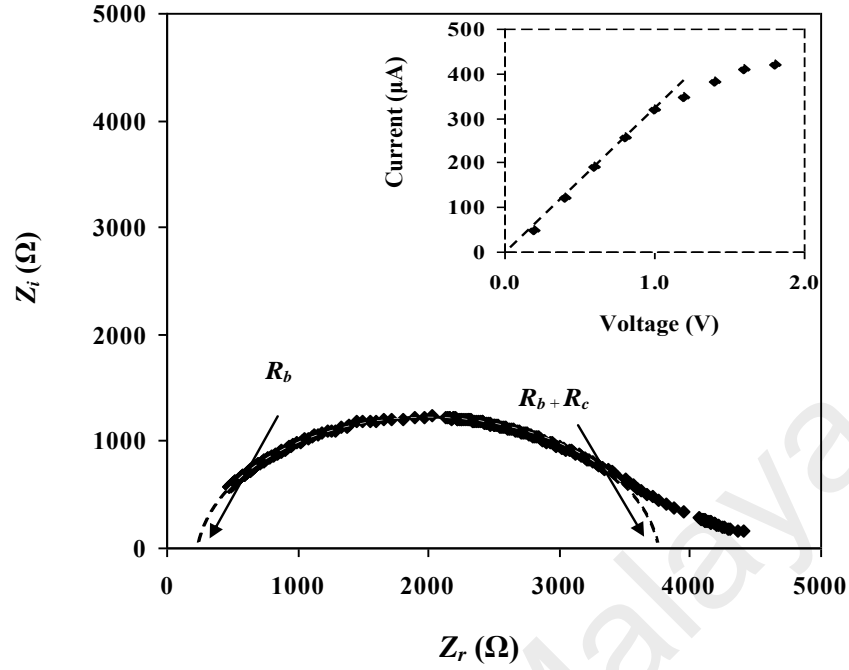
Figure 6.12: Impedance plot for $MnO_2/B3/MnO_2$ cell at room temperature. Inset is I_{ss} as a function of voltage at room temperature.

6.7 Dielectric Constant and Dielectric Loss Studies

Numerous dielectric data such as complex dielectric constant, ε^* and complex modulus constant, M^* are evaluated from the complex impedance data, Z^*. Both real, ε_r and imaginary, ε_i parts of complex dielectric constant are related to the measured Z_r and Z_i as followed:

$$\varepsilon_r = \frac{Z_i}{\omega C_o (Z_r^{\,2} + Z_i^{\,2})} \tag{6.14}$$

$$\varepsilon_i = \frac{Z_r}{\omega C_o (Z_r^{\,2} + Z_i^{\,2})} \tag{6.15}$$

131

where C_0 is vacuum capacitance and ω is angular frequency. Here, $C_0 = \varepsilon_0 A/t$ and $\omega = 2\pi f$, ε_0 is the permittivity of free space and f is the frequency. ε_r represents the dielectric constant or capacity to store the electric charge, while ε_i represents the amount of energy losses to move ions and align dipoles when the electric field polarity reverses rapidly (Woo, Majid, & Arof, 2012).

The frequency dependence of ε_r and ε_i in salted system at room temperature are shown in Figures 6.13 (a) and (b) respectively while Figure 6.14 (a) and (b) shows the salt dependence of ε_r and ε_i at selected frequencies. Since the charge is made up of H^+ ions, the increase in dielectric constant represents the increase in number of H^+ ions. It is observed that the variation of ε_r and ε_i follow the same trend as the conductivity result as the highest conducting sample has the highest values of ε_r and ε_i. As the NH_4I content increases up to 40 wt.%, it leads to the increment of charge stored in the electrolytes as well as the number density of mobile ions, hence increases the conductivity (Khiar & Arof, 2011). However, at larger salt concentration, distances between ions become smaller hence the ions re-associate to become neutral ion pairs. This reduces number density of free ions as well as its mobility that in turn loss their contribution on conductivity.

(a)

(b)
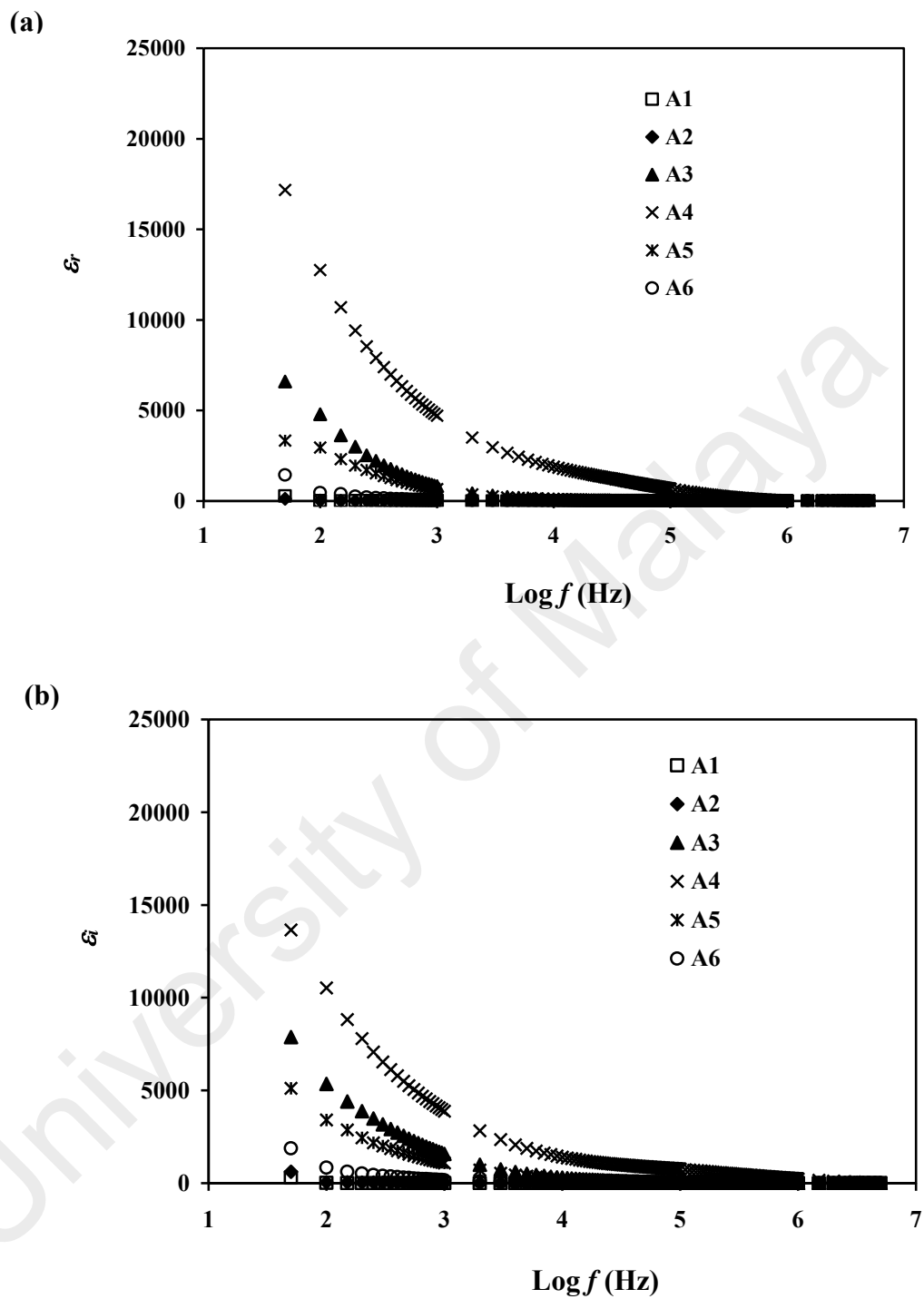
Figure 6.13: Frequency dependence of (a) ε_r and (b) ε_i at room temperature in salted system.

133

(a)
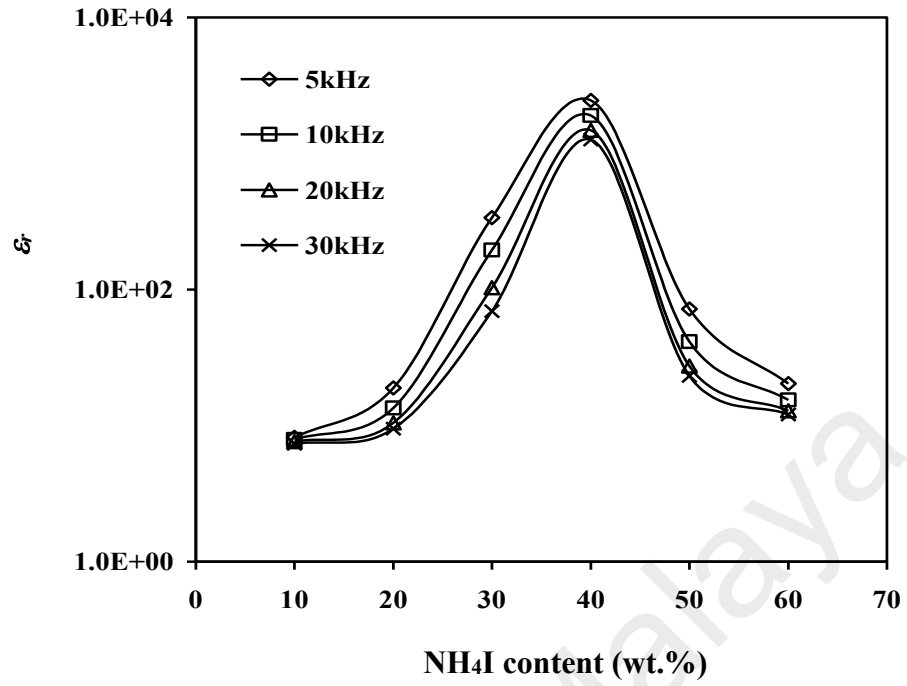
(b)
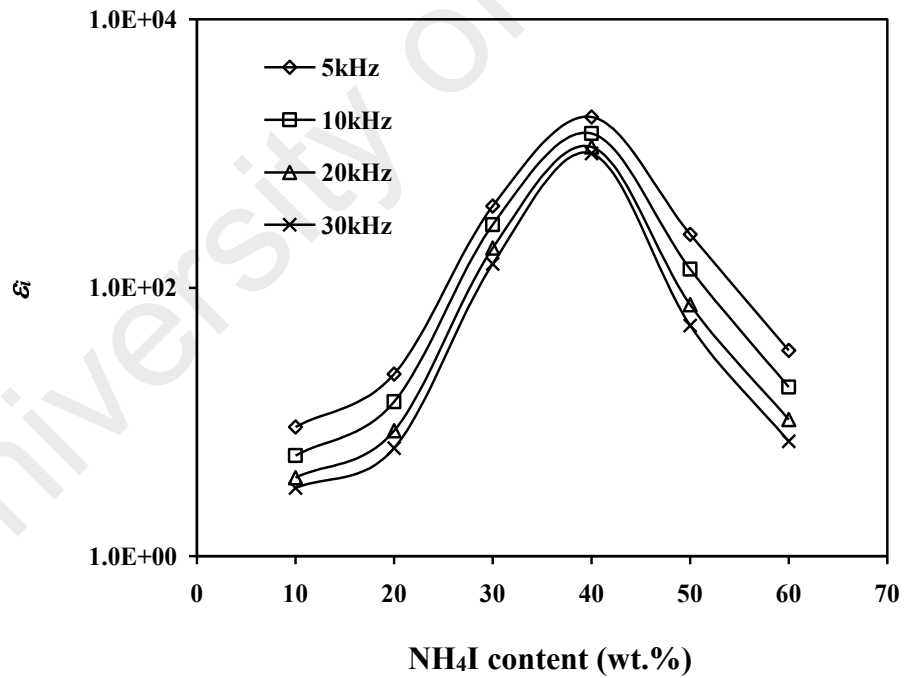
Figure 6.14: The dependence of (a) ε_r and (b) ε_i at room temperature for selected frequencies in salted system.

The frequency dependence of ε_r and ε_i in plasticized system at room temperature are shown in Figures 6.15 (a) and (b) respectively while Figure 6.16 (a) and (b) show the glycerol dependence of ε_r and ε_i at selected frequencies, respectively. Similar phenomena as shown in salted system can be observed in plasticized system.

(a)

(b)
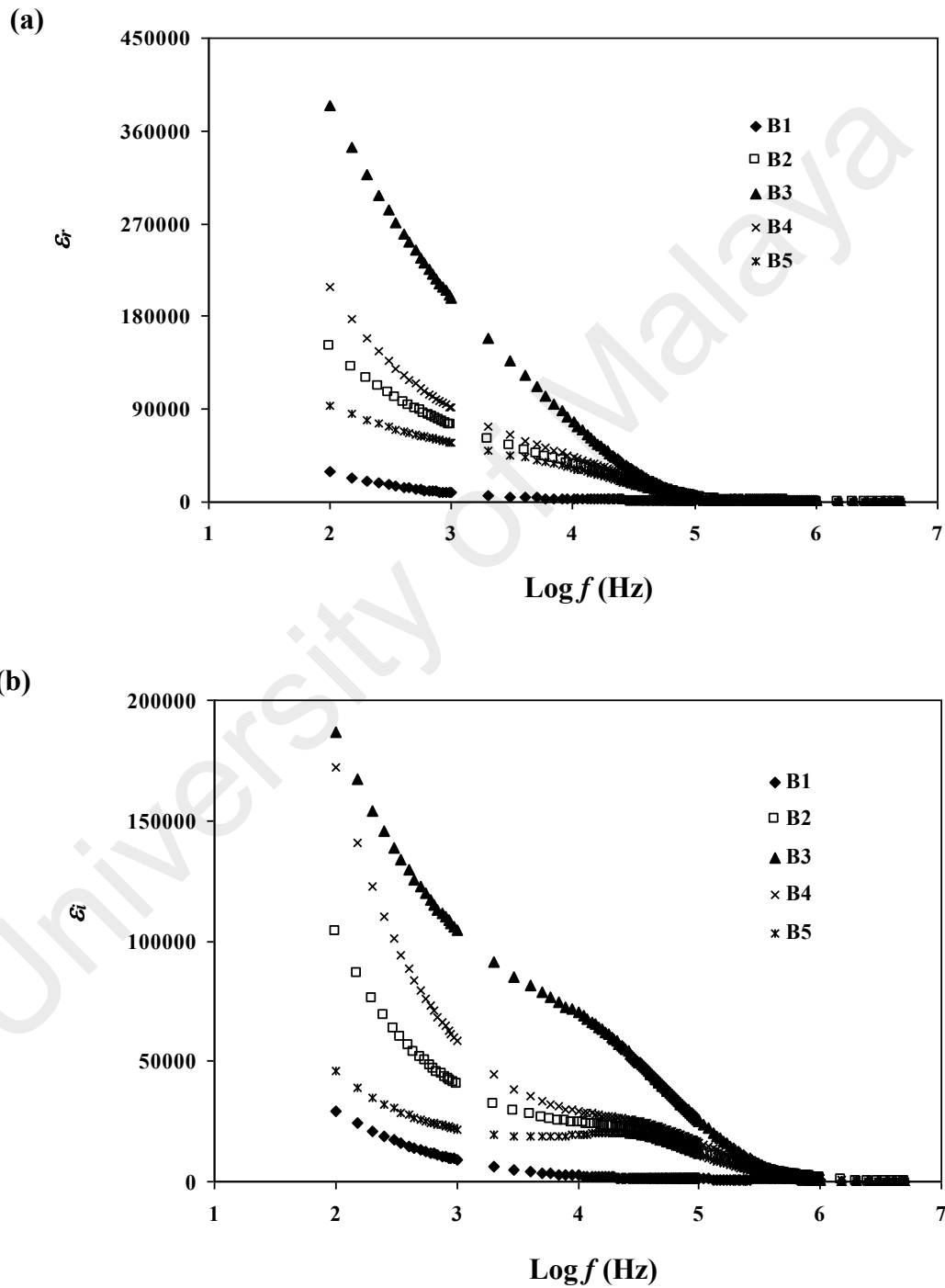
Figure 6.15: Frequency dependence of (a) ε_r and (b) ε_i at room temperature in plasticized system.

(a)
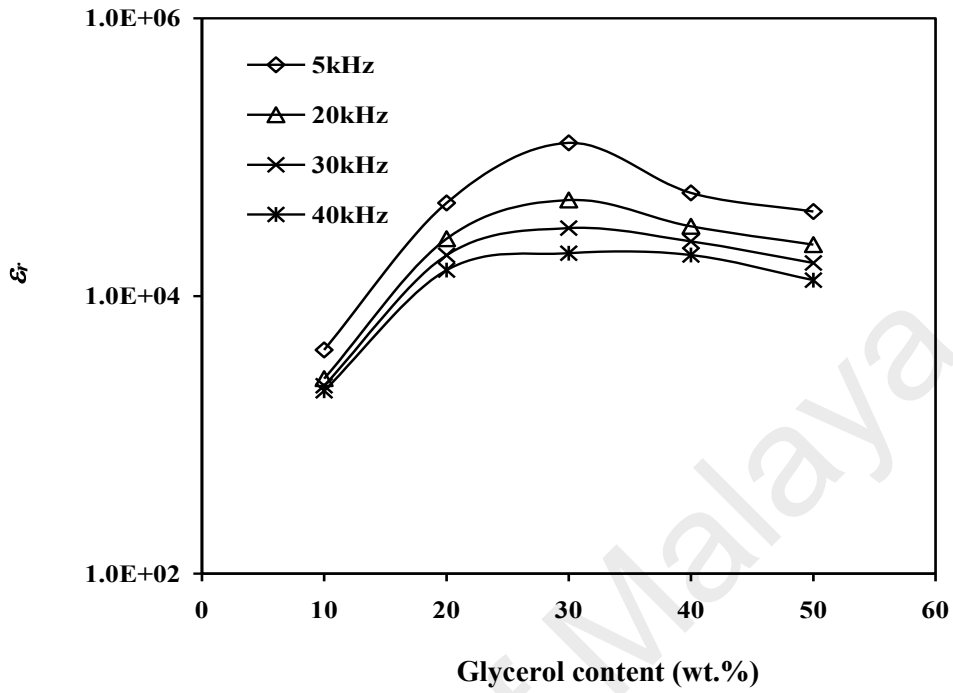
(b)
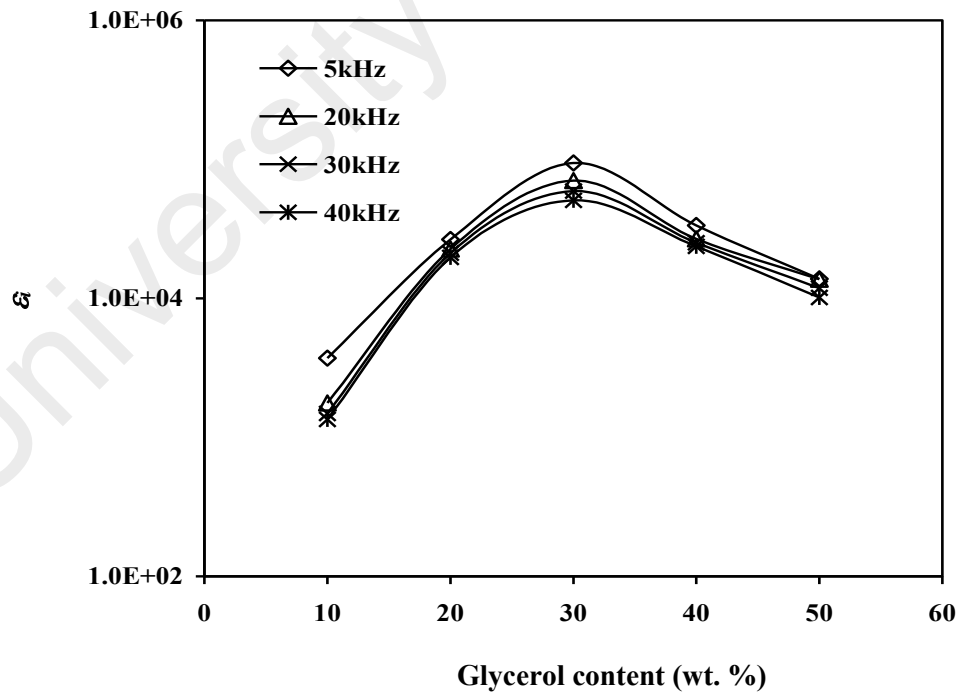
Figure 6.16: The dependence of (a) ε_r and (b) ε_i at room temperature for selected frequencies in plasticized system.

Dispersion with a high value of ε_r and ε_i is observed in the low frequency region which is attributed to the dielectric polarization effect. Due to its high dielectric constant, glycerol is able to dissociate more salt to cations and anions, resulting in an increase in number density of mobile ions (Buraidah et al., 2009). This indicates that the increase in conductivity is due to the increase in the concentration of mobile ions (Khiar & Arof, 2010). Both ε_r and ε_i rise towards low frequencies due to the electrode polarization and space charge effects, confirming the non-Debye behavior of all electrolytes in salted and plasticized systems (Khiar & Arof, 2010). The periodic reversal of the electric field occurs rapidly at high frequencies, which disable the ions from orienting according to the direction of the electric field hence the trapped ions start to accumulate at the interface of the electrode-electrolyte, leading to the decrease in the values of ε_r and ε_i (Woo et al., 2012). The dielectric trend presented in this work is comparable with the work done by Aziz et al. (2012). Khiar & Arof (2011) also reported that the dielectric study for starch/chitosan-NH$_4$NO$_3$ system follows the same trend as their conductivity result. However, beyond the addition of 30 wt% of glycerol, ε_r is observed to decrease, which follows the same trend as their conductivity results. Shukur et al. (2013) also reported that as more plasticizer was added, more undissociated salt become ions, hence increased the stored charge in the electrolyte.

The variation of ε_r and ε_i, with temperature for the highest conducting electrolyte at selected frequencies in salted system are shown in Figure 6.17 (a) and (b) while in plasticized system are shown in Figure 6.18 (a) and (b). The values of ε_r and ε_i increase as the temperature increases. This phenomenon proves that the salt undergoes greater dissociation as the temperature increased, hence resulting in an increase in number of free ions and assists the conductivity increment (Winie & Arof, 2004). This result

supports the transport parameters analysis in Tables 6.4 to 6.11 where the number density of ion increases with temperature.

(a)

(b)
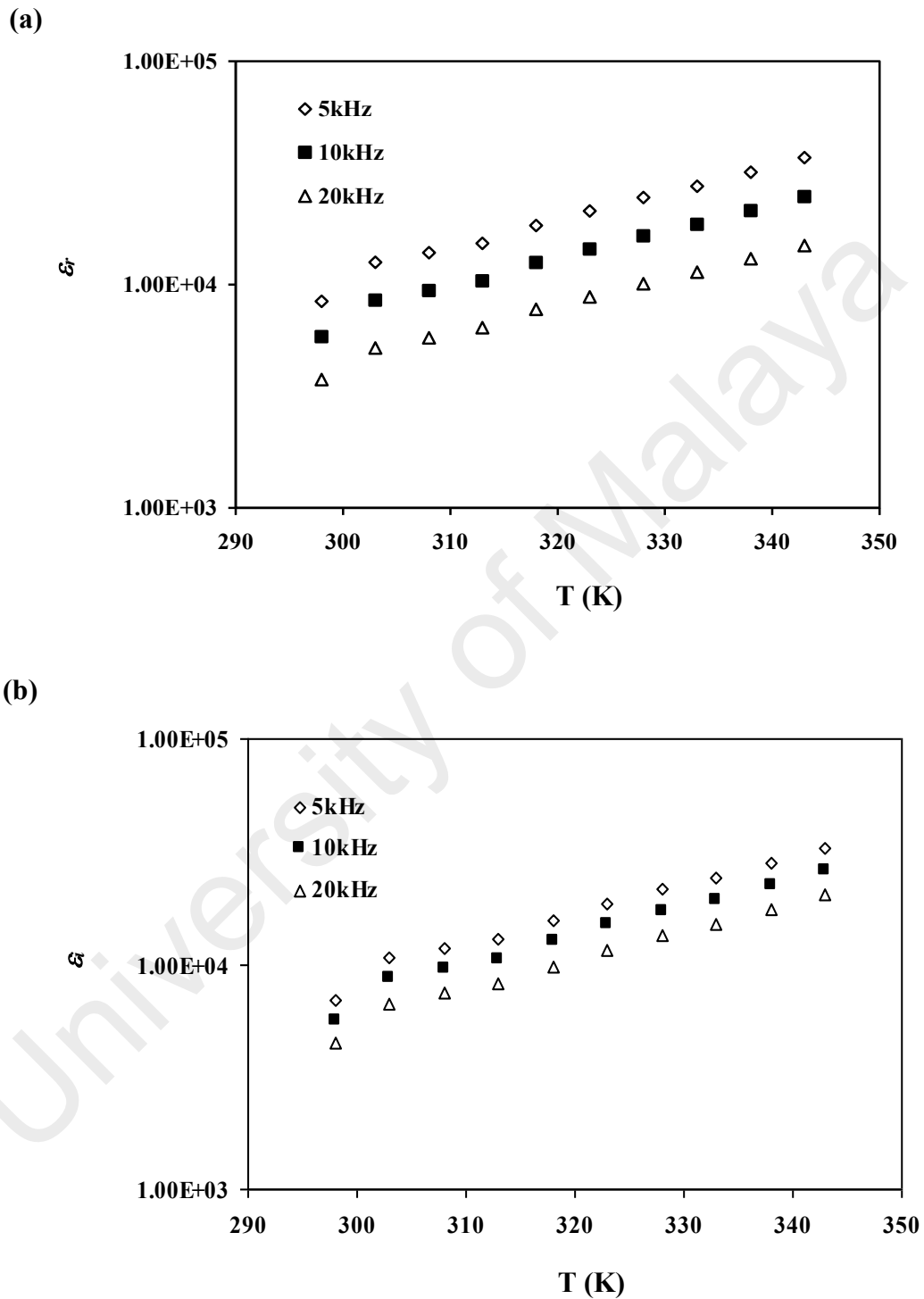
Figure 6.17: The dependence of (a) ε_r and (b) ε_i on temperature for A4 at selected frequencies.

(a)
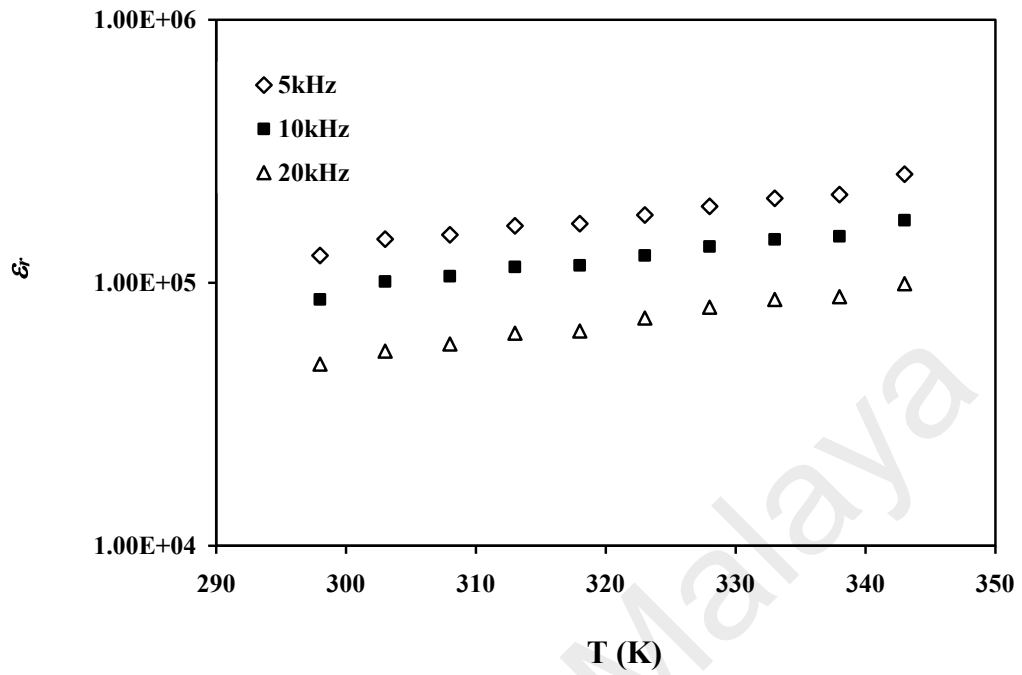
(b)
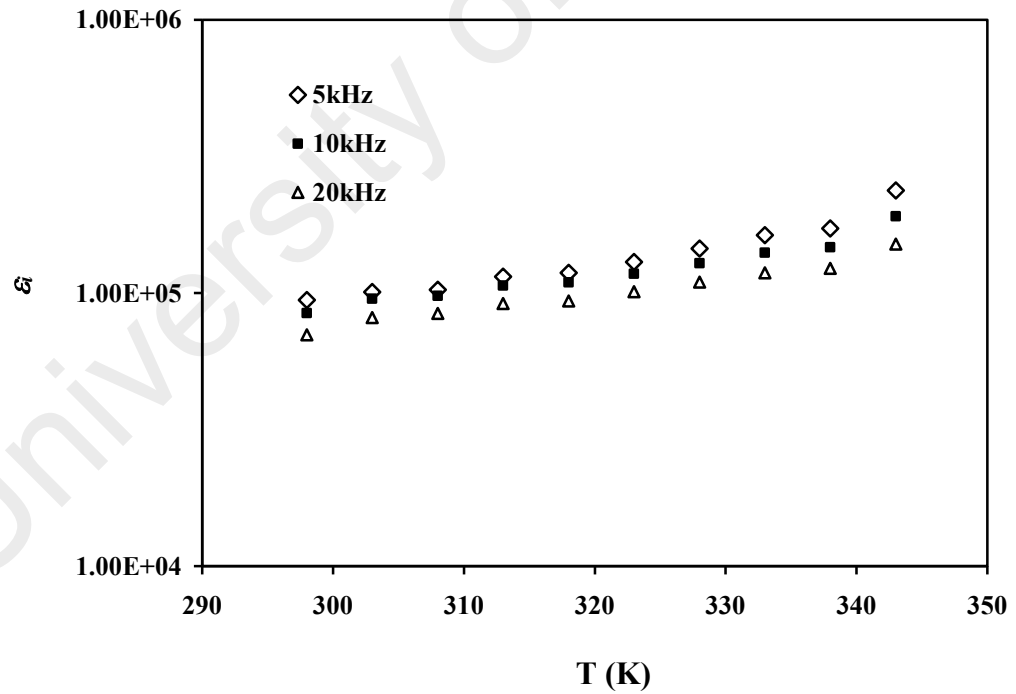
Figure 6.18: The dependence of (a) ε_r and (b) ε_i on temperature for B3 at selected frequencies.

6.8   Electrical Modulus Studies

The dielectric studies can be further discussed based on electrical modulus studies. Complex electrical modulus, M^* is defined from complex dielectric constant, ε^* using the following equations:

$$M^* = M_r + jM_i = \frac{1}{\varepsilon_r^*} \tag{6.16}$$

where:

$$M_r = \frac{\varepsilon_r}{(\varepsilon_r^2 + \varepsilon_i^2)} \tag{6.17}$$

$$M_i = \frac{\varepsilon_i}{(\varepsilon_r^2 + \varepsilon_i^2)} \tag{6.18}$$

where M_r and M_i are real and imaginary parts of the electrical modulus. Electrical modulus is useful to analyze electrical relaxation processes because it is defined as the reciprocal of complex relative permittivity according to Equation (6.16). Figure 6.19 (a) and (b) show the variation of M_r with frequency for the electrolytes in salted and plasticized systems, respectively, at room temperature. It can be seen that M_r approaches zero at low frequency region which indicates the electrode polarization effect has been suppressed and neglected (Woo et al., 2012). The M_r values are increased with frequency where the peaks exist at high frequency. This is an indicator that the polymer electrolytes are ionic conductors (Ramesh & Arof, 2001). In Figure 6.19 (a), only A4 peak cannot be observed. As the conductivity increased, the spectra are shifted to the
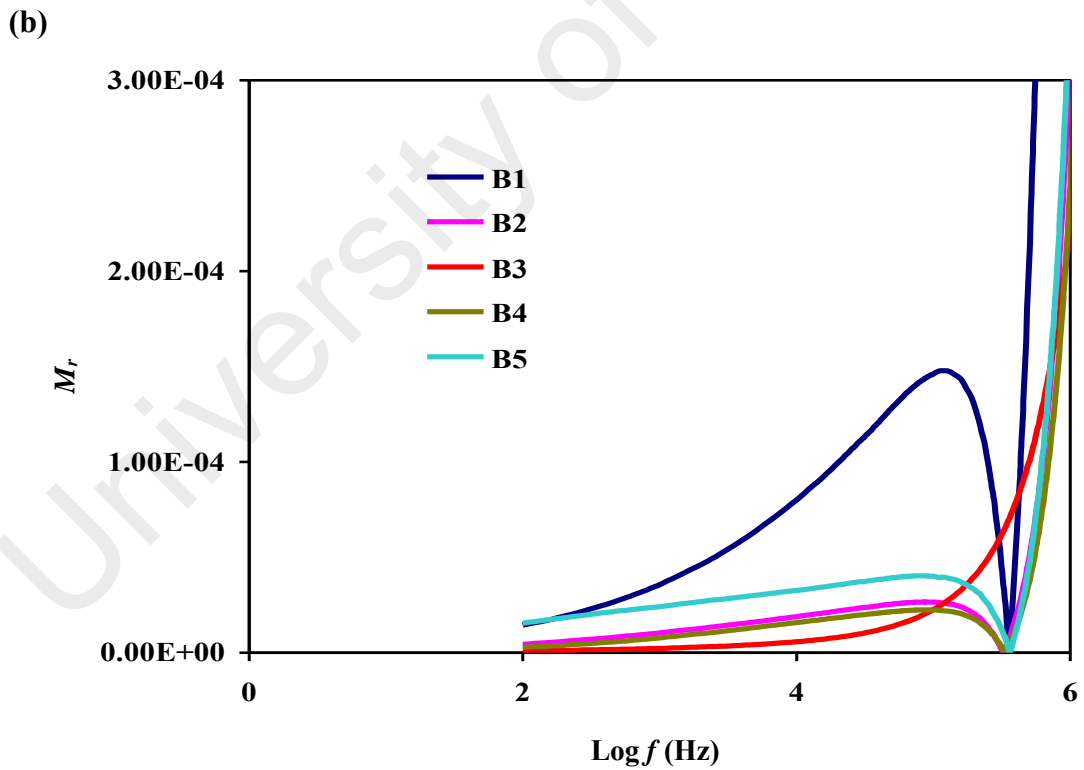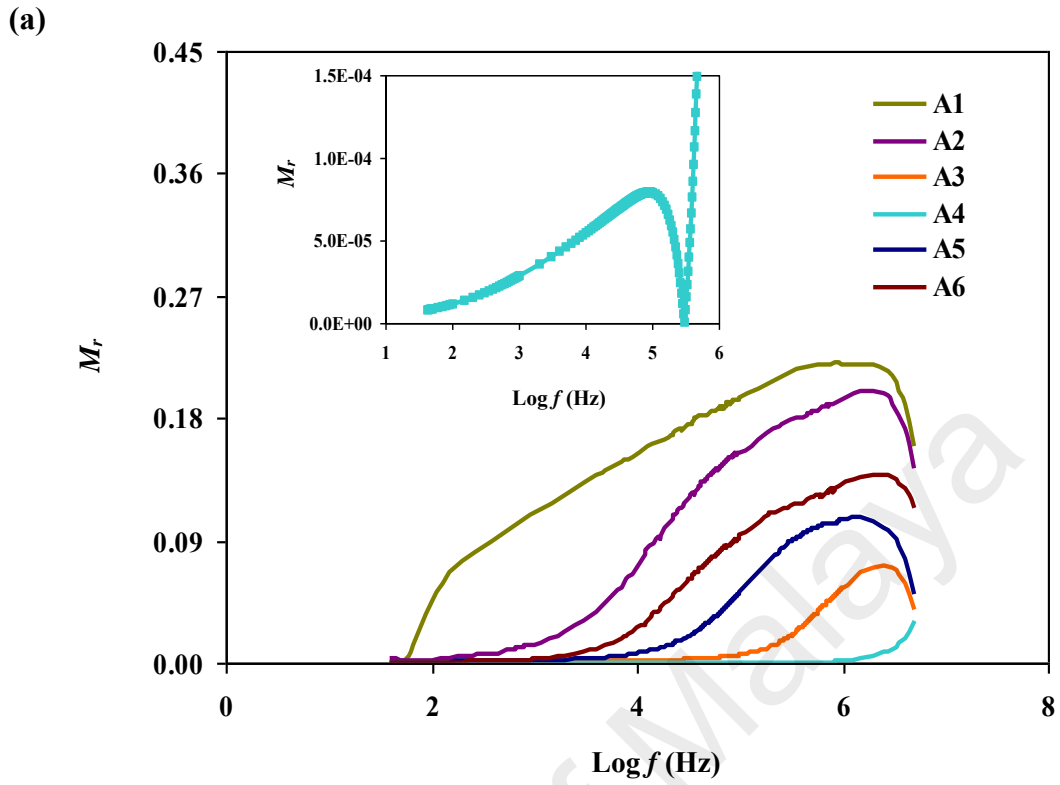
Figure 6.19: The dependence of M_r on frequency at room temperature for electrolytes in (a) salted and (b) plasticized systems. The inset in (a) is the dependence of M_r for A4 at lower frequency region.

right beyond the frequency window hence show only the dispersion part. Figure 6.20 (a) and (b) show the variation of M_r with frequency for A4 and B3, respectively, at various temperatures.

(a)

(b)
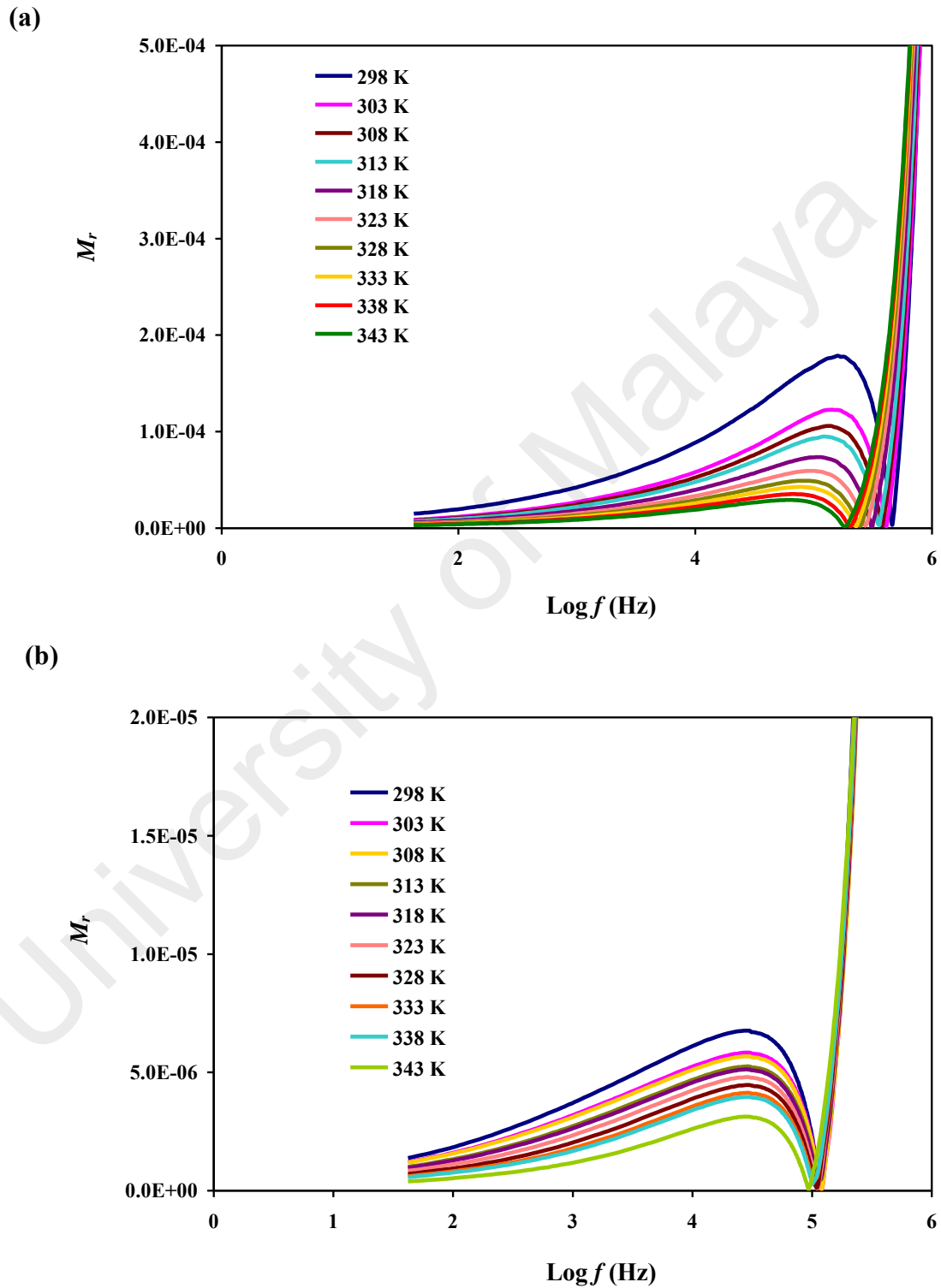
Figure 6.20: The dependence of M_r on temperature for (a) A4 and (b) B3.

The reduction of M_r values with respect to the increment of temperature is due to the increased in mobility of the charge carriers and the polymer segments (Aziz, Abidin, & Arof, 2010). As the conductivity increases, the spectra shift to the right beyond the frequency window due to the distribution of relaxation processes spread over a wide range of frequencies (Patro & Hariharan, 2009a). The absence of peaks in the M_r figures results from the fact that M_r is equivalent to ε_r which represents the ability of the materials to store charge or energy (Aziz et al., 2010).

Figure 6.21 (a) and (b) represents the variation of M_i with frequency for the electrolytes in salted and plasticized systems, respectively, at room temperature. The figures show similar pattern with M_r where the M_i values reduce with respect to the increment of temperature which is due to the large value of capacitance associated with the electrode polarization effect (Patro & Hariharan, 2009b). The relaxation time of M_i or t_{Mi} can be calculated from the relation of:

$$t_{Mi}\omega_{peak} = 1 \tag{6.19}$$

where ω_{peak} is the angular frequency of the M_i relaxation peak. The peaks are shifted towards higher frequencies with shorter relaxation time as the conductivity increases is correlated with the relaxation mechanisms (Mishra & Rao, 1998). Generally, relaxation time represents the efforts of the charge carriers to obey the direction of applied field (Winie & Arof, 2004). In Figure 6.21 (a), only A4 peak cannot be observed within the frequency window while all peaks in plasticized systems are located beyond the frequency window. The values of t_{Mi} for selected electrolytes in salted system are presented in Table 6.12.

(a)

(b)
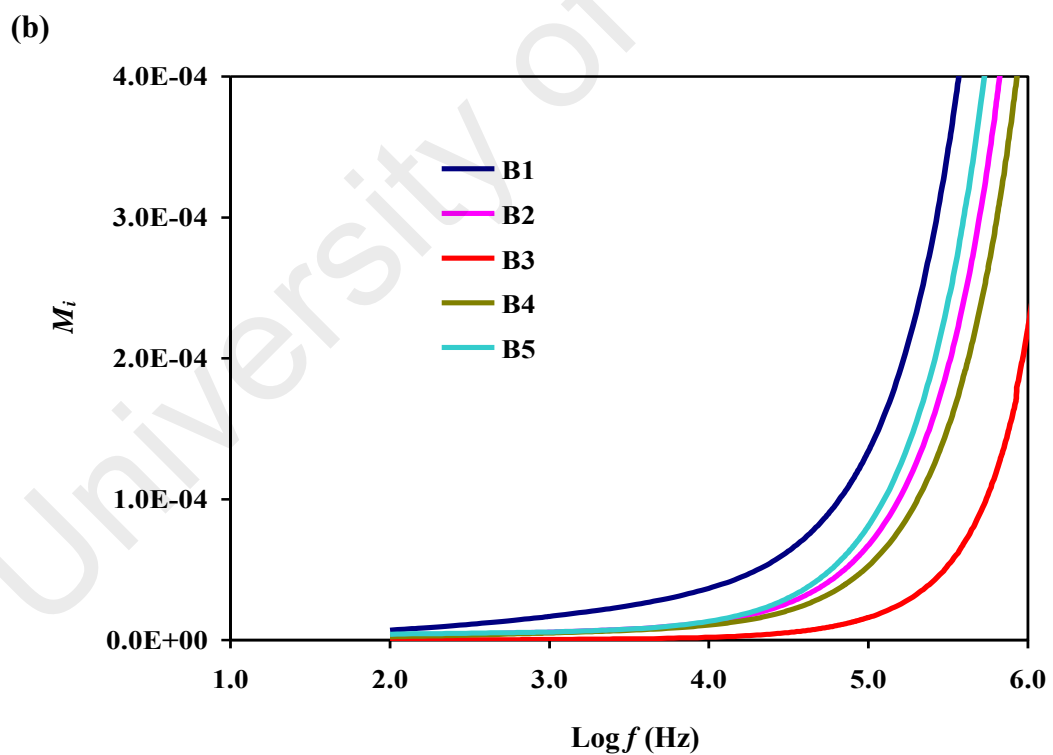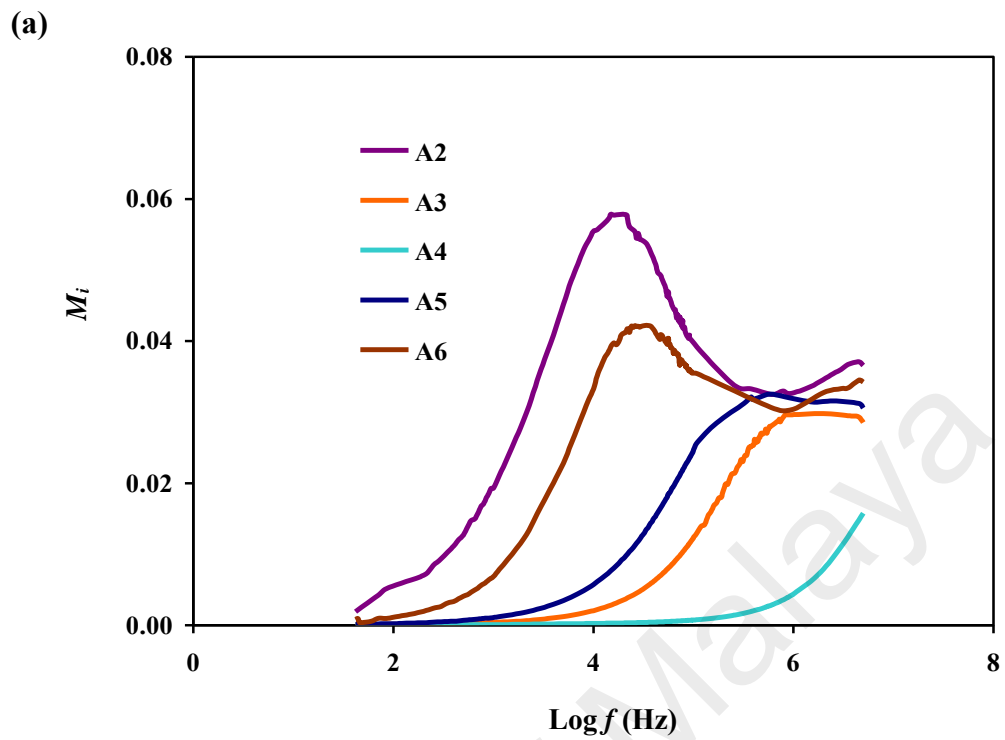
Figure 6.21: The dependence of M_i on frequency at room temperature for electrolytes in (a) salted and (b) plasticized systems.

Table 6.12: Relaxation time of M_i at room temperature in salted system.

Sample	t_{Mi} (s)
A1	7.96×10^{-4}
A2	1.06×10^{-5}
A3	1.85×10^{-7}
A5	2.79×10^{-7}
A6	6.12×10^{-6}

The variation of the t_{Mi} values demonstrates the sequence of the conductivity trend. A3 is observed to possess the lowest t_{Mi} value of 1.85×10^{-7} following its highest conductivity value among others meanwhile A1, which has the lowest conductivity value possesses the t_{Mi} value of 7.96×10^{-4}. Figure 6.22 (a) and (b) exhibit the variation of M_i with frequency at various temperatures for the highest conducting electrolyte in salted (A4) and plasticized (B3) systems, respectively. The long tail is also associated with the high capacitance values of the electrodes at low frequency due to accumulation of charge carriers at the electrode-electrolyte interface (Aziz et al., 2010). No peaks can be observed due to frequency limitation.

(a)

(b)
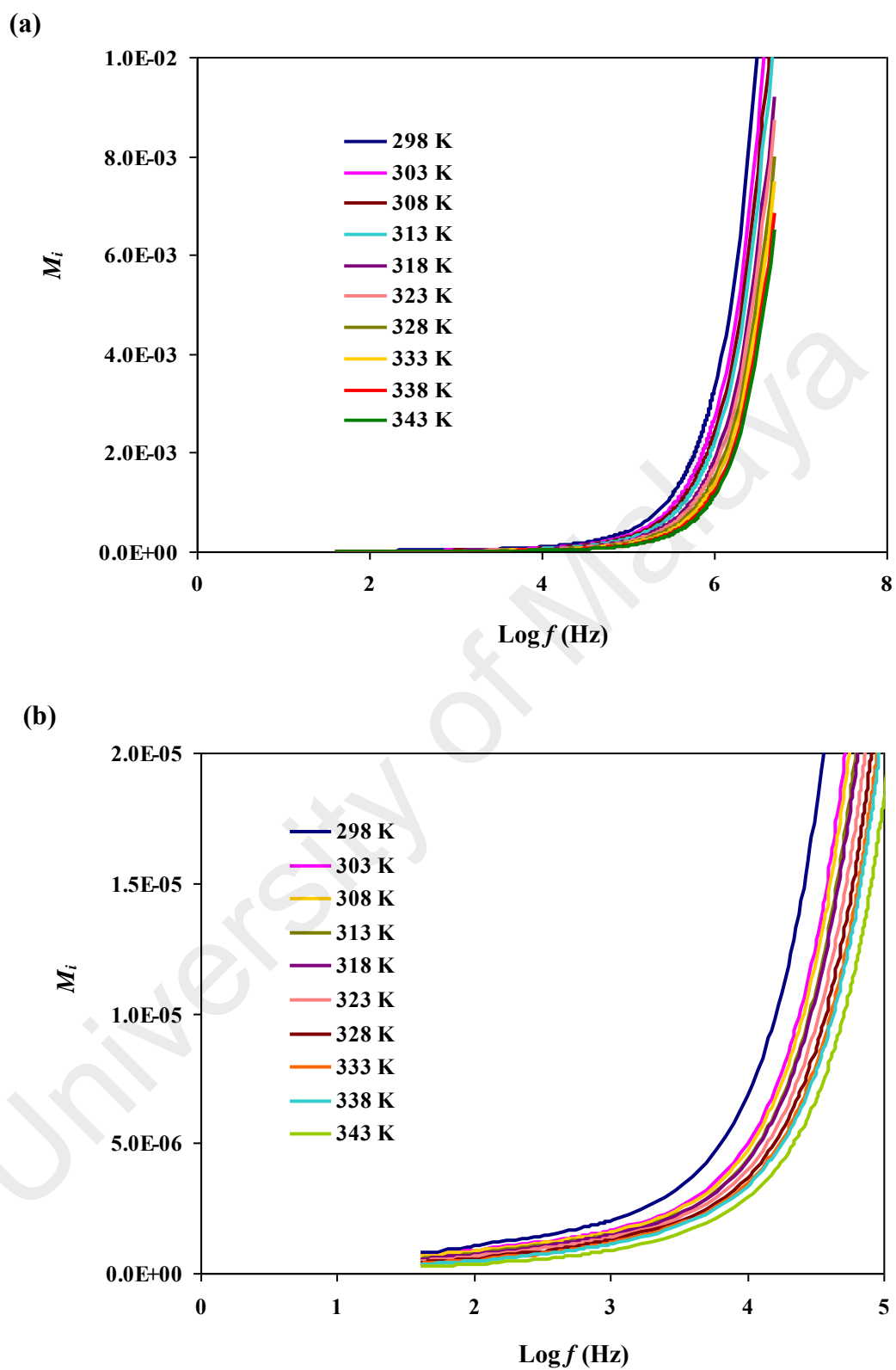
Figure 6.22: The dependence of M_i on frequency at various temperatures for (a) A4 and (b) B3.

6.9   Conduction Mechanisms

The ionic conduction mechanism of an electrolyte can be determined by employing Jonscher's universal power law (Murugaraj, Govindaraj, & George, 2003; Psarras, Manolakaki, & Tsangaris, 2003):

$$\sigma(\omega) = A\omega^s + \sigma_{dc} \tag{6.20}$$

where $\sigma(\omega)$ is the total conductivity, A is temperature dependent parameter, s is the power law exponent and σ_{dc} is frequency independent dc conductivity. The ac conductivity, σ_{ac} is presented by $A\omega^s$, hence:

$$\sigma(\omega) = \sigma_{ac} + \sigma_{dc} \tag{6.21}$$

The σ_{ac} can also be obtained using:

$$\sigma_{ac} = \varepsilon_o \varepsilon_i \omega \tag{6.22}$$

where $\varepsilon_r \tan \delta = \varepsilon_i$. By substituting $\sigma_{ac} = A\omega^s$ into Equation 6.22, the value of s can be evaluated from the following relation:

$$\ln \varepsilon_i = \ln \frac{A}{\varepsilon_o} + (s-1)\ln \omega \tag{6.23}$$

The value of exponent s is obtained from the slope of the plot of $\ln \varepsilon_i$ against $\ln \omega$ in Figure 6.23. In the present work, the studied frequency range is $64 \leq f \leq 93$ k Hz.

(a)

(b)
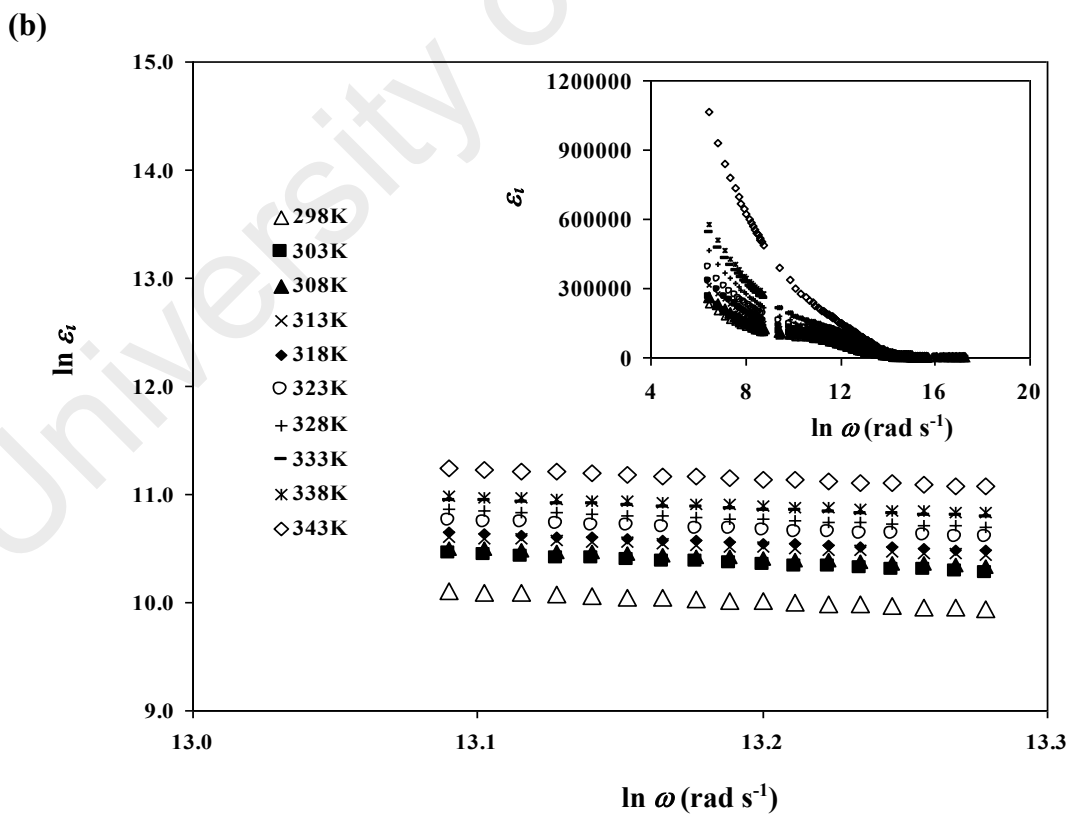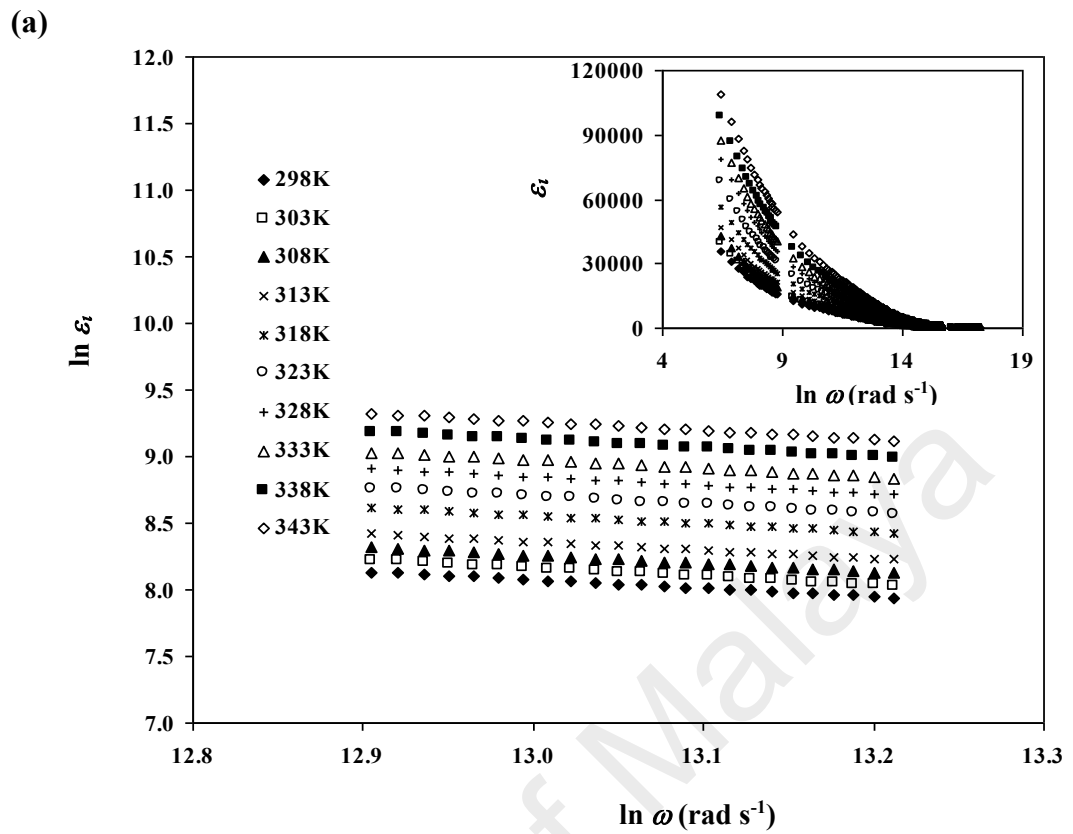
Figure 6.23: ln ε_i versus ln ω at different temperatures for (a) A4 and (b) B3.

This is because at higher frequency region, the electrode polarization occurs at minimum rate or does not occur at all (Buraidah et al., 2009; Kadir, Teo, Majid, & Arof, 2009). Figure 6.24 shows the plot of *s* against temperature for the highest conducting electrolyte sample. The exponent *s* is found to be independent of temperature which is shown by the small gradient where in this work are 0.00008 and -0.00008 for A4 and B3, respectively.
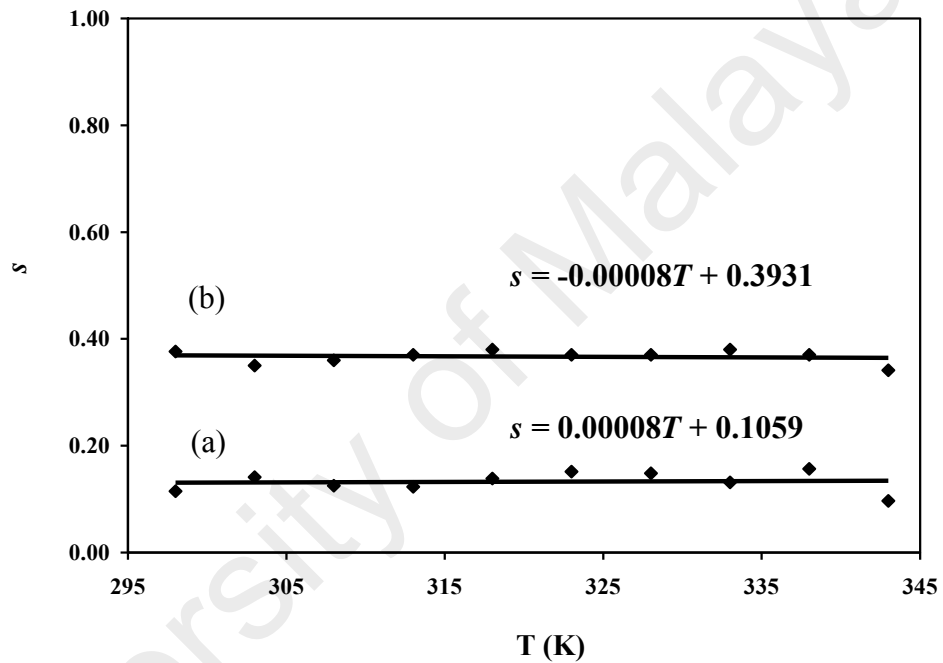
Figure 6.24: Plot *s* versus *T* for (a) A4 and (b) B3.

A few theoretical models have been developed to correlate the behavior of the conduction mechanism within a material with the temperature dependence of exponent *s*. In correlated behavior hopping (CBH), the exponent *s* is temperature dependent where the exponent $s \rightarrow 1$ as the $T \rightarrow 0$ K (Winie & Arof, 2004). In the overlapping large polaron tunneling (OLPT), the exponent s will decrease up to certain temperature before decreases back (Kufian, Majid, & Arof, 2007). When the exponent *s* increases with increasing temperature, the phenomena can be inferred as small polaron hopping (SPH)

(Samsudin & Isa, 2012). The final model is quantum mechanical tunneling (QMT). In QMT, the exponent or index *s* is independent of temperature. From the observations on the behavior of the index *s* with temperature, it can be inferred that QMT model is more applicable in explaining the conduction mechanism of the polymer electrolytes in both systems (Buraidah & Arof, 2011). According to Majid & Arof (2007), these ions are able to tunnel through the potential barrier that exists between two possible complexation sites. Psarras et al. (2003) has defined hopping as the displacement of a charge carrier from one site to another neighboring site and occurs not just by jumping over a potential barrier but can also be accompanied by mechanical tunneling.

6.10 Thermal Analysis

Thermal analysis has been used for many years as a suitable method to characterize the polymer materials. The thermal properties of polymer complexes give useful information regarding stability, stiffness and miscibility of the blends (Lewandowska, 2009; Mano, Koniarova, & Reis, 2003; Rao, Ashokan, & Shridhar, 2000). Thermogravimetric analysis (TGA) analysis has been analyzed to study the thermal stability and decomposition temperature of the polymers. For example, Bonilla et al. (2014) reported the decomposition of PVA-chitosan occurred at three stages, which is similar with the results reported by Lewandowska (2009). Differential scanning calorimetry (DSC) has been accepted by most researchers as the most suitable technique to study the miscibility, phase transition and thermal behavior of the blends. (Barbani et al., 2005; Liu et al., 2009) mentioned that glass transition temperature; T_g; which can be determined by DSC, is one of the critical properties for a polymer blend.

6.10.1 TGA Analysis

On the addition of NH$_4$I the decomposition temperature of pure starch/chitosan film has decreased as shown in Figure 6.25. During the heating process, the chains in polymer electrolyte are incapable to sustain its original form. This could be due to the interaction of the salt with polymer backbone as proven by FTIR and XRD characterizations. A2 and A4 samples start to decompose between 165 to 190˚C which is lower by ~60˚C of the unsalted polymer blending, PB2. A work by Noor, Majid, Arof, Djurado, Neto, & Pawlicka (2012) reported that during this degradation stage, the samples suffer the endothermic reactions of oxidation and hydrolysis followed by polysaccharide pyrolysis exothermic reactions. Moreover, salt is well-known as hygroscopic in nature (Liew et al., 2013).
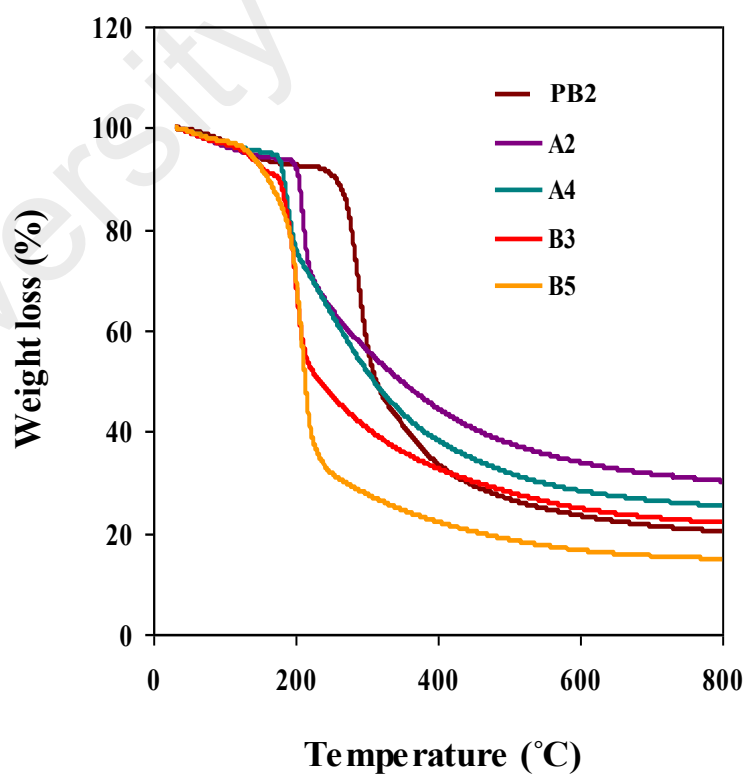
Figure 6.25: TGA thermograms of PB2, A2, A4, B3 and B5 films.

Hence, they declined in heat resistivity resulted from the disruption of strong hydrogen-bonding networks (Ramesh et al., 2012). However, the presence of NH$_4$I has lessened the total weight loss, which provides evidence that the thermal stability of pure starch/chitosan film has been improved. At 130-170˚C temperature range, the plasticized polymer electrolyte starts to decompose due to the degradation of glycerol (Ayala et al., 2012). The glycerol has softened the polymer backbone; enhance the flexibility by increasing the amorphous area, hence easy for disruption. The total weight loss corresponds to this stage is ~ 60% with final residue of ~ 20%. Nevertheless, it is still a promising candidate for battery application where its operating temperature is normally reported in the range of 30-80°C (Liew, Ong, Lim, Lim, Teoh, & Ramesh, 2013).

6.10.2 DSC Analysis

Segmental motions of polymer chain play a big role in ionic mobility as well as in conductivity (Woo, Majid, & Arof, 2013). Glass transition temperature or T_g is one of the important characteristics in determining the amorphousness of a material. The addition of salt has shifted the glass transition to lower T_g value, which indicates that the salt is able to break the intermolecular interaction and hydrogen bonding within the polymer molecules thus increased the segmental motion and became highly amorphous (Sudhakar & Selvakumar, 2013). Zeleznak & Hoseney (1987) also proposed that the T_g of a highly amorphous compound may occur below room temperature. A4 exhibits lower T_g compared to A2 as shown in Figures 6.26 and 6.27, proving the higher intermolecular motion in A4 which chosen to be plasticized with glycerol. Zeleznak & Hoseney (1987) reported that the T_g increases as the crystallinity increases due to more restriction of segmental motions which may lead to the formation of inter and intrachain

152
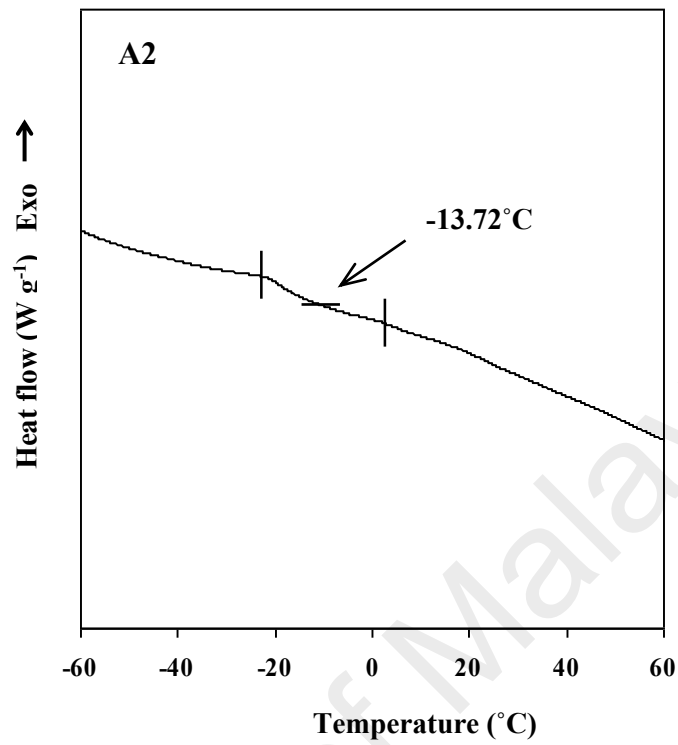
Figure 6.26: The DSC thermogram of glass transition temperature, T_g of A2.
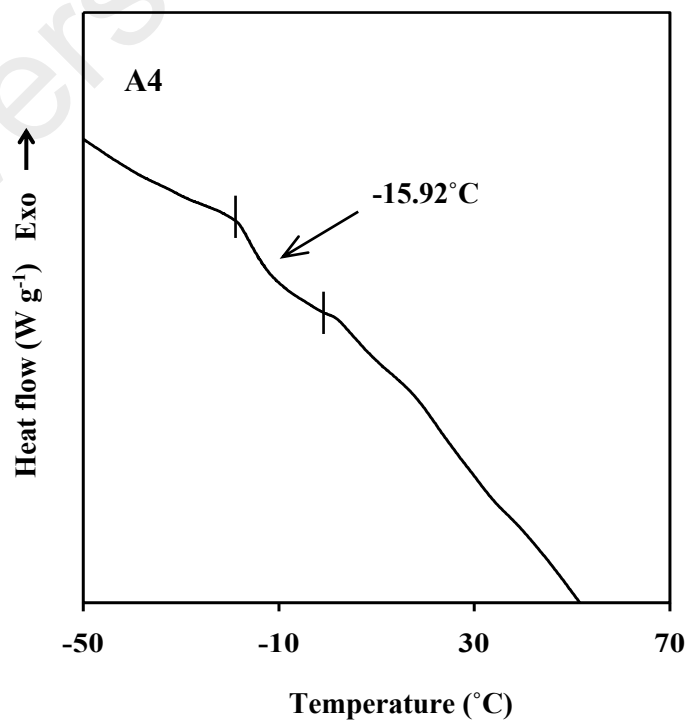
Figure 6.27: The DSC thermogram of glass transition temperature, T_g of A4.

hydrogen bonding. The crystalline areas act as physical crosslinks in the polymer network thus restrict the movement of the polymer molecules, hence lead to the decrement of conducitivity.

The addition of glycerol has further decreased the T_g as depicted in Figures 6.28 and 6.29 for sample B3 and B5, respectively. The plasticizer has suppressed the crystallinity of the polymer electrolyte by promoting the segmental motion of the polymer chains (Bergo et al., 2009; Liu et al., 2013; Sakurai et al., 2000). B3 exhibits the lowest T_g, which support the conductivity result.
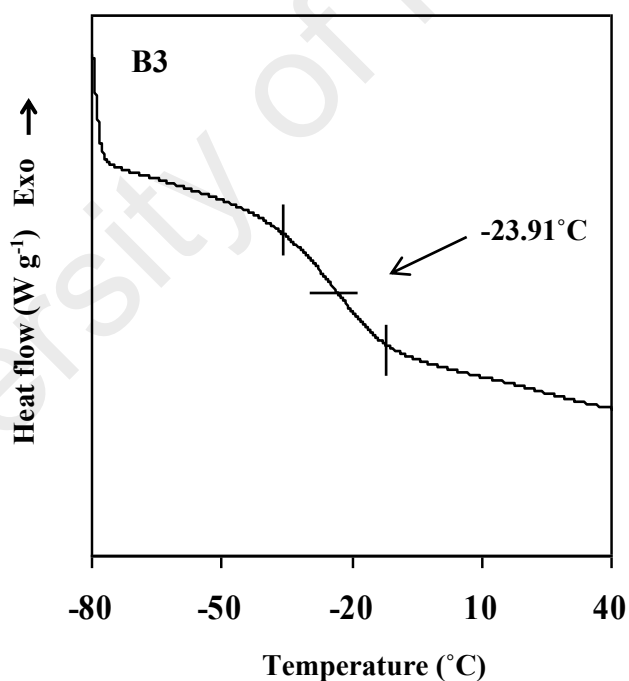
Figure 6.28: The DSC thermogram of glass transition temperature, T_g of B3.

The T_g value however is observed to increase as more than 30 wt.% of glycerol is added as shown in Figure 6.29 The existence of too much glycerol leading to ionic

crosslinks and formation of linkages among the glycerol molecules which may increase the rigidity of the sample (Noor, Majid, & Arof, 2013). This phenomenon resulted in conductivity decrement.
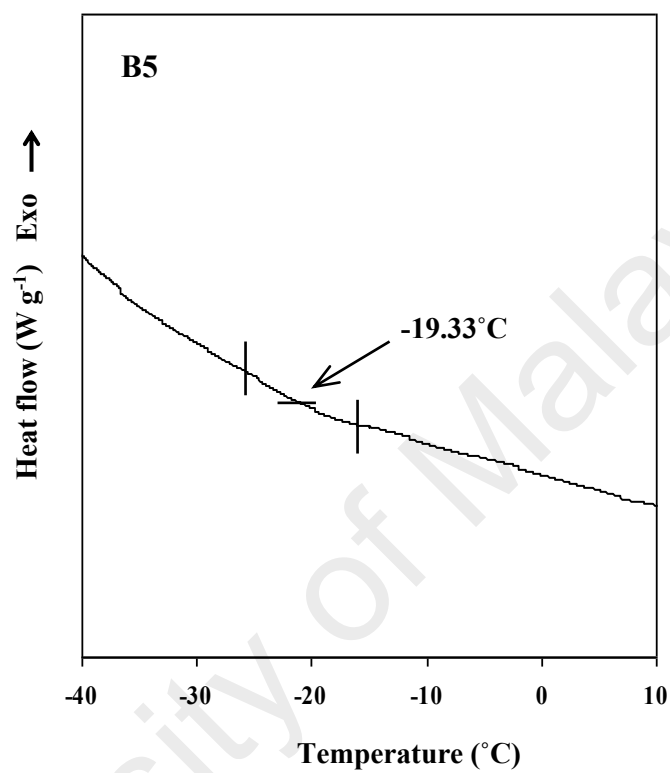
Figure 6.29: The DSC thermogram of glass transition temperature, T_g of B5.

6.11 Summary

The conductivity trend at room and high temperature for both salted and plasticized systems are presented in this chapter. The addition of 40 wt.% NH$_4$I (A4) in salted system leads to the highest conductivity of $(3.04 \pm 0.32) \times 10^{-4}$ S cm^{-1} with E_a value of 0.20 eV. Further conductivity enhancement has been determined by the addition of glycerol which leads to a maximum value of $(1.28 \pm 0.07) \times 10^{-3}$ S cm^{-1} with 30 wt.% of glycerol (B3). The lowest E_a obtained is 0.18 eV. All electrolytes in salted and plasticized systems follow Arrhenius rule since linear relationships are observed in the temperature dependence conductivity plots. The Rice and Roth model has been applied to investigate the variation of number density, n and mobility of the ions, μ. It is proven that the n and μ play an important roles in influencing the ionic conduction. Ionic transference number study has revealed that the charge transport in polymer electrolytes is dominated by the ions. The dielectric properties for both systems have also been presented in this chapter. The trend of ε_r and ε_i as well as M_r and M_i is in accordance with the conductivity trend. The variation of the t_{Mi} values demonstrates the sequence of the conductivity trend where a high conducting sample exhibits low t_{Mi}. The conduction mechanism represents A4 and B3 is QMT. TGA analysis indicates that the electrolyte can stand more than 150°C. DSC result has proved the homogeneity and miscibility of the blend among the components. The T_g values also verifies the conductivity trend.

CHAPTER 7: X-RAY DIFFRACTION (XRD) AND FIELD EMISSION SCANNING ELECTRON MICROSCOPY (FESEM) ANALYSES

7.1   Introduction

In this chapter, X-ray diffraction (XRD) and field emission scanning electron microscopy (FESEM) results are discussed for selected samples in salted; starch/chitosan-NH$_4$I and plasticized; starch/chitosan-NH$_4$I-glycerol systems. Based on the results in previous chapter, further characterizations have been carried out for the salted and plasticized systems to ensure that the electrolytes show compatibility for fabrication purposes and are promising to provide good performance. XRD analysis has been carried out to study the crystallinity of the samples containing different concentrations of NH$_4$I and glycerol. In conjunction with XRD study, FESEM analysis has been carried out to study the miscibility between the components in the polymer blend. Kadir et al. (2010) stated that micrographs analysis has given some answers to the decrement in conductivities in PVA-chitosan-NH$_4$NO$_3$-EC system. Alias et al. (2014) reported that the XRD and FESEM results showed changes due to the addition of salt and plasticizer with different concentrations in chitosan-NH$_4$CH$_3$COO-EC system. These studies give better understanding and support the FTIR and electrical impedance studies which have been discussed in Chapter 5 and 6, respectively.

7.2   XRD and FESEM Micrographs of Starch/chitosan-NH₄I System

The XRD patterns for the selected unplasticized samples are shown in Figure 7.1. It can be observed that A1, A2 and A4 diffractograms show amorphous nature without any obvious crystalline peaks. The addition of 60 wt.% NH₄I in A6 film is signified by the appearance of several sharp peaks which appear at $2\theta = 21.2°, 24.5°, 34.9°, 41.2°,$ 43.1°, 50.2°, 55.1°, 56.6°, 62.7° and 67.0°. The sharp peaks are attributed to NH₄I which are similar to those reported by Buraidah and Arof (2011). These peaks revealed that NH₄I is crystalline in nature (Hema et al., 2009; Jyothi, Kumar, & Murthy, 2014). For further confirmation of the XRD patterns due to the occurrence of overlapping patterns, the diffractograms were deconvoluted using Gaussion distribution. The areas under the deconvoluted peaks were used to calculate the degree of crystallinity using the same equation as Equation (4.1).

.

Figures 7.2 to 7.5 show the results of deconvolution pattern of PB2, A1, A2 and A4 films. All patterns reveal the existence of two distinct amorphous peaks which are originated from PB2. This observation proves that the amorphousness of pure blend is retained in the salted electrolytes. In amorphous region, rapid segmental motions due to flexible backbones of the polymeric chain increases the chance for the charge carriers to mobile which leads to higher ionic conductivity (Rajendran et al., 2001). Figure 7.2 shows that PB2 exhibits four crystalline peaks located at $2\theta = 14.2°, 16.9°, 23.9°$ and 27.9°.
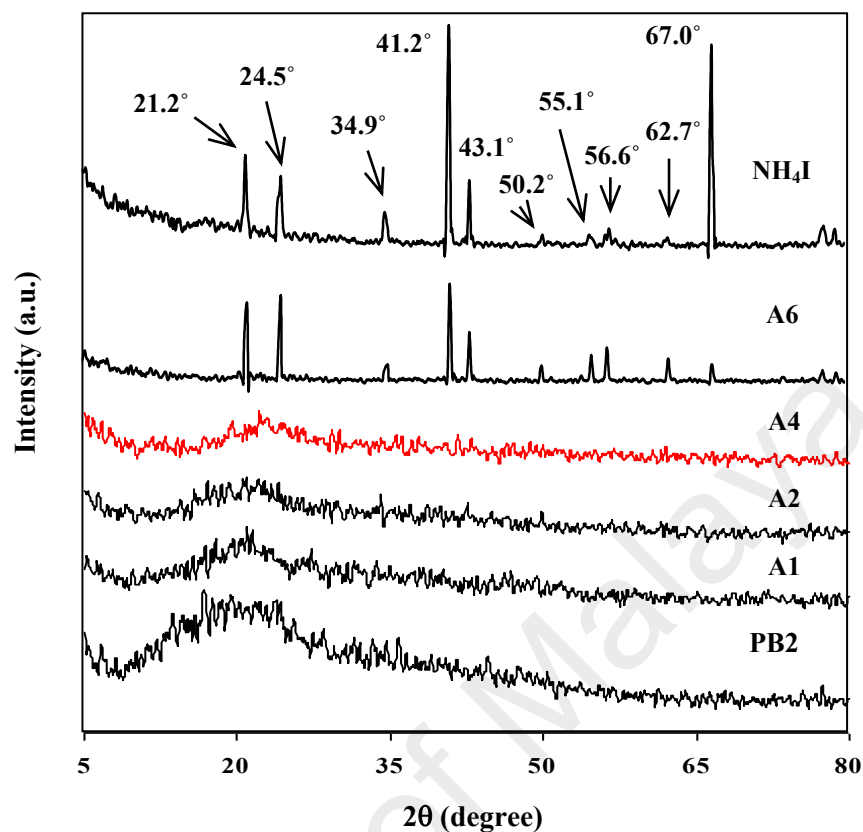
Figure 7.1: XRD patterns of selected samples in salted system.

In the XRD patterns of A1 in Figure 7.3, the crystalline peak attributed to NH_4I is situated at $2\theta = 21.0°$. The two peaks as depicted in the diffractogram of PB2 in Figure 7.2 disappear with the addition of NH_4I. A work by Bhide & Hariharan (2007) suggested that the diffraction peaks become broader and less intense with the addition of salt. However, another two crystalline peaks in PB2 at $2\theta = 23.9°$ and $27.9°$ can be observed in the XRD patterns of A1 with small shifts, which located at $2\theta = 23.1°$ and $26.7°$. This result proves that the polymer blend is interacted with the salt and still retained its behavior.
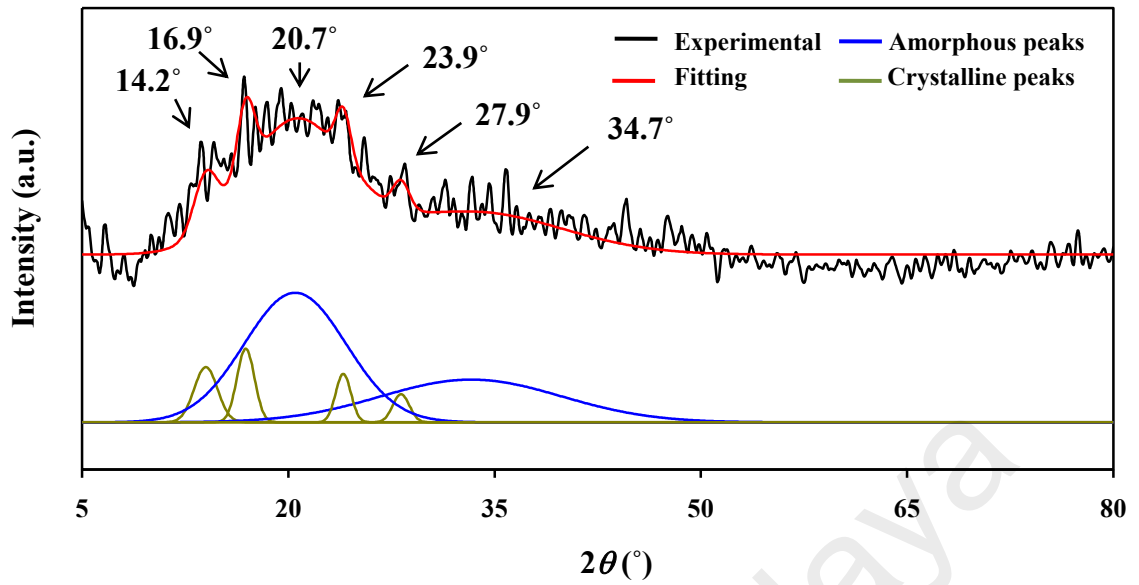
Figure 7.2: Deconvolution pattern of PB2.
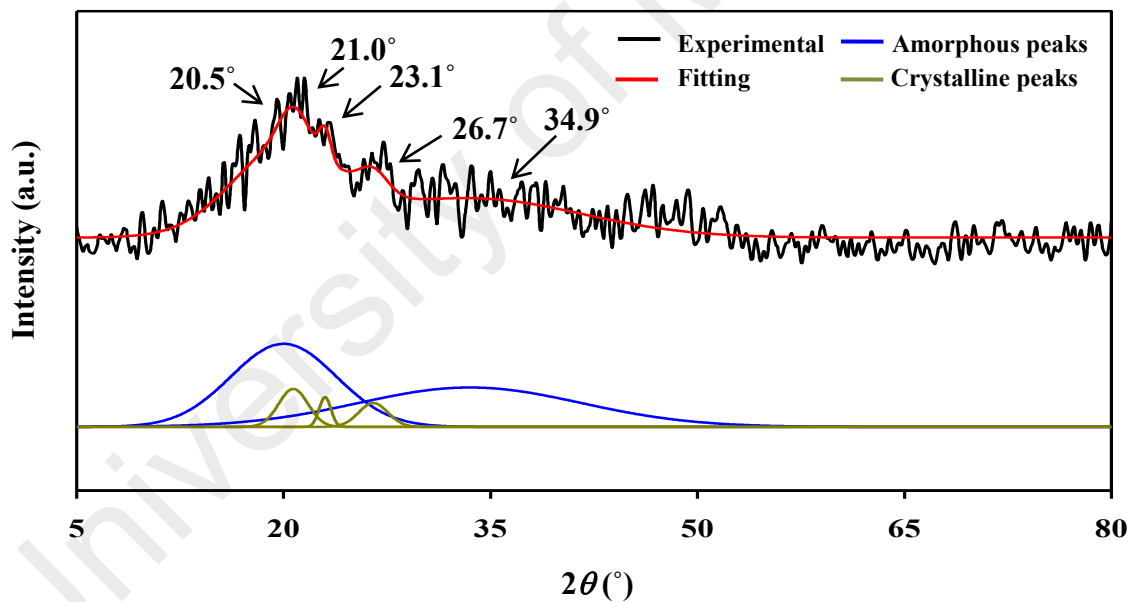
Figure 7.3: Deconvolution pattern of A1.

A2 shows almost similar diffraction pattern with A1 as can be seen in Figure 7.4. The crystalline peak which attributed to NH$_4$I is found at $2\theta = 20.7°$. The other two crystalline peaks originated from PB2 are further shifted and located at $2\theta = 22.4°$ and $25.9°$.
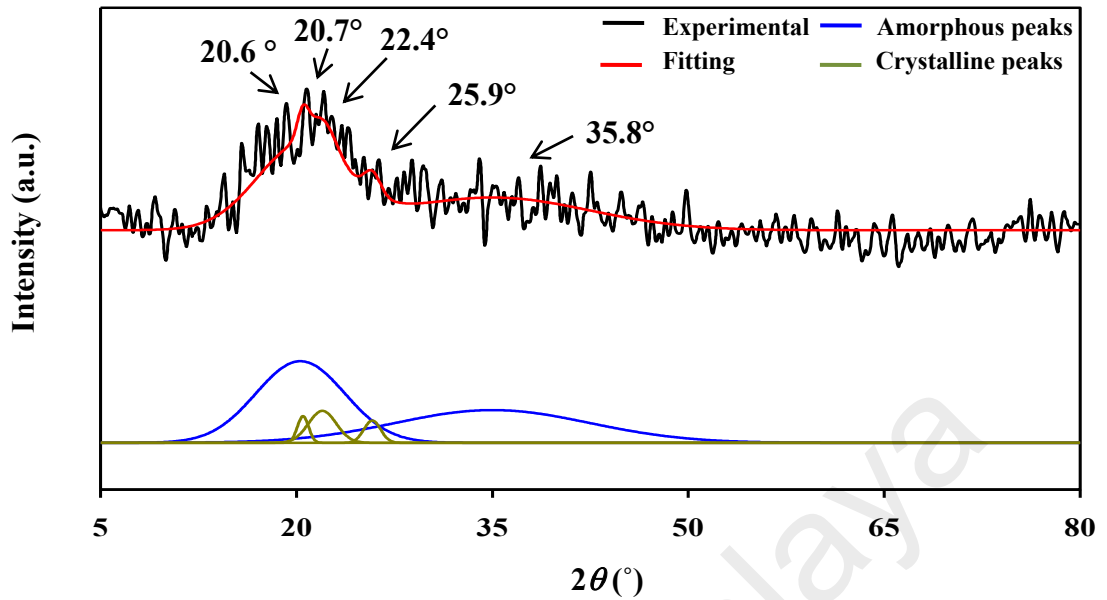
Figure 7.4: Deconvolution pattern of A2.

However, in A4 diffraction pattern as shown in Figure 7.5, only one peak from PB2 is observed at $2\theta = 22.6°$ while two new peaks have appeared at $2\theta = 19.7°$ and 24.7°, which suggests a good interaction between salt and polymer blend host (Noor et al., 2013). Hodge, Edward, & Simon (1996) reported that the addition of other molecules such as water and salt will attach to the hydroxyl groups on the macromolecules hence destroys the crystallinity by changing the configuration from crystalline to amorphous. The molecules will become free mobile ions and the hydrogen bonding is destructed or relocated. At this salt concentration, the highest conductivity in salted system has been achieved.
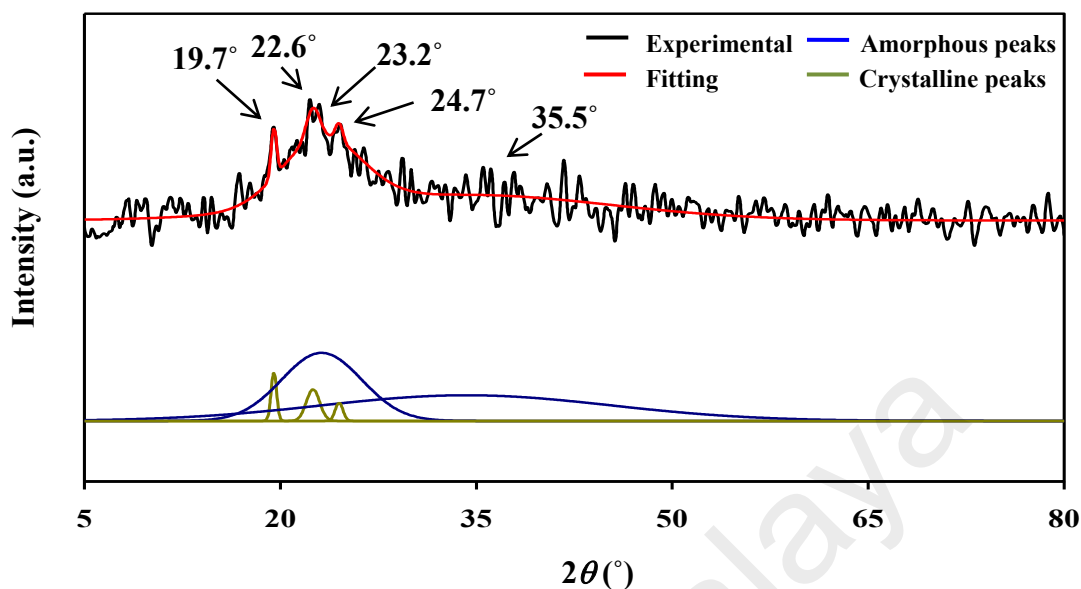
Figure 7.5: Deconvolution pattern of A4.

Table 7.1 lists the crystallinity values for selected electrolytes in the salted system. The changes in crystallinity can be used to interpret the conductivity behavior of the samples (Mohamad, Mohamed, Yahya, Othman, Ramesh, Alias, & Arof, 2003). A4 which has the highest conductivity value exhibits the lowest degree of crystallinity indicating that the conductivity increases as the amorphousness of the electrolyte is improved.

Table 7.1: Degree of crystallinity of selected samples in salted system.

Samples	Degree of crystallinity
PB2	15.30
A1	10.95
A2	10.24
A4	6.13

The electrolyte which contains more than 40 wt.% of NH$_4$I exhibits high intensity of crystalline peak as shown in Figure 7.1. It can be clearly seen that A6 is highly crystalline which is attributed to the recrystallization of NH$_4$I out of the film surface. At this concentration, there are too many ions where the ions become closer to each other. The polymer host is no longer able to accommodate the salt which leads to the recombination of the ions and resulted in conductivity decrement (Kadir et al., 2010).

Figures 7.6 to 7.9 show the FESEM micrographs at 1K × and 5K × magnifications of A1, A2, A4 and A5, respectively, in salted system. A1 and A2 show small particles with rough surfaces which attributed to the salt accommodated by the starch/chitosan blend. A4 has been detected as the most amorphous film in salted system according to the deconvolution of XRD diffractograms. From the micrographs as depicted in Figure 7.8, it can be clearly seen that A4 exhibits a porous structure compared to A1 and A2 in Figures 7.6 and 7.7, respectively. As mentioned in a report written by Xi et al. (2006), the ionic conductivity of an electrolyte is influenced by the porosity since the pore connectivity is important for the transportation of the charge carriers in the electrolyte. Thus, the conductivity increment on the addition of 40 wt.% salt in this work is affected by the porous structure of the electrolyte.
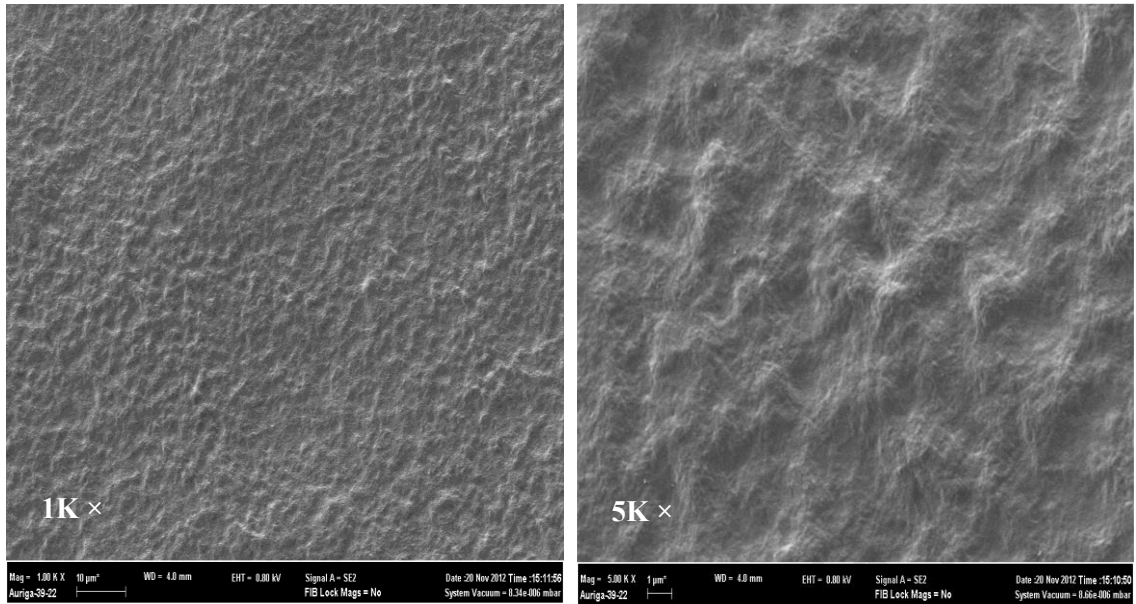
Figure 7.6: FESEM micrograph of A1.
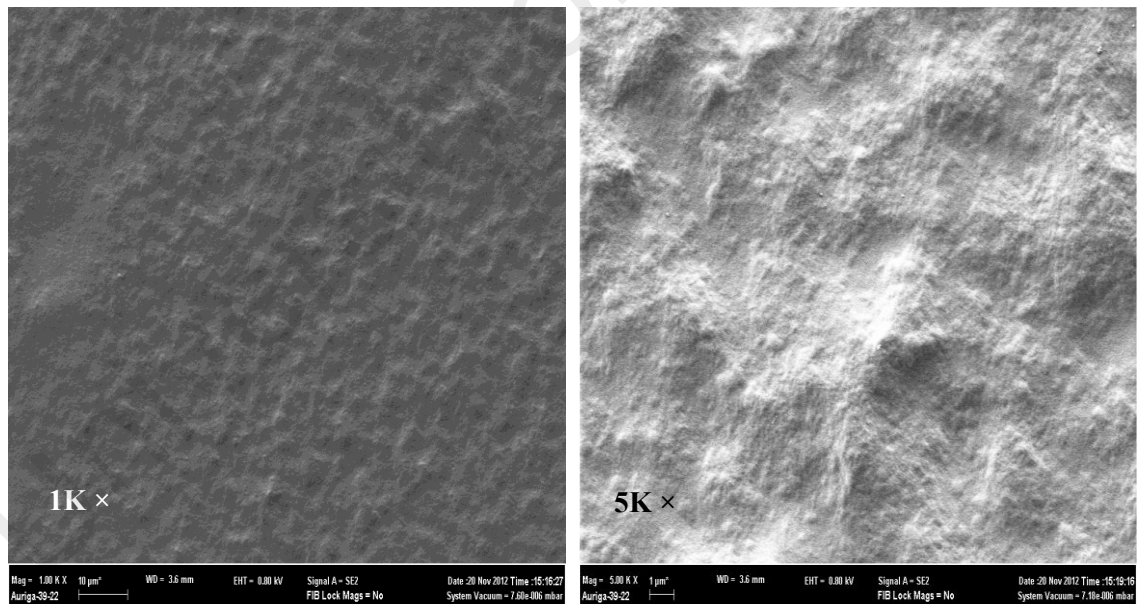
Figure 7.7: FESEM micrograph of A2.
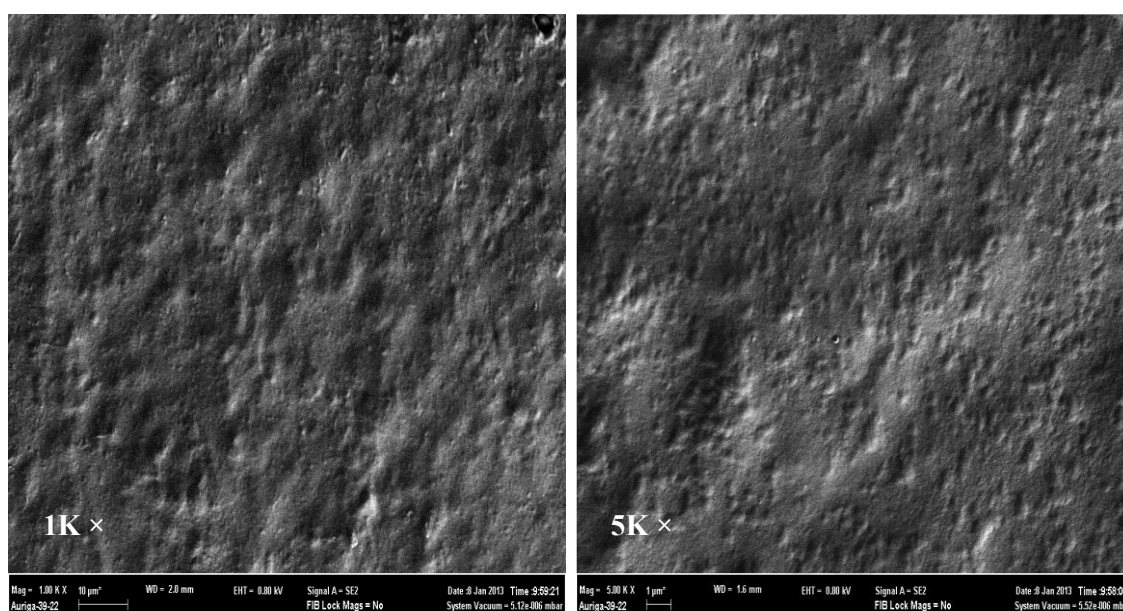
Figure 7.8: FESEM micrograph of A4.

When more than 40 wt.% salt was added, the morphology consists of solid particles that have suspended out of the surface, as shown in Figure 7.9 and 7.10 for A5 and A6, respectively. These solid particles are attributed to the recrystallization of the salt since the polymer host is unable to accommodate the salt, resulting in recombination of the ions. This phenomenon contributes to the loss of a significant amount of charge carriers, which leads to a decrease in conductivity (Kadir et al., 2010). Moreover, the result is in good agreement with XRD pattern which shows that the samples are highly crystallined when more than 40 wt.% NH4I is added. Thus, FESEM has helped to support and strengthen the conductivity studies in the present work.
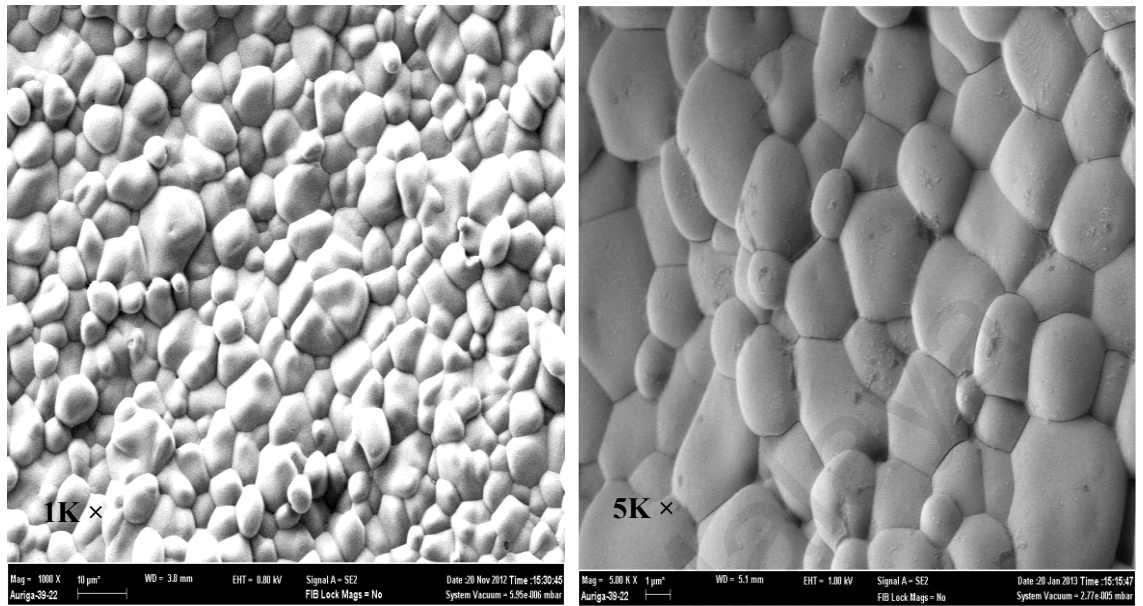
Figure 7.9: FESEM micrograph of A5.
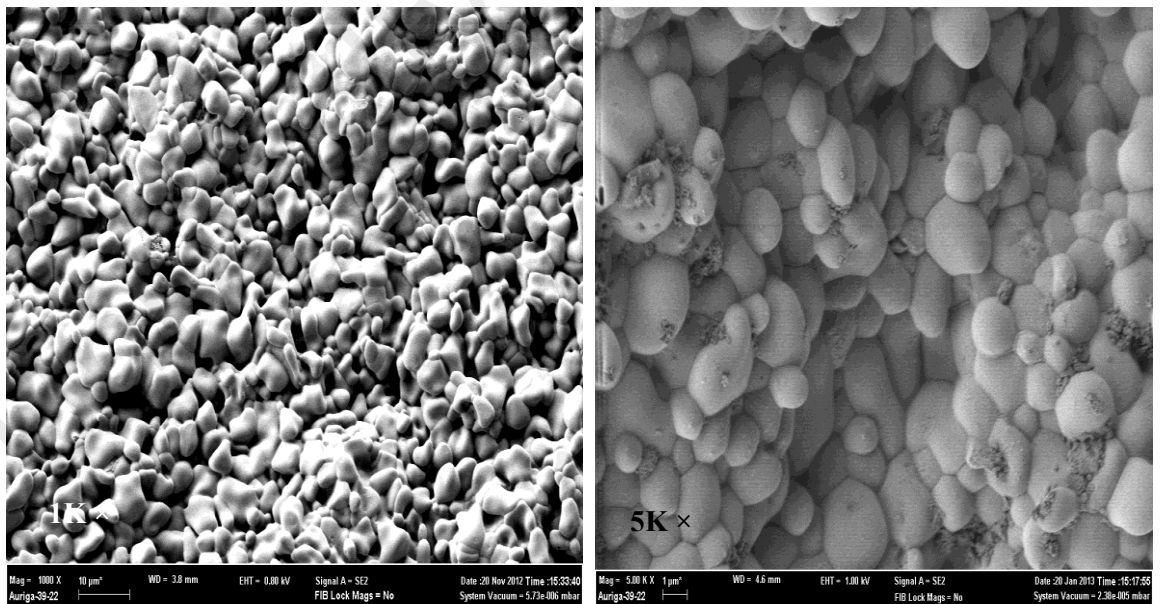
Figure 7.10: FESEM micrograph of A6.

7.3   XRD and FESEM Micrographs in Starch/chitosan-NH4I-Glycerol System

XRD analysis has also been carried out to study the crystallinity of the samples containing different concentrations of glycerol. The incorporation of glycerol is expected to reduce the crystalline phase of the salted electrolytes. The XRD patterns for selected plasticized samples are shown in Figure 7.11, where B3 exhibits the broadest peak. Further addition of glycerol beyond this optimized concentration increases the crystalline region of the sample. Thus, the changes in crystallinity can be used to interpret the conductivity behavior of the samples. For further confirmation of the XRD patterns due to the occurrence of overlapping patterns, the diffractograms are deconvoluted using the same method applied for salted system.
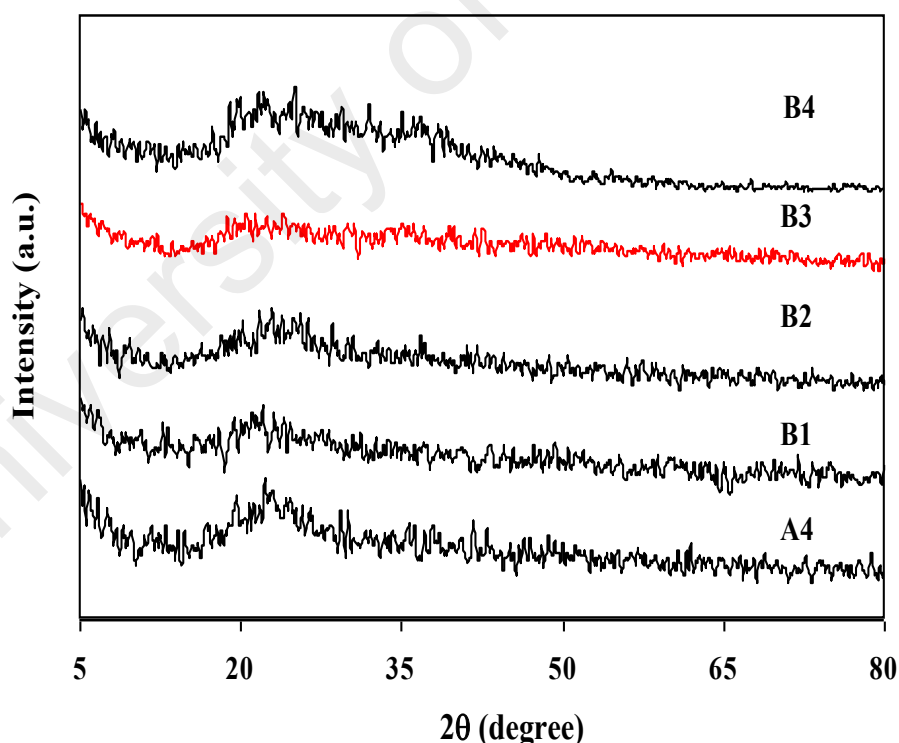
Figure 7.11: XRD patterns of selected samples in plasticized system.

The deconvolution patterns of B1, B2, B3 and B4 are shown in Figures 7.12 to 7.15, respectively. Three amorphous peaks are observed in all of the XRD patterns. This amorphous nature produces greater ionic diffusivity as well as higher ionic conductivity (Mohamad et al., 2003). Crystalline peaks which attributed to the salt have appeared at 2θ = 21.5°, 22.5°, 20.2° and 22.2° in B1, B2, B3 and B4 electrolytes, respectively. The existence of these crystalline peaks proves that the salt characteristic is retained in the plasticized electrolytes. As can be seen in Figure 7.12, a new peak appears at 2θ = 27.9° in B1 XRD pattern, which proves the interaction between the polymer blend, salt and glycerol.
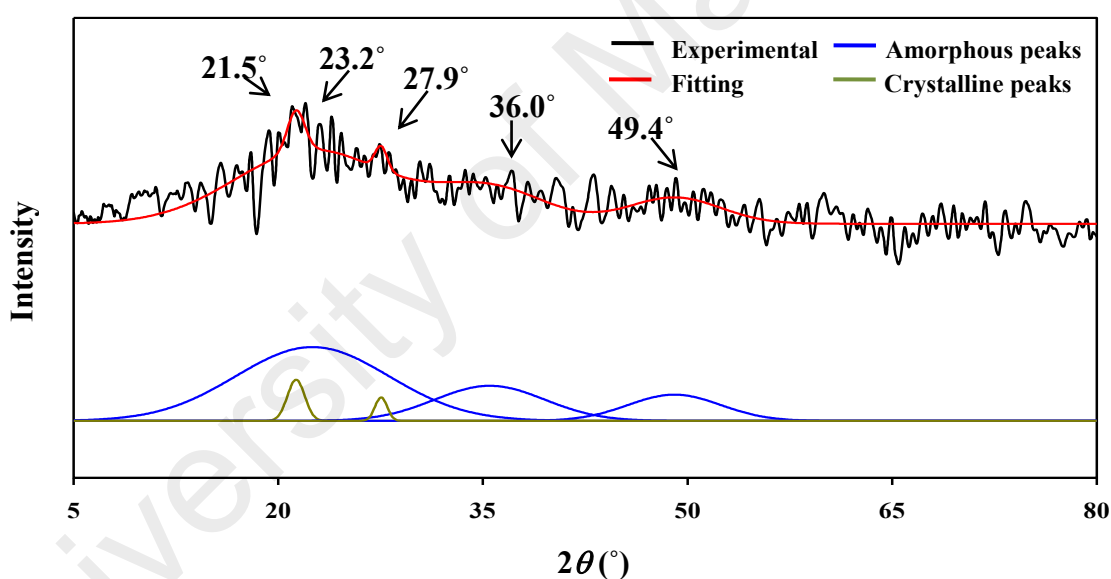
Figure 7.12: Deconvolution patterns of B1.

The appearance of a new peak at 2θ = 28.6° in B2 electrolyte as shown in Figure 7.13; is inferred as a good interaction between the components. However, the intensity of the new peak is found decreased in B3 as shown in Figure 7.14, inferring that the presence of 30 wt.% glycerol promotes the salt dissociation that turns the excess

salt to become ions, hence prevent the salt from being recrystallized. Moreover, the amorphous peak at $2\theta = 48.4°$ is found broader in B3 compared to other electrolytes. At this glycerol concentration, the highest conductivity in plasticized system has been achieved.
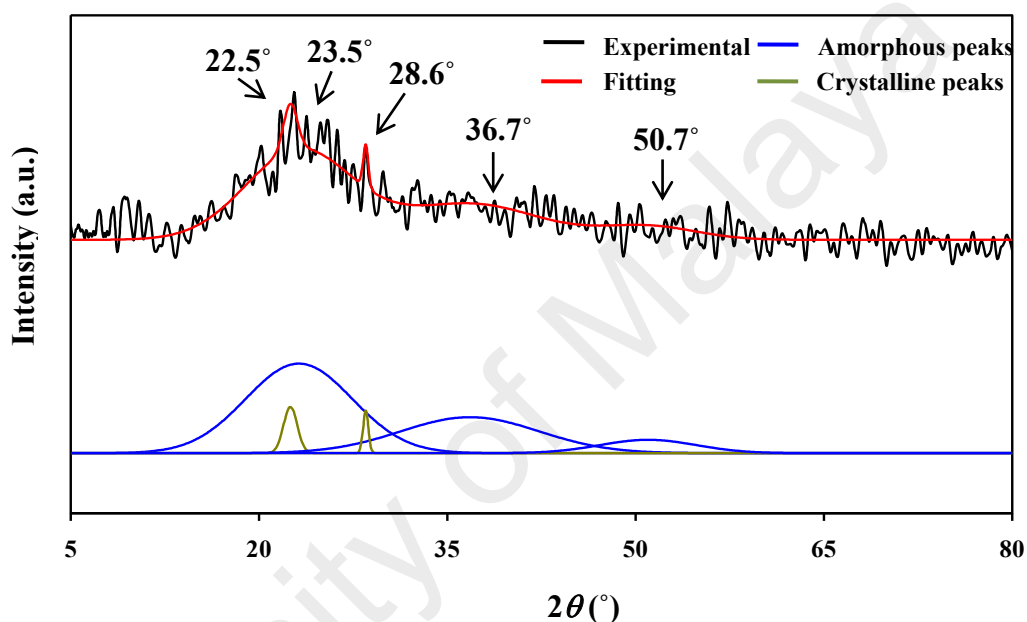
Figure 7.13: Deconvolution patterns of B2.

Further addition of glycerol beyond this optimized concentration increases the crystalline region of the sample. The appearance of new crystalline peaks at $2\theta = 19.8°$, 25.4° and 32.0° has increased the degree of crystallinity of the electrolyte. The conductivity of B4 starts to drop since there is too much glycerol content which leads to more interaction of the glycerol molecules among themselves.

169
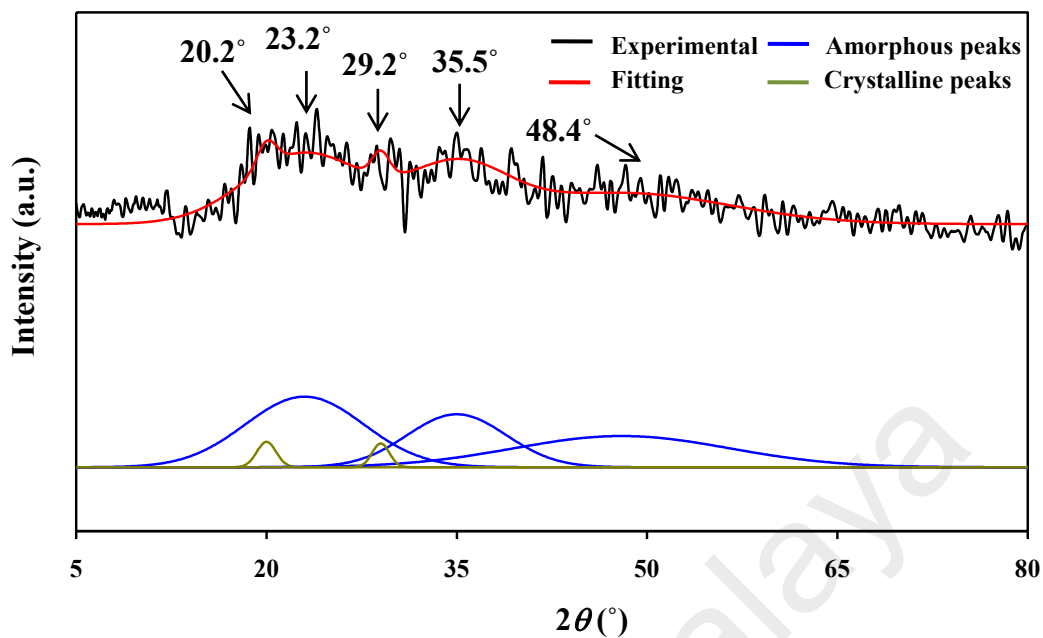
Figure 7.14: Deconvolution patterns of B3.
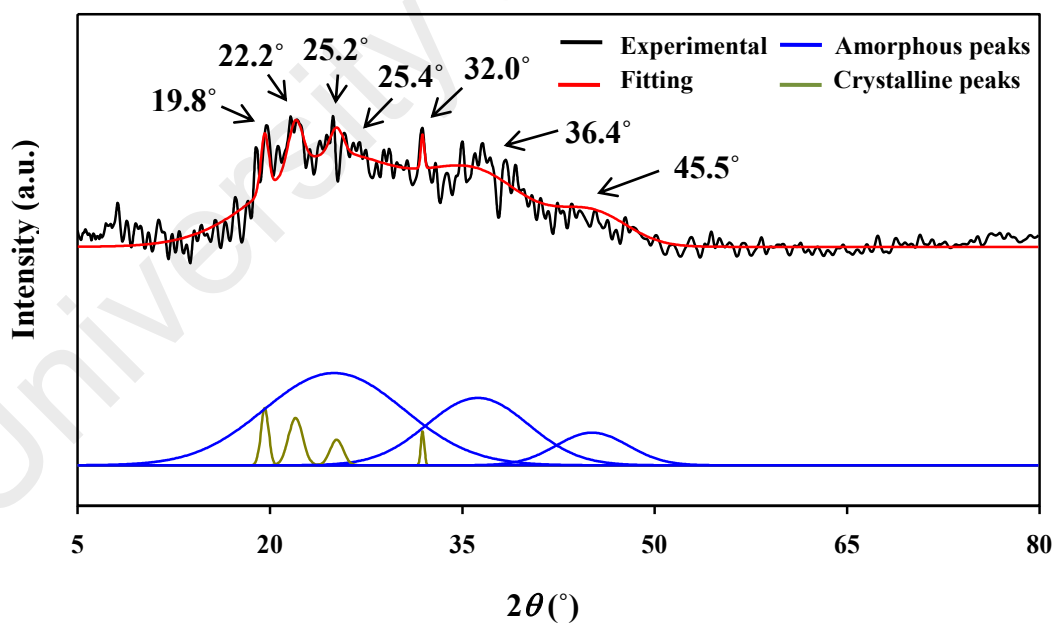
Figure 7.15: Deconvolution patterns of B4.

Table 7.2 lists the degree of crystallinity for electrolytes in plasticized system. Conductivity increases as the degree of crystallinity decreases. The decrease in the degree of crystallinity can be evidenced from the disappearance of several peaks in the films (Liu et al., 2013). In amorphous region, rapid segmental motions of polymeric chain increases the mobility of charge carriers, which leads to higher ionic conductivity (Rajendran, Kannan, & Mahendran, 2001). A work by Liu et al. (2013) also reported that the crystallinity of starch/chitosan films was decreased with the increasing amount of glycerol up to 10% (w/w), which leads to conductivity increment.

Table 7.2: Degree of crystallinity of selected electrolytes in plasticized system.

Samples	Degree of Crystallinity
B1	5.38
B2	5.21
B3	4.25
B4	6.00

Figures 7.16 to 7.19 show the micrographs of starch/chitosan samples with 40 wt.% NH$_4$I at different glycerol concentrations. From these micrographs, it can be seen that glycerol has prevented the salt from recrystallizing out of the membrane and assists the salt dissociation hence leading to an increase in number density of mobile ions (Kadir et al., 2010). As depicted in Figure 7.16, the addition of 10 wt.% of glycerol in B1 has transformed the surface to become clear and smoother which is influenced by the existence of plasticizer.

171
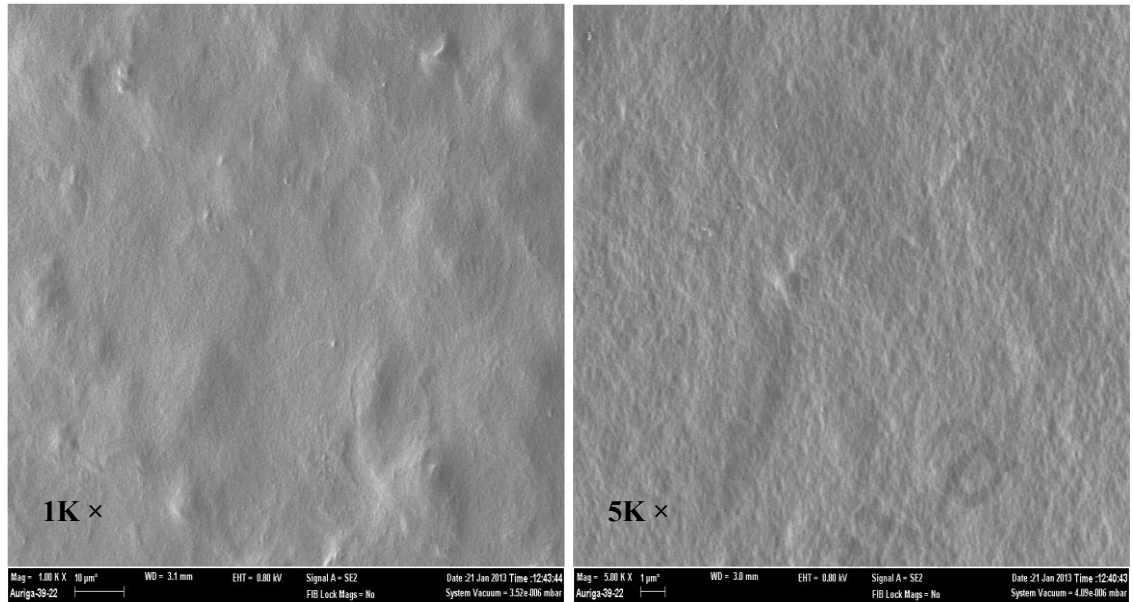
Figure 7.16: FESEM micrograph of B1.

Figure 7.17 shows that the morphology consists of grains which are uniformly dispersed on the surface with the addition of 20 wt.% glycerol in B2. The addition of 30 wt.% glycerol in B3 shows the presence of indistinct spherulites with some boundaries separating a few regions as can be seen in Figure 7.18. This result proves a decrease in crystallinity of the electrolytes where the highest ionic conductivity is attained (Pradhan, Choudhary, & Samantaray, 2008; Ravi, Song, Gu, Tang, & Zhang, 2015).
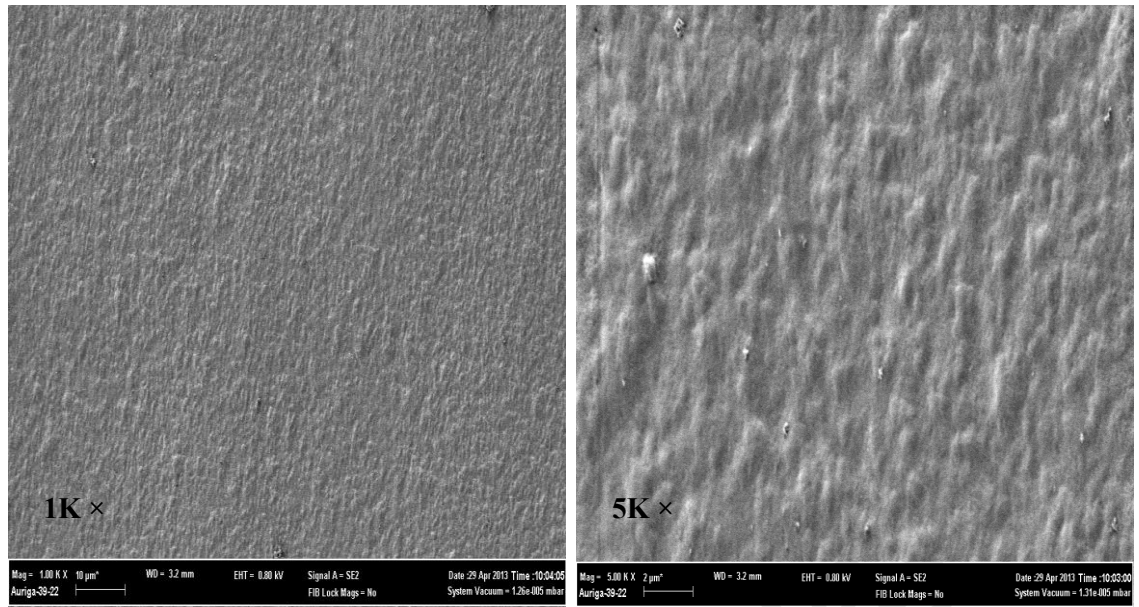
Figure 7.17: FESEM micrograph of B2.
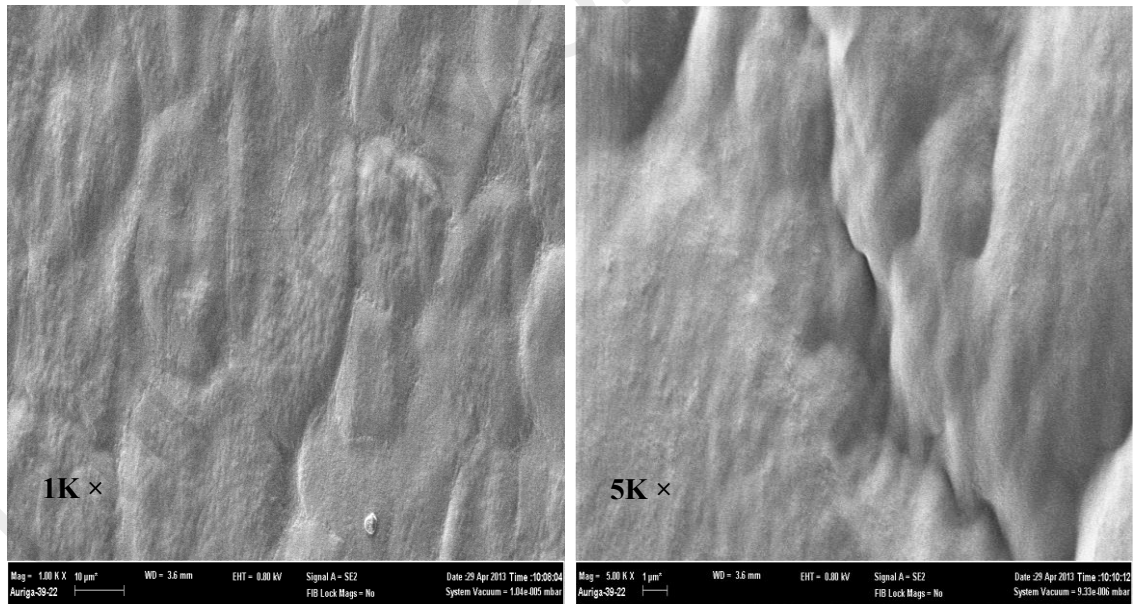
Figure 7.18: FESEM micrograph of B3.

With further addition of glycerol up to 40 wt.% as shown in Figure 7.19, the film becomes denser as the spherulites reappeared. This allows the formation of microcrystalline junctions and promotes recrystallization of salt resulting in the decrement of conductivity, which consistent with XRD results as discussed in previous section.
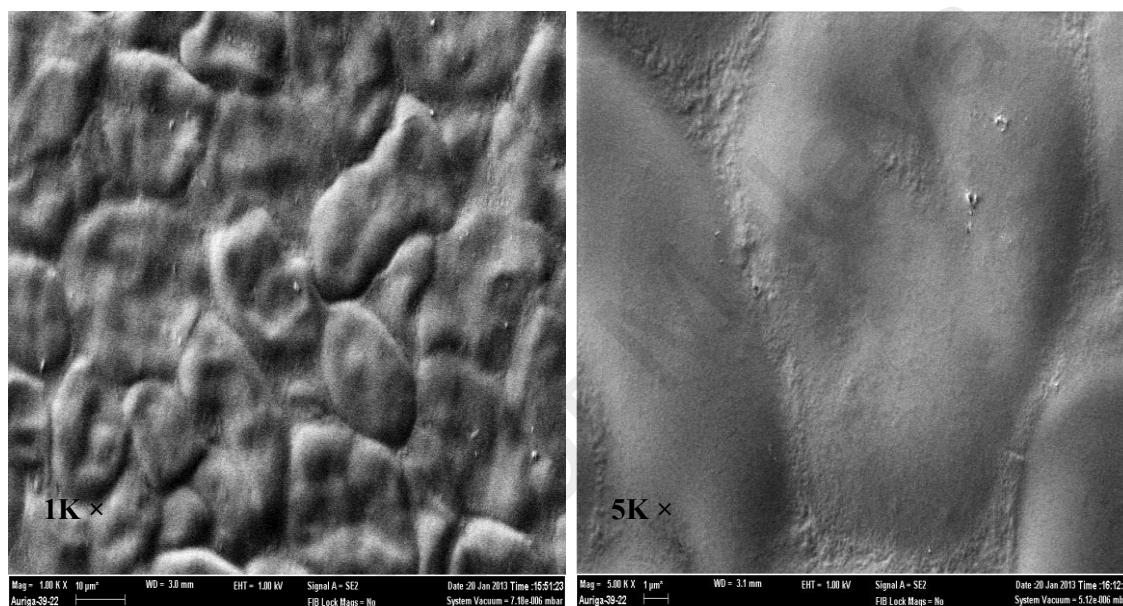
Figure 7.19: FESEM micrograph of B4.

7.4   Summary

From XRD and FESEM analysis of electrolytes in salted and plasticized systems, it can be seen that pure polymer blend becomes more amorphous with the addition of NH_4I, followed by plasticization with glycerol. Deconvolution plays a big role in studying the crystallinity and structural changes due to overlapping in the XRD patterns. A4 which gives the highest conductivity in salted system has the most amorphous and porous structure with low crystallinity value. Due to the lowest degree of crystallinity and smooth surface based on XRD and FESEM results, respectively, B3 gives the highest conductivity and satisfies its impedance spectroscopy results. This electrolyte was used in the fabrication of electrochemical devices in this work.

CHAPTER 8: CHARACTERIZATIONS AND FABRICATION OF ELECTROCHEMICAL DEVICES

8.1   Introduction

The properties of starch/chitosan-NH$_4$I have been analyzed and discussed in the previous chapters. In this chapter, the highest conducting electrolyte in the plasticized system has been used for the fabrication of the EDLC and proton batteries. B3 attains the conductivity value of $(1.28 \pm 0.07) \times 10^{-3}$ S cm^{-1} and the characterization results exhibit good characteristics for electrochemical devices application purposes. Electrochemical device based on hydrogen ion; H$^+$; have the potential to perform as other types of devices including solar cell, nickel and lithium batteries.

8.2   Electrochemical Stability of Electrolyte

Determination of the electrochemical stability window in order to evaluate the feasibility of these materials as well as the ability of the electrolytes to endure the operating voltage is found important to study prior to applications in electrochemical devices (Ng & Mohamad, 2008). The working voltage range is tested using LSV and the corresponding voltammogram is presented in Figure 8.1. The voltage applied for this study was in the range of 0 to 2.5 V at sweep rate 1 mV s^{-1}. From the LSV voltammogram, it is observed that the decomposition voltage of the polymer electrolyte is around 1.90 V. This potential window range is sufficient from the EDLC application point of view since the standard electrochemical window for energy devices is ~1 V (Pratap, Singh, & Chandra, 2006). Other researchers also reported the same range of the decomposition voltage for their polymer electrolytes. For example, Shukur et al. (2013)

reported that the voltage breakdown for the chitosan-PEO-NH_4NO_3-EC electrolyte is 1.75 V. Kadir et al., (2010) reported that the voltage breakdown for PVA-chitosan-NH_4NO_3-EC is ~1.70 V.
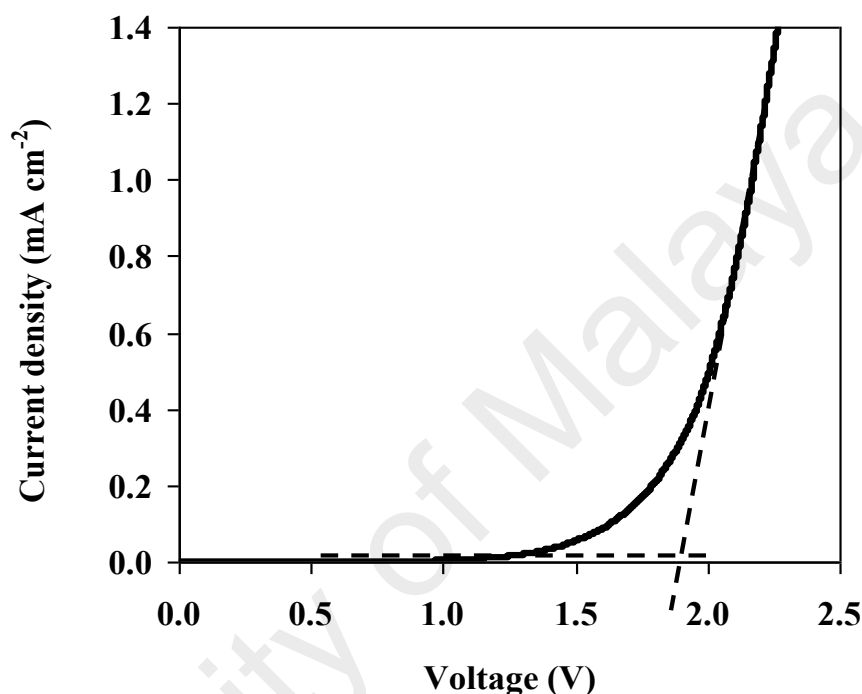
Figure 8.1: Linear sweep voltammetry curve for B3 at 1 mV s⁻¹.

8.3   Primary Proton Battery

The open circuit potential (OCP) characteristic of the fabricated battery was measured at room temperature using B3 for 24 hours and is shown in Figure 8.2. Both primary and secondary batteries employ the same anodes and cathodes materials, hence the occurrence of reactions are the same in both type of batteries. It can be seen that the cell potential is initially higher for a few hours before stabilized at (1.31 ± 0.03) V. This phenomenon could be due to the oxidation of anode (Samsudin et al., 2014). Based on

the result, it can be concluded that the battery is practically stable in an open circuit condition. All possible reactions that take place at anode and cathode are listed from Equation 8.1 to 8.4 (Alias et al., 2014; Shukur & Kadir 2015b). At cathode, MnO_2 is reduced by accepting two electrons. At the anode, two electrons are released to the outer circuit thus the Zn is oxidized, while $ZnSO_4 \cdot 7H_2O$ provides the H^+ ions. Other researchers also reported similar reactions (Alias et al., 2014; Samsudin et al., 2014; Shukur & Kadir, 2015b).
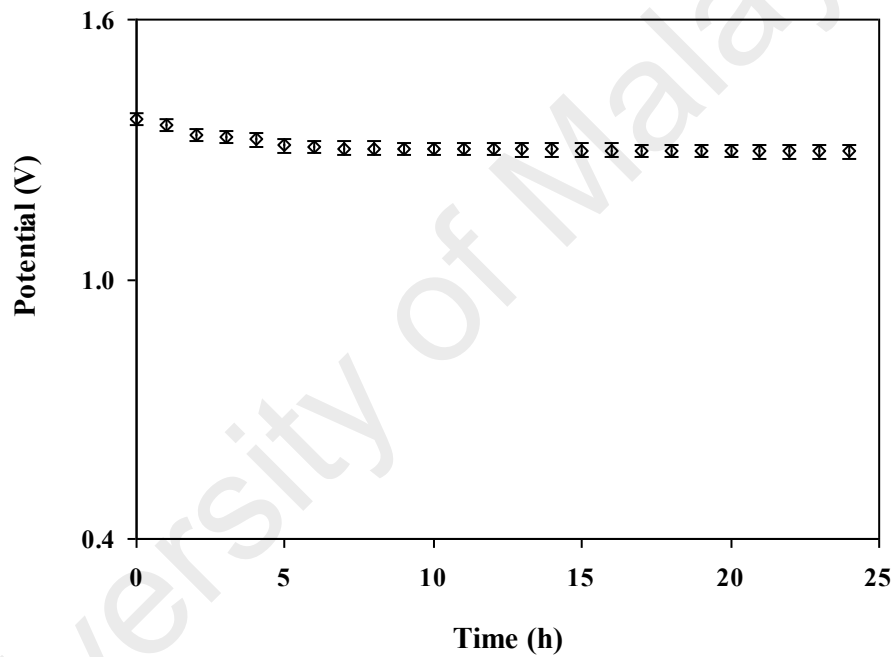
Figure 8.2: OCP of proton battery for 24 hrs.

Anode: $$Zn \longrightarrow Zn^{2+} + 2e^-$$ $E° = 0.76$ V (8.1)

$$ZnSO_4 \cdot 7H_2O \longrightarrow 7H^+ + 7OH^- + ZnSO_4$$ $E° = -0.82$ V (8.2)

Cathode: $$MnO_2 + 2e + 4H^+ \longrightarrow Mn^{2+} + 2H_2O$$ $E° = 1.22$ V (8.3)

Overall: $$Zn + ZnSO_4 \cdot 7H_2O + MnO_2 + 2e + 4H^+ \longrightarrow Zn^{2+} + 2e^- + 7H^+ + 7OH^- + ZnSO_4 + Mn^{2+} + 2H_2O$$ $E° = 1.28$ V (8.4)
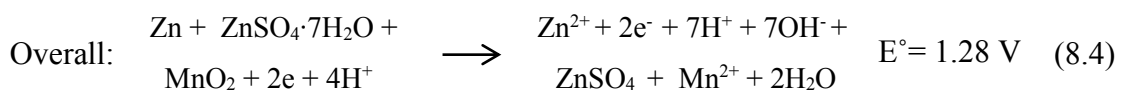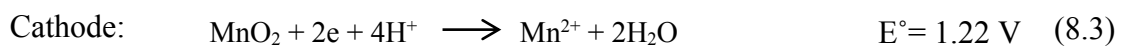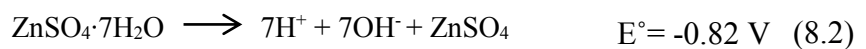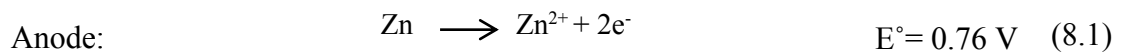
There are few factors that may affect the difference between the theoretical and experimental result of OCP, including the concentration and transportation of ions within the electrolyte (Samsudin et al., 2014). In theory, the overall reaction of the proton battery should provide the potential of 1.28 V. Result of OCP shows that the potential of the proton battery in this work is 1.31 V, which is higher than the expected proton battery potential. This suggests that the fabricated proton battery is practically stable in an open cell condition (Jamaludin & Mohamad, 2010; Samsudin et al., 2014). Deraman et al. (2013) reported that the OCP of electrolyte; polyvinyl chloride (PVC) with ammonium trifluoromethane sulfonate ($NH_4CF_3SO_3$) and ionic liquid, butyltrimethyl ammonium bis (trifluoromethyl sulfonyl) imide (BATS) as plasticizer; remained constant at ~ 1.30 V for 24 h. Samsudin et al. (2014) reported that their batteries based on carboxymethyl cellulose-NH_4Br; resulted on an OCP of 1.36 V for 24 h. Table 8.1 exhibits the comparison of OCP value in the present work with other works which employ the same anode and cathode active materials.

Figure 8.3 depicts the discharge profiles of the proton batteries at different constant currents. As the current increases, the plateau region shortens. It can be observed that the voltage reaches its flat plateau at ~ 1.10 V for a few hours before it dropped significantly. A plateau region is the region where the proton battery potential reaches a flat discharge rate (Samsudin et al., 2014). At 0.10 mA, the proton battery reaches its plateau discharge and lasted for around 70 hours before the voltage dropped immediately. The difference can be seen when the battery was discharged at 2.00 mA, the plateau region was lasted after 45 minutes. The oxidation of Zn and reduction of MnO_2 has formed secondary product; Mn_2O_3-ZnO which is a semiconductor particle (Rahman, Gruner, Al-Ghamdi, Daous,Khan, & Asiri, 2013). This formation is the

Table 8.1: Comparison of OCP value in the present work with other reports.

Electrolytes	OCP (V)	Time (h)	References
PVP-sulfamic acid (SA)-PEG	~1.36	Not stated	Bella, Hirankumar, & Devaraj, 2014
PVC-NH$_4$CF$_3$SO$_3$-BATS	~1.30	24	Deraman et al., 2013
Carboxymethyl cellulose-NH$_4$Br	1.36	24	Samsudin et al., 2014
Starch/chitosan-NH$_4$I-glycerol	1.31	24	Present work

reason of potential decrement at ~ 1.10 V due to increment of the charge transfer resistance (Wang et al., 2005). Using the value of the discharge time at plateau region ($t_{plateau}$) and i which is the constant current, the discharge capacity (Q) was calculated using the following equation:

$$Q = it_{plateau}$$

(8.5)

Table 8.2 shows the discharge capacity of primary proton batteries at different constant currents. The discharge capacity shows an increment as the discharge current decreases. A faster reaction is required at higher discharge current. However, the charge and proton transfer cannot attain the required speed (Wang et al., 2005). In addition, the ion concentration varies along the pores depth thus leading to a more non-uniform H$^+$ insertion process (Roscher, Bohlen, & Vetter, 2011). Samsudin et al. (2014) reported
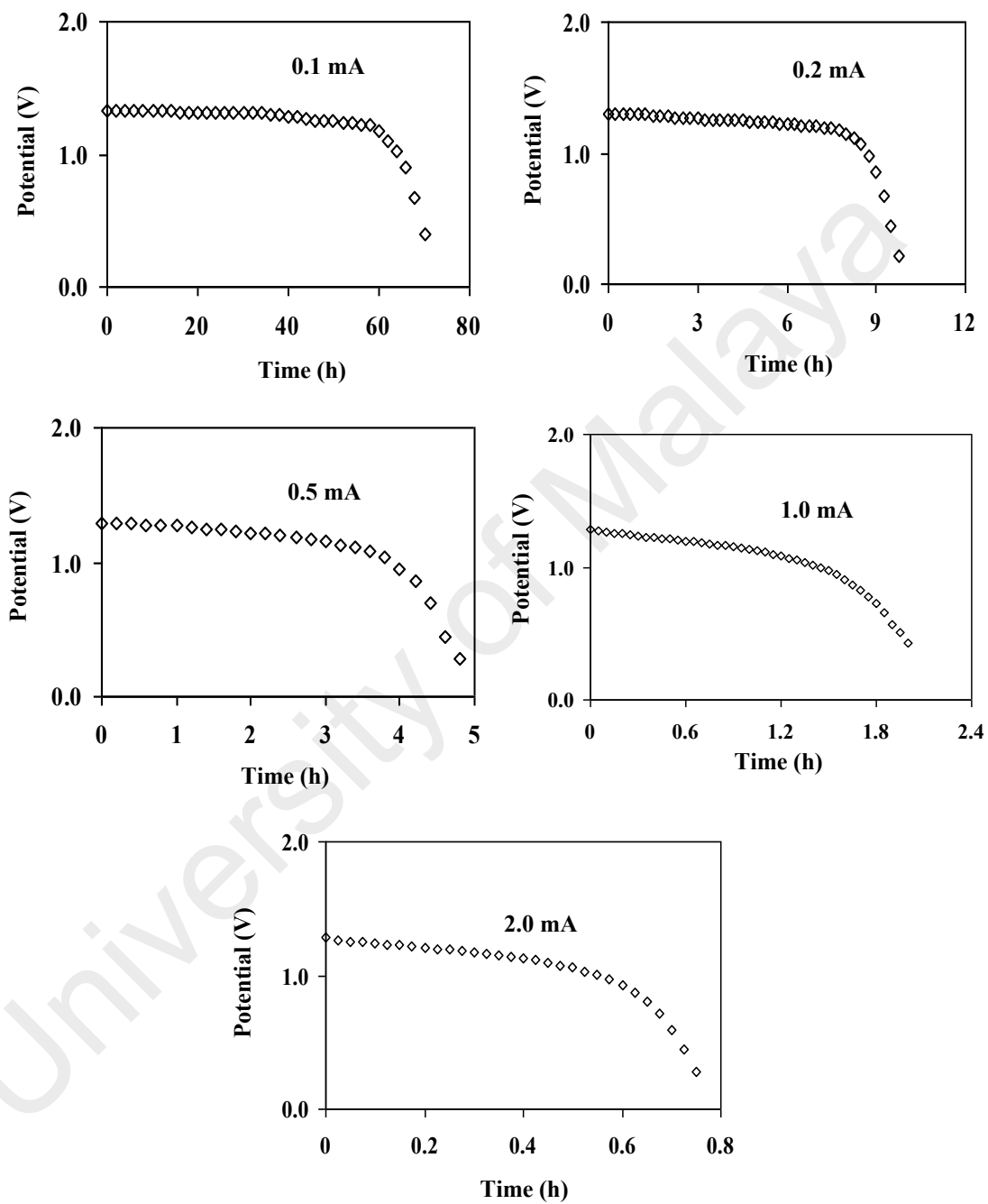
Figure 8.3: Discharge profiles of primary proton batteries at different constant currents.

Table 8.2: Discharge capacity of the primary proton batteries at different constant currents.

Discharge current (mA)	Q (mA h)
2.00	1.10
1.00	1.50
0.50	1.70
0.20	1.75
0.10	6.00

that at 0.50 mA, the battery lasted less than 2 hours which could be attributed to the low diffusion rate of H^+ ions and the ability of the cell to deliver its electrical energy. From the literature, the Q value obtained in this work is found comparable with other reports as presented in Table 8.3.

The *I-V* and *J-P* characteristics for the primary proton batteries are presented in Figure 8.4. The ohmic contributions which dominated the electrode polarization give a linear type of *I-V* plot as shown in the figure. The *I-V* plot is represented by the equation:

$$V = V_0 - Ir \tag{8.6}$$

where V_0 is the OCP and r is the internal resistance which is calculated from the gradient of the plot.

Table 8.3: Comparison of discharge capacity (Q) value in the present work with other reports at different constant discharge currents.

Discharge current (mA)	Discharge capacity, Q (mA h)			
	Starch/chitosan-NH₄I-glycerol (present work)	Carboxymethyl cellulose-NH₄Br (Samsudin et al., 2014)	Chitosan-NH₄NO₃-EC (Ng & Mohamad, 2006)	Starch/chitosan-NH₄Cl-glycerol (Shukur & Kadir, 2015)
0.10	6.00	3.73	-	9.36
0.20	1.75	-	-	-
0.25	-	2.70	-	4.57
0.40	-	-	-	1.37
0.50	1.70	0.35	-	-
0.60	-	-	-	1.04
1.00	1.50	-	17	-
2.00	1.10	-	-	-

Figure 8.4: Plot of *I-V* and *J-P* of primary proton batteries.

The value of the internal resistance is found to be 62.30 Ω which could be attributed to the oxidation of the electrodes. From the *J-P* plot, it can be observed that the maximum power density is (4.00 ± 0.06) mW cm^{-2} while the short circuit current of the batteries is 17.70 mA. This power density value is higher than those reported by Jamaludin et al. (2010) and Alias et al. (2014).

8.4   Secondary Proton Battery

Stabilizing and maintaining the H$^+$ supply in anode is crucial in order to obtain a rechargeable battery hence good and suitable reversible cathodic/anodic half-cell reactions are required (Pandey, Lakshmi, & Chandra, 1998). The highest conducting electrolyte solution (B3) has been added as one of the components in cathode which is believed may assist the intercalation and deintercalation of proton in the cathode active materials. The proton is then entering the anode through the electrolyte during the battery is recharging (Kadir et al., 2010). Figure 8.5 depicts the charge-discharge profiles of secondary or rechargeable proton battery using a constant current of 0.40 mA. The cycle starts with the discharging of the battery to 1.00 V before regain its potential up to 1.33 V after been recharged. The charge-discharge process cycled for 60 times and lasted for about ~80 hours.

The specific discharge capacities (Q_S) have been calculated with respect to the weight of active cathode material (MnO$_2$) and plotted as shown in Figure 8.6. The Q_s value is found to decrease from 3.17 mAh g^{-1} to 1.36 mAh g^{-1} at the 2nd cycle. This phenomenon is attributed to the imperfection of the electrode-electrolyte contact at the beginning of the battery cycle (Mohamad et al., 2003). The Q_s value is then increases during the 3rd and the 4th cycle and reached 3.06 mA h g^{-1}. This shows an improvement
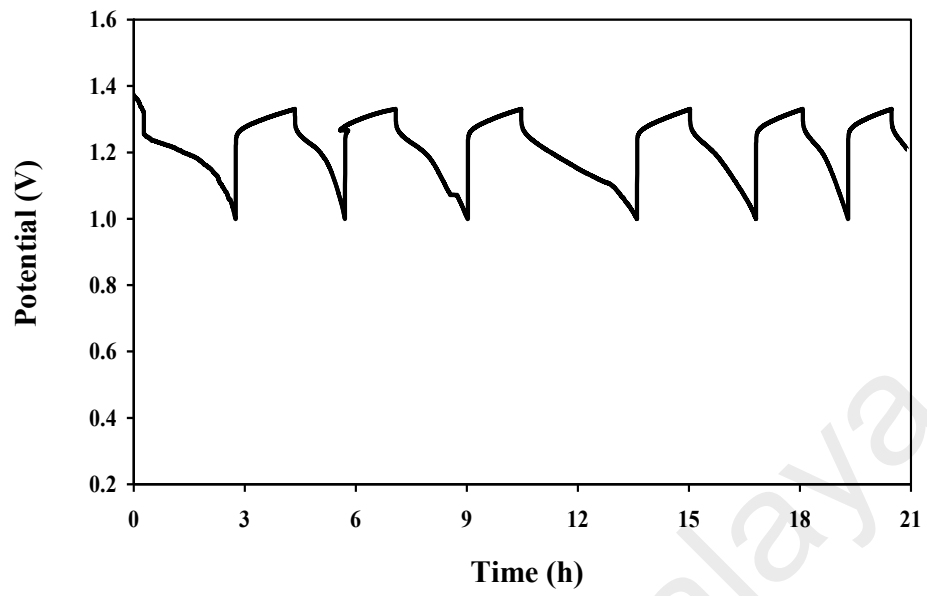
Figure 8.5: Charge-discharge profiles of the secondary proton battery**.**
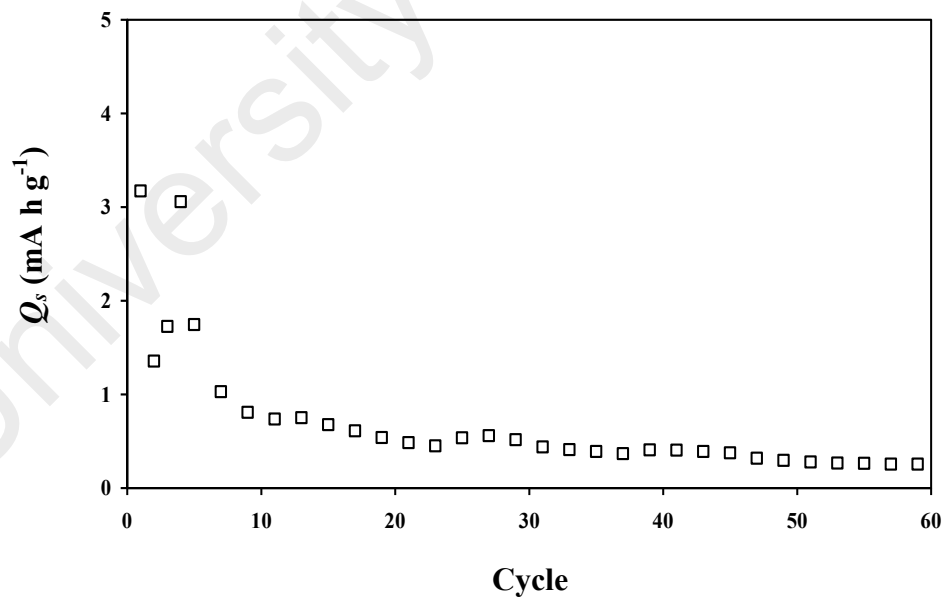
Figure 8.6: Specific discharge capacity versus cycle number.

in the electrode-electrolyte contact which generates active materials on the electrodes surface to oscillate in $ZnSO_4.7H_2O$ discharge state hence increases the Q_s value (Samsudin et al., 2014). The Q_s value is found almost constant from the 6th cycle to the 60th cycle since the intercalation of proton at cathode has been stabilized at an almost constant rate (Shukur & Kadir, 2015b). The same phenomenon has also been reported by other researchers (Kadir et al., 2010; Samsudin et al., 2014; Shukur & Kadir, 2015b). Beyond the 60th cycle, Q_s value is gradually decreases due to the poor interfacial stability of the electrode. This phenomenon will develop a large interfacial resistance between the electrode and the electrolyte. Kadir et al. (2010) reported that their rechargeable proton battery was studied at 0.30 mA with Q_s values between 0.50-2.20 mAh g^{-1}. The discharge capacity reported in the present work is found higher than their results. A discharge capacity of ~0.53 mAh was reported by Lakshmi and Chandra (2002) for their cell which recharged up to 7 cycles for 36 hours. Pratap et al. (2006) reported that their battery can be recharged for 9 cycles before having significant loss in voltage. They concluded that their battery was found more suitable for low current density applications, which is relevant with the present work.

8.5   EDLC Characterization

The EDLC was characterized using cyclic voltammetry (CV) and galvanostatic charge-discharge analysis. CV analysis may help to further understand the electrolyte electrochemical behavior during the charge-discharge process. The CV is studied at various scan rates, as shown in Figure 8.7. The figure shows that the curves are nearly rectangular without any obvious peaks observed, which justifies the absence of redox reactions or electron transfer process in the electrolyte (Arof et al., 2012; Lim, Teoh, Liew, & Ramesh, 2014b). This also proves that reversible charge-discharge processes

occur at a constant rate on the electrode-electrolyte interfaces over the complete cycles (Lim et al., 2014a).

The slight deviation from the rectangular shape of the CV curves is attributed to the internal resistance and carbon porosity (Kadir & Arof, 2011). Liew & Ramesh (2015) reported a CV profile with almost similar shape reported in this work and suggested that is due to poor electrode-electrolyte interfaces contact. The poor contact will give difficulties to the ions to be absorbed onto the electrode surface. The rectangular area becomes larger at higher scan rate, meaning that the voltammetric current is directly proportional to the scan rate. This voltammogram explains that EDLC is scan rate dependent which is a characteristic of capacitor cells.
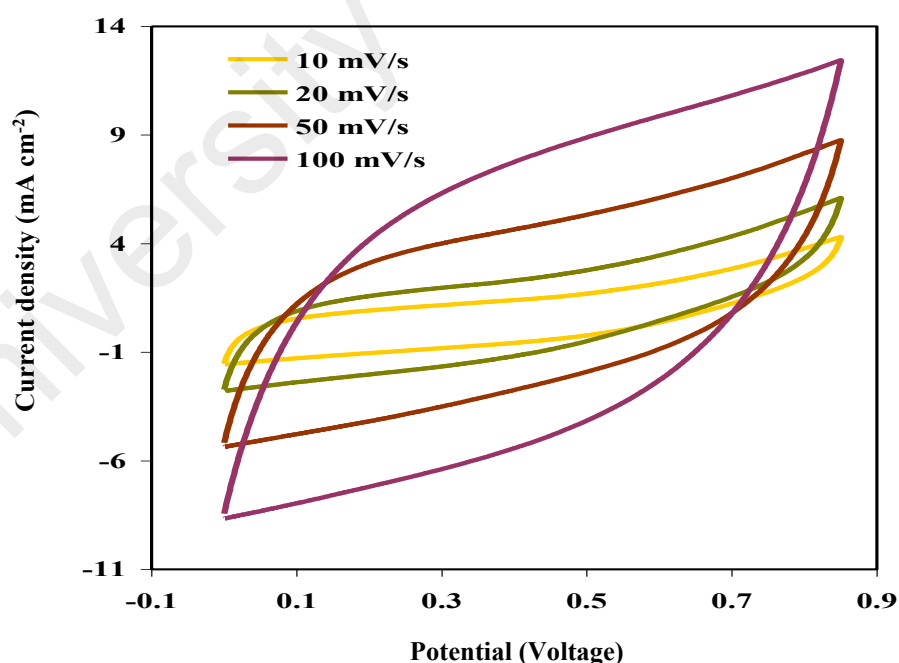
Figure 8.7: Cyclic voltammograms of B3 at different scan rates.

The behavior of EDLC is examined under constant current of charge-discharge condition. Selected cycles of the charging and discharging curves performance of EDLC using the highest conducting electrolyte; B3; are shown in Figure 8.8. The charge-discharge process is carried out at room temperature at a current density of 0.04 mA cm^{-2} between 0 to 0.85 V.
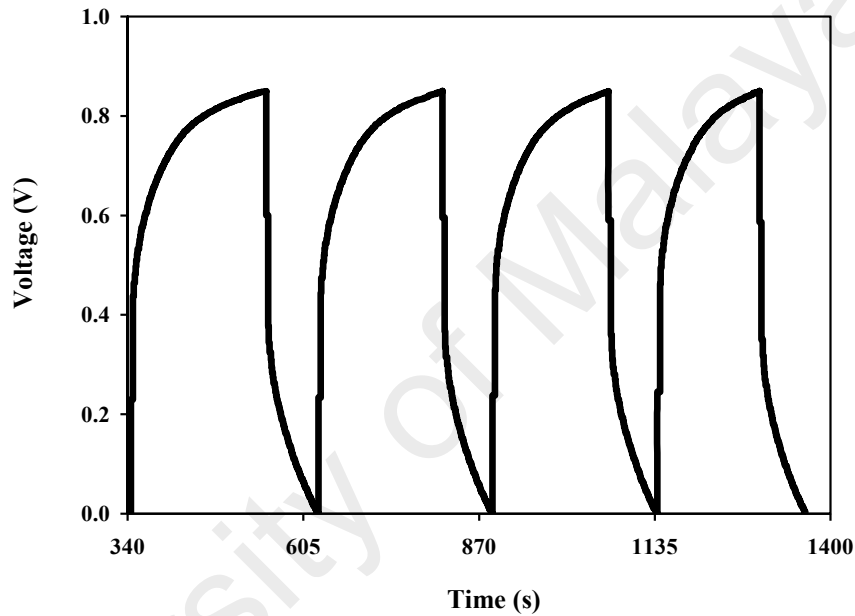
Figure 8.8: Charge-discharge curves of EDLC.

An internal resistance drop or referred as equivalent series resistance (ESR) represents the resistive behavior of EDLC (Pandey et al., 2011). ESR is determined from the potential drop when discharging the EDLC using equation:

$$ESR = \frac{V_{drop}}{i} \tag{8.7}$$

188

where V_{drop} is the potential drop during the charge-discharge process and i is current in unit ampere. ESR ranges from 2.0 to 3.0 kΩ. ESR is caused from the resistance of the electrode-electrolyte contact, hence may affect the process during the early stage (Arof et al., 2014). This sudden drop upon discharging process is directed to the resistance within the electrolyte, current collector and the inter-resistance between the current collector and the electrolyte (Lim et al., 2014b). The ohmic loss could also attribute to the voltage drop due to current leakage through the side area of the EDLC (Matsuda, Honjo, Tatsumisago, & Minami, 1998). This phenomenon leads to polymer electrolyte depletion which then developed the cell resistance. The migration and accumulation of ions on the double layer of the EDLC can also decrease the amount of mobile charge carriers and finally deplete the electrolyte film.

The value of specific capacitance, C_s on selected cycles from the galvanostatic charge-discharge measurement is calculated using the equation:

$$C_s = \frac{i}{m}\left(\frac{1}{s}\right) \tag{8.8}$$

where m is the mass of active material and s is the slope of the discharge curve. The specific capacity, Q_S refers to the amount of charge passing through outer circuit during charge-discharge process per unit mass. The values of Q_S were obtained from the following equation:

$$Q_S = \frac{t_d i}{m} \tag{8.9}$$

where t_d is the discharge time.

Figure 8.9 represents the calculated discharge C_s and Q_s on selected cycles from the galvanostatic charge-discharge measurement. The capacitance of the EDLC starts at 5240 mF g^{-1} and decreases before remains constant up to 50th cycle where the C_s is 1820 mF g^{-1}. The higher C_s during the first 20 cycles suggests that the material has a good potential for EDLC fabrication (Arof et al., 2012). The reduction of capacitance over the cycle number suggests the formation of ion pairs due to the ion aggregation process which then caused the electrolyte depletion (Liew & Ramesh, 2015). During the rapid charge-discharge process, more ions might paired up compared to transported which leads to the decrement of the number of mobile charge carriers. The ions which should accumulate to form an electrical double layer at the electrode-electrolyte boundaries also have reduced, hence reducing the capacitance of EDLC and increasing the internal resistance (Liew, Ramesh, & Arof, 2014b). During the charging state, few ions still remain in the polymer matrix which significantly affects the charging and
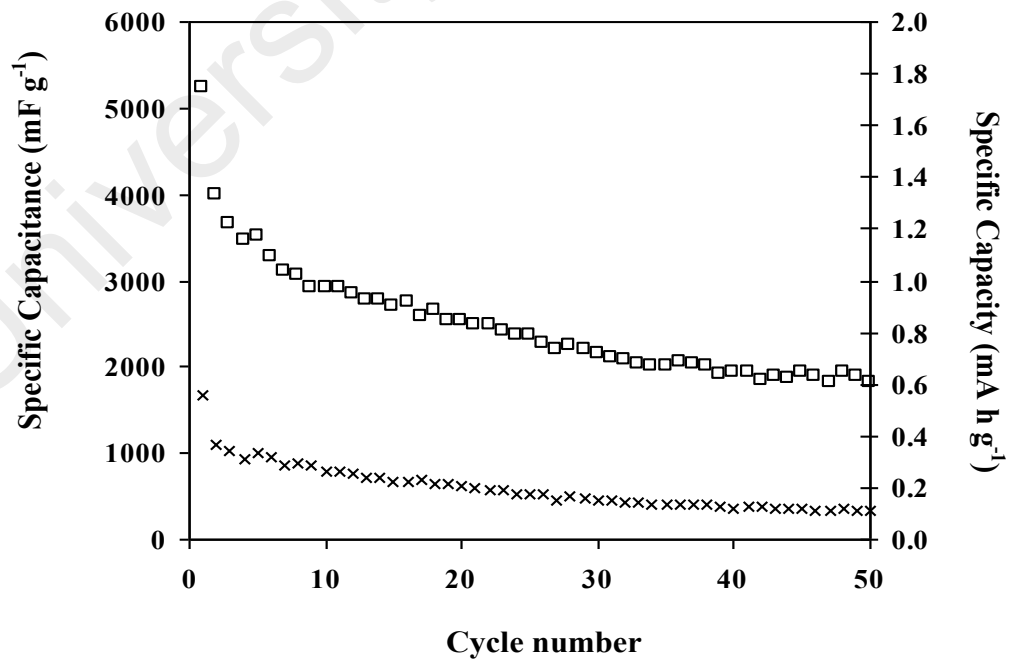
Figure 8.9: Specific discharge capacitance and capacity versus cycle number.

discharging process (Sudhakar & Selvakumar, 2012). The value of Q_s obtained is almost constant at ~0.15 mA h g^{-1} and exhibits the same trend with C_s as shown in Figure 8.9. The C_s value obtained in this work is compared with other reports as presented in Table 8.4.

The processes involve absorption and desorption of ions where both anions and cations contribute over the formation of electrical double layer. The cations; H$^+$ or NH$_4^+$; are attracted to the negatively charge electrode and form the charge accumulation on its surface. At the same time, the electrons are released and moved from positive to negative electrode once the electric field is applied (Liew et al., 2014b). The anions from polymer electrolyte; iodide ion or I$^-$; attracted to the positively charged surface and replace the electrons by ion absorption process when the voltage is applied within the EDLC. However, due to large atomic size (radius = 140 pm) and its bulky characteristic, I ion is hard to be attached and adsorbed on the electrode surface. The mobility of an ion will reduce as the size is increased (Shukur et al., 2013). This will reduce the amount of ions which will accumulate to form the double layer, hence produces a lower capacitance.

Table 8.4: Comparison of specific discharge capacity (C_s) values in the present work with other reports.

Electrolytes	Electrode materials	Specific capacitance, C_s on the first cycle (mF g^{-1})	Cycle number	References
PMMA-LiBOB-PC-EC	Carbonaceous material from *mata kucing (Dimocarpus longan)* fruit shells	685	50	Arof et al., 2012
PMMA-LiBOB-PC-EC	Activated carbon	521	50	Arof et al., 2012
MC-NH$_4$NO$_3$	Activated carbon	1670	15	Shuhaimi, Majid, & Arof, 2009
Chitosan-PEO-NH$_4$NO$_3$-EC	Activated carbon	106.53	140	Shukur et al., 2013
PEO-LiTf-EMITf	MWCNT (multi walled carbon nanotube)	1700-2100	NA	Pandey et al., 2011
PEO-Mg(Tf)$_2$-EMITf	MWCNT	2600-3000	NA	Pandey et al., 2011
Starch/chitosan-NH$_4$I-glycerol	Activated carbon	5240	50	Present work

8.6 Summary

The EDLC and proton batteries have been fabricated by employing the B3 sample. From the LSV result, it can be observed that the sample is electrochemically stable up to 1.9 V. The OCP of the proton batteries after 24 hours is (1.31 ± 0.03) V, which is higher than the theoretical potential. The discharged capacity of the primary batteries is enhanced by lowering the discharge current where the primary proton battery can stand up to 65 hours when discharged at 0.10 mA. The internal resistance, short circuit current and the power density of the primary proton batteries are 62.30 Ω, 17.70 mA and (4.00 ± 0.06) mW cm^{-2}, respectively. The secondary proton battery has been charged and discharged at 0.40 mA for 60 cycles. The EDLC provides the specific capacitance value of 1820-5240 mF g^{-1}. CV analysis shows that the faradaic or electron transfer process did not occur during the charge-discharge process. These results conclude that NH$_4$I can be a good proton provider in this biomaterial proton battery for low current density devices.

CHAPTER 9: DISCUSSION

Polymer electrolyte (PE) is an interdisciplinary field which combined the disciplines of polymer science, advanced materials, electrochemistry and inorganic chemistry. The science of electrolyte has attracted vast interest and demand since the past few decades from both industry and academia due to the potential shown for applications in energy devices including proton batteries (Bella et al., 2014), supercapacitors (Sivaraman et al., 2003), fuel cells (Urban et al., 2001) and sensors (Vonau et al., 2012).

Liquid electrolyte has been well-known in energy technology as a separator in devices that helps the ions to carry the charges. The use of liquid electrolytes has caused several disadvantages such as flammable, volatile and corrosive solvent and gas leakage which can cause irritation to human body (Noor et al., 2013). As the problems arose, researchers start to replace liquid electrolytes with polymer electrolytes. The research on PE which inspired by Armand (1994) has started to get intense research and development on new types of polymer electrolytes by varying the polymers selection and the charge provider along with its physical and chemical properties.

Pollution and shortage of fossil resources has become the reasons to mankind to look for cheap and safe but efficient technology that could replace the current energy devices. The development of PE based on natural polymers has been evolved due to environmental concerns and also to overcome the increasing price of petroleum sources to build energy devices (Bouchet et al., 2013). These natural polymers are easily biodegradable, which makes these materials interesting and good options for replacement. Several natural biopolymers that receive most attentions are including

cellulose (Kim et al., 2016), chitosan (Winie & Arof, 2004) and starch (Khiar & Arof, 2011).

In the present work, attention is given on developing starch/chitosan blend based biopolymer electrolytes. Corn starch has been chosen since the amylose content which is highly amorphous constitute of 27 % (Amaka et al., 2013; Association, 2006). This amount is higher compared to other types of starches. Furthermore, corn starch is a low cost material and easy to obtain for electrolyte preparation. The hydroxyl group in starch is available for formation of hydrogen bondings which in turn will favor the ionic mobility (Lu et al., 2009). The choice of chitosan to be blended with starch in this work has been made since previous works by other researchers have shown that this blend film exhibits improved characteristics compared to when they present individually. These characteristics are including more flexible, biodegradable, good mechanical strength as well as high ionic conductivity (Shukur & Kadir, 2015a; Shukur et al., 2013; Xu et al., 2005). The amino and hydroxyl groups attach to chitosan have prepared this polymer readily for hydrogen bonding interactions (Sugimoto et al., 1998).

In the present work, acetic acid is used as solvent. Blending polymer in acetic acid medium has been reported to obtain good functional properties and mechanical strength (Prokhorov et al., 2016). Meanwhile, the heating process up to 80°C will activate the starch molecules hence enhance the reaction rate by gelatinization (Diop, Li, Xie, & Shi, 2011). It is important for the starch granules to undergo gelatinization process because the existence of amylose and amylopectin exhibits semi-crystalline structure in the granules hence requires more energy for disruption (Park et al., 2007).

The compatibility of starch and chitosan to serve as polymer blend host is proven in Chapter 4. FTIR analysis has revealed that dissolving starch and chitosan in acetic acid has shifted the hydroxyl bands, showing that hydrogen bonding interactions have occurred between OH group of starch, OH and NH group of chitosan and OH group of acetic acid. The shiftings at carboxamide and amine regions as shown in Figure 4.3 are correlated to the protonated of NH_2 group to become NH_3^+ and also the hydrogen bonding formed at O atom of O=C-NHR (Nie et al., 2005). Deconvolution of XRD patterns is carried out in order to investigate the crystallinity of the various ratios of starch and chitosan and presented in Figures 4.8 and 4.9. The deconvolution of overlapping peaks has revealed that the polymers still retain their individual behaviors in the polymer blend film based on the existence of the original peaks. PB2 exhibits the lowest degree of crystallinity among all, proving that the crystalline domains is suppressed by blending starch and chitosan hence ready to serve as polymer host.

TGA analysis of the blend film also shows that it possesses both starch and chitosan characteristics by reducing the decomposition temperature compared to chitosan film and increasing the remaining material if compared to starch film. The T_g of selected polymer blend films exhibit the intermediate value between the T_g of starch and the T_g of chitosan, proving the interaction effects of miscible and compatible polymers (Bonilla et al., 2014). The addition of starch and chitosan has interrupted the molecules arrangement in starch film, hence shifted slightly the T_g value. It is presented in Figure 4.15 that PB2 possesses the lowest T_g value, confirming the high amorphous region in the blend compared to other ratios. The smoothness of PB2 surface area and the surface of cross-sections is another strong evidence on the compatibility and miscibility of starch and chitosan for this ratio. The absence of undissolved granules and the shrinkage

pattern based on the surface and cross-sections micrographs as shown in Figure 4.21 has brought to the conclusion that PB2 is the best candidate to serve as the blend host.

The results on the interaction at molecular level of the components in polymer blend can be proven based on FTIR analysis in Chapter 5. The deconvolution technique has been used to verify the overlapping patterns of different bands. The peaks of the asymmetry vibration; $\upsilon_{as}(NH_4^+)$ mode and symmetry vibration; $\upsilon_s(NH_4^+)$ from salt are detected to be overlapped with OH bonding in salted and plasticized systems, which implied that the salt characteristic is retained in all electrolytes. The broad and intensed hydroxyl bands prove the multihydroxyl structure exist in the electrolytes which will provide good interactions with polysaccharide group through hydrogen bonding (Liu et al., 2013). The shifting of the bands in carboxamide region is inferred due to hydrogen bonding interaction of H^+ and NH_4^+ at C=O (Nie et al., 2005). The bands shifting at 1490-1570 cm^{-1} are attributed to hydrogen bonding interaction at amine group. The changes in wavenumbers 955-1055 cm^{-1} can further justify the interactions between the components in the polymer blend.

Ionic conductivity is the most important study in this work in order to verify the suitability of this polymer electrolyte to be fabricated in electrochemical devices. As discussed and calculated based on Cole-Cole plots in Chapter 6, B3 exhibits the highest capacitance value which suggests that the addition of glycerol as plasticizer has created new pathways for ion conduction hence promoted ions dissociation and increased the number density and mobility of ions (Buraidah et al, 2009). The highest conductivity at room temperature in salted system is $(3.04 \pm 0.32) \times 10^{-4}$ S cm^{-1}, which is achieved when 40 wt.% of NH$_4$I is added. This A4 sample gives the lowest E_a which is 0.200 eV and the highest average values of n and μ which are 6.07×10^{18} cm^{-3} and 3.16×10^{-4}

cm^2 V^{-1} s^{-1}, respectively, in salted system. All electrolytes in salted system show Arrhenian characteristic as the conductivities exhibit linear relation with temperature, which presented in Figure 6.8. The E_a values are determined from Arrhenius plots where E_a, n and μ values are correlated by Rice and Roth model using Equation (2.2). These results imply that in salted system, A4 has the highest number of mobility and density of charge carriers hence reducing the energy barrier for ion conduction. Higher conductivity is obtained in this work if compared to the starch-NH4I electrolyte ($\sim$ 2.40 $\times$ 10^{-4} S cm^{-1}) which is done by Kumar et al. (2012) and chitosan-NH4I electrolyte (3.73 $\times$ 10^{-7} S cm^{-1}) which is done by Buraidah et al. (2009). This result justifies the contribution of polymer blending technique in conductivity enhancement where A4 gives the highest ionic conductivity and requires the lowest energy to move around due to the lowest E_a value.

This A4 sample is then plasticized with various concentrations of glycerol. Plasticization method has been widely used by researchers to optimize the ionic conductivity as well as to improve their electrolytes in term of mechanical and electrochemical properties (Ramesh & Arof, 2001). Glycerol is chosen in this work due to its compatibility with starch-based film as reported by Marcondes et al. (2010) and Zhai, Yoshii, & Kume (2003). Compatibility is the most significant and major characteristic for effective plasticization (Vieira, da Silva, dos Santos, & Beppu, 2011). Furthermore, its low melting point (18°C) and high boiling point (290°C) avoids glycerol from boiling or melting at the temperature range used in this study (Speight & Speight, 2002). High dielectric constant (ε) possessed by glycerol is 42.5, which is higher than some other plasticizer including ethylene sulfite or ES (ε=39.6) (Azli, Manan, & Kadir, 2015) and dimethylacetamide or DMA (ε=37.8). The high dielectric constant of glycerol which can weaken the force between the cation and anion of the salt

will cause the salt to be easily dissociated to become free ions (Gondaliya et al., 2013). In addition, glycerol provides the new pathways for ion conduction due to the existence of hydroxyl groups which will complex with cations (H^+ and NH_4^+) during ionic conduction (Shukur & Kadir, 2015).

The highest conductivity at room temperature which is $(1.28 \pm 0.07) \times 10^{-3}$ S cm^{-1} is obtained when 30 wt.% of glycerol is added (B3). The addition of more that 30 wt.% glycerol has decreased the conductivity due to the formation of microcrystalline linkages among the glycerol molecules and further allow the recrystallization of salt (Bergo et al., 2009). Marcondes et al. (2010) also reported that the plasticization of starch-based film is best with 30 wt.% of glycerol. The films start to be difficult to handle and failed to form a good film when more than 30 wt.% of glycerol is used. This result is supported with transport properties by Rice and Roth model as tabulated in Tables 6.4 to 6.11. B3 gives the lowest E_a which is 0.182 eV and the highest average values of n and μ which are $1.33 \times 10^{19}\,cm^{-3}$ and $6.08 \times 10^{-4}\,cm^2\,V^{-1}\,s^{-1}$, respectively. It can be concluded that the conductivity enhancement is influenced by the mobility and number density of ions as related by Equation (2.1). All electrolytes in plasticized system follow Arrhenius rule as the conductivities exhibit linear relation with temperature and the plots are presented in Figure 6.8.

Transference number analysis is important to be carried out to determine the type of conducting species involved in this work (Sekhar et al., 2012). Since ions play the biggest role in conduction, the ionic transference number, $t_{ion;}$ must be higher than the electronic transference number, t_e. As calculated in Equation (6.11), the t_{ion} for the highest conducting electrolyte is 0.991 while the t_e is 0.009. Based on Figure 6.10, it can be seen that the initial current is high before drop and saturated at 0.3 μA. The

199

electrodes used for transference number is ion blocking stainless steel electrodes, where only electrons can pass through the electrodes and carry the current while the ions will be trapped between the electrodes (Woo et al., 2011).

Another critical parameter to be analyzed is cation transference number, t_+; since cation is the major contributor during the charge-discharge process of a proton battery. Watanabe's technique has been used to calculate t_+ by sandwiching the highest conducting electrolyte between two reversible MnO_2 electrodes. By using Equation (5.12), the value of t_+ is calculated to be 0.40. This measurement could be affected by ions association, but this observation is sufficient for the determination of ions transportation process.

The study of dielectric constant; ε_r and dielectric loss; ε_i at room temperature has been carried out for both salted and plasticized systems. The variation of ε_r and ε_i follow the same trend as conductivity results, as the highest conducting sample has the highest values of ε_r and ε_i. The charge stored is increased in electrolytes as the conductivity increases. In plasticized system, glycerol is able to dissociate more salt to become ions hence produced higher number of density and mobility of ions. It also can be seen from Figure 6.13 that at high frequencies, both ε_r and ε_i are unable to follow the fast reversal of electric field and finally the ions will accumulate at the electrode-electrolyte interface. This phenomenon will decrease the values of ε_r and ε_i and confirmed the non-Debye behavior of the electrolytes. The electrical modulus where M_r and M_i are real and imaginary parts of the electrical modulus, respectively, has also been studied to analyze the electrical relaxation process of the electrolytes. Electrical modulus is most suitable to be studied at low frequencies region according to Equation (6.16). The low M_r and M_i at low frequencies indicates that the electrode polarization effect is neglected (Woo et

al., 2012). At high temperature, the electrical modulus is reduced due to the increased of charge carriers mobility (Aziz et al., 2010). Relaxation time which represents the effort of the charge carriers to obey the applied field direction is also found lower as the conductivity increased. The conduction mechanism predicted based on Jonscher's universal power law is quatum mechanical tunneling or QMT for both systems. Besides hopping, the ions are tunneling through the potential barrier between the complexation sites (Majid & Arof, 2007).

The stability of the electrolytes is further investigated based on TGA analysis. The decomposition temperature of A2 and A4 is in the range of 165 to 190°C as shown in Figure 6.25, which is lower than the polymer blending electrolyte. B3 and B5 samples start to decompose at 130-170°C temperature range. This decrement is attributed to the improvement of flexibility by enhancing the amorphous area, hence easier for disruption (Ramesh et al., 2012). In this amorphous region, the polymer segmental region will support the ionic migration hence lowering the T_g (Woo et al., 2013). Determination of T_g is significant to enhance the understanding of the conductivity trend due to the attribution of segmental motion. The T_g is found lower as the conductivity increased due to the flexible polymer backbone which allows an easy ions movement (Liew et al., 2014b). As the crystallinity increases, the T_g is found higher due to the restricted segmental motions which then leads to the formation of cross-linkings within the polymer and resulted on declining of conductivity.

The compatibility of the electrolytes is further characterized using XRD and FESEM analyses. The deconvolution technique has been carried out to differentiate the overlapping patterns. It can be seen from Figure 7.1 that the amorphousness of the polymer blend is increased with the addition of salt. The FESEM micrographs exhibit

small particles with rough surface pattern as depicted in Figures 7.6 and 7.7. A4 exhibits porous structure as shown in Figure 7.8 which can be related to the pore connectivity during the charge carriers transportation (Xi et al., 2006). The ionic conductivity is high while the crystallinity is low at this salt percentage. However, when more than 40 wt.% of salt is added, the sharp peaks which attributed to salt start to appear. As shown in Figure 7.9 and 7.10, the solid particles which suspended out of surface are attributed to the recrystallization of salt. The ions recombine since the polymer host is failed to accommodate the salt, hence decreases the conductivity (Kadir et al., 2010). The degree of crystallinity is also calculated and discovered that a high conducting electrolyte exhibits high amorphousness with low crystallinity value. This result proves that in amorphous region, the flexible backbones of polymer will cause to rapid segmental motions thus increases the chances of the charge carriers to move around and leads to higher conductivity (Rajendran et al., 2001). The salt molecules will react with the hydroxyl groups of the polymers and destruct the local hydrogen bonding which able the ions for movement.

The addition of glycerol will further suppress the crystalline region which proven from the absence of several crystalline peaks as depicted in Figures 7.12 to 7.14. The FESEM micrographs exhibit smoother surface during the addition of plasticizer. Different surface pattern are obtained as the glycerol content is increased. For the highest conducting electrolyte, indistinct spherulites with some boundaries appear which a proof of low crystallinity as reported by Ravi et al. (2015). This result is further strengthen when the degree of crystallinity values are found lower for the plasticized electrolytes. Glycerol promotes the dissociation of salt to become free ions by providing new pathways for ion conduction (Shukur, 2015). The addition of more than 30 wt.% glycerol leads to the appearance of new crystalline peaks hence resulting on high degree

of crytallinity as tabulated in Table 7.2. This accompanied with the decrement of ionic conductivity due to excess of glycerol content.

The development of lithium (Li^+) based energy devices is not foreign to researchers from industry and academia. Major attention has been given to Li^+ ion due to high energy density, hence Li^+ ion batteries have been exposed to various applications (Xu, 2004). This popularity however failed to deny the problems implicated from this technology, from exploded hand phones to grounded airplanes (Williard, He, Hendricks, & Pecht, 2013). Polymer electrolyte is used to separate the electrodes in a cell by preventing internal short circuit. The organic solvent containing lithium salt in the cell plays a role as a medium for ions transportation but this solution is easily volatile hence this type of battery faces major drawbacks due to safety, cost and difficult to handle (Bouchet et al., 2013). Another type of battery that has been investigated for few decades is alkaline batteries. However, the formation of intermediate species during the battery cycling process leads to chemical corrosion enhancement and leakage (Dell, 2000).

Proton (H^+) based conducting electrolytes have been recognized as an alternative ionic conductor in electrochemical device applications (Alias et al., 2014; Buraidah & Arof, 2011). This is because of the small radius of H^+ compared to Li^+ which makes H^+ better for intercalation into the layered structure of cathode (Mishra et al., 2014). For battery application, most of the proton conducting electrolytes are electrochemically decomposed at 1 to 2 V compared to Li^+ electrolytes (4 V) (Kadir et al., 2010; Pratap et al., 2006; Yang et al., 2008). However, due to the low cost of electrode and electrolyte materials used for proton batteries as well as no safety issues associated with them, proton batteries appear as a good alternative for low energy density battery applications

(Mishra et al., 2014; Pratap et al., 2006). Even though throw-away or primary batteries are still desirable, consumers start to pay attention to the rechargeable or secondary batteries due to economical benefits (Dell, 2000).

LSV has been carried out to study the operating voltage that can be endured by the electrolyte prior to electrochemical devices applications. It is found that B3 decomposed at around 1.90 V which concludes that this sample is suitable and ready to be fabricated. The open circuit potential (OCP) shows that cell potential is initially higher for a few hours before stabilized at (1.31 ± 0.03) V. It is concluded that the battery is practically stable in an open circuit condition.

Primary batteries are discharged at different constant currents. All discharge profiles show that the voltage reaches flat plateau at ~1.10 V before dropped significantly due to the increment of charge transfer resistance (Wang et al., 2005). The discharge capacities of the proton batteries are calculated using Equation (8.5) and tabulated in Table 8.2. The discharge capacity value is high when low discharge current is used. At high discharge current, a fast reaction is required but the charge transfer cannot attain the required speed which leads to a low diffusion rate of H^+ ions hence unable to deliver the electrical energy (Samsudin et al., 2014). The Q values obtained in this work are found comparable with other reports as presented in Table 8.3. From the *I-V* and *J-P* plots, the internal resistance is found to be 62.30 Ω which could be attributed to the oxidation of the electrodes. The maximum power density is (4.00 ± 0.06) mW cm^{-2} while the short circuit current of the batteries is 17.70 mA. This power density value is higher than those reported by Jamaludin et al. (2010) and Alias et al. (2014).

Secondary proton battery fabrication has been tested at 0.40 mA and cycled for 60 times. The Q_s value is found to decrease from 3.17 mAh g^{-1} to 1.36 mAh g^{-1} during the 2nd cycle due to the imperfection of the electrode-electrolyte contact at the early stage of the process (Mohamad et al., 2003). The Q_s value is then increases during the 3rd and the 4th cycle and reaches 3.06 mA h g^{-1} due to the improvement of electrode-electrolyte contact (Samsudin et al., 2014). During the 6th cycle to the 60th cycle, the Q_s value is found constant since the intercalation of proton at cathode has been stabilized at an almost constant rate (Shukur & Kadir, 2015b). These results are better than that reported by Kadir et al. (2010) and concluded as suitable to be applied in low current density devices.

The cyclic voltammetry or CV analysis has been carried out to study the electrochemical behavior of B3 during the charge-discharge process. It is observed the redox reaction or electron transfer process does not occur during the process due to the absence of any visible peaks based on the plots presented in Figure 8.7 (Lim et al., 2014b). It also clarifies the reversible charge-discharge process occurs at a constant rate on the electrode-electrolyte interfaces and explained the scan rate dependent behavior of an EDLC. The capacitance of the EDLC starts at 5240 mF g^{-1} and decreases before remains constant up to 50th cycle where the C_s is 1820 mF g^{-1}, which suggests that the material has a good potential for EDLC fabrication (Arof et al., 2012). The C_s value obtained in this work is compared with other reports as presented in Table 8.4.

The reduction of capacitance over the cycle number suggests the formation of ion pairs due to the ion aggregation process which then caused the reduction of mobile charge carriers number (Liew & Ramesh, 2015). Both anions and cations contribute over the formation of electrical double layer in an EDLC. The cations; H^+ or NH_4^+; are

attracted to the negatively charge electrode and form the charge accumulation on its surface while the anions from polymer electrolyte; iodide ion or I⁻; attracted to the positively charged surface and replace the electrons by ion absorption process when the voltage is applied within the EDLC (Liew et al., 2014b). However, the large atomic size (radius = 211 pm) of I ion makes it hard to be attached and adsorbed on the electrode surface. The mobility of an ion will reduce as the size is increased (Shukur et al., 2013). This will reduce the amount of ions which will accumulate to form the double layer, hence produces a lower capacitance.

CHAPTER 10: CONCLUSIONS AND FUTURE WORKS

10.1   Conclusions

Three polymer electrolytes systems were successfully prepared via solution casting technique; starch/chitosan, starch/chitosan-NH$_4$I and starch/chitosan-NH$_4$I-glycerol. The preparation of salted system was made based on characterization results on the starch/chitosan blend films including:

- FTIR results have revealed the interaction at molecular level when starch was blending with chitosan.

- The degree of crystallinity of each ratio of starch and chitosan was calculated based on XRD analysis and 80 wt.% of starch/20 wt.% of chitosan was found as the most amorphous ratio.

- The water content and the decomposition temperature of the blend film exhibits intermediate characteristics of both starch and chitosan individual films, proving that the thermal stability behavior of both films were retained in PB2 film.

- The T_g values of the blended films fell at the intermediate range of the individual polymers which confirmed a good miscibility of both polymers. The lowest T_g value given by PB2 is another proof that PB2 is highly amorphous compared to other ratios.

- The smooth pattern of the cross-sections surface exhibited by PB2 has concluded that PB2 is the most suitable and compatible blend to serve as polymer host.

The addition of 40 wt.% NH_4I has enhanced the conductivity in salted system up to $(3.04 \pm 0.32) \times 10^{-4}$ S cm^{-1} due to several reasons:

- Highly amorphous which resulted on higher conductivity. Amorphousness was determined based on low degree of crystallinity value and low value of T_g.

- The enhancement of mobility and number density of charge carriers as the salt was added.

- The lower lattice energy of salt (605.3 kJ mol^{-1}) and larger anionic size of I (211 pm) resulted on easier dissociation of salt.

- Conductivity values are increased as the temperature increased which follows the Arrhenius theory. During the heating process, the ions vibrate faster hence less energy was needed for ionic conduction hence produced lower E_a.

Plasticization technique has increased the conductivity up to $(1.28 \pm 0.07) \times 10^{-3}$ S cm^{-1} with the addition of 30 wt.% of glycerol due to some reason as listed below:

- The high dielectric constant possessed by the glycerol helped in the dissociation of salt to become free ions.

- The number of density and mobility of ions were further increased since more free ions were produced. This also can be determined based on dielectric studies.

- Glycerol also provides alternative pathways for ionic conduction which was proven by lower E_a value.

- The amorphousness of plasticized electrolytes was further enhanced which was proven by lower degree of crystallinity.

In transference number analysis, the total ionic transference number obtained was 0.991 while the cation transference number, t_+ for the highest conducting electrolyte was found to be 0.40. LSV measurements reveal that the electrolyte was

electrochemically stable up to 1.90 V. The discharged capacity of the primary batteries was enhanced by lowering the discharge current e. g. primary proton battery can stand up to 65 hours when discharged at 0.10 mA. The internal resistance, short circuit current and the power density of the primary proton batteries were 62.30 Ω, 17.70 mA and (4.00 ± 0.06) mW cm^{-2}, respectively. The secondary proton battery has been charged and discharged at 0.40 mA for 60 cycles. The capacitance of the EDLC started at 5240 mF g^{-1} and decreased before it remained constant up to 50th cycle where the C_s is 1820 mF g^{-1}. These results concluded that NH$_4$I can be a good proton provider in this biomaterial proton battery for low current density devices.

10.2   Contribution of the Thesis

The aim of this thesis is to prepare a natural polymer electrolyte-based which approach a reliable and compatible energy device performance with high conductivities. The motivation behind this doctoral work is to produce a stable electrolyte in term of physical, chemical and thermal through a cost-effective methodology. This work focuses on the selection of NH$_4$I as the dopant salt which not yet used in proton batteries and EDLC applications, hence giving rise to novel material with promising characteristics for low current density devices. This work also shows an effort on understanding the characteristics of a good electrolyte which may enhance the devices performance and provide the guidelines for energy devices designs in the future.

10.3 Future Works

In the future, a few significant steps should be taken to produce an improved electrolyte in term of electrical, physical and chemical characteristics including:

- Increasing the conductivity by employing double salt system technique. Two different sources of charge carriers may prevent the formation of ions aggregation hence increases the density of ions (Ramesh & Arof, 2000; Subramaniam et al., 2012).

- Modifying the structure and enhancing the ionic conductivity by introducing inorganic nanosize-filler such as aluminium oxide (Al_2O_3) (Chand, Rai, Agrawal, & Patel, 2011), zinc oxide (ZnO) (Noor et al., 2011) and cadmium oxide (CdO) (Ravindran et al., 2015).

- Applying comb-branched or grafting copolymers. This method involving low molecular weight of polymer which will be grafted to another polymer backbone (Subramaniam et al., 2012). The flexibility of the polymer chain will be improved while reducing the degree of crystallinity and T_g which in turn resulting on higher conductivity (Zhang et al., 2011).

- Employing mixed aprotic solvent system for example the mixture of propylene carbonate, PC and ethylene carbonate, EC. This technique give the possibility to enhance the conductivity by two orders of magnitude due to high degree of dissociation and rapid ionic migration (Deepa et al., 2002; Tobishima, Hayashi, Nemoto, & Yamaki, 1997)

Further improvements can be done on proton batteries and EDLC performance including:

- Varying the electrode material such as employing vanadium (IV) oxide (V_2O_5) as positive electrode (Alias et al., 2014) or synthesizing new anode or cathode materials for better electrochemical performance (Liu et al., 2017; Liu et al., 2017).

- Building nanostructure material with various carbon-based materials to avoid significant loss and poor cyclic stability including carbon nanotube or CNT, carbon fibers and graphene (Guo et al., 2015; Liu et al., 2017).

- Employing gold nanowires for higher power storage, improving stability and longer cycle lifetime (Le Thai, Chandran, Dutta, Li, & Penner, 2016).

- Insertion of mixed metal oxide for the electrodes (Choi et al., 2016) or increasing the activated carbon surface area (Shukur, 2015).

Even though the fabrication carried out in this work is more suitable for low-power applications, a device with stable performance and friendly to the environment is expected to be used for a long time. Further improvements are necessary; hence the resulting products are not just following the latest trend but instead will be beneficial to the human race.

REFERENCES

Alias, S. S., Chee, S. M., & Mohamad, A. A. (2014). Chitosan–ammonium acetate–ethylene carbonate membrane for proton batteries. *Arabian Journal of Chemistry,* 1-12.

Amaka, M., Amaka, M., Ngadi, M., Ejebe, C., Nwankpa, C., Danbaba, N., Ndindeng, S., Manful, J. (2013). Study on the gelatinization properties and Amylose content of Rice varieties from Nigeria and Cameroun. *International Journal of Nutrition and Food Sciences, 2*, 181-186.

Armand, M. (1994). The history of polymer electrolytes. *Solid State Ionics, 69*(3–4), 309-319.

Arof, A., Amirudin, S., Yusof, S., & Noor, I. (2014). A method based on impedance spectroscopy to determine transport properties of polymer electrolytes. *Physical Chemistry Chemical Physics, 16*(5), 1856-1867.

Arof, A., Kufian, M., Syukur, M., Aziz, M., Abdelrahman, A., & Majid, S. (2012). Electrical double layer capacitor using poly (methyl methacrylate)–C_4BO_8Li gel polymer electrolyte and carbonaceous material from shells of mata kucing (Dimocarpus longan) fruit. *Electrochimica Acta, 74*, 39-45.

Arof, A., Shuhaimi, N., Alias, N., Kufian, M., & Majid, S. (2010). Application of chitosan/iota-carrageenan polymer electrolytes in electrical double layer capacitor (EDLC). *Journal of Solid State Electrochemistry, 14*(12), 2145-2152.

Arof, A., Shuhaimi, N., Amirudin, S., Kufian, M., Woo, H., & Careem, M. (2014). Polyacrylonitrile–lithium bis (oxalato) borate polymer electrolyte for electrical double layer capacitors. *Polymers for Advanced Technologies, 25*(3), 265-272.

Association, C. R. (2006). Corn oil. *On line: http://www. corn. org/CornOil. pdf Accessed on September, 30*(2010), 96-20.

Avella, M., De Vlieger, J. J., Errico, M. E., Fischer, S., Vacca, P., & Volpe, M. G. (2005). Biodegradable starch/clay nanocomposite films for food packaging applications. *Food Chemistry, 93*(3), 467-474.

Ayala, G., Agudelo, A., & Vargas, R. (2012). Effect of glycerol on the electrical properties and phase behavior of cassava starch biopolymers. *Dyna, 79*(171), 138-147.

Aziz, S., Abidin, Z., & Arof, A. (2010). Influence of silver ion reduction on electrical modulus parameters of solid polymer electrolyte based on chitosan-silver triflate electrolyte membrane. *Express Polymer Leter, 5*, 300-310.

Aziz, N., Majid, S., & Arof, A. (2012). Synthesis and characterizations of phthaloyl chitosan-based polymer electrolytes. *Journal of Non-Crystalline Solids, 358*(12), 1581-1590.

Azli, A., Manan, N., & Kadir, M. (2015). Conductivity and dielectric studies of lithium trifluoromethanesulfonate doped polyethylene oxide-graphene oxide blend based electrolytes. *Advances in Materials Science and Engineering, 2015*.

Ban, W., Song, J., Argyropoulos, D. S., & Lucia, L. A. (2006). Improving the physical and chemical functionality of starch-derived films with biopolymers. *Journal of Applied Polymer Science, 100*(3), 2542-2548.

Barbani, N., Bertoni, F., Ciardelli, G., Cristallini, C., Silvestri, D., Coluccio, M., & Giusti, P. (2005). Bioartificial materials based on blends of dextran and poly (vinyl alcohol-co-acrylic acid). *European Polymer Journal, 41*(12), 3004-3010.

Bel'Nikevich, N., Bobrova, N., Bronnikov, S., Kalyuzhnaya, L., & Budtova, T. (2004). Properties of some chitosan-containing blends and films therefrom. *Russian Journal of Applied Chemistry, 77*(2), 313-318.

Bella, R. D., Hirankumar, G., & Devaraj, P. (2014). Characterization of plasticized proton conducting polymer electrolyte and its application in primary proton battery. *International Journal of ChemTech Research, 6*(13), 5372-5377.

Berger, J., Reist, M., Mayer, J. M., Felt, O., Peppas, N., & Gurny, R. (2004). Structure and interactions in covalently and ionically crosslinked chitosan hydrogels for biomedical applications. *European Journal of Pharmaceutics and Biopharmaceutics, 57*(1), 19-34.

Bergo, P., Sobral, P., & Prison, J. (2009). Physical properties of cassava starch films containing glycerol. *Food Engineering Department*.

Bhargav, P. B., Mohan, V. M., Sharma, A., & Rao, V. N. (2009). Investigations on electrical properties of (PVA: NaF) polymer electrolytes for electrochemical cell applications. *Current Applied Physics, 9*(1), 165-171.

Bhide, A., & Hariharan, K. (2007). Ionic transport studies on $(PEO)_6$:$NaPO_3$ polymer electrolyte plasticized with PEG400. *European Polymer Journal, 43*(10), 4253-4270.

Bhavani, S., Ravi, M., & Rao, V. N. Studies on electrical properties of PVA: $NiBr_2$ complexed polymer electrolyte films for battery applications. *International Journal of Engineering Science and Innovatove Technology, 3*(4), 426-434.

Bonilla, J., Fortunati, E., Atarés, L., Chiralt, A., & Kenny, J. M. (2014). Physical, structural and antimicrobial properties of polyvinyl alcohol-chitosan biodegradable films. *Food Hydrocolloids, 35*, 463-470.

Bouchet, R., Maria, S., Meziane, R., Aboulaich, A., Lienafa, L., Bonnet, J.-P., Phan, T. N. P., Bertin, D., Gigmes, D., Devaux, D., Denoyel, R. & Armand, M. (2013). Single-ion BAB triblock copolymers as highly efficient electrolytes for lithium-metal batteries. *Nature materials, 12*(5), 452-457.

Bourtoom, T., & Chinnan, M. S. (2008). Preparation and properties of rice starch–chitosan blend biodegradable film. *LWT-Food Science and Technology, 41*(9), 1633-1641.

Buraidah, M., & Arof, A. (2011). Characterization of chitosan/PVA blended electrolyte doped with NH 4 I. *Journal of Non-Crystalline Solids, 357*(16), 3261-3266.

Buraidah, M., Teo, L., Majid, S., & Arof, A. (2009). Ionic conductivity by correlated barrier hopping in NH 4 I doped chitosan solid electrolyte. *Physica B: Condensed Matter, 404*(8), 1373-1379.

Burke, A., Yilmaz, E., Hasirci, N., & Yilmaz, O. (2002). Iron (III) ion removal from solution through adsorption on chitosan. *Journal of Applied Polymer Science, 84*(6), 1185-1192.

Cerqueira, M. A., Souza, B. W., Teixeira, J. A., & Vicente, A. A. (2012). Effect of glycerol and corn oil on physicochemical properties of polysaccharide films-A comparative study. *Food hydrocolloids, 27*(1), 175-184.

Chand, N., Rai, N., Agrawal, S., & Patel, S. (2011). Morphology, thermal, electrical and electrochemical stability of nano aluminium-oxide-filled polyvinyl alcohol composite gel electrolyte. *Bulletin of Materials Science, 34*(7), 1297-1304.

Chandra, S., Tolpadi, S., & Hashmi, S. (1988). Transient ionic current measurement of ionic mobilities in a few proton conductors. *Solid State Ionics, 28*, 651-655.

Chandra, M. L., Karthikeyan, S., Selvasekarapandian, S., Pandi, D. V., Monisha, S., & Packiaseeli, S. A. (2016). Characterization of high ionic conducting PVAc–PMMA blend-based polymer electrolyte for electrochemical applications. *Ionics*, 1-12.

Chang, C., & Zhang, L. (2011). Cellulose-based hydrogels: Present status and application prospects. *Carbohydrate Polymers, 84*(1), 40-53.

Chen, P.-Y., Lee, C.-P., Vittal, R., & Ho, K.-C. (2010). A quasi solid-state dye-sensitized solar cell containing binary ionic liquid and polyaniline-loaded carbon black. *Journal of Power Sources, 195*(12), 3933-3938.

Cheng, J., Jeong, E. Y., & Dou, E. (2016). Samsung to permanently discontinue Galaxy Note 7 smartphone. *The Wall Street Journal.*

Chen, R. H., Lin, J. H., & Yang, M. H. (1994). Relationships between the chain flexibilities of chitosan molecules and the physical properties of their casted films. *Carbohydrate Polymers, 24*(1), 41-46.

Cheung, M. K., Wan, K. P., & Yu, P. H. (2002). Miscibility and morphology of chiral semicrystalline poly-(R)-(3-hydroxybutyrate)/chitosan and poly-(R)-(3-hydroxybutyrate-co-3-hydroxyvalerate)/chitosan blends studied with DSC, 1H T1 and T1ρ CRAMPS. *Journal of Applied Polymer Science, 86*(5), 1253-1258.

Choi, Y. I., Lee, S., Kim, S. K., Kim, Y.-I., Cho, D. W., Khan, M. M., & Sohn, Y. (2016). Fabrication of ZnO, ZnS, Ag-ZnS, and Au-ZnS microspheres for photocatalytic activities, CO oxidation and 2-hydroxyterephthalic acid synthesis. *Journal of Alloys and Compounds, 675*, 46-56.

Colomban, P. (1992). *Proton Conductors: Solids, membranes and gels-materials and devices* (Vol. 2): Cambridge University Press.

De Kruif, C., & Tuinier, R. (2001). Polysaccharide protein interactions. *Food Hydrocolloids, 15*(4), 555-563.

Deepa, M., Sharma, N., Agnihotry, S., Singh, S., Lal, T., & Chandra, R. (2002). Conductivity and viscosity of liquid and gel electrolytes based on LiClO$_4$, LiN (CF$_3$SO$_2$)$_2$ and PMMA. *Solid State Ionics, 152*, 253-258.

Dehnad, D., Mirzaei, H., Emam-Djomeh, Z., Jafari, S.-M., & Dadashi, S. (2014). Thermal and antimicrobial properties of chitosan–nanocellulose films for extending shelf life of ground meat. *Carbohydrate Polymers, 109*, 148-154.

Dell, R. (2000). Batteries: fifty years of materials development. *Solid State Ionics, 134*(1), 139-158.

Deraman, S., Mohamed, N., & Subban, R. (2013). Conductivity and Electrochemical Studies on Polymer Electrolytes Based on Poly Vinyl (chloride)-Ammonium Triflate-Ionic Liquid for Proton Battery. *International Journal of Electrochemical Science, 8*, 1459-1468.

Diop, C. I. K., Li, H. L., Xie, B. J., & Shi, J. (2011). Effects of acetic acid/acetic anhydride ratios on the properties of corn starch acetates. *Food chemistry, 126*(4), 1662-1669.

Elgadir, M. A., Akanda, M. J. H., Ferdosh, S., Mehrnoush, A., Karim, A. A., Noda, T., & Sarker, M. Z. I. (2012). Mixed biopolymer systems based on starch. *Molecules, 17*(1), 584-597.

Famá, L., Gerschenson, L., & Goyanes, S. (2009). Starch-vegetable fibre composites to protect food products. *Carbohydrate Polymers, 75*(2), 230-235.

Fadzallah, I., Majid, S., Careem, M., & Arof, A. (2014). A study on ionic interactions in chitosan–oxalic acid polymer electrolyte membranes. *Journal of Membrane Science, 463*, 65-72.

Freitas, J. N. d., Gonçalves, A. d. S., De Paoli, M.-A., Durrant, J. R., & Nogueira, A. F. (2008). The role of gel electrolyte composition in the kinetics and performance of dye-sensitized solar cells. *Electrochimica Acta, 53*(24), 7166-7172.

Frost, R. L., & Johansson, U. (1998). Combination bands in the infrared spectroscopy of kaolins-a DRIFT spectroscopic study. *Clays and Clay Minerals, 46*(4), 466-477.

Fujiwara, N., Yao, M., Siroma, Z., Senoh, H., Ioroi, T., & Yasuda, K. (2011). Reversible air electrodes integrated with an anion-exchange membrane for secondary air batteries. *Journal of Power Sources, 196*(2), 808-813.

Galeski, A., Argon, A. S., & Cohen, R. (1991). Deconvolution of X-ray diffraction data to elucidate plastic deformation mechanisms in the uniaxial extension of bulk nylon 6. *Macromolecules, 24*(13), 3945-3952.

Ganesan, S., Muthuraaman, B., Mathew, V., Madhavan, J., Maruthamuthu, P., & Suthanthiraraj, S. A. (2008). Performance of a new polymer electrolyte incorporated with diphenylamine in nanocrystalline dye-sensitized solar cell. *Solar Energy Materials and Solar Cells, 92*(12), 1718-1722.

Gauthier, M., Belanger, A., Fauteu, D., Harvey, P. E., Kapfer, B., Duval, M., & Muller, D. (1986). Recent Progress in the Development of Rechargeable Lithium Batteries Based on Polymer Electrolytes. In *Journal Of The Electrochemical Society* ,133(8), C292-C293.

Gao, H., & Lian, K. (2010). Characterizations of proton conducting polymer electrolytes for electrochemical capacitors. *Electrochimica Acta, 56*(1), 122-127.

Ghanbarzadeh, B., Almasi, H., & Entezami, A. A. (2010). Physical properties of edible modified starch/carboxymethyl cellulose films. *Innovative Food Science & Emerging Technologies, 11*(4), 697-702.

Ghosh, A., Wang, C., & Kofinas, P. (2010). Block copolymer solid battery electrolyte with high Li-ion transference number. *Journal of the Electrochemical Society, 157*(7), A846-A849.

Gondaliya, N., Kanchan, D. K., & Sharma, P. (2013). Effect of a plasticizer on a solid polymer electrolyte. *Society of Plastic Engineers*, 2417.

Guo, X., Han, J., Zhang, L., Liu, P., Hirata, A., Chen, L., Fujita, T., Chen, M. (2015). A nanoporous metal recuperated MnO_2 anode for lithium ion batteries. *Nanoscale, 7*(37), 15111-15116.

Han, D. G., & Choi, G. M. (1998). Computer simulation of the electrical conductivity of composites: the effect of geometrical arrangement. *Solid State Ionics, 106*(1), 71-87.

Harun, N., Ali, R., Ali, A., & Yahya, M. (2011). Conductivity studies on cellulose acetate-ammonium tetrafluoroborate based polymer electrolytes. *Materials Research Innovations, 15*(s2), s168-s172.

Hasegawa, M., Isogai, A., Onabe, F., Usuda, M., & Atalla, R. H. (1992). Characterization of cellulose-chitosan blend films. *Journal of applied polymer science, 45*(11), 1873-1879.

Hashmi, S., Kumar, A., Maurya, K., & Chandra, S. (1990). Proton-conducting polymer electrolyte. I. The polyethylene oxide + NH_4ClO_4 system. *Journal of Physics D: Applied Physics, 23*(10), 1307.

Hatta, F., Kudin, T., Subban, R., Ali, A., Harun, M., & Yahya, M. (2009). Plasticized PVA/PVP–KOH Alkaline solid polymer blend electrolyte for electrochemical cells. *Functional Materials Letters, 2*(03), 121-125.

Hejazi, R., & Amiji, M. (2003). Chitosan-based gastrointestinal delivery systems. *Journal of controlled release, 89*(2), 151-165.

Hema, M., Selvasekarapandian, S., Arunkumar, D., Sakunthala, A., & Nithya, H. (2009). FTIR, XRD and ac impedance spectroscopic study on PVA based

polymer electrolyte doped with NH$_4$X (X= Cl, Br, I). *Journal of Non-Crystalline Solids, 355*(2), 84-90.

Hema, M., Selvasekerapandian, S., Hirankumar, G., Sakunthala, A., Arunkumar, D., & Nithya, H. (2009). Structural and thermal studies of PVA:NH$_4$I. *Journal of Physics and Chemistry of Solids, 70*(7), 1098-1103.

Hema, M., Selvasekerapandian, S., Sakunthala, A., Arunkumar, D., & Nithya, H. (2008). Structural, vibrational and electrical characterization of PVA-NH$_4$Br polymer electrolyte system. *Physica B: Condensed Matter, 403*(17), 2740-2747.

Hodge, R., Edward, G. H., & Simon, G. P. (1996). Water absorption and states of water in semicrystalline poly (vinyl alcohol) films. *Polymer, 37*(8), 1371-1376.

Hofmann, A., Schulz, M., & Hanemann, T. (2013). Gel electrolytes based on ionic liquids for advanced lithium polymer batteries. *Electrochimica Acta, 89*, 823-831.

Howell, F., Bose, R., Macedo, P., & Moynihan, C. (1974). Electrical relaxation in a glass-forming molten salt. *The Journal of Physical Chemistry, 78*(6), 639-648.

Jagannath, J., Nanjappa, C., Das Gupta, D., & Bawa, A. (2003). Mechanical and barrier properties of edible starch–protein-based films. *Journal of Applied Polymer Science, 88*(1), 64-71.

Jaipal Reddy, M., & Chu, P. P. (2002). Ion pair formation and its effect in PEO:Mg solid polymer electrolyte system. *Journal of Power Sources, 109*(2), 340-346.

Jamaludin, A., & Mohamad, A. (2010). Application of liquid gel polymer electrolyte based on chitosan-NH$_4$NO$_3$ for proton batteries. *Journal of Applied Polymer Science, 118*(2), 1240-1243.

Jayaweera, E. N., Ranasinghe, C. S. K., Kumara, G. R. A., Wanninayake, W. M. N. M. B., Senarathne, K. G. C., Tennakone, K., Rajapakse, R. M. G., & Ileperuma, O. A. (2015). Novel Method to Improve Performance of Dye-sensitized Solar Cells Based on Quasi-solid Gel-Polymer Electrolytes. *Electrochimica Acta, 152*(0), 360-367.

Johan, M. R., & Ting, L. M. (2011). Structural, thermal and electrical properties of nano manganese-composite polymer electrolytes. *International Journal of Electrocheical Science, 6*, 4737-4748.

Johansson, A., Gogoll, A., & Tegenfeldt, J. (1996). Diffusion and ionic conductivity in Li (CF$_3$SO$_3$) PEG 10 and LiN(CF$_3$SO$_2$)$_2$ PEG10. *Polymer, 37*(8), 1387-1393.

Jones, A. G. (2014). Compensation of the Meyer-Neldel Compensation Law for H diffusion in minerals. *Geochemistry, Geophysics, Geosystems, 15*(6), 2616-2631.

Jyothi, N. K., Kumar, K. V., & Murthy, P. N. (2014). FTIR, XRD and DC Conductivity Studies of Proton Conducting Gel Polymer Electrolytes based on

Polyacrylonitrile (PAN). *International Journal of ChemTech Research, 6*(13), 5214-5219.

Kadir, M., & Arof, A. (2011). Application of PVA-chitosan blend polymer electrolyte membrane in electrical double layer capacitor. *Materials Research Innovations, 15*(2), s217-s220.

Kadir, M., Majid, S., & Arof, A. (2010). Plasticized chitosan-PVA blend polymer electrolyte based proton battery. *Electrochimica Acta, 55*(4), 1475-1482.

Kadir, M., Aspanut, Z., Majid, S., & Arof, A. (2011). FTIR studies of plasticized poly (vinyl alcohol)–chitosan blend doped with NH_4NO_3 polymer electrolyte membrane. *Spectrochimica Acta Part A: Molecular and Biomolecular Spectroscopy, 78*(3), 1068-1074.

Kadir, M. A., Teo, L., Majid, S., & Arof, A. (2009). Conductivity studies on plasticised PEO/chitosan proton conducting polymer electrolyte. *Materials Research Innovations, 13*(3), 259-262.

Kawahara, M., Morita, J., Rikukawa, M., Sanui, K., & Ogata, N. (2000). Synthesis and proton conductivity of thermally stable polymer electrolyte: poly (benzimidazole) complexes with strong acid molecules. *Electrochimica Acta, 45*(8), 1395-1398.

Khanmirzaei, M. H., & Ramesh, S. (2013). Ionic transport and FTIR properties of lithium iodide doped biodegradable rice starch based polymer electrolytes. *International Journal of Electrochemical Science*, *8*(7), 9977-9991.

Khiar, A., & Arof, A. (2011). Electrical properties of starch/chitosan-NH_4NO_3 polymer electrolyte. *World Academy Of Science, Engineering And Technology, 59*, 23-27.

Khiar, A. A., & Arof, A. (2010). Conductivity studies of starch-based polymer electrolytes. *Ionics, 16*(2), 123-129.

Khiar, A., Puteh, R., & Arof, A. (2006). Conductivity studies of a chitosan-based polymer electrolyte. *Physica B: Condensed Matter, 373*(1), 23-27.

Khoo, C. G., Frantzich, S., Rosinski, A., Sjöström, M., & Hoogstraate, J. (2003). Oral gingival delivery systems from chitosan blends with hydrophilic polymers. *European Journal of Pharmaceutics and Biopharmaceutics, 55*(1), 47-56.

Kim, J.-H., Gu, M., Lee, D. H., Kim, J.-H., Oh, Y.-S., Min, S. H., Kim, B. S., & Lee, S.-Y. (2016). Functionalized nanocellulose-integrated heterolayered nanomats toward smart battery separators. *Nano Letters*, *16*(9), 5533-5541.

Kötz, R., & Carlen, M. (2000). Principles and applications of electrochemical capacitors. *Electrochimica acta*, *45*(15), 2483-2498.

Kroeze, J. E., Hirata, N., Schmidt-Mende, L., Orizu, C., Ogier, S. D., Carr, K., Gratzel, M., & Durrant, J. R. (2006). Parameters Influencing Charge Separation in Solid-State Dye-Sensitized Solar Cells Using Novel Hole Conductors. *Advanced Functional Materials, 16*(14), 1832-1838.

Kufian, M., Majid, S., & Arof, A. (2007). Dielectric and conduction mechanism studies of PVA-orthophosphoric acid polymer electrolyte. *Ionics, 13*(4), 231-234.

Kumar, M., Tiwari, T., & Srivastava, N. (2012). Electrical transport behaviour of bio-polymer electrolyte system: Potato starch + ammonium iodide. *Carbohydrate Polymers, 88*(1), 54-60.

Lau, C., & Mi, Y. (2002). A study of blending and complexation of poly (acrylic acid)/poly (vinyl pyrrolidone). *Polymer, 43*(3), 823-829.

Leal Filho, L. S., Seidl, P. R., Correia, J. C. G., & Cerqueira, L. (2000). Molecular modelling of reagents for flotation processes. *Minerals engineering, 13*(14), 1495-1503.

Leceta, I., Guerrero, P., & De La Caba, K. (2013). Functional properties of chitosan-based films. *Carbohydrate Polymers, 93*(1), 339-346.

Le Thai, M., Chandran, G. T., Dutta, R. K., Li, X., & Penner, R. M. (2016). 100k Cycles and Beyond: Extraordinary Cycle Stability for MnO2 Nanowires Imparted by a Gel Electrolyte. *ACS Energy Letters, 1*, 57-63.

Lewandowska, K. (2009). Miscibility and thermal stability of poly (vinyl alcohol)/chitosan mixtures. *Thermochimica Acta, 493*(1), 42-48.

Liew, C. W., Ong, Y., Lim, J., Lim, C., Teoh, K., & Ramesh, S. (2013). Effect of ionic liquid on semi–crystalline poly (vinylidene fluoride-co-hexafluoropropylene) solid copolymer electrolytes. *International Journal of Electrochemical Science, 8*, 7779-7794.

Liew, C.-W., Ramesh, S., & Arof, A. (2014a). A novel approach on ionic liquid-based poly (vinyl alcohol) proton conductive polymer electrolytes for fuel cell applications. *International Journal of Hydrogen Energy, 39*(6), 2917-2928.

Liew, C.-W., Ramesh, S., & Arof, A. (2014b). Good prospect of ionic liquid based-poly (vinyl alcohol) polymer electrolytes for supercapacitors with excellent electrical, electrochemical and thermal properties. *International Journal of Hydrogen Energy,, 39*(6), 2953-2963.

Liew, C.-W., & Ramesh, S. (2015). Electrical, structural, thermal and electrochemical properties of corn starch-based biopolymer electrolytes. *Carbohydrate Polymers, 124*, 222-228.

Lim, C.-S., Teoh, K., Liew, C.-W., & Ramesh, S. (2014a). Capacitive behavior studies on electrical double layer capacitor using poly (vinyl alcohol)–lithium perchlorate based polymer electrolyte incorporated with TiO2. *Materials Chemistry and Physics, 143*(2), 661-667.

Lim, C.-S., Teoh, K., Liew, C.-W., & Ramesh, S. (2014b). Electric double layer capacitor based on activated carbon electrode and biodegradable composite polymer electrolyte. *Ionics, 20*(2), 251-258.

Liu, H., Adhikari, R., Guo, Q., & Adhikari, B. (2013). Preparation and characterization of glycerol plasticized (high-amylose) starch–chitosan films. *Journal of Food Engineering, 116*(2), 588-597.

Liu, H., Xie, F., Yu, L., Chen, L., & Li, L. (2009). Thermal processing of starch-based polymers. *Progress in polymer science, 34*(12), 1348-1368.

Liu, H., Chaudhary, D., Yusa, S.-i., & Tadé, M. O. (2011). Glycerol/starch/Na+-montmorillonite nanocomposites: a XRD, FTIR, DSC and 1 H NMR study. *Carbohydrate Polymers, 83*(4), 1591-1597.

Liu, H., Hu, Z., Su, Y., Ruan, H., Hu, R., & Zhang, L. (2017). MnO_2 nanorods/3D-rGO composite as high performance anode materials for Li-ion batteries. *Applied Surface Science, 392*, 777-784.

Liu, P., Yu, L., Liu, H., Chen, L., & Li, L. (2009). Glass transition temperature of starch studied by a high-speed DSC. *Carbohydrate Polymers, 77*(2), 250-253.

Liu, X., Cao, Y., Zheng, H., & Feng, C. (2017). Synthesis and electrochemical performances of FeVO 4· xH 2 O and $FeVO_4$· xH_2O/graphene as novel anode materials. *Materials letters, 187*, 15-19.

Lörcks, J. (1998). Properties and applications of compostable starch-based plastic material. *Polymer Degradation and Stability, 59*(1–3), 245-249.

Lopez, O., Garcia, M., Villar, M., Gentili, A., Rodriguez, M., & Albertengo, L. (2014). Thermo-compression of biodegradable thermoplastic corn starch films containing chitin and chitosan. *LWT-Food Science and Technology, 57*(1), 106-115.

Lozano-Castello, D., Cazorla-Amorós, D., Linares-Solano, A., Shiraishi, S., Kurihara, H., & Oya, A. (2003). Influence of pore structure and surface chemistry on electric double layer capacitance in non-aqueous electrolyte. *Carbon, 41*(9), 1765-1775.

Lu, D., Xiao, C., & Xu, S. (2009). Starch-based completely biodegradable polymer materials. *Express polymer letters, 3*(6), 366-375.

MacCallum, J. R., & Vincent, C. A. (1989). *Polymer electrolyte reviews* (Vol. 2): Springer Science & Business Media.

Majid, S., & Arof, A. (2005). Proton-conducting polymer electrolyte films based on chitosan acetate complexed with NH_4NO_3 salt. *Physica B: Condensed Matter, 355*(1), 78-82.

Majid, S., & Arof, A. (2007). Electrical behavior of proton-conducting chitosan-phosphoric acid-based electrolytes. *Physica B: Condensed Matter, 390*(1), 209-215.

Malathi, J., Kumaravadivel, M., Brahmanandhan, G., Hema, M., Baskaran, R., & Selvasekarapandian, S. (2010). Structural, thermal and electrical properties of PVA–$LiCF_3SO_3$ polymer electrolyte. *Journal of Non-Crystalline Solids, 356*(43), 2277-2281.

Malheiro, V. N., Caridade, S. G., Alves, N. M., & Mano, J. F. (2010). New poly (ε-caprolactone)/chitosan blend fibers for tissue engineering applications. *Acta Biomaterialia, 6*(2), 418-428.

Mano, J., Koniarova, D., & Reis, R. (2003). Thermal properties of thermoplastic starch/synthetic polymer blends with potential biomedical applicability. *Journal of Materials Science: Materials in Medicine, 14*(2), 127-135.

Marcondes, R. F., D'Agostini, P. S., Ferreira, J., Girotto, E. M., Pawlicka, A., & Dragunski, D. C. (2010). Amylopectin-rich starch plasticized with glycerol for polymer electrolyte application. *Solid State Ionics, 181*(13), 586-591.

Martino, V. P., Pollet, E., & Avérous, L. (2011). Novative biomaterials based on chitosan and poly (ε-caprolactone): elaboration of porous structures. *Journal of Polymers and the Environment, 19*(4), 819-826.

Matet, M., Heuzey, M.-C., Pollet, E., Ajji, A., & Avérous, L. (2013). Innovative thermoplastic chitosan obtained by thermo-mechanical mixing with polyol plasticizers. *Carbohydrate Polymers, 95*(1), 241-251.

Mathew, S., & Abraham, T. E. (2008). Characterisation of ferulic acid incorporated starch-chitosan blend films. *Food hydrocolloids, 22*(5), 826-835.

Matsuda, A., Honjo, H., Tatsumisago, M., & Minami, T. (1998). Electric double-layer capacitors using HClO 4-doped silica gels as a solid electrolyte. *Solid State Ionics, 113*, 97-102.

Mendoza, N., Paraguay-Delgado, F., & Hu, H. (2012). Effect of different acid and lithium salt used in polyethylene glycol–titanium oxide based solvent-free electrolytes on electrochromic performance of WO_3 thin films. *Solar Energy, 86*(4), 997-1003.

Michael, M., Jacob, M., Prabaharan, S., & Radhakrishna, S. (1997). Enhanced lithium ion transport in PEO-based solid polymer electrolytes employing a novel class of plasticizers. *Solid State Ionics, 98*(3), 167-174.

Mishra, K., Hashmi, S. A., & Rai, D. K. (2014). Studies on a proton battery using gel polymer electrolyte. *High Performance Polymers, 26*(6), 672-676.

Mishra, R., & Rao, K. (1998). Electrical conductivity studies of poly (ethyleneoxide)-poly (vinylalcohol) blends. *Solid State Ionics, 106*(1), 113-127.

Mohamad, A. A., & Arof, A. K. (2007). Plasticized alkaline solid polymer electrolyte system. *Materials Letters, 61*(14), 3096-3099.

Mohamad, A. A., Mohamed, N. S., Yahya, M. Z. A., Othman, R., Ramesh, S., Alias, Y., & Arof, A. K. (2003). Ionic conductivity studies of poly (vinyl alcohol) alkaline solid polymer electrolyte and its use in nickel–zinc cells. *Solid State Ionics, 156*(1), 171-177.

Morni, N., Mohamed, N., & Arof, A. (1997). Silver nitrate doped chitosan acetate films and electrochemical cell performance. *Materials Science and Engineering: B, 45*(1), 140-146.

Murugaraj, R., Govindaraj, G., & George, D. (2003). AC conductivity and its scaling behavior in lithium and sodium bismuthate glasses. *Materials letters, 57*(11), 1656-1661.

Muscat, D., Adhikari, B., Adhikari, R., & Chaudhary, D. (2012). Comparative study of film forming behaviour of low and high amylose starches using glycerol and xylitol as plasticizers. *Journal of Food Engineering, 109*(2), 189-201.

Naoi, K., & Morita, M. (2008). Advanced polymers as active materials and electrolytes for electrochemical capacitors and hybrid capacitor systems. *The Electrochemical Society Interface, 17*(1), 44-48.

Neto, C. d. T., Giacometti, J., Job, A., Ferreira, F., Fonseca, J., & Pereira, M. (2005). Thermal analysis of chitosan based networks. *Carbohydrate Polymers, 62*(2), 97-103.

Ng, L., & Mohamad, A. (2006). Protonic battery based on a plasticized chitosan-NH$_4$NO$_3$ solid polymer electrolyte. *Journal of Power Sources, 163*(1), 382-385.

Ng, L., & Mohamad, A. (2008). Effect of temperature on the performance of proton batteries based on chitosan-NH$_4$NO$_3$-EC membrane. *Journal of Membrane Science, 325*(2), 653-657.

Nian, Y. R., & Teng, H. (2003). Influence of surface oxides on the impedance behavior of carbon-based electrochemical capacitors. *Journal of Electroanalytical Chemistry, 540*, 119-127.

Nie, B., Stutzman, J., & Xie, A. (2005). A vibrational spectral maker for probing the hydrogen-bonding status of protonated Asp and Glu residues. *Biophysical journal, 88*(4), 2833-2847.

Nik Aziz, N., Idris, N., & Isa, M. (2010). Solid polymer electrolytes based on methylcellulose: FT-IR and ionic conductivity studies. *International Journal of Polymer Analysis and Characterization, 15*(5), 319-327.

Noor, S., Ahmad, A., Talib, I., & Rahman, M. (2011). Effect of ZnO nanoparticles filler concentration on the properties of PEO-ENR50-LiCF$_3$SO$_3$ solid polymeric electrolyte. *Ionics, 17*(5), 451-456.

Noor, I., Majid, S., Arof, A., Djurado, D., Neto, S. C., & Pawlicka, A. (2012). Characteristics of gellan gum–LiCF$_3$SO$_3$ polymer electrolytes. *Solid State Ionics, 225*, 649-653.

Noor, I., Majid, S., & Arof, A. (2013). Poly (vinyl alcohol)–LiBOB complexes for lithium–air cells. *Electrochimica Acta, 102*, 149-160.

Okajima, K., Ohta, K., & Sudoh, M. (2005). Capacitance behavior of activated carbon fibers with oxygen-plasma treatment. *Electrochimica Acta, 50*(11), 2227-2231.

Osman, Z., & Arof, A. (2003). FTIR studies of chitosan acetate based polymer electrolytes. *Electrochimica Acta, 48*(8), 993-999.

Othman, R., Basirun, W. J., Yahaya, A. H., & Arof, A. (2001). Hydroponics gel as a new electrolyte gelling agent for alkaline zinc-air cells. *Journal of Power Sources, 103*(1), 34-41.

Pandey, G., Kumar, Y., & Hashmi, S. (2011). Ionic liquid incorporated PEO based polymer electrolyte for electrical double layer capacitors: a comparative study with lithium and magnesium systems. *Solid State Ionics, 190*(1), 93-98.

Pandey, K., Lakshmi, N., & Chandra, S. (1998). A rechargeable solid-state proton battery with an intercalating cathode and an anode containing a hydrogen-storage material. *Journal of power sources*, *76*(1), 116-123.

Park, I. M., Ibáñez, A. M., Zhong, F., & Shoemaker, C. F. (2007). Gelatinization and Pasting Properties of Waxy and Non-waxy Rice Starches. *Starch-Stärke, 59*(8), 388-396.

Park, K.-W., Ahn, H.-J., & Sung, Y.-E. (2002). All-solid-state supercapacitor using a Nafion polymer membrane and its hybridization with a direct methanol fuel cell. *Journal of Power Sources, 109*(2), 500-506.

Pereira, A. G. B., Paulino, A. T., Nakamura, C. V., Britta, E. A., Rubira, A. F., & Muniz, E. C. (2011). Effect of starch type on miscibility in poly (ethylene oxide)(PEO)/starch blends and cytotoxicity assays. *Materials Science and Engineering: C*, *31*(2), 443-451.

Patro, L. N., & Hariharan, K. (2009a). AC conductivity and scaling studies of polycrystalline SnF_2. *Materials Chemistry and Physics, 116*(1), 81-87.

Patro, L. N., & Hariharan, K. (2009b). Frequency dependent conduction characteristics of mechanochemically synthesized $NaSn_2F_5$. *Materials Science and Engineering: B, 162*(3), 173-178.

Pawlicka, A., Sabadini, A. C., Raphael, E., & Dragunski, D. C. (2008). Ionic conductivity thermogravimetry measurements of starch-based polymeric electrolytes. *Molecular Crystals and Liquid Crystals, 485*(1), 804-816.

Perera, K., & Dissanayake, M. (2006). Conductivity variation of the liquid electrolyte, EC: PC: $LiCF_3SO$ with salt concentration. *Sri Lankan Journal of Physics, 7*, 1-5.

Piculell, L., Bergfeldt, K., & Nilsson, S. (1995). Factors determining phase behaviour of multi component polymer systems. *Biopolymer mixtures*, 13-35.

Ponez, L., Sentanin, F. C., Majid, S. R., Arof, A. K., & Pawlicka, A. (2012). Ion-conducting membranes based on gelatin and containing LiI/I2 for electrochromic devices. *Molecular Crystals and Liquid Crystals*, *554*(1), 239-251.

Pradhan, D. K., Choudhary, R., & Samantaray, B. (2008). Studies of dielectric relaxation and AC conductivity behavior of plasticized polymer nanocomposite electrolytes. *International Journal of Electrochemical Science, 3*(5), 597-608.

Pratap, R., Singh, B., & Chandra, S. (2006). Polymeric rechargeable solid-state proton battery. *Journal of Power Sources, 161*(1), 702-706.

Prokhorov, E., Luna-Bárcenas, G., González-Campos, J., Kovalenko, Y., García-Carvajal, Z., & Mota-Morales, J. (2016). Proton conductivity and relaxation properties of chitosan-acetate films. *Electrochimica Acta, 215*, 600-608.

Przyłuski, J., & Wieczorek, W. (1991). Proton polymeric electrolytes-a review. *Synthetic Metals, 45*(3), 323-333.

Psarras, G., Manolakaki, E., & Tsangaris, G. (2003). Dielectric dispersion and ac conductivity in-Iron particles loaded-polymer composites. *Composites Part A: Applied Science and Manufacturing, 34*(12), 1187-1198.

Qian, X., Gu, N., Cheng, Z., Yang, X., Wang, E., & Dong, S. (2001). Impedance study of $(PEO)_{10}$ $LiClO_4-Al_2O_3$ composite polymer electrolyte with blocking electrodes. *Electrochimica Acta, 46*(12), 1829-1836.

Qiao, J.-L., Yoshimoto, N., Ishikawa, M., & Morita, M. (2002). Acetic acid-doped poly (ethylene oxide)-modified poly (methacrylate): a new proton conducting polymeric gel electrolyte. *Electrochimica Acta, 47*(21), 3441-3446.

Qiao, J., Fu, J., Lin, R., Ma, J., & Liu, J. (2010). Alkaline solid polymer electrolyte membranes based on structurally modified PVA/PVP with improved alkali stability. *Polymer, 51*(21), 4850-4859.

Raducha, D., Wieczorek, W., Florjanczyk, Z., & Stevens, J. (1996). Nonaqueous H_3PO_4-doped gel electrolytes. *The Journal of Physical Chemistry, 100*(51), 20126-20133.

Rahman, M. M., Gruner, G., Al-Ghamdi, M. S., Daous, M. A., Khan, S. B., & Asiri, A. M. (2013). Chemo-sensors development based on low-dimensional codoped Mn_2O_3-ZnO nanoparticles using flat-silver electrodes. *Chemistry Central Journal, 7*(1), 1.

Raj, C. J., & Varma, K. (2010). Synthesis and electrical properties of the (PVA) 0.7 (KI) 0.3·x H_2SO_4 ($0 \leq x \leq 5$) polymer electrolytes and their performance in a primary Zn/MnO_2 battery. *Electrochimica Acta, 56*(2), 649-656.

Rajendran, S., Kannan, R., & Mahendran, O. (2001). Study on Li ion conduction behaviour of the plasticized polymer electrolytes based on poly acrylonitrile. *Materials letters, 48*(6), 331-335.

Rajendran, S., Mahendran, O., & Krishnaveni, K. (2003). Effect of CeO_2 on Conductivity of PMMA/PEO Polymer Blend Electrolytes. *Journal of New Materials for Electrochemical Systems, 6*(1), 25-28.

Rajendran, S., Sivakumar, M., & Subadevi, R. (2004). Investigations on the effect of various plasticizers in PVA-PMMA solid polymer blend electrolytes. *Materials letters, 58*(5), 641-649.

Ramesh, S., & Arof, A. (2000). Electrical conductivity studies of polyvinyl chloride-based electrolytes with double salt system. *Solid State Ionics, 136*, 1197-1200.

Ramesh, S., & Arof, A. (2001). Ionic conductivity studies of plasticized poly (vinyl chloride) polymer electrolytes. *Materials Science and Engineering: B, 85*(1), 11-15.

Ramesh, S., Liew, C. W., & Arof, A. K. (2011). Ion conducting corn starch biopolymer electrolytes doped with ionic liquid 1-butyl-3-methylimidazolium hexafluorophosphate. *Journal of non-crystalline solids, 357*(21), 3654-3660.

Ramesh, S., Shanti, R., & Morris, E. (2012). Studies on the thermal behavior of CS: LiTFSI:[Amim] Cl polymer electrolytes exerted by different [Amim] Cl content. *Solid State Sciences, 14*(1), 182-186.

Ramesh, S., Yahaya, A., & Arof, A. (2002). Dielectric behaviour of PVC-based polymer electrolytes. *Solid State Ionics, 152*, 291-294.

Rao, R. V., Ashokan, P., & Shridhar, M. (2000). Study of cellulose acetate hydrogen phthalate (CAP)-poly methyl methacrylate (PMMA) blends by thermogravimetric analysis. *Polymer Degradation and Stability, 70*(1), 11-16.

Rao, M., Geng, X., Liao, Y., Hu, S., & Li, W. (2012). Preparation and performance of gel polymer electrolyte based on electrospun polymer membrane and ionic liquid for lithium ion battery. *Journal of Membrane Science, 399*, 37-42.

Ravi, M., Song, S., Gu, K., Tang, J., & Zhang, Z. (2015). Electrical properties of biodegradable poly (ε-caprolactone): lithium thiocyanate complexed polymer electrolyte films. *Materials Science and Engineering: B, 195*, 74-83.

Ravindran, D., Vickraman, P., Sankarasubramanian, N., & Sornakumar, T. (2015). Conductivity studies on nano CdO dispersed PVC-PVdF polymer nano composite electrolytes. *International Journal of ChemTech Research, 7*(3), 1318-1322.

Rice, M., & Roth, W. (1972). Ionic transport in super ionic conductors: a theoretical model. *Journal of Solid State Chemistry, 4*(2), 294-310.

Richardson, S., & Gorton, L. (2003). Characterisation of the substituent distribution in starch and cellulose derivatives. *Analytica Chimica Acta, 497*(1), 27-65.

Rivas, B. L., Pereira, E. D., & Moreno-Villoslada, I. (2003). Water-soluble polymer-metal ion interactions. *Progress in polymer science, 28*(2), 173-208.

Rotta, J., Minatti, E., & Barreto, P. L. M. (2011). Determination of structural and mechanical properties, diffractometry, and thermal analysis of chitosan and hydroxypropylmethylcellulose (HPMC) films plasticized with sorbitol. *Food Science and Technology (Campinas), 31*(2), 450-455.

Roscher, M. A., Bohlen, O., & Vetter, J. (2011). OCV hysteresis in Li-ion batteries including two-phase transition materials. *International Journal of Electrochemistry, 2011.*

Sakurai, K., Maegawa, T., & Takahashi, T. (2000). Glass transition temperature of chitosan and miscibility of chitosan/poly (N-vinyl pyrrolidone) blends. *Polymer, 41*(19), 7051-7056.

Salleh, E., Muhamad, I. I., & Khairuddin, N. (2009). Structural characterization and physical properties of antimicrobial (AM) starch-based films. *World Academy of Science, Engineering and Technology, 55*, 432-440.

Samsudin, A., & Isa, M. (2012). Structural and electrical properties of carboxy methylcellulose-dodecyltrimethyl ammonium bromide-based biopolymer electrolytes system. *International Journal of Polymeric Materials, 61*(1), 30-40.

Samsudin, A., Lai, H., & Isa, M. (2014). Biopolymer materials based carboxymethyl cellulose as a proton conducting biopolymer electrolyte for application in rechargeable proton battery. *Electrochimica Acta, 129*, 1-13.

Samsudin, A., Khairul, W. M., & Isa, M. (2012). Characterization on the potential of carboxy methylcellulose for application as proton conducting biopolymer electrolytes. *Journal of Non-Crystalline Solids, 358*(8), 1104-1112.

Sarasam, A., & Madihally, S. V. (2005). Characterization of chitosan–polycaprolactone blends for tissue engineering applications. *Biomaterials, 26*(27), 5500-5508.

Sekhar, P. C., Kumar, P. N., & Sharma, A. (2012). Effect of plasticizer on conductivity and cell parameters of (PMMA+ $NaClO_4$) polymer electrolyte system. *IOSR Journal of Applied Physics, 2*, 1-6.

Sell, S. A., Wolfe, P. S., Garg, K., McCool, J. M., Rodriguez, I. A., & Bowlin, G. L. (2010). The use of natural polymers in tissue engineering: a focus on electrospun extracellular matrix analogues. *Polymers, 2*(4), 522-553.

Selvasekarapandian, S., Hirankumar, G., Kawamura, J., Kuwata, N., & Hattori, T. (2005). 1 H solid state NMR studies on the proton conducting polymer electrolytes. *Materials letters, 59*(22), 2741-2745.

Sen, A., & Bhattacharya, M. (2000). Residual stresses and density gradient in injection molded starch/synthetic polymer blends. *Polymer, 41*(26), 9177-9190.

Shalu, Singh, V. K., & Singh, R. K. (2015). Development of ion conducting polymer gel electrolyte membranes based on polymer PVdF-HFP, BMIMTFSI ionic liquid and the Li-salt with improved electrical, thermal and structural properties. *Journal of Materials Chemistry C, 3*, 7305-7318.

Shuhaimi, N., Majid, S., & Arof, A. (2009). On complexation between methyl cellulose and ammonium nitrate. *Materials Research Innovations, 13*(3), 239-242.

Shuhaimi, N., Teo, L., Majid, S., & Arof, A. (2010). Transport studies of NH_4NO_3 doped methyl cellulose electrolyte. *Synthetic Metals, 160*(9), 1040-1044.

Shuhaimi, N., Teo, L., Woo, H., Majid, S., & Arof, A. (2012). Electrical double-layer capacitors with plasticized polymer electrolyte based on methyl cellulose. *Polymer bulletin, 69*(7), 807-826.

Shukur, A. Fadhlullah, M. (2015). *Characterization of ion conducting solid biopolymer electrolytes based on starch-chitosan blend and application in electrochemical devices/Muhammad Fadhlullah bin Abd. Shukur.* University of Malaya.

Shukur, M., Ithnin, R., Illias, H., & Kadir, M. (2013). Proton conducting polymer electrolyte based on plasticized chitosan–PEO blend and application in electrochemical devices. *Optical Materials, 35*(10), 1834-1841.

Shukur, M., Ithnin, R., & Kadir, M. (2014a). Electrical properties of proton conducting solid biopolymer electrolytes based on starch–chitosan blend. *Ionics, 20*(7), 977-999.

Shukur, M., Ithnin, R., & Kadir, M. (2014b). Electrical characterization of corn starch-LiOAc electrolytes and application in electrochemical double layer capacitor. *Electrochimica Acta, 136*, 204-216.

Shukur, M., Ibrahim, F., Majid, N., Ithnin, R., & Kadir, M. (2013). Electrical analysis of amorphous corn starch-based polymer electrolyte membranes doped with LiI. *Physica Scripta, 88*(2), 025601.

Shukur, M., & Kadir, M. (2015a). Electrical and transport properties of NH₄Br-doped cornstarch-based solid biopolymer electrolyte. *Ionics, 21*(1), 111-124.

Shukur, M., & Kadir, M. (2015b). Hydrogen ion conducting starch-chitosan blend based electrolyte for application in electrochemical devices. *Electrochimica Acta, 158*, 152-165.

Shukur, M., Majid, N., Ithnin, R., & Kadir, M. (2013). Effect of plasticization on the conductivity and dielectric properties of starch–chitosan blend biopolymer electrolytes infused with NH₄Br. *Physica Scripta, 2013*(T157), 014051.

Shukur, M. F., Yusof, Y. M., Zawawi, S. M. M., Illias, H. A., & Kadir, M. F. Z. (2013). Conductivity and transport studies of plasticized chitosan-based proton conducting biopolymer electrolytes. *Physica Scripta, 2013*(T157), 014050.

Simon, P., & Gogotsi, Y. (2008). Materials for electrochemical capacitors. *Nature materials, 7*(11), 845-854.

Singh, P., Chandra, S., & Chandra, A. (2002). Polymer electrolyte composites with dispersed semiconductors. *Journal of Materials Science Letters, 21*(18), 1393-1395.

Sivaraman, P., Hande, V., Mishra, V., Rao, C. S., & Samui, A. (2003). All-solid supercapacitor based on polyaniline and sulfonated poly (ether ether ketone). *Journal of Power Sources, 124*(1), 351-354.

Speight, J. G., & Speight, J. (2002). *Chemical and process design handbook*: McGraw-Hill New York.

Stephan, A. M. (2006). Review on gel polymer electrolytes for lithium batteries. *European Polymer Journal, 42*(1), 21-42.

Stuchell, Y. M., & Krochta, J. M. (1994). Enzymatic treatments and thermal effects on edible soy protein films. *Journal of Food Science, 59*(6), 1332-1337.

Subramaniam, R. T., Morris, E., Yee, L. P., & Chiam-Wen, L. (2012). Characterization of High Molecular Weight Poly (vinyl Chloride)-Lithium Tetraborate Electrolyte Plasticized by Propylene Carbonate: *INTECH Open Access Publisher*.

Sudhakar, Y., & Selvakumar, M. (2012). Lithium perchlorate doped plasticized chitosan and starch blend as biodegradable polymer electrolyte for supercapacitors. *Electrochimica Acta, 78*, 398-405.

Sudhakar, Y., Selvakumar, M., & Bhat, D. K. (2013). LiClO₄-doped plasticized chitosan and poly (ethylene glycol) blend as biodegradable polymer electrolyte for supercapacitors. *Ionics, 19*(2), 277-285.

Sudhakar, Y., & Selvakumar, M. (2013). Ionic conductivity studies and dielectric studies of Poly (styrene sulphonic acid)/starch blend polymer electrolyte containing LiClO4. *Journal of Applied Electrochemistry, 43*(1), 21-29.

Sugimoto, M., Morimoto, M., Sashiwa, H., Saimoto, H., & Shigemasa, Y. (1998). Preparation and characterization of water-soluble chitin and chitosan derivatives. *Carbohydrate Polymers, 36*(1), 49-59.

Suh, J.-K. F., & Matthew, H. W. (2000). Application of chitosan-based polysaccharide biomaterials in cartilage tissue engineering: a review. *Biomaterials, 21*(24), 2589-2598.

Suriani, I., & Mohd, R. (2012). Thermolysis and conductivity studies of poly (ethylene oxide)(PEO) based polymer electrolytes doped with carbon nanotubes. *International Journal of Electrochemical Science, 7*, 2596-2615.

Syahidah, S. N. & Majid, S. R. (2013). Super-capacitive electro-chemical performance of polymer blend gel polymer electrolyte (GPE) in carbon-based electrical double-layer capacitors. *Electrochemical Acta, 112*, 678-685.

Tabuchi, J., Saito, T., Kibi, Y., & Ochi, A. (1993). Large capacitance electric double layer capacitor using activated carbon/carbon composite. *Components, Hybrids, and Manufacturing Technology, IEEE Transactions on, 16*(4), 431-436.

Taib, N. U., & Idris, N. H. (2014). Plastic crystal-solid biopolymer electrolytes for rechargeable lithium batteries. *Journal of Membrane Science, 468*, 149-154.

Tambelli, C., Donoso, J., Regiani, A., Pawlicka, A., Gandini, A., & LeNest, J.-F. (2001). Nuclear magnetic resonance and conductivity study of HEC/polyether-based polymer electrolytes. *Electrochimica Acta, 46*(10), 1665-1672.

Tan, H., Aziz, A. A., & Aroua, M. (2013). Glycerol production and its applications as a raw material: A review. *Renewable and Sustainable Energy Reviews, 27*, 118-127.

Tarabay, J., & Karami, N. (2015). *Nickel Metal Hydride battery: Structure, chemical reaction, and circuit model.* Paper presented at the Technological Advances in Electrical, Electronics and Computer Engineering (TAEECE), 2015 Third International Conference on.

Teoh, K., Ramesh, S., & Arof, A. (2012). Investigation on the effect of nanosilica towards corn starch–lithium perchlorate-based polymer electrolytes. *Journal of Solid State Electrochemistry, 16*(10), 3165-3170.

Tian, H., Tang, Z., Zhuang, X., Chen, X., & Jing, X. (2012). Biodegradable synthetic polymers: preparation, functionalization and biomedical application. *Progress in polymer science, 37*(2), 237-280.

Tiwari, T., Srivastava, N., & Srivastava, P. (2011). Electrical transport study of potato starch-based electrolyte system. *Ionics, 17*(4), 353-360.

Tobishima, S.-I., Hayashi, K., Nemoto, Y., & Yamaki, J.-I. (1997). Ethylene carbonate/propylene carbonate/2-methyl-tetrahydrofuran ternary mixed solvent electrolyte for rechargeable lithium/amorphous V_2O_5-P_2O_5 cells. *Electrochimica Acta, 42*(11), 1709-1716.

Trivedi, D. (1998). Influence of the anion on polyaniline. *Journal of Solid State Electrochemistry, 2*(2), 85-87.

Tuhin, M. O., Rahman, N., Haque, M., Khan, R. A., Dafader, N., Islam, R., Nurnabi, M., Tonny, W. (2012). Modification of mechanical and thermal property of chitosan-starch blend films. *Radiation Physics and Chemistry, 81*(10), 1659-1668.

Urban, P. M., Funke, A., Müller, J. T., Himmen, M., & Docter, A. (2001). Catalytic processes in solid polymer electrolyte fuel cell systems. *Applied Catalysis A: General, 221*(1–2), 459-470.

van den Broek, L. A., Knoop, R. J., Kappen, F. H., & Boeriu, C. G. (2015). Chitosan films and blends for packaging material. *Carbohydrate Polymers, 116*, 237-242.

Velazquez-Morales, P., Le Nest, J.-F., & Gandini, A. (1998). Polymer electrolytes derived from chitosan/polyether networks. *Electrochimica Acta, 43*(10), 1275-1279.

Vieira, M. G. A., da Silva, M. A., dos Santos, L. O., & Beppu, M. M. (2011). Natural-based plasticizers and biopolymer films: A review. *European Polymer Journal, 47*(3), 254-263.

Vilaseca, F., Mendez, J., Pelach, A., Llop, M., Canigueral, N., Girones, J., Turon, X., Mutje, P. (2007). Composite materials derived from biodegradable starch polymer and jute strands. *Process Biochemistry, 42*(3), 329-334.

Vincent, C. A. (1987). Polymer electrolytes. *Progress in solid state chemistry, 17*(3), 145-261.

Vicentini, N., Dupuy, N., Leitzelman, M., Cereda, M., & Sobral, P. (2005). Prediction of cassava starch edible film properties by chemometric analysis of infrared spectra. *Spectroscopy Letters, 38*(6), 749-767.

Vonau, C., Zosel, J., Paramasivam, M., Ahlborn, K., Gerlach, F., Vashook, V., & Guth, U. (2012). Polymer based materials for solid electrolyte sensors. *Solid State Ionics, 225*(0), 337-341.

Vroman, I., & Tighzert, L. (2009). Biodegradable polymers. *Materials, 2*(2), 307-344.

Walker Jr, C. W., & Salomon, M. (1995). Plasticizers for Solid Polymer Electrolytes: DTIC Document.

Wang, S., Shen, L., Tong, Y., Chen, L., Phang, I., Lim, P., & Liu, T. (2005). Biopolymer chitosan/montmorillonite nanocomposites: preparation and characterization. *Polymer Degradation and Stability, 90*(1), 123-131.

Watanabe, M., Nagano, S., Sanui, K., & Ogata, N. (1988). Estimation of Li+ transport number in polymer electrolytes by the combination of complex impedance and potentiostatic polarization measurements. *Solid State Ionics, 28*, 911-917.

Watanabe, M., & Nishimoto, A. (1995). Effects of network structures and incorporated salt species on electrochemical properties of polyether-based polymer electrolytes. *Solid State Ionics, 79*, 306-312.

Williard, N., He, W., Hendricks, C., & Pecht, M. (2013). Lessons learned from the 787 Dreamliner issue on lithium-ion battery reliability. *Energies, 6*(9), 4682-4695.

Winie, T., & Arof, A. (2004). Dielectric behaviour and AC conductivity of LiCF3SO3 doped H-chitosan polymer films. *Ionics, 10*(3-4), 193-199.

Winie, T., Ramesh, S., & Arof, A. K. (2009). Studies on the structure and transport properties of hexanoyl chitosan-based polymer electrolytes. *Physica B: Condensed Matter, 404*(21), 4308-4311.

Woo, H., Majid, S., & Arof, A. (2011a). Conduction and thermal properties of a proton conducting polymer electrolyte based on poly (ε-caprolactone). *Solid State Ionics, 199*, 14-20.

Woo, H., Majid, S., & Arof, A. (2011b). Transference number and structural analysis of proton conducting polymer electrolyte based on poly (ε-caprolactone). *Materials Research Innovations, 15*(s2), s49-s54.

Woo, H., Majid, S., & Arof, A. (2012). Dielectric properties and morphology of polymer electrolyte based on poly (ε-caprolactone) and ammonium thiocyanate. *Materials Chemistry and Physics, 134*(2), 755-761.

Woo, H., Majid, S., & Arof, A. (2013). Effect of ethylene carbonate on proton conducting polymer electrolyte based on poly (ε-caprolactone)(PCL). *Solid State Ionics, 252*, 102-108.

Wright, P. V. (1975). Electrical conductivity in ionic complexes of poly (ethylene oxide). *British Polymer Journal, 7*(5), 319-327.

Wu, I. D., & Chang, F.-C. (2007). Determination of the interaction within polyester-based solid polymer electrolyte using FTIR spectroscopy. *Polymer, 48*(4), 989-996.

Wu, Y. P., Ji, M. Q., Qi, Q., Wang, Y. Q., & Zhang, L. Q. (2004). Preparation, Structure, and Properties of Starch/Rubber Composites Prepared by Co-Coagulating Rubber Latex and Starch Paste. *Macromolecular rapid communications, 25*(4), 565-570.

Xi, J., Qiu, X., Li, J., Tang, X., Zhu, W., & Chen, L. (2006). PVDF–PEO blends based microporous polymer electrolyte: Effect of PEO on pore configurations and ionic conductivity. *Journal of Power Sources, 157*(1), 501-506.

Xu, K. (2004). Nonaqueous liquid electrolytes for lithium-based rechargeable batteries. *Chemical reviews, 104*(10), 4303-4418.

Xu, M., Ivey, D., Xie, Z., & Qu, W. (2015). Rechargeable Zn-air batteries: Progress in electrolyte development and cell configuration advancement. *Journal of Power Sources, 283*, 358-371.

Xu, Y., & Hanna, M. A. (2005). Physical, mechanical, and morphological characteristics of extruded starch acetate foams. *Journal of Polymers and the Environment, 13*(3), 221-230.

Xu, Y., Kim, K. M., Hanna, M. A., & Nag, D. (2005). Chitosan-starch composite film: preparation and characterization. *Industrial Crops and Products, 21*(2), 185-192.

Yamanaka, N., Kawano, R., Kubo, W., Masaki, N., Kitamura, T., Wada, Y., Watanabe, M., & Yanagida, S. (2007). Dye-sensitized TiO2 solar cells using imidazolium-type ionic liquid crystal systems as effective electrolytes. *The Journal of Physical Chemistry B, 111*(18), 4763-4769.

Yang, D.-j., Fu, X.-k., & Gong, Y.-f. (2008). Study on the preparation and performances of P (VAc-MMA) polymer electrolytes for lithium ion battery. *Chinese Journal of Polymer Science, 26*(04), 375-380.

Yang, H., Yu, C., Song, Q., Xia, Y., Li, F., Chen, Z., Li, X., Yi, T., & Huang, C. (2006). High-temperature and long-term stable solid-state electrolyte for dye-sensitized solar cells by self-assembly. *Chemistry of Materials, 18*(22), 5173-5177.

Yap, K. S. (2012). *Characteristics of PMMA-grafted natural rubber polymer electrolytes/Yap Kiat Sen.* University of Malaya.

Yin, Y. J., Yao, K. D., Cheng, G. X., & Ma, J. B. (1999). Properties of polyelectrolyte complex films of chitosan and gelatin. *Polymer International, 48*(6), 429-432.

Yu, L., Dean, K., & Li, L. (2006). Polymer blends and composites from renewable resources. *Progress in polymer science, 31*(6), 576-602.

Zeleznak, K., & Hoseney, R. (1987). The Glass Transition in Starch1. *Cereal Chem, 64*(2), 121-124.

Zhai, M., Yoshii, F., & Kume, T. (2003). Radiation modification of starch-based plastic sheets. *Carbohydrate Polymers, 52*(3), 311-317.

Zhai, M., Zhao, L., Yoshii, F., & Kume, T. (2004). Study on antibacterial starch/chitosan blend film formed under the action of irradiation. *Carbohydrate Polymers, 57*(1), 83-88.

Zhang, H., & Wang, J. (2009). Vibrational spectroscopic study of ionic association in poly (ethylene oxide)–NH4SCN polymer electrolytes. *Spectrochimica Acta Part A: Molecular and Biomolecular Spectroscopy, 71*(5), 1927-1931.

Zhang, P., Yang, L., Li, L., Ding, M., Wu, Y., & Holze, R. (2011). Enhanced electrochemical and mechanical properties of (PVDF-HFP)-based composite polymer electrolytes with SiO 2 nanowires. *Journal of Membrane Science, 379*(1), 80-85.

Zobel, H., Young, S., & Rocca, L. (1988). Starch gelatinization: An X-ray diffraction study. *Cereal Chemistry, 65*(6), 443-446.

LIST OF PUBLICATIONS AND PAPERS PRESENTED

List of publications related to the thesis:

Yusof, Y. M., Illias, H., Shukur, M., & Kadir, M. (2016). Characterization of starch-chitosan blend-based electrolyte doped with ammonium iodide for application in proton batteries. *Ionics*, 1-17.

Yusof, Y. M., Shukur, M., Illias, H., & Kadir, M. (2014). Conductivity and electrical properties of corn starch-chitosan blend biopolymer electrolyte incorporated with ammonium iodide. *Physica Scripta, 89*(3), 035701.

Yusof, Y. M., Majid, N. A., Kasmani, R. M., Illias, H. A., & Kadir, M. F. Z. (2014). The effect of plasticization on conductivity and other properties of starch/chitosan blend biopolymer electrolyte incorporated with ammonium iodide. *Molecular Crystals and Liquid Crystals*, *603*(1), 73-88.

Other publications:

Yusof, Y. M., Illias, H. A., & Kadir, M. F. Z. (2014). Incorporation of NH_4Br in PVA-chitosan blend-based polymer electrolyte and its effect on the conductivity and other electrical properties. *Ionics*, *20*(9), 1235-1245.

Yusof, Y. M., Illias, H., Shukur, M., & Kadir, M. (2016). Electrochemical Characterizations and the effect of glycerol in biopolymer electrolytes based on methylcellulose-potato starch blend**,"** *Molecular Crystals and Liquid Crystals*, 627(1), 220-233.

Shukur, M. F., **Yusof, Y. M.**, Zawawi, S. M. M., Illias, H. A., & Kadir, M. F. Z. (2013). Conductivity and transport studies of plasticized chitosan-based proton conducting biopolymer electrolytes. *Physica Scripta*, *2013*(T157), 014050.

List of Conferences

1.   Yusof, Y. M., Shukur, M. F., Illias, H. A., Kadir, M. F. Z., "Conductivity And Electrical Properties Of Corn Starch-Chitosan Blend Biopolymer Electrolyte Incorporated With Ammonium Iodide," 21st World Forum on Advanced Materials (POLYCHAR 21), Gwangju, Korea (March 2013).

2.   Yusof, Y. M., Illias, H. A., Kadir, M. F. Z., "Incorporation of NH_4Br in PVA-Chitosan Blend-Based Polymer Electrolyte and Its Effect on The Conductivity and Other Electrical Properties," 4th International Conference On Functional Materials And Devices (ICFMD2013), Penang, Malaysia (May 2013).

3.   Yusof, Y. M., "Potential Applications of Ammonium Iodide as Proton Provider in Starch-Chitosan Blend Based Biopolymer Electrolyte in Electrochemical Devices," 7th HOPE Meeting with Nobel Laureates (HOPE), Tokyo, Japan (March 2015).